TAMPEREEN TEKNILLINEN YLIOPISTO
TAMPERE UNIVERSITY OF TECHNOLOGY

Ilkka Rytöluoto

Large-Area Multi-Breakdown Characterization of Polymer Films: A New Approach for Establishing Structure–Processing–Breakdown Relationships in Capacitor Dielectrics

Julkaisu 1356 • Publication 1356

Tampere 2015

Tampereen teknillinen yliopisto. Julkaisu 1356
Tampere University of Technology. Publication 1356

Ilkka Rytöluoto

Large-Area Multi-Breakdown Characterization of Polymer Films: A New Approach for Establishing Structure–Processing–Breakdown Relationships in Capacitor Dielectrics

Thesis for the degree of Doctor of Science in Technology to be presented with due permission for public examination and criticism in Tietotalo Building, Auditorium TB109, at Tampere University of Technology, on the 8th of January 2016, at 12 noon.

Tampereen teknillinen yliopisto - Tampere University of Technology
Tampere 2015

Supervisors

Adjunct Professor Kari Lahti
Department of Electrical Engineering
Tampere University of Technology

Associate Professor Kari Kannus
Department of Electrical Engineering
Tampere University of Technology

Pre-examiners

Professor Alun Vaughan
Electronics and Computer Science
Faculty of Physical Sciences and Engineering
University of Southampton

Professor Stanislaw Gubanski
High Voltage Engineering
Department of Materials and Manufacturing Technology
Chalmers University of Technology

Opponent

Professor Emeritus Keith Nelson
Department of Electrical, Computer and Systems Engineering
Rensselaer Polytechnic Institute

ISBN 978-952-15-3637-3 (printed)
ISBN 978-952-15-3663-2 (PDF)
ISSN 1459-2045

Abstract

The ever-growing need for high-energy density and high operation temperature capacitive energy storage for next-generation applications has necessitated research and development on new dielectric materials for film capacitors. Consequently, various new approaches offering unique ways to tailor dielectric properties of polymers have recently emerged, and new materials such as dielectric polymer nanocomposites (PNC) are envisioned as potential next-generation dielectrics. Establishment of optimized formulation and processing conventions is however necessary in order to achieve improvement in dielectric breakdown properties. Importantly however, such material development puts dielectric breakdown strength assessment of polymer films in a central role in guiding material development process towards highly optimized functional materials. This is not a trivial task though, as the current state-of-the-art breakdown strength measurement techniques rarely provide statistically sufficient amounts of breakdown data from the application point-of-view, thus leading to impaired evaluation of the practical breakdown performance in film capacitors.

In this thesis, a new large-area multi-breakdown measurement method enabling detailed dielectric breakdown characterization of polymer films is developed and evaluated. Various aspects encompassing sample film preparation, measurement procedure, breakdown progression, discharge event characterization, breakdown field determination, data validation and statistical analysis are systematically and critically discussed. A data qualification process based on the self-healing discharge energy and breakdown voltage characteristics is developed and shown to be a sensible and convenient way to exclude non-breakdown events from the measurement data prior to Weibull statistical analysis. The measurement method is shown to enable high-statistical-accuracy breakdown characterization of both metallized and non-metallized polymer films of different nature, including laboratory-scale, pilot-scale and commercial-grade capacitor films. Statistical aspects on the area dependence are discussed and the problematic nature of Weibull area-extrapolation of small-area breakdown data to represent larger film areas is exemplified. The fundamental differences between the large-area multi-breakdown and the small-area single-breakdown measurement methods and the statistical aspects thereof are analyzed in more detail by the Monte Carlo simulation method.

The large-area multi-breakdown method is utilized to carry out a comprehensive analysis on structure–processing–breakdown relationships in conventional polymer and polymer nanocomposite films. Analysis on the effects of film processing, structure and morphology on the large-area multi-breakdown response of cast- and bi-axially oriented isotactic polypropylene (PP) films emphasizes the determining effect of processing-dependent film morphology in large-area dielectric breakdown response of PP films. Commercial capacitor-grade bi-axially oriented polypropylene (BOPP) films are shown to exhibit differences in breakdown distribution structure and weak point behavior in comparison to the laboratory-scale BOPP films, presumably due to differences in raw

material, additives, thermal history and processing. Breakdown characterization of commercial metallized polymer films as a function of inter-layer pressure also emphasizes the importance of careful breakdown characterization under authentic operation stresses in order to ensure proper design and operation in practical applications.

BOPP-based polymer nanocomposite (PNC) films are studied with a particular emphasis on the effects of various compositional, structural and film processing factors on the breakdown behavior of laboratory- and pilot-scale melt-compounded BOPP nanocomposite films incorporating silica and/or calcium carbonate nanofillers. The optimum nano-filler content is found to reside at the low fill-fraction range (∼1 wt-%), however, the fill-fraction itself is not the only determining factor, as compounds with equal nanoparticle content but with differences in e.g. compounder screw speed are found to exhibit large differences in breakdown response. Indications of possible silica-antioxidant interaction are also reported. Structural imaging of the films shows that nano-structural features cannot solely explain the observed large-area breakdown behavior — this aspect points towards large-area approach being necessary for the imaging techniques as well in order to reliably establish a link between structural properties and engineering breakdown strength. The results point out that up-scaling of PNC production is sensible with conventional melt-blending technology, although further development and optimization of nanocomposite formulations and processing are seen as necessary. Analysis on the ramp-rate-dependence of the breakdown response in dielectric polymer nanocomposite films also provides perspective on the importance of careful breakdown assessment when dielectric films of more complex internal structure are studied.

Preface

This dissertation work was carried out at the Department of Electrical Engineering (DEE) at Tampere University of Technology (TUT) during the years 2012–2015. The research has been conducted under various research projects in co-operation with the Finnish Funding Agency for Innovation (TEKES), VTT Technical Research Centre of Finland, Borealis AG, TUT / Optoelectronics Research Centre (ORC), University of Jyväskylä / Nanoscience Centre, DuPont Teijin Films, Terichem Tervakoski Oy, Alstom Grid Oy, KEMET Electronics Oy, Sachtleben Pigments Oy and Extron Engineering Oy. Additional funding in the form of personal grants from Ulla Tuominen Foundation, the Finnish Science Foundation for Economics and Technology (KAUTE) and Walter Ahlström Foundation are greatly appreciated.

Firstly I want to express my sincere gratitude to my initial supervisor late Associate Professor Kari Kannus for originally accepting me into the high-voltage research group of DEE to work on my M.Sc. thesis in 2011 and thereafter for giving me the opportunity to continue my work towards the doctoral degree – his support and suggestions along the way were highly valued. Above all, my deepest gratitude is addressed to my main supervisor Adjunct Professor Kari Lahti for his outstanding guidance, encouragement and kindness throughout my academic career. I am most indebted to him for his expertise on high voltage engineering and for always keeping his office door open for inspiring discussions regarding my thesis work; without his efforts this thesis would be much less than what is presented here. I am also grateful to the thesis pre-examiners, Prof. Alun Vaughan from the University of Southampton and Prof. Stanislaw Gubanski from the Chalmers Technical University, for their valuable comments and suggestions. Furthermore, I am indebted to Prof. Emer. Keith Nelson for agreeing to act as an opponent in the public examination of my thesis.

Among all my colleagues, I am most indebted to my high-voltage colleagues M.Sc. Minna Niittymäki, M.Sc. Hannes Ranta and M.Sc. Mikael Ritamäki for their valuable support and contributions both in work- and non-work-related matters; it was the high team spirit and humor which kept me going everyday and I'm sure the friendships we developed will last a lifetime. I also want to thank other personnel at DEE, in particular Pentti Kivinen, Pekka Nousiainen and Hannu Nieminen for their craftsmanship in building the test benches used for the multi-breakdown measurements, Terhi Salminen, Nitta Laitinen and Merja Teimonen for taking care of practical matters and all the others for providing an enjoyable working atmosphere.

I have been very fortunate to collaborate with and learn from a number of experts in various research projects during my research career. I hereby want to thank all the participants of the NANOPOWER project and the various industry-driven projects I've been involved in for their efforts and feedback. While a complete list of all the individuals would be too expansive to be included here, the following persons deserve special mention. I especially want to thank Lic.Sc.(Tech) Mikko Karttunen, M.Sc. Satu Pasanen and

Lic.Sc.(Tech) Outi Härkki from VTT Technical Research Centre of Finland for their valuable work on material processing and for their superb cooperative attitude; your efforts were easily one of the key factors for me to get things done during my thesis work. D.Sc.(Tech) Suvi Virtanen and Prof. Mika Pettersson from University of Jyväskylä are thanked for their insightful work and comments on structural imaging of polymer nanocomposites and for co-authoring some of my papers. I am particularly grateful for the collaboration and the many interesting discussions with the people from Borealis AG, especially Antonis Gitsas, Franck Jacobs, Gunilla Herrgård, Torvald Vestberg, Päivi Pitkänen, Peter Denifl, Alexander Reznichenko and Esa Kokko. Lucien Schosseler from DuPoint Teijin Films is also greatly acknowledged for the collaboration and insightful discussions on the self-healing breakdown characteristics of metallized polymer films.

The last paragraph is devoted for all the people outside the work who deserve special mention. I am very grateful to all my friends for all the unforgettable experiences we've had together so far; many thanks for keeping my head (somewhat) intact, you know who you are. Last but definitely not least I would like to express my warmest gratitude to my parents, Irja and Risto, and my sister Raisa for their immense love, support and encouragement throughout my studies and in my life; words cannot begin to describe my appreciation and gratitude for all you have done for me.

Tampere, October 2015

Ilkka Rytöluoto

Contents

Acronyms

2-p	2-parameter
Al_2O_3	Alumina
ArPTU	Aromatic polythiourea
ArPU	Aromatic polyurea
aPP	Atactic polypropylene
$BaTiO_3$	Barium titanate
BOPP	Bi-axially oriented polypropylene
$CaCO_3$	Calcium carbonate
x-PP	Crosslinked polypropylene-BSt copolymer
CDF	Cumulative distribution function
DMDCS	Dichlorodimethylsilane
DBS	Dielectric breakdown strength
PNC	Dielectric polymer nanocomposites
HMDS	Hexamethyldisilazane
HVPS	High voltage power source
HVP	High voltage probe
HVAC	High-voltage alternating current
HVDC	High-voltage direct current
HEV	Hybrid electric vehicle
PP-OH	Hydroxyl-functionalized polypropylene
iPP	Isotactic polypropylene
K-S test	Kolmogorov-Smirnov statistical test
MD	Machine direction
MDO	Machine direction orientation
MgO	Magnesia
MLE	Maximum-likelihood estimation
MFR	Melt flow rate
Meta-ArPU	Meta-aromatic polyurea
MOS	Metal-oxide-semiconductor
CH_3	Methyl
MS	Methoxysilane
NANOPOWER	”Novel Polymer Nanocomposites for Power Capacitors”
NLR	Non-linear regression
Thio	Oligothiophene
PD	Partial discharge
Irganox 1010	Phenolic antioxidant; pentaerythritol tetrakis(3-(3,5-di-tert-butyl-4-hydroxyphenyl)propionate)
P(VDF-CTFE)	Poly(vinylidene fluoride-chlorotrifluoroethylene)

P(VDF-HFP)	Poly(vinylidene fluoride-hexafluoropropylene)
P(VDF-TrFE-CFE)	Poly(vinylidene fluoride-trifluoroethylene-chlorofluoroethylene)
P4VP	Poly-4-vinylpyridine
PC	Polycarbonate
PE	Polyethylene
PEN	Polyethylene naphthalate
PET	Polyethylene terephthalate
PGMA	Polyglycidylmethacrylate
PI	Polyimide
aHNP	Polymer-grafted nanoparticle
PMMA	Polymethyl methacrylate
PMP	Polymethylpentene
PPS	Polyphenylene sulphide
PP	Polypropylene
PS	Polystyrene
PTFE	Polytetrafluoroethylene
PVDF	Polyvinylidene fluoride
SEM	Scanning electron microscopy
SiO_2	Silica
SD	Standard deviation
sPP	Syndiotactic polypropylene
TiO_2	Titania
TEM	Transmission electron microscopy
TD	Transverse direction
TDO	Transverse direction orientation
TES	Triethoxyvinylsilane
TrFE	Trifluoroethylene
TMPS	Trimethoxy(propyl)silane
Irgafos 168	Phosphite antioxidant; tris(2,4-ditert-butylphenyl)phosphite
WAXS	Wide-angle X-ray scattering
VI	Vinylsilane

Nomenclature

α	Weibull scale parameter
$\alpha(P)$	A function which relates inter-layer pressure to the discharge energy
α_i	Weibull scale parameter of sub-population i
β	Weibull shape parameter
β_i	Weibull shape parameter of sub-population i
γ	Weibull location parameter (threshold field)
ρ_i	Breakdown channel resistivity
ρ_m	Metallization resistivity
$\tan\delta$	Dissipation factor
τ_{sh}	Discharge duration
ε_0	Vacuum permittivity ($\approx 8.854 \times 10^{-12}\,\mathrm{F/m}$)
ε_r	Dielectric constant (relative permittivity)
A	Active area
A_s	Sample area
A_{tot}	Total film area
A_c	Capacitor area
A_m	Metal hole area
A_{sh}	De-metallized area
a	Weibull shape parameter of time; experimentally definable constant; left-truncation point
a_{min}	Minimum energy threshold
b	Weibull shape parameter of voltage (electric field); voltage dependence coefficient (self-healing process); slope of the power regression line; right-truncation point
C	Capacitance, constant of proportionality
C_{dut}	Capacitance of the test capacitor
C_{eff}	Total effective capacitance partaking in the self-healing process
C_o	Output capacitance of the DC high-voltage supply
C_p	Parallel capacitance
C_s	Stray capacitance of the measurement system
c	Experimentally definable constant
D	Electric displacement
D_{max}	Electric displacement at the highest field (i.e. breakdown field E_{bd})
d_f	Thickness of the dielectric layer
d_{avg}	Average film thickness
d_{cast}	Target cast film thickness
E	Electric field strength
$E_{5\%}$	5 % breakdown (field) percentile
$E_{63.2\%}$	63.2 % breakdown (field) percentile

$E_{95\%}$	95 % breakdown (field) percentile
E_{bd}	Breakdown field
$E_{\min}$	Weakest measured breakdown field
E_{sh}	Discharge energy
$F(i,n)$	Failure probability
$F_i(x)$	Cumulative failure distribution
F_{tot}	Total compressive force
g	Gravitation constant ($9.81\,\mathrm{m/s^2}$)
H_0	Null hypothesis
$h(t)$	Weibull hazard function
h_m	Metallization thickness
I^{α}_{hkl}	Intensity of α-diffraction peak with (hkl) defining the Miller's index of the crystallographic plane
I^{β}_{hkl}	Intensity of β-diffraction peak with (hkl) defining the Miller's index of the crystallographic plane
I_{peak}	Peak current
$i_d(t)$	Discharge current
k	Experimentally definable constant
k_β	β-form crystal index
L_f	Free-space length
m	Total mass of the test capacitor and the lower steel plate
N_i/N	Portion (%) of sub-population i
n	Total amount of breakdown data points
P	Inter-layer pressure
q_m	Latent heat of vaporization (metallization layer)
R_{ser}	Series resistance
R_m	Impulse current measurement resistor
R_s	Metallization sheet resistance
S	Number of sub-populations
T_m	Crystalline melting temperature
T_{cr}	Chill-roll temperature
T_{cylinder}	Cylinder temperature
T_{die}	Die temperature
T_{max}	Maximum operation temperature
t_{pre}	Pre-heating time
T_{set}	Bi-axial orientation (set) temperature
t	Time
t_d	Time since first trigger event
U	Voltage
U_{bd}	Breakdown voltage
u	Volumetric energy density
$u_{dut}(t)$	Test capacitor voltage
$u_{id}(t)$	Voltage signal corresponding to discharge current
u_{max}	Maximum volumetric energy density

List of publications

This thesis is based on the following original publications which are referred to in the text as [P1]–[P8]:

[P1] I. Rytöluoto and K. Lahti, "New approach to evaluate area-dependent breakdown characteristics of dielectric polymer films," *IEEE Transactions on Dielectrics and Electrical Insulation*, vol. 20, no. 3, pp. 937–946, 2013.

[P2] I. Rytöluoto and K. Lahti, "Effect of film thickness and electrode area on the dielectric breakdown characteristics of metallized capacitor films," in *23rd Nordic Insulation Symposium (NORD-IS 13)*, pp. 33–38, 2013.

[P3] I. Rytöluoto and K. Lahti, "Effect of inter-layer pressure on dielectric breakdown characteristics of metallized polymer films for capacitor applications," in *Proceedings of IEEE International Conference on Solid Dielectrics, ICSD*, pp. 682–687, 2013.

[P4] I. Rytöluoto, K. Lahti, M. Karttunen, M. Koponen, S. Virtanen, and M. Pettersson, "Influence of low amounts of nanostructured silica and calcium carbonate fillers on the large-area dielectric breakdown performance of bi-axially oriented polypropylene," in *2014 IEEE Conference on Electrical Insulation and Dielectric Phenomena (CEIDP)*, pp. 655–658, 2014.

[P5] I. Rytöluoto, K. Lahti, M. Karttunen, and M. Koponen, "Large-area dielectric breakdown performance of polymer films – Part I : Measurement method evaluation and statistical considerations on area-dependence," *IEEE Transactions on Dielectrics and Electrical Insulation*, vol. 22, no. 2, pp. 689–700, 2015.

[P6] I. Rytöluoto, K. Lahti, M. Karttunen, M. Koponen, S. Virtanen, and M. Pettersson, "Large-area dielectric breakdown performance of polymer films – Part II: Interdependence of filler content, processing and breakdown performance in polypropylene-silica nanocomposites," *IEEE Transactions on Dielectrics and Electrical Insulation*, vol. 22, no. 4, pp. 2196–2206, 2015.

[P7] I. Rytöluoto, K. Lahti, M. Ritamäki, and M. Karttunen, "The role of film processing in the large-area dielectric breakdown performance of nano-silica-BOPP films," in *24th Nordic Insulation Symposium (NORD-IS 15)*, pp. 63–68, 2015.

[P8] I. Rytöluoto, M. Ritamäki, K. Lahti, and M. Karttunen, "DC ramp rate effect on the breakdown response of SiO_2-BOPP nanocomposites," in *IEEE International Conference on the Properties and Applications of Dielectric Materials (ICPADM)*, pp. 496–499, 2015.

Chapter 1

Introduction

Capacitors, which allow energy to be stored in an electric field within a polarized dielectric medium and then released over short periods of time under controlled conditions, are vastly utilized in virtually every field of electrical engineering for storage and management of electrical energy. Typical targets of application include low and high frequency filtering duties in both AC and DC systems, pulsed-power applications, power conditioning and power factor correction as well as various coupling, tuning and bypass operations. Currently, the major commercially available capacitor technologies include film, ceramic, electrolytic and electric double layer capacitors, each of which are based on a different dielectric medium and have their own application-specific advantages and disadvantages. As the focus of this thesis is on the dielectric breakdown properties of film capacitor insulation, the other classes of capacitor technology are not discussed further here. Essentially, film capacitor elements comprise of two electrodes separated by a thin laminar dielectric layer in a wound configuration. Thin (µm–range) dielectric polymer films of e.g. polypropylene (PP) are almost exclusively used in film capacitors today as they offer excellent dielectric breakdown strength, low dielectric losses, easy film processability, good mechanical properties and low cost. Film capacitors are further categorized into film-foil and metallized film capacitors. Oil-impregnated film-foil capacitors comprising of separate sheets of thin metal foil electrodes and dielectric film are generally directed towards very high current applications in which low inductance and low dielectric losses are required, a typical example being high-voltage AC capacitors for power factor correction in power systems. On the other hand, metallized film capacitors, which comprise of polymer films with extremely thin metal electrodes evaporated directly on the film surface, offer several advantages over film-foil capacitors with the single most significant one being the self-healing breakdown capability. Metallized film technology enables gracefully-aging dry capacitor designs with operation voltages substantially close to the large-area breakdown strength of the dielectric film, thus leading to much higher energy densities than those achievable in film-foil capacitors. Such features are crucial for many pulsed power and power electronics applications which require high volumetric capacitive energy density without compromising operation reliability. [1–5]

However, due to the ever-growing need for high-energy density and high operation temperature capacitors for next-generation applications such as hybrid electric vehicles (HEV), smart grids, high-voltage direct current (HVDC) transmission and grid converters for photovoltaic and wind power systems, the current state-of-the-art polymer film dielectrics lag behind the stringent requirements of the industry [1–3, 6–8]. In response, raw material producers and capacitor film manufacturers are compelled to develop

new material and film solutions for the end-users while maintaining an economically and environmentally sound approach. At present, various approaches offering unique ways to tailor the dielectric properties of polymers exist, among which e.g. dielectric polymer nanocomposites have received an increasing amount of attention recently [9–11]. Importantly however, such material research and development also necessitates detailed dielectric characterization methods in order to guide and optimize the development process towards highly optimized functional materials. From the application point-of-view, assessment of dielectric breakdown properties of polymer films is of utmost importance during development and evaluation of new capacitor dielectrics [12]. This is not a trivial task though, as considering film capacitors or entire capacitor banks, for which very large areas (from several tens up to thousands of m^2) of polymer film are utilized, and for which the operative electric field is mandated by the electrical weak points in the polymer film, accurate statistical knowledge of the low probability dielectric breakdown behavior is a prerequisite for safe and reliable operation. Indeed, it is often found that conventional small-area single-breakdown measurement methods as described in e.g. IEC-60234 standard [13, 14] rarely provide realistic picture of the practical dielectric breakdown performance of polymer films, especially regarding the low breakdown probability region. Poor statistical significance further complicates material evaluation as a compromise between the sample size and measurement convenience is often made. These challenges were also encountered during NANOPOWER research project (Novel Polymer Nanocomposites for Power Capacitors), a project focusing on PP-nanocomposite film development for power capacitors on which the author of this thesis has also been working — this sparked off interest in the development of large-area breakdown characterization method in order to provide new insight into the breakdown behavior of polymeric capacitor films.

1.1 Objectives of the thesis

The main objectives of the thesis can be summarized as:

- Development and evaluation of a measurement method enabling large-area dielectric breakdown characterization of polymer films with high statistical accuracy.
- Large-area dielectric breakdown and self-healing characterization of metallized and non-metallized polymer-based films, including various laboratory-scale, pilot-scale and commercial capacitor-grade polymer films.
- Analysis of the interdependence of film processing, structure, morphology, bi-axial orientation and large-area dielectric breakdown response in polypropylene films.
- Development of understanding on how various compositional, structural and film processing factors affect the breakdown response of laboratory- and pilot-scale BOPP nanocomposite films with silica and/or calcium carbonate nanofillers.

1.2 Author contributions

The author was the main author in all the associated publications [P1]–[P8] under the supervision of Adjunct Professor Kari Lahti. The author developed the large-area multi-breakdown measurement and analysis methodologies, wrote the MATLAB and LabVIEW programs, performed all the breakdown measurements, analyzed the data and wrote all the manuscripts. Detailed author contributions are as follows:

- The laboratory- and pilot-scale polypropylene-nanocompounds studied in [P4, P6, P7, P8] were formulated and manufactured by VTT Technical Research Centre of Finland for the purposes of the NANOPOWER project. Scanning electron microscope (SEM) imaging of the nanocompounds studied in [P6, P7] was done by VTT. The SEM particle analysis and free-space length determination in [P7] were done by the author. The manuscript sections describing the polypropylene-nanocompound processing steps and structural imaging were written by Lic.Sc.(Tech) Mikko Karttunen and later edited by the author. M.Sc.(Tech) Mikael Ritamäki helped the author in sample preparation tasks in [P7, P8].
- Transmission electron microscope (TEM) imaging of the polypropylene-nanocomposite films in [P4, P6] was performed by D.Sc.(Tech) Suvi Virtanen and Prof. Mika Pettersson at University of Jyväskylä. Free-space length determination in [P6] was done by D.Sc.(Tech) Suvi Virtanen. Analysis on structural features was done together by D.Sc.(Tech) Suvi Virtanen and the author. The manuscript sections on TEM structural imaging in [P4, P6] were written by D.Sc.(Tech) Suvi Virtanen and later edited by the author.
- Sub-chapter 4.1 is based on a journal article manuscript still under preparation at the time of completion of this thesis. The cast- and bi-axially oriented polypropylene films were manufactured by VTT Technical Research Centre of Finland and Borealis Polyolefine GmbH (Linz, Austria) for the purposes of MatPro3-project. The wide-angle X-ray scattering (WAXS) study of the cast- and bi-axially oriented PP film crystalline structures was performed by Ph.D. Antonis Gitsas. In sub-chapter 4.1, the parts describing the sample manufacturing and WAXS-analysis were written by M.Sc.(Tech) Satu Pasanen and Ph.D. Antonis Gitsas and later edited by the author. The author carried out the breakdown measurements, analyzed the data and wrote sub-chapter 4.1. M.Sc.(Tech) Mikael Ritamäki helped the author in sample preparation tasks.
- The commercial capacitor-grade polymer films studied in [P1, P2, P3, P5, P8] and in sub-chapter 4.2 were kindly provided by Tervakoski Films Group, DuPont Teijin Films and Alstom Grid Oy.

1.3 Structure of the thesis

This thesis is written in the form of compilation dissertation based on the aforementioned publications and other additional material. The rest of the thesis is structured as follows. Chapter 2 presents the background of the thesis with the main focus on film capacitor dielectrics, dielectric polymer nanocomposites, dielectric breakdown and self-healing phenomena in polymer films and polymer film breakdown measurement. Chapter 3 presents and evaluates the large-area multi-breakdown measurement method and discusses various statistical aspects; the methodologies described in Chapter 3 are in fundamental role throughout this thesis. Thereafter, based on the large-area multi-breakdown methodologies, the following two chapters analyze the breakdown characteristics of various polymer films intended for film capacitor applications. The focus of Chapter 4 is on processing-structure-breakdown relationships in small-scale and industrial-scale polypropylene films. Chapter 5 is focused on dielectric polymer nanocomposite films, with a particular emphasis on the effects of various compositional, structural and film processing factors on the breakdown behavior of laboratory- and pilot-scale polypropylene-based nanocomposite films. Finally, conclusions are drawn and future topics are proposed in Chapter 6.

Chapter 2

Background: Next-generation capacitor dielectrics, design considerations and dielectric breakdown phenomenon

This chapter makes an overview of the state-of-the-art of existing film capacitor dielectrics and various potential technological approaches to overcome their limitations. While the main emphasis is put on dielectric polymer nanocomposites and their breakdown properties, alternative approaches are shortly reviewed as well in order to provide wider perspective on the current trends in polymer dielectric development for capacitive energy storage. Thereafter, in order to lay foundations for the large-area multi-breakdown approach, the latter part of the chapter discusses dielectric breakdown and self-healing phenomena in polymers, polymer film breakdown measurement and considerations thereof.

2.1 Present state, energy density and future of film capacitor dielectrics

Dielectric materials with high capacitive energy storage ability, low dielectric loss, high temperature stability, high charge-discharge efficiency and self-healing capability play a key role in short-term capacitive energy storage purposes in modern power electronics and electric power systems. Currently, the main polymers employed in film capacitors encompass low-permittivity, high dielectric strength polymers such as bi-axially oriented polypropylene (BOPP), polyethylene terephthalate (PET), polyethylene naphthalate (PEN) and polyphenylene sulphide (PPS) [3, 5], out of which BOPP represents the current state-of-the-art due to its superior dielectric strength (small-area breakdown strength of $>700\,\mathrm{V/\mu m}$), very low loss ($\tan\delta{\sim}0.018\%$) and excellent self-healing capability in metallized form [15–19]. Indeed, BOPP is widely applied in a broad range of applications ranging from e.g. oil-impregnated HVAC capacitor banks for reactive power compensation in power systems to high-energy density metallized film capacitors for pulsed power applications. Polyesters such as PET and PEN are more oriented towards electronics applications for which dielectric losses are less critical and high temperature stability is required [20]. For high temperature applications up to $\sim150\,^{\circ}\mathrm{C}$ where BOPP is inapplicable due to its limited maximum operation temperature, the variety of dielectrics is effectively limited to polyphenylene sulphide (PPS), a relatively recent substitute for the now largely discontinued polycarbonate (PC) [21], which however suffers from a high cost (nearly 10 times that of BOPP) and poor self-healing capability in metallized film capacitors [2, 22].

Although other polymers such as polyimide (PI) and polytetrafluoroethylene (PTFE) show potential for high-temperature capacitor applications, they are generally considered unsuitable due to e.g. difficulties in film processability, thickness and cost, and in the case of PTFE, due to poor breakdown strength [22]. However, polymethylpentene (PMP) has been recently demonstrated to exhibit great potential for high-temperature applications [23]. The main dielectric properties of the above polymers are listed on Table 2.1.

The main issue with the current polymers from the application point-of-view is that they suffer from limited energy densities due to their low dielectric constants (ε_r∼2–4) originating from their weakly- or non-polar molecular structures. Fundamentally, the maximum volumetric energy density u_{max} of a dielectric material can be expressed as [11, 24]:

$$u_{max} = \int_0^{D_{max}} E \, dD \underbrace{= \frac{1}{2} D_{max} E_{bd} = \frac{1}{2} \varepsilon_r \varepsilon_0 E_{bd}^2}_{\text{For linear dielectrics only}} \tag{2.1}$$

where E is the electric field strength, D is the electric displacement, ε_r is the dielectric constant, ε_0 is the vacuum permittivity ($\approx 8.854 \times 10^{-12}\,\mathrm{F/m}$) and D_{max} is the electric displacement at the highest field (i.e. breakdown field E_{bd}). In Equation (2.1), the left-hand side integral expression is generally applicable for all dielectric materials regardless of the nature of its dielectric response. The right-hand side of Equation (2.1) is applicable for linear dielectrics only (such as BOPP), i.e. for materials which exhibit linear relationship between the electric displacement and the applied electric field (i.e., $D = \varepsilon_r \varepsilon_0 E$). In capacitor applications, the practical energy density is greatly reduced from the maximum energy density of the dielectric as a substantial safety-margin has to be kept from the short-term small-area breakdown strength of the polymer film due to the area-dependence of the breakdown performance [16, 39–41, P1], film aging processes [12, 42] and limitations in the self-healing breakdown capability [43, 44, P3]. Other constraints such as device packaging reduce the final energy density even further [45]. Thus, the maximum energy density of BOPP (∼5 J cm^{-3}) cannot be reached in practical applications; instead, the energy densities of the state-of-the-art metallized BOPP capacitors are limited to ∼2 J cm^{-3} [1, 25] which lags behind the current requirements of the industry.

Consequentially, it is not surprising that a considerable amount of research on novel dielectric polymers has emerged over the last years in an effort to outperform the capacitive energy storage ability and reliability of the existing capacitor dielectrics. Certain development strategies for high-energy density polymer dielectrics are readily identifiable from Equation (2.1), i.e., the theoretical energy density of a dielectric can be increased by increasing the breakdown strength, electric displacement and/or dielectric constant. Various approaches ranging from novel polymers such as PVDF-based co- and terpolymers [8, 24], chemically modified (functionalized) polymers [46] and dielectric polymer nanocomposites [9, 47] have been studied extensively in pursuit of further increase in capacitor energy density. Some of the most interesting material candidates are reviewed and compared with the existing capacitor dielectrics in the following, with an emphasis on dielectric polymer nanocomposites which constitute a major class of materials studied in this thesis.

2.2 High polar polymers

Much of the recent research on high-energy density polymers has been focused on high polar polymers exhibiting high dipole-densities, as utilization of the orientational

Table 2.1. Dielectric properties of various commercial and in-development polymers for film capacitor applications.

Material	ε_r (at 1 kHz)	E_{bd} (MV m^{-1})	$\tan\delta$ (% at 1 kHz)	T_{max} (°C)	u (J cm^{-3})[a]	u_{max} (J cm^{-3})[b]	References
BOPP	2.2	720	0.018	105	1–2.0	5.0	[5, 20, 24, 25]
PET	3.3	695	0.5	125	1–1.5	7.1	[5, 20, 24]
PEN	3.2	528	0.34	125	1–1.5	3.9	[5, 20, 24]
PPS	3.0	550	0.03	200	1–1.5	4.0	[5]
PC	2.8	722	0.15	125	0.5–1	6.5	[5, 20, 24]
PI	3.4	427	0.25	250	1–1.5	2.7	[5, 26]
PTFE	2.0	165	0.01	240	N/A	0.2	[27, 28]
PMP	2.2	N/A	0.03	175	N/A	N/A	[23]
PVDF	12.0	590	1.8	125	2.4	18.5	[5, 7]
P(VDF-TrFE-CFE)	52.0	400	N/A	125	N/A	10.0	[29]
P(VDF-CTFE)	13.0	618	3	125	N/A	25.0	[30]
P(VDF-HFP)	15.0	700	N/A	125	N/A	25.0	[31]
ArPU	4.2	800	0.5	200	N/A	12.0	[32]
ArPTU	4.5	800	0.6	150	N/A	22.0	[33–35]
Meta-ArPU	5.6	670[c]	1.5	170	N/A	13.0	[34, 36]
x-PP[d]	3.0	645	N/A	N/A	N/A	2.8	[37]
PP-OH[e]	4.5	600[c]	N/A	N/A	N/A	7.4	[38]

[a] Practical energy density in film capacitors.

[b] Either (i) the maximum energy density calculated as $u_{max} = \frac{1}{2}\varepsilon_0\varepsilon_r E_{bd}^2$ or (ii) the highest reported energy density calculated from a measured P-E loop.

[c] Reported value. However, appropriate statistical analysis has not been reported.

[d] Crosslinked PP-BSt copolymer (3.65 mol-% BSt content)

[e] iPP-OH copolymer (4.2 mol-% OH content)

polarization is seen as one of the most promising approaches for achieving both high dielectric constant and low dielectric loss [7, 8]. Polyvinylidene fluoride (PVDF) is a non-linear, ferroelectric fluoropolymer which inherently exhibits a relatively high permittivity (∼12) and high small-area dielectric breakdown strength (600 V/µm). Although PVDF and its typical copolymer with trifluoroethylene (TrFE) show theoretical potential for high energy density applications due to their high-polar nature, they are practically unsuitable for film capacitors due to their limited recoverable energy densities and high dielectric losses (∼1.8%) which originate from their high remnant polarization level. However, conversion of PVDF into relaxor ferroelectric by irradiation or defect modification (i.e. by introducing defects such as bulky side groups into the polymer chain) has received great attention lately, as it has been shown to decrease the polarization hysteresis and increase the recoverable energy density markedly. As reviewed in e.g. [7, 8, 24] and exemplified in Table 2.1 and Figures 2.1a–b, various defect-modified PVDF-based co- and terpolymers with side groups of e.g. chlorofluoroethylene (CFE) [29], chlorotrifluoroethylene (CTFE) [30] or hexafluoropropylene (HFP) [31] have been reported to exhibit remarkable maximum recoverable energy densities of up to $\sim 25\,\mathrm{J\,cm^{-3}}$ and small-area breakdown strengths nearly comparable to that of BOPP. Further work is still needed however, as the materials still exhibit high dielectric losses at high fields (see e.g. Figure 2.1b) [48] and their maximum operation temperatures are limited to ∼125 °C [7]. Moreover, the defect modification processes may be expensive and require strict process condition control [49] which may impede up-scaling and practical employment in film capacitors. Polymer blend or cross-linking approaches can however lead to further improvements in high-field dielectric loss properties of PVDF-based materials [35].

Other recently-studied promising groups of strongly polar materials include e.g. various aromatic polymers and functionalized PPs. High-dipole-density aromatic polyurea- (ArPU) and aromatic polythiourea- (ArPTU) based thin films [32–34, 36, 50] have been found to exhibit attractive and thermally stable dielectric properties, with dielectric constants in the range of ∼4–6, reasonably low dielectric loss levels, high small-area dielectric strengths and promising maximum energy densities up to $\sim 22\,\mathrm{J\,cm^{-3}}$, see Table 2.1 and Figure 2.1c. In contrast to BOPP which suffers from reduced energy efficiency at high-fields (>500 MV/m) due to the high-field conduction phenomenon [51], ArPTU in particular has been reported to exhibit superior high-field loss characteristics (Figure 2.1d) [33]. It has been argued that amorphous high-polar polymers with large dipoles exhibit high intrinsic dielectric strengths due to electron-trapping [33] and electron-dipole scattering mechanisms [52]. Meanwhile, various functionalized PP copolymers with polar side groups or cross-linked structure demonstrate improved dielectric properties in comparison to pure polypropylene; PP-OH copolymers with small fractions of polar OH-side groups have been shown to increase the dielectric constant to almost double of that of pure PP with no major increase in dielectric loss (Figure 2.1e) [53, 54], while cross-linkable PP-BSt copolymers (x-PP) show systematically increasing small-area breakdown strength with increasing BSt cross-linker content (Figure 2.1f) [37]. However, similarly as for the PVDF-based materials, film processability and large-scale manufacturing issues also concern the above polymers. High dipolar materials such as ArPTU cannot be fabricated into freestanding thin films by conventional melt-blending techniques which severely hinders their large-scale manufacturing and usage [35]. Development of bi-axially oriented PP-OH copolymer films will require changes in the film manufacturing process due to the altered crystallization temperature and kinetics of PP-OH [55]. Other aspects such as maintaining high dielectric strength over large film areas [45], polymer aging processes [12] and capacitor design constraints [56–58] further increase the complexity of material design for high energy density capacitor applications.

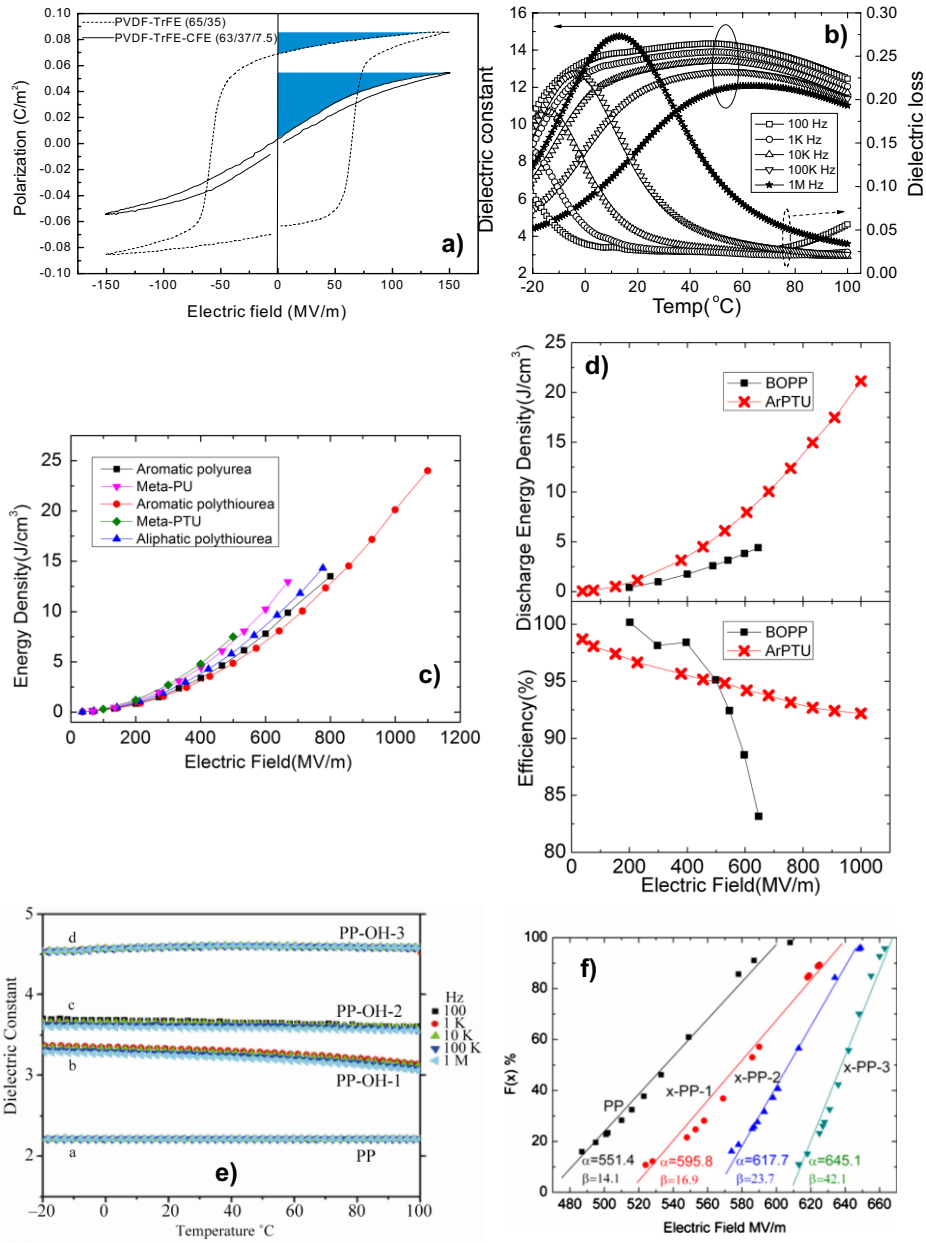

Figure 2.1. Dielectric properties of various high-polar, high energy density polymers. The figures are adapted from the respective publications. **a)** Polarization-electric field (P-E) response of P(VDF-TrFE) and P(VDF-TrFE-CFE) depicting non-linear dielectric response [29]. The shaded areas correspond to the recoverable energy density in accordance to Equation (2.1). **b)** Dielectric constant and losses of P(VDF-CTFE) as a function of temperature [30]. **c)** Energy densities of various aromatic polyurea- and polythiourea based films [34]. **d)** Energy density and efficiency of ArPTU in comparison to PP [33, 35]. **e)** Dielectric constants of various PP-OH copolymers (0.7, 1.8 and 4.2 mol-% of OH) in comparison to PP [53]. **f)** Dielectric strengths of various BSt-crosslinked PP films (0.64, 2.97 and 3.65 mol-% BSt) in comparison to neat PP [37].

2.3 Dielectric polymer nanocomposites

2.3.1 Fundamental aspects and the role of the interface

Dielectric polymer nanocomposites (PNC), i.e. polymeric composites incorporating a homogeneously dispersed phase of inorganic filler particles with at least one dimension of <100 nm, represent a relatively new class of advanced materials with enhanced dielectric properties [9, 59–61]. Various polymer matrices such as polyethylene (PE), polypropylene (PP), polystyrene (PS), PVDF and epoxy resins incorporating inorganic nanofillers such as silica (SiO_2), calcium carbonate ($CaCO_3$), barium titanate ($BaTiO_3$) layered silicate, titania (TiO_2), alumina (Al_2O_3) and magnesia (MgO) have been demonstrated to exhibit many desirable property improvements in e.g. dielectric strength [62], voltage endurance [63], partial discharge (PD) resistance [64], treeing resistance [65] and space charge properties [66]. It is thus not surprising that the nanodielectric approach has received widespread attention recently with a considerable amount of research also focusing on high energy density capacitor dielectrics [11, 67].

Essentially, the unique and attractive dielectric properties of PNCs are thought to arise from the interface between the polymeric host and the nanometric filler particles. In contrast to conventional microparticle-filled composites for which the interface is insignificant, decreasing the particle size towards nanometric scale strongly increases the filler-matrix interfacial volume fraction due to the enormous specific surface area of the nanometric particles, see Figure 2.2a. Consequentially, the interfacial volume and its properties can become dominant in a well-dispersed PNC system, thus offering a unique way to tailor the material properties by choosing the base constituents and designing the interface between them. The interfacial layer thickness has been postulated to range from <1 nm up to several tens of nm depending on the level of chemical and physical interaction between the nanoparticles and the polymer matrix [68, 69]. Chemical surface modification of the nanoparticles is therefore in an essential role in modifying the bonding and assuring compatibility with the polymer matrix, but also in preventing agglomeration of the nanoparticles which would otherwise subdue the benefits achievable through proper nanostructuration. While surface treatment by e.g. silane coupling agents is relatively common [61, 66, 70, P4, P6, P7, P8], more intricate processes involving polymer-grafed nanoparticles have also emerged recently [62, 71]. As shown schematically in Figure 2.2b, proper compatibilization enhances the filler-matrix interaction and may result in profound changes in the polymer structure. Various PNC interface models such as the intensity model by Lewis [72], the multi-core model by Tanaka [68] and the polymer chain alignment model by Andritsch [73, 74] propose that the innermost layer consisting of polymer chains strongly bonded to the nanoparticle surface is highly aligned and immobilized and further affects the morphology of the surrounding polymer matrix (bound and affected layer). A diffuse electrical double layer forming a long-distance dipole is thought to overlap the above physical layers [68, 75]. It has been suggested that the interfacial volume exhibits major changes in polymer crystallinity, chain mobility, conformation and entanglement as well as free volume, local charge distribution and trap site density and depth [9], which, in turn, are reflected to the dielectric properties of the whole PNC system.

2.3.2 Dielectric breakdown strength of polymer nanocomposites

Considering the current trends in the PNC development for next-generation capacitor applications, two prevailing directions with the foundations on Equation (2.1) can be distinguished, namely (i) increasing the permittivity or (ii) improving the dielectric breakdown

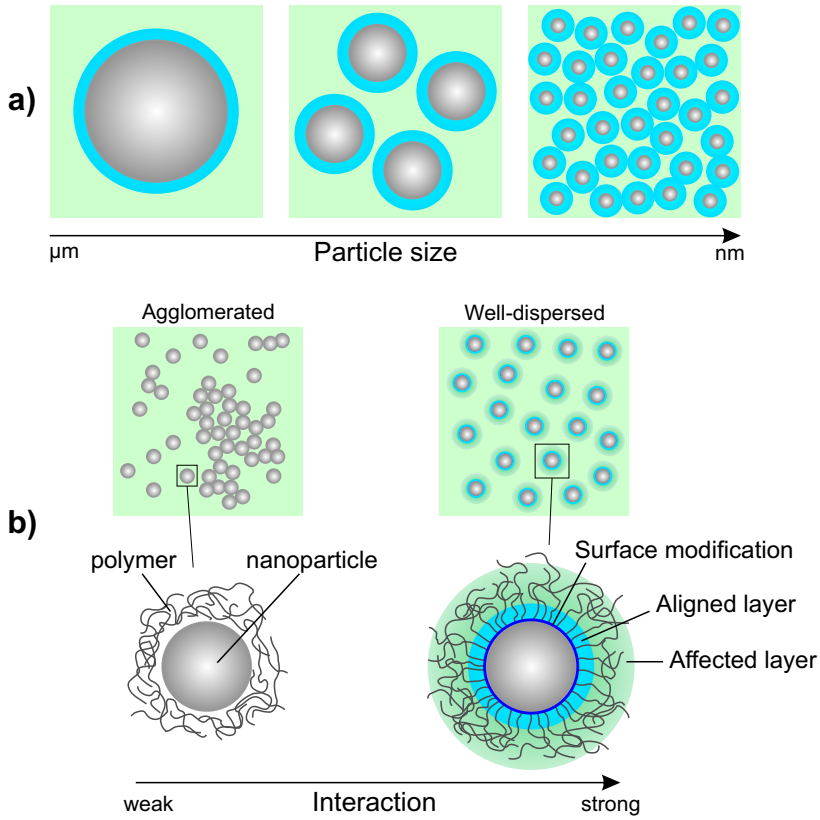

Figure 2.2. a) Schematic illustration of the particle-size-dependence of interfacial volume in polymer composites. With decreasing particle size the volume fraction of the interface becomes dominant. **b)** Schematical illustration of the effect of nanoparticle surface treatment on the dispersion and distribution of nanoparticles and on the properties of the interface. Proper surface treatment prevents excess agglomeration and results in major restructuring of the surrounding polymer matrix. The polymer chain alignment model in (b) is adapted from [73, 74]

properties. Regardless of which approach is taken however, maintaining high dielectric breakdown strength (DBS) is a prerequisite for capacitor applications. Breakdown properties of PNCs have been shown to be strongly influenced by the dielectric compatibility between the polymer matrix and the nanofillers, nanoparticle functionalization, filler content, morphology, degree of mixing and material processing [63, 76–78, P4, P6].

Incorporation of high-permittivity nanoparticles into a polymer matrix with a moderate to high dielectric strength seems attractive from the viewpoint of combining the best aspects of both the constituents. Indeed, PNCs comprising of high-permittivity surface-modified ceramic nanoparticles such as $BaTiO_3$ and a low-permittivity polymer matrix have been extensively studied in an attempt increase the energy density [79–82]. However, as a high nanoparticle volume fraction of ceramic particles (10–50 vol-%) is needed in order to increase the effective permittivity of the composite [83, 84], excess local field enhancement due to the mismatch between the matrix-filler permittivities, formation of percolative pathways, nanoparticle agglomeration and increased porosity systematically decrease the DBS in comparison to the neat polymer [82, 85, 86], hence

negating improvement in practical energy density. While new approaches such as core-shell structured high-permittivity nanoparticles are seen as one possible solution to prevent particle agglomeration and control the dielectric losses at high fill-fractions [87, 88], realization of high energy density through incorporation of high-permittivity nanoparticles while maintaining high DBS remains a challenging task.

With permittivity-matching nanofillers the main focus remains in improving the dielectric breakdown properties of the neat polymer, as no major increase (or conversely, a decrease [9, 73]) in PNC permittivity is expected. This approach also forms an integral part of this thesis (Chapter 5) and deserves a more in-depth literature survey with a particular emphasis on the effect of silica fillers on DBS. Figure 2.3 presents the relative change in DC and/or AC DBS for various PNC systems as a function of nano-silica content, including (but not limited to) PNC materials intended for capacitor applications. Improvement in short-term DC and/or AC DBS and breakdown distribution homogeneity may be achieved with polymer nanocomposites of permittivity-matching constituents and preferably with low fill-fractions (<5 wt-%), as reported e.g. for nano-silica-filled cross-linked polyethylene (XLPE) [63, 89], core functionalized nano-silica-filled epoxy [62] and nano-silica-filled BOPP films [64, P4, P6]. These improvements are typically attributed to favorable charge scattering, trapping and space charge properties at the filler-matrix interface [65, 89]. However, a number of studies also report a systematic reduction especially in DC DBS with an increasing nano-silica content (see Figure 2.3a), with one of the underlying reasons possibly being e.g. filler agglomeration. Proper nanoparticle dispersion and distribution in the polymer host have been necessitated in order to achieve improved breakdown performance [77]. The potential advantageous effect of smooth nanodispersion on the breakdown performance can be overwhelmed if micro-aggregates are present in the material, as demonstrated in the case of nano-$CaCO_3$-filled BOPP films in [90]. Agglomerated nanoparticles and their effect on the surrounding polymer may result in irregular regions for permittivity and conductivity, thus leading to local field enhancement and premature breakdown [73]. Possible space charge accumulation at the agglomerate interfaces may also negatively impact especially the DC breakdown properties of PNCs [P6, P8].

Interestingly, the dielectric properties of the polymer matrix also play a significant role in the DBS of the nanocomposite. In [92], the effect of well-dispersed nano-silica on the DC DBS of melt-blended amorphous polymethyl methacrylate (PMMA), PI, poly-4-vinylpyridine (P4VP) and PS matrices was studied up to very high fill fractions (50 vol-%), see Figure 2.3a. In the higher breakdown strength polymers (PMMA and PI), the inclusion of nano-silica systematically reduced the DBS which was attributed to silica particles acting as failure-inducing defect sites providing a lower energy failure mode into the composite. In contrast, with the low breakdown strength matrices (P4VP and PS) and with moderate fill fractions (<15 vol-%), silica was found to improve the DBS, presumably by hindering the propagation of failure induced from the low dielectric strength matrix by charge trapping and scattering. At the highest loadings, the breakdown performance of all the nanocomposites was found to converge to a silica-inherent region ($\sim$450 V/µm in [92]) as the failure mode of silica became dominant. In a further study concerning polymer-grafted silica nanoparticles (aHNP) with even narrower inter-particle spacing and superior dispersion in comparison to the above melt blended variants, the trend in DBS as a function of silica content remained similar although a reduction in dielectric loss was achieved [71]. These results are significant as they suggest that good silica nano-dispersion alone may not be sufficient for improving the DBS, but rather it is the combination of matrix-filler selection, good dispersion and favorable charge trapping properties at the interface which may lead to improvement in DBS properties.

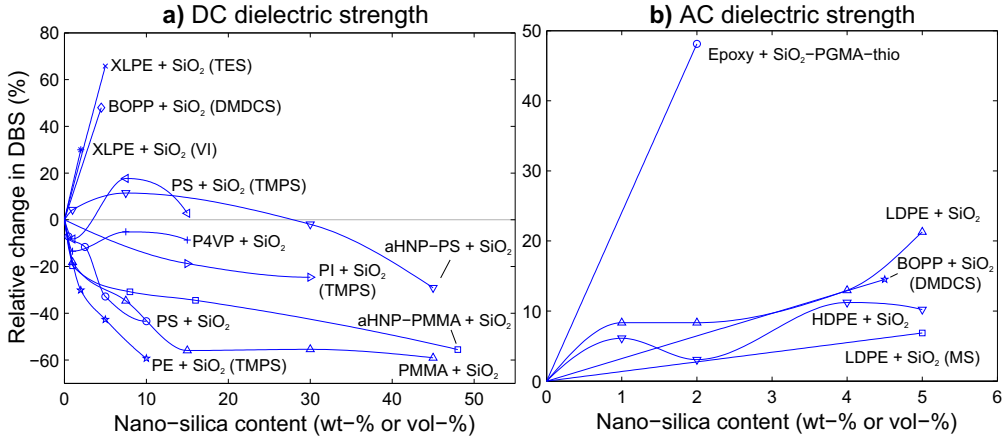

Figure 2.3. Relative change in short-term **a)** DC and **b)** AC dielectric strength in various PNC systems from the literature as a function of nano-silica content. In a) the materials are from [63, 64, 71, 91–94]. In b) the materials are from [62, 64, 95, 96]. Nanoparticle surface-treatment is indicated in parenthesis if specified in the original publication. TES = triethoxyvinylsilane, DMDCS = dichlorodimethylsilane, VI = vinylsilane, TMPS = trimethoxy(propyl)silane, aHNP = polymer-grafted nanoparticle (see [71]), PGMA = polyglycidylmethacrylate, thio = oligothiophene, PGMA = polyglycidylmethacrylate, MS = methoxysilane.

In summary, nanodielectrics certainly exhibit interesting and potential breakdown properties, but they also pose many research challenges. As recently reviewed by Lau *et al.* [61], the main challenges in the field of dielectric polymer nanocomposites are related to preventing nanoparticle agglomeration and finding proper ways to engineer polymer/nanoparticle interfaces. The role of electroactive surface functionalization is particularly emphasized, as supported by recent studies on e.g. bimodal-polymer-brush-grafted silica-epoxy nanocomposites [62, 97]. Lastly, it is necessary to remark that apart from their breakdown properties alone, dielectric polymer nanocomposite may also offer many other advantageous properties for film capacitor applications, such as improved PD resistance [64, 98]. Lastly, from the device perspective, the current metallized film capacitor technology may pose further challenges, as the limited current carrying capability of the capacitor end-connections [57] in particular may represent a bottleneck even if the combination of high permittivity, high DBS and low losses is achieved in polymer nanocomposites.

2.4 Dielectric breakdown in polymer films

2.4.1 Overview of dielectric breakdown mechanisms and engineering breakdown strength

It is challenging to identify the actual origin and underlying mechanism of dielectric breakdown in polymers as the final process leading to the catastrophic failure of insulation layer is essentially a complicated sum of many different and often competing (or even accumulating) processes [12, 99–101]. It is generally agreed though that the process preceding a breakdown involves an abrupt increase in the conduction current and that ultimately, the final stage of electrical failure is always of thermal nature. Several classical breakdown models describing isolated processes are postulated in the literature and they

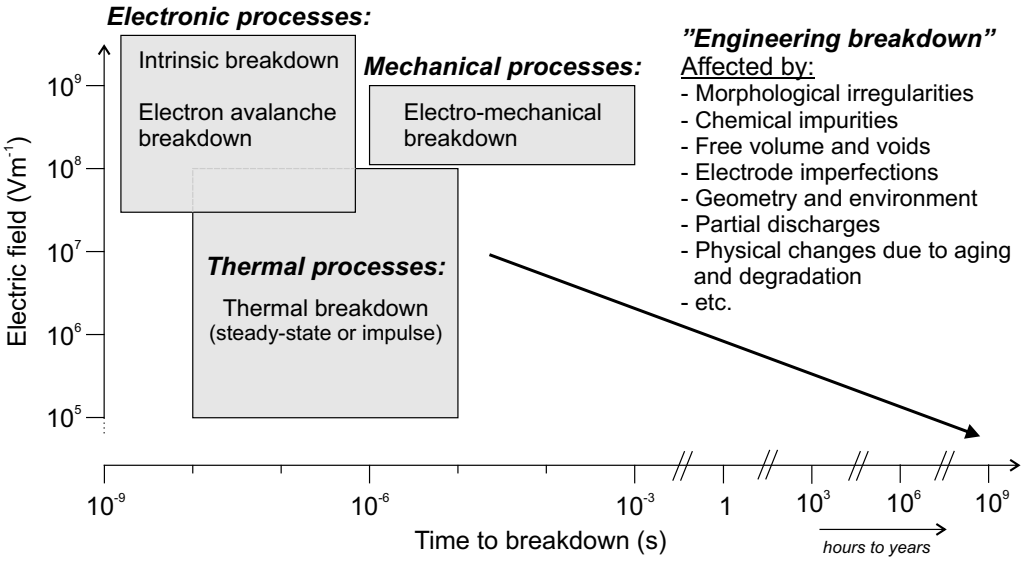

Figure 2.4. Schematical overview of various dielectric breakdown mechanisms and factors affecting the "engineering breakdown strength" of polymers. The time and electric field scales depicting the interrelation of the presented mechanisms and factors were adapted from [12].

can be categorized to electronic, thermal and electro-mechanical breakdown models. It is thought that under given circumstances, the breakdown mechanism yielding the lowest breakdown strength is usually predominant. Based on literature [12, 99–103], Figure 2.4 and the following discussion attempt to shortly summarize the basic aspects of the aforementioned breakdown mechanisms, their effective electric field ranges and time scales, and other factors constituting dielectric breakdown in polymers.

Fundamentally, a property common for electronic, thermal and electromechanical breakdown processes is that they all describe a certain imbalance situation leading to runaway and breakdown under high electric field and in a very small time scale. Purely electronic breakdown, either caused by the number or the energy of mobile electrons reaching unstable magnitudes in the crystalline regions under extremely high electric fields, is considered as the ultimate limit of a "perfect" solid insulator. In intrinsic breakdown the rate at which free electrons gain energy from the electric field exceeds the rate at which they lose energy to the lattice by electron-phonon scattering or other mechanisms. In electron avalanche or impact ionization process the initial high-energy free electrons collide and release trapped or bound electrons, and given that the new generation of electrons can result in more collisions, a chain-reaction-like charge multiplication and catastrophic failure of the lattice may occur. In a similar fashion, thermal breakdown is postulated to occur due to thermal imbalance in amorphous regions arising from the rate of heat generated by Joule heating and dielectric losses exceeding the rate at which the heat can be lost to the surroundings, thus leading to thermal runaway and breakdown. It is remarked here that the DC breakdown process of thin polymer films is postulated to be due to the thermal breakdown mechanism [104]. Lastly, electromechanical breakdown model describes a mechanical deformation process in which (at elevated temperature) the mechanical compression due to electrostatic attraction of the electrodes exceeds the maximum elasticity of the insulation, thus leading to thinning of the insulation layer, further increase in electrostatic compression and ultimately runaway.

In practice, none of the above mechanisms can be postulated exclusively as a reason for breakdown; even under controlled conditions practical insulation layers break down at much lower "engineering breakdown fields" as no perfection in material structure nor complete exclusion of extrinsic factors influencing the breakdown process can ever be achieved. For instance, measurement of intrinsic breakdown strength is very challenging, as even with careful measurement of well-controlled samples at low temperatures it is hard to reach the extreme electric field stresses required for intrinsic breakdown before the material breaks down due to other reasons. Factors such as morphology and crystalline interfaces in amorphous or semi-crystalline polymers, molecular motion, internal defects, free volume, chemical impurities, additives such as antioxidants etc. have been shown to affect breakdown behavior of polymers, and these are obviously dependent on the material composition and processing. In the framework of this thesis, the aforementioned aspects are discussed in more depth in Chapters 4 and 5. Further, it is important to consider that under service conditions and with operation fields much lower than the short-term breakdown strength of the insulation, physical changes due to long-term aging and degradation (due to e.g. partial discharges) further influence the breakdown behavior of polymers. In conclusion, while ultimate material properties such as intrinsic breakdown strength undeniably provide insight into the inherent material properties, assessment of "engineering breakdown" of polymeric insulation, such as capacitor films, is of great interest from the practical point-of-view.

2.4.2 Dielectric breakdown measurement and considerations thereof

Measurement of DBS is of fundamental importance during the development and optimization phase of novel polymeric materials for capacitive energy storage purposes in film capacitors. The measurement is typically realized as a short-term ramp-to-breakdown measurement of small film samples by using cylindrical edge-rounded bulk metal electrodes [13, 14], or as is becoming more common recently, by utilizing metallized polymer films as the electrodes [92, 105–108] which can be easily renewed for each measurement in order to eliminate the effect of electrode wear and pitting. Electrode area, sample thickness, surrounding environment, temperature, voltage form, ramp rate etc. affect the breakdown strength and should be carefully considered [109–112]. Weibull or other extreme-value distributions are then utilized for the statistical analysis of the breakdown data [113]. The cumulative distribution function (CDF) of a 3-parameter Weibull distribution is of form [12, 109]:

$$F(x) = \begin{cases} 1 - \exp\left\{-\left(\dfrac{x-\gamma}{\alpha}\right)^{\beta}\right\} & , x \geq \gamma \\ 0 & , x < \gamma \end{cases} \tag{2.2}$$

where x is the measured variable (e.g. breakdown voltage), α is the scale parameter which corresponds to the value of x at the $1 - 1/e \approx 63.2\%$ failure probability (i.e. the characteristic breakdown field), β is the shape parameter depicting the slope of the theoretical distribution and the location parameter γ is the threshold field magnitude below which breakdown cannot occur. 2-parameter Weibull distribution, which is most commonly utilized for the analysis of dielectric breakdown data, is obtained from Equation (2.2) by stating a zero location parameter ($\gamma = 0$).

Due to the inherently stochastic nature of the breakdown process in polymer films, a large number of breakdowns has to be collected in order to gain a sufficiently high statistical significance for making comparisons among materials and for guiding the material optimization process [12]. Considering film capacitors or entire capacitor banks,

for which very large areas (from several tens up to thousands of m^2) of polymer film are utilized, and for which the operative electric field is mandated by the electrical weak points in the polymer film, accurate statistical knowledge of the low dielectric breakdown probability region with reasonably narrow confidence bounds is a prerequisite for safe and reliable operation [45]. In practical terms, the amount of data required for obtaining a high statistical confidence approaches several tens or hundreds of breakdowns [16]. Although a few automatic systems for the breakdown voltage measurement of polymer films have been developed [16, 39], manual breakdown measurement with small electrodes in the mm^2–cm^2 range still seems to be the generally prevailing method which forces a trade-off between the sample size and measurement convenience to be made. This is also evident from the literature reviewed in the previous section.

The breakdown strength evaluation is further complicated by the area and volume dispersion of weak points in the film which may show as distinct defect distributions differing from the inherent breakdown distribution of the polymer itself [12, 109]. The weak points in dielectric films may not be due to the inherent properties of the material itself but due to extrinsic factors such as defects, chemical impurities or voids in the material volume or due to improper material processing [12, 114]. Indeed, several experimental [15, 26, 40, 115, P1] and theoretical [41] studies on the area-dependence present breakdown results which significantly deviate from a single 2-parameter Weibull distribution particularly in the low breakdown probability region. In such a case, manual small-area breakdown measurement, which inherently tends to measure breakdowns corresponding to the high probability region [15], may result in over-optimistic breakdown strength estimate and extrapolation of the breakdown distribution to represent a larger active area becomes unreliable. Thus, it can be concluded that in addition to a sufficiently large number of breakdown points, a relatively large total film area should also be covered. These aspects will be discussed in more depth in Chapter 3.

2.4.3 Self-healing breakdown phenomenon and its utilization for breakdown measurement

Metallized dielectric films have a unique ability to undergo self-healing[1] breakdown [4, 5, 42], a process which is shown schematically in Figure 2.5a. When a breakdown occurs in the dielectric film, a portion of the stored capacitive energy is discharged through the breakdown channel which leads to rapid increase of current density and temperature in the metallization layer surrounding the fault spot. Light emission spectroscopy investigations indicate that the Joule-heating-induced temperature rise at the fault spot during self-healing of Al-metallized PP can reach 6500–7200 K [116, 117]. Consequentially, a portion of the metallization layer around the fault spot is vaporized (typically in the range of a few mm^2, see e.g. Figure 2.5b) and high-pressure gaseous by-products from the metal vaporization and polymer film decomposition processes expand rapidly away from the clearing site along the interface between adjacent film layers [118, 119]. The arc extinction is argued to occur when the energy available for the process becomes less than the critical power density required for sustaining the arc [44, 116, 120, 121], with this being strongly dependent on the breakdown voltage, capacitance, metallization material and resistivity (thickness) and interfacial pressure. The total duration τ_{sh} of the self-healing process is in the range of a few µs or less depending on the aforementioned parameters. As a result of the self-healing process, the fault spot is spontaneously isolated from the remaining intact electrode and the insulation capability of the film is restored.

[1] Also sometimes referred to as 'clearing' or 'self-quenching' in the relevant literature.

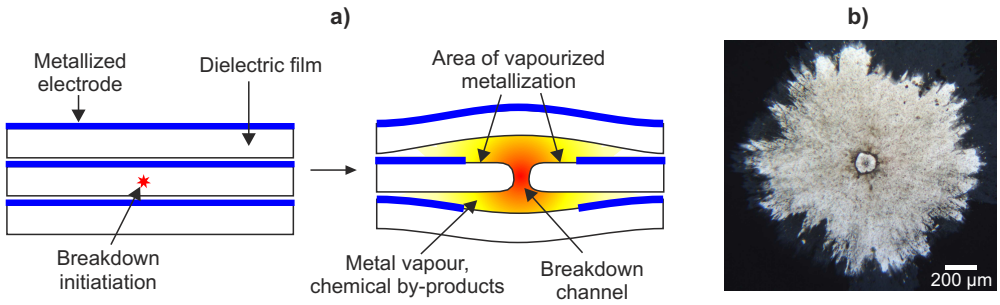

Figure 2.5. a) Schematical illustration of the self-healing breakdown process (adapted from [19, 122]. **b)** Stereo microscope image of a clearing spot on 4 µm PEN film showing the breakdown channel at the center and the de-metallized area surrounding it.

The self-healing process can be characterized by the energy E_{sh} discharged during self-healing, and based on the experimental work by several authors it can be expressed as [5, 123]:

$$E_{sh} = \frac{kU_{bd}^{b}C}{R_s^c \alpha(P)} = aU_{bd}^{b} \tag{2.3}$$

where U_{bd} is the breakdown voltage, C is the capacitance, R_s is the metallization sheet resistance, $\alpha(P)$ is a function which relates inter-layer pressure to the discharge energy and a, b, c and k are experimentally definable constants. An estimate for the voltage dependence coefficient b is often reported to be ∼4 although the coefficient may be rather varied from 2 up to 6 depending on experimental conditions [19, 124]. For the coefficient c, values in the range of 1.8–2 are often given in the literature [42, 43]. Inter-layer pressure, which in metallized film capacitors originates from the winding tension and film shrinkage during heat treatment [119, 125], has a profound effect on the self-healing breakdown process as is also indicated by Equation (2.3). As studied by Tortai *et al.*, inter-layer pressure confines the expansion of the breakdown plasma and increases the critical power density required for sustaining the arc [117]. Finite element method simulations of Qin *et al.* also suggest that while inter-layer pressure hinders the gas expansion in radial direction, the axial expansion is actually promoted so that the gaseous products flow more quickly away from the clearing site [119]. Thus, inter-layer pressure results in more efficient self-healing, reduced discharge energy and smaller de-metallized area. Moreover, Klein [126] has also derived a simplified criterion for the self-healing breakdown:

$$\frac{\varepsilon_0 \varepsilon_r \rho_m A_c \log(A_c/A_m)}{8\pi\rho_i h_m^2} E_{bd}^2 \geq q_m \tag{2.4}$$

where A_c and A_m are the capacitor area and metal hole area, respectively, h_m is the metallization thickness, ρ_m and ρ_i are the metallization and breakdown channel resistivities, respectively, E_{bd} is the breakdown field and q_m is the latent heat of vaporization of the metallization. The left-hand side of (2.4) corresponds to the energy delivered to the self-healing process and the right-hand side corresponds to the amount of energy required for electrode clearing. Considering the fact that the capacitance $C = \varepsilon_0 \varepsilon_r A_c d_f^{-1}$, where d_f is the thickness of the dielectric, and the breakdown field $E_{bd} = U_{bd}/d_f$, a similarity between Equations (2.3) and (2.4) is noticed, although Equation (2.4) does not take the effect of inter-layer pressure into account. In any case, Equations (2.3) and (2.4) together suggest that good self-healing capability is promoted by maintaining a sufficiently high discharge energy level.

Aside from its obvious advantages in film capacitor applications, self-healing breakdown capability also offers an attractive alternative approach for manual or automatic breakdown measurement techniques, with the obvious advantage being the ability to measure a statistically large amount of breakdowns from the given sample area in a convenient way. Indeed, as pioneered by Klein and co-workers [126–129], and reviewed in e.g. [12, 130], the self-healing breakdown technique has been extensively applied to very thin metal-oxide-semiconductor (MOS) structures for studying the breakdown mechanisms of e.g. silicon or aluminum oxides under AC, DC and impulse voltage conditions. In principle, a test capacitor comprising of a sample film with evaporated metal electrodes is prepared, a desired voltage stress is applied across it and the breakdown voltages and/or times to breakdown are recorded [130]. Klein [126, 131] has observed both single-hole breakdowns and propagating breakdown patterns, depending on the amount of series resistance limiting the current from the external power source. For statistical analysis of the breakdown data, a simple histogram approach [126, 132] or more intricate Weibull analysis [133–136] have been previously applied. Although the self-healing technique has been previously applied for studying the breakdown properties of some polymers such as PET, PE [130, 132, 133, 137], and more recently multilayered PC/PVDF-HFP films [136], it is still a somewhat less frequently utilized breakdown measurement technique for polymer films at the present. The self-healing breakdown measurement approach forms the foundation for the large-area multi-breakdown characterization method in this thesis, as will be discussed in the following chapter.

Chapter 3

Large-area multi-breakdown measurement of polymer films: Implementation, evaluation and statistical considerations

The purpose of this chapter is to present and evaluate the large-area multi-breakdown measurement method utilized in the associated publications [P1]–[P8]. Various aspects encompassing the sample film preparation, measurement procedure, breakdown progression, discharge event characterization, breakdown field determination, data validation and statistical analysis are discussed. Implications of the area-dependence and the applicability of the Weibull area-scaling are also discussed.

3.1 Experimental details

The studied film types included:

- Laboratory-scale films, non-metallized, $d_f \approx 15$–25 µm
- Pilot-scale films, non-metallized, $d_f \approx 15$–17 µm
- Capacitor-grade films, both metallized and non-metallized, $d_f \approx 4$–15 µm

The laboratory-scale films were manufactured by VTT Technical Research Centre of Finland. In general, the film processing steps included pre-mixing and compounding of raw materials (unstabilized polymer powder, antioxidants and nanofillers), cast film extrusion and bi-axial orientation by Brückner KARO IV film-stretching machine, resulting in $\sim$ 360 mm x 360 mm BOPP film sheets. In one of the trials commercial PP-pellets were directly melt-extruded into cast films (no compounding step required) and thereafter bi-axially oriented as described above. Some of the compounds manufactured by VTT were also chosen for a pilot-scale film trial. Pilot-scale films were produced at a Brückner pilot film line in Denmark. Commercial capacitor-grade BOPP films (manufactured by both tenter and bubble processes) were obtained from Tervakoski Films Group, DuPont Teijin Films and Alstom Grid Oy. More detailed information about the studied films can be found from the associated publications [P1]–[P8].

The general steps of the large-area multi-breakdown measurement from initial sample film material to final statistical analysis and conclusions are depicted in Figure 3.1. As a wide variety of polymer films was studied in this thesis and the associated publications, the experimental procedures were adapted on a case-by-case basis. The main features of the

realization of large-area multi-breakdown measurement of polymer films are summarized in the following sub-chapters. More in-depth details can be found from the associated publications [P1]–[P8].

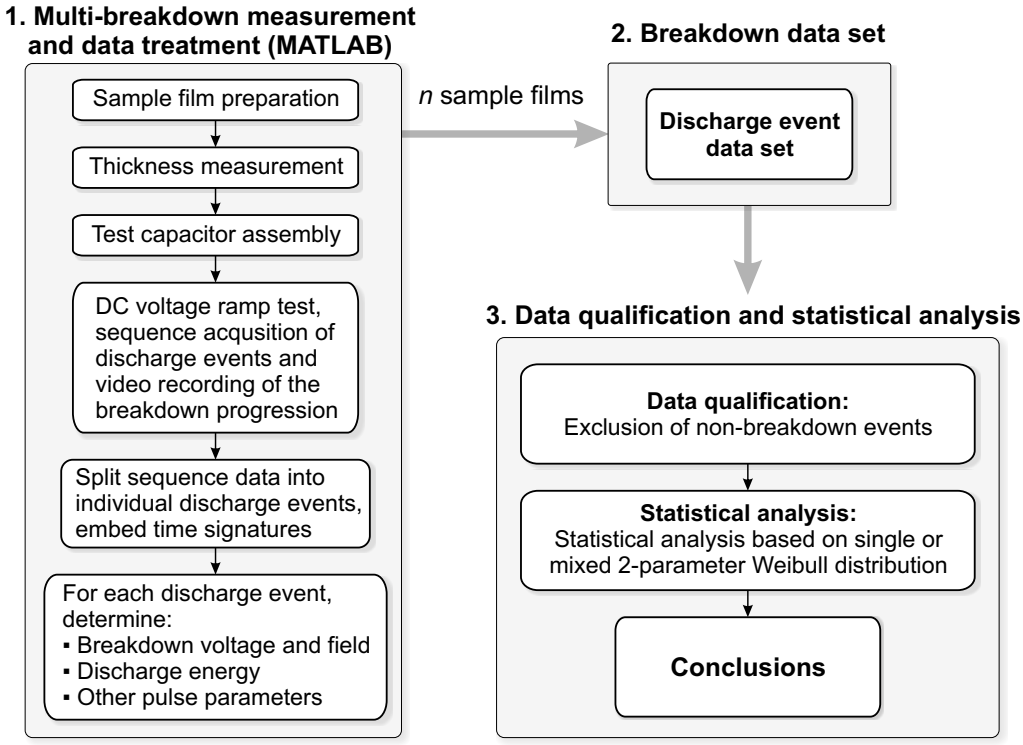

Figure 3.1. General steps of the large-area multi-breakdown measurement and analysis.

3.1.1 Sample preparation and test capacitor structure

In the standard case, the non-metallized sample films were cut to 110 mm x 110 mm dimensions for the multi-breakdown measurement. Capacitor-grade and pilot-scale film samples were cut directly from the film rolls. Laboratory-scale film samples were cut from the central part of the oriented film always when possible (one sample per oriented film). However, if sample material was limited in quantity (as in [P4, P5, P6]), the full oriented sheets were first divided into four quadrants and then cut into actual film samples in order to utilize the available film as efficiently as possible (four samples per oriented film). Thorough film thickness mapping was seen necessary for the laboratory- and pilot-scale films in order to avoid error in the breakdown field calculation later on. This was considered particularly important for the laboratory-scale films, as the bi-axial orientation process with the Brückner KARO IV stretcher inherently results in some degree of thickness deviation with the outer film regions being thicker than the central region [138]. Thickness of each sample film was measured systematically at 25 points covering a 100 mm x 100 mm area with LE1000-1 high-precision thickness measurement gauge (accuracy 0.1 µm, resolution 0.05 µm) using a ball-point measurement tip and a constant measurement force of 0.6–0.85 N. Sample film thickness mapping was performed for all the samples except for the capacitor-grade films for which the average thickness

given by the manufacturer was used. Schematical illustration of the sample film and thickness measurement points is presented in Figure 3.2a.

In order to realize the self-healing multi-breakdown measurement of non-metallized sample films, two 90 mm wide sheets of commercial Zn-Al-metallized BOPP film (12 µm Tervakoski PSX film, main metallization body resistivity R_s = 5–12 Ω/sq.) were used as electrode films above and under the sample film with the metallized surfaces facing towards the sample film, thus forming a test capacitor with an active area of 81 cm^2 [P4]–[P8]. In the case of metallized capacitor-grade samples, the test capacitor was formed by utilizing the one-sided metallization of the sample film as one electrode and a separate sheet of metallized film as another, with a polyimide spacer film in between the films to prevent flashover across the region where the top film overlapped with the edge of the bottom film [P1, P2, P3]. Alternatively, the need for spacer film can be omitted by utilizing the metallized film free margin. The test capacitor was sandwiched between two sheets of 100 µm thick transparent polyester film in order to provide mechanical support for the films during the breakdown measurement. The whole film arrangement was then fastened to a test bench consisting of a Bakelite bottom plate and a transparent acrylic plastic top plate. Electrical contacts with the metalized films were made by clamping the electrode films between two smooth aluminum bars at the both ends of the test capacitor unit. The aluminum clamps were lightly tightened by terminal screws and connections to the high voltage supply and ground were made accordingly. No excessive interface discharging between the metallized layers and the connector was observed (provided that a sufficiently low discharge energy level is maintained [P1]). The condition of the aluminum surfaces was monitored and if necessary, they were cleaned and polished between measurements. The test capacitor structures for non-metallized and metallized sample films are depicted in Figures 3.2b and 3.2c, respectively. Photographs of sample films are presented in Appendix A, Figure A.1.

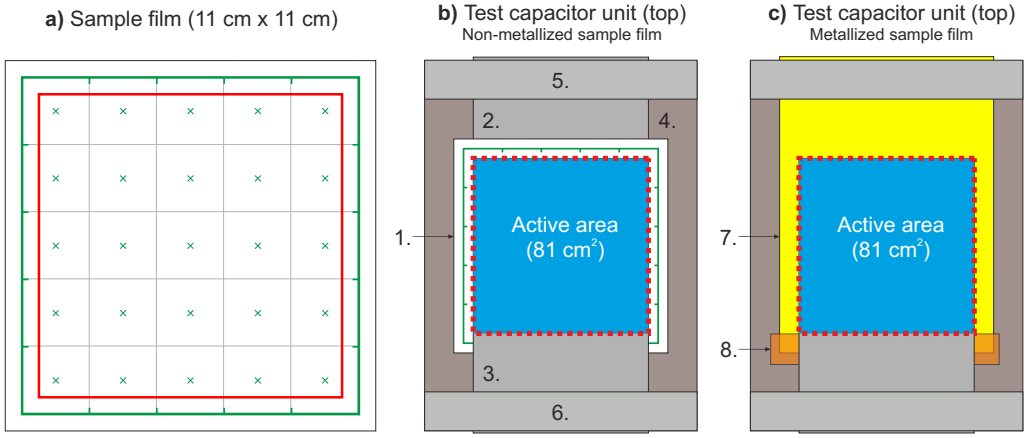

Figure 3.2. a) Sample film dimensions, thickness measurement points (green) and active area (red). **b)** Test capacitor structure for non-metallized sample films, respectively. **1**: Non-metallized sample film, **2**–**3**: Metallized electrode films (metallized surfaces facing towards the sample film), **4**: Bakelite bottom plate, **5**–**6**: aluminum clamp electrodes (to high voltage and ground). **c)** Test capacitor structure for metallized sample films. **7**: metallized sample film (metallized surface facing down), **8**: polyimide spacer film. The transparent top plate is excluded from b) and c).

3.1.2 Measurement circuit

The measurement circuit (Figure 3.3) used for the multi-breakdown measurement consisted of a Spellman SL 1200 DC high voltage source (1200 W nominal power) in parallel with the test capacitor unit C_{dut}. The control voltage (0 – 10 V) used for ramping up the DC voltage source was generated with a National Instruments PCI-6221 DAQ card and LabVIEW software. The current limit of the DC source was set to 9 mA. A resistive voltage divider (Spellman HVD 100-1, R_1:R_2 = 10000:1) parallel to C_{dut} was used for general monitoring of the measurement voltage in LabVIEW. In [P1, P2, P3], an additional capacitor C_p in parallel with C_{dut} was used as a fast charge storage buffer during a breakdown in the test capacitor. In principle, as the energy discharged during a self-healing breakdown is proportional to the total effective capacitance $C_{eff} = C_p + C_{dut}$ (see Equation (2.3), the effect of capacitor size on the self-healing can be simulated by varying the size of C_p. It is remarked here that the output capacitance C_o of the DC high voltage source and the stray capacitance of the system C_s also affect the self-healing breakdown characteristics (the exact values of C_o and C_s are however unknown). Optionally, the current flow $i_s(t)$ from the DC high voltage source to the fault can be limited by using a resistor R_{ser} in series with the DC source. However, $R_{\text{ser}} = 0\,\Omega$ was used for the measurements (unless otherwise specified).

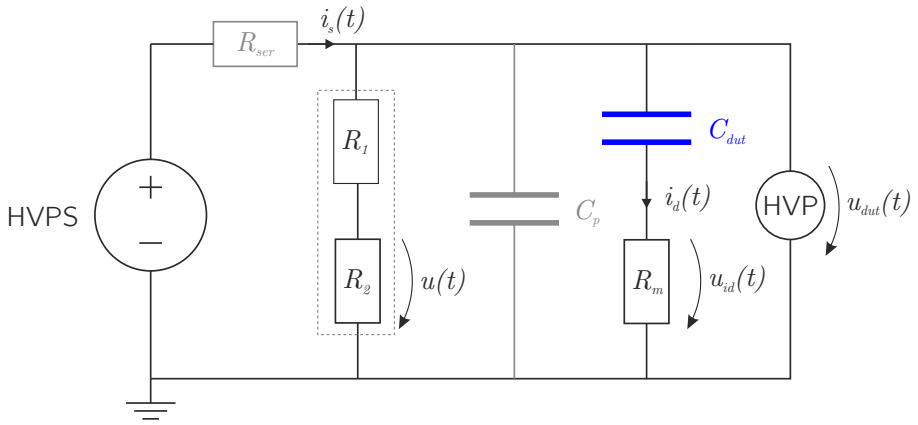

Figure 3.3. Large-area multi-breakdown measurement circuit. HVPS=high voltage power source, R_1:R_2 = 10000:1, C_p=parallel capacitance (optional), C_{dut}=test capacitor, R_m=impulse current measurement resistor, HVP=high voltage probe (1000x attenuation). See Appendix A, Figure A.2 for a photograph of the test setup.

For the high-resolution acquisition of discharge events, the voltage $u_{id}(t)$ corresponding to the discharge current $i_d(t)$ and the voltage $u_{dut}(t)$ across the test capacitor unit during each discharge event were measured by means of a 1.0330 Ω impulse current measurement resistor and a Tektronix P6015A high voltage probe, respectively. The discharge current and test capacitor voltage signals along with the trigger time information of each discharge event were recorded with a high-resolution 12-bit oscilloscope (Lecroy HRO 66Zi) operated in the sequence-acquisition mode and triggered to the positive rising edge of the discharge current signal. The sequential discharge current and test capacitor voltage raw data were imported and split into individual discharge events in MATLAB with a custom-made GUI-based program (see Figure A.3). This allowed a detailed determination of the breakdown voltage, voltage drop, peak current, discharge energy and various pulse time parameters for each event. The discharge energy E_{sh} during each event was calculated

by integrating the product of the test capacitor voltage and discharge current over the discharge duration τ_{sh}:

$$E_{sh} = \int_0^{\tau_{sh}} u_{dut}(t) i_d(t) dt \tag{3.1}$$

A video was recorded from the top of the test capacitor unit for the whole duration of the breakdown measurement (except in [P1, P2, P3]), allowing detailed chronological analysis of the breakdown progression of the sample after the measurement. Based on the discharge event trigger times, the video could then be reduced to a series of freeze-frames depicting the breakdown progression in MATLAB.

3.1.3 Test procedure

The breakdown measurements of thin (<10 µm) samples were performed in atmospheric air. For thicker samples, mineral oil immersion (Shell Diala DX) in accordance with the IEC-60243 standard [13] was utilized in order to suppress the occurrence of partial discharges and surface flashovers. In principle, the standard voltage ramp rate during the breakdown measurement was set to $30\,\mathrm{V\,s^{-1}}$ which is in a similar range as previously used for self-healing breakdown measurements [130]. In the case of thicker samples however, the DC voltage was first raised to approximately 40–60 % of the probable short-time breakdown voltage with a fast ramp speed of $400\,\mathrm{V\,s^{-1}}$ in order to decrease the time required for the measurement, after which a slow ramp speed of $30\,\mathrm{V\,s^{-1}}$ was used for measuring the breakdown events, roughly in accordance with the slow rate-of-rise test defined in the IEC-60243-1 standard [13] (Figure 3.4a). The voltage was ramped up until no more discharge events could be measured from the sample area or until the oscilloscope memory was filled up. 6–10 sample films were typically measured per material (486–810 $\mathrm{cm^2}$ total measured film area). A typical self-healing breakdown event measured from a laboratory-stretched PP-1 film sample from [P5] is presented in 3.4b showing a discharge current pulse with an oscillating component and an abrupt voltage drop at the instant of the breakdown followed by a voltage recharge period.

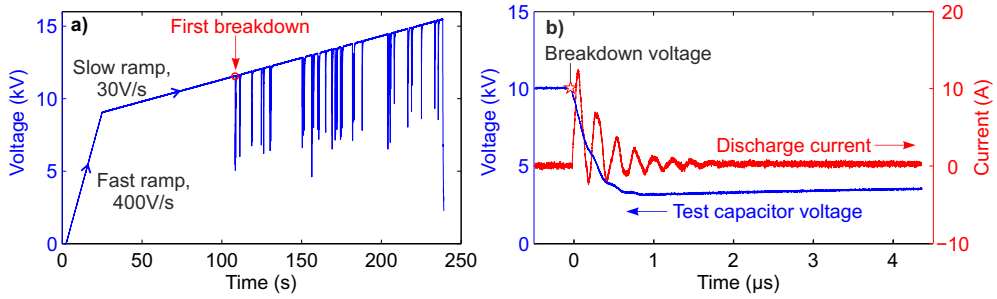

Figure 3.4. **a)** Test capacitor voltage during the breakdown measurement of a laboratory-stretched PP-1 film sample from [P5]. Self-healing breakdown events can be distinguished as transitory voltage drops. **b)** Discharge current pulse $i_d(t)$ and test capacitor voltage $u_{dut}(t)$ during the first self-healing breakdown event. Calculated breakdown field and discharge energy were $544\,\mathrm{V/\mu m}$ and 17.53 mJ, respectively.

It should be noted here that as the data acquisition was triggered to the discharge current signal, not all the recorded discharge events were actual breakdowns. This was done deliberately though in order to gather all the events that occurred during the

multi-breakdown measurement for more detailed analysis. Alternatively, triggering could also be based on the voltage drop during a breakdown (e.g. by AC coupling the capacitor voltage in order to remove the DC ramp component), thus avoiding non-shorting partial discharges to be recorded.

3.1.4 Breakdown field determination

Breakdown fields (E_{bd}) of each measured discharge event were calculated by dividing the corresponding breakdown voltage (U_{bd}) by the film thickness d_f. Provided that film thickness deviation over the active area is relatively small, the breakdown field calculation can be based on an average sample film thickness approach [13], as the error in the breakdown field calculation will be negligible. With the aid of the video recording, the average film thickness d_{avg} was calculated as arithmetic mean of the corresponding thickness map segment thicknesses where breakdowns had occurred by the end of the breakdown measurement (assuming normal distribution). The adequacy of normal distribution to represent the film thickness data is presented in Figure 3.5a–c for the laboratory-scale, pilot-scale and commercial capacitor-grade films, respectively. Although not mathematically perfect, normal distribution was found to result in reasonably good fit to the thickness data and overall, average film thickness calculated as arithmetic mean was found justified and practical. Alternatively, the breakdown fields can be calculated event-by-event by rigorously determining the average thickness around the each discharge spot by means of the video recording and the sample film thickness map in MATLAB. If a discharge event occurred in the middle part of a thickness segment, the segment thickness was used; otherwise an average of the surrounding segment thicknesses was used. Albeit more laborious, this was found to minimize the error in breakdown field calculation due to thickness deviation, as will be discussed later.

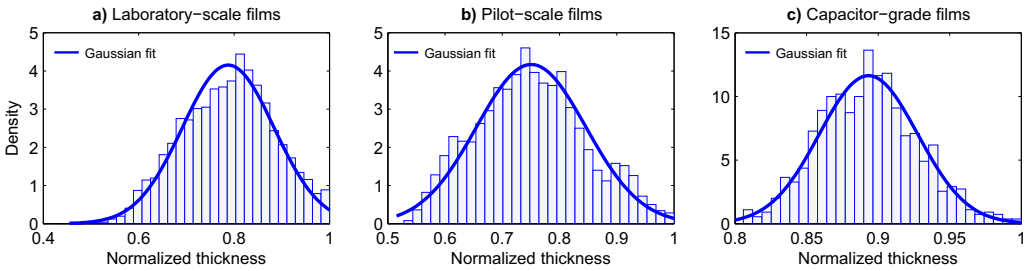

Figure 3.5. Normalized film thickness histograms of **a)** laboratory-scale, **b)** pilot-scale and **c)** commercial capacitor-grade films. The histograms represent 1.82 m^2, 1.27 m^2 and 0.34 m^2 total film areas, respectively. Solid lines show Gaussian fits. Detailed description of the film processing parameters of the laboratory- and pilot-scale films is given in [P5, P6]. The commercial film was 14.4 µm Hazy BOPP film by Tervakoski Films Group.

3.1.5 Data qualification procedure

As the self-healing multi-breakdown measurement at voltage levels exceeding several kV may often lead to various non-breakdown events occurring at the active area and close to the electrical contacts, it was considered critical to qualify only the breakdown events which appear independent from each other for further statistical analysis. A breakdown data selection procedure based on the discharge energy characteristics (Equation (2.3)) of the self-healing process was thus utilized for excluding non-breakdown events from

the measurement data. The main hypothesis is that discharge events with the discharge energies and breakdown voltages not following the trend set by the first breakdowns may be attributed to successive breakdowns occurring close to or at previous breakdown sites or to other non-breakdown events. The data qualification procedure is elaborated and evaluated in more depth later.

3.1.6 Statistical analysis

For the statistical analysis of the qualified breakdown data, 2-parameter (2-p) Weibull distributions and additively mixed 2-p Weibull distributions were utilized. As discussed in Section 2.4.2 the cumulative distribution function of a 2-p Weibull distribution is of form [12, 109]:

$$F(x) = \ 1 - \exp\left\{-\left(\frac{x}{\alpha}\right)^{\beta}\right\} \quad , x \geq 0 \tag{3.2}$$

where x is the measured variable (e.g. breakdown voltage) and α and β are the Weibull scale and shape parameters, respectively. More specifically, the cumulative breakdown probability as a function of time and voltage can be expressed as [12, 139]:

$$F(U,t) = 1 - \exp\left\{-C\int_0^t at^{a-1}[U(t)]^b dt\right\} \tag{3.3}$$

where U is the voltage, t is the time, C is the constant of proportionality and a and b are the Weibull shape parameters of time and voltage, respectively. Breakdown field E can be incorporated simply as $E = U/d$. Under progressive test conditions, assuming linear voltage increase and initial voltage of zero, $U(t) = dU/dt \times t = \dot{U} \times t$ and Equation 3.3 becomes:

$$F(U) = 1 - \exp\left\{-C\frac{a}{a+b}\dot{U}^{-a}U^{a+b}\right\} \tag{3.4}$$

Equation 3.4 can be written in a form analogous to the 2-p Weibull distribution from Equation 3.2 with a Weibull shape parameter $\beta = a + b$. Therefore it is emphasized that although a ramp test *appears* to measure breakdown voltage (or field), it actually reflects both the time and voltage functions. This aspect is discussed in more depth in sub-chapter 5.3.

In some cases, a single 2-p Weibull distribution is not sufficient for representing the whole breakdown data set as the breakdowns may be due to different origins, each with their own distinct failure distribution $F_i(x)$. Utilization of additively or multiplicatively mixed 2-p Weibull distributions is then proposed [113], given that a physically meaningful explanation for the distribution type and each sub-population can be made [99]. Fischer argues that a multiplicatively mixed Weibull distribution is physically more reasonable when considering an ensemble of identical samples which can fail due to different competing mechanisms [99, 140]. On the other hand, additively mixed distributions may occur when the sample ensemble contains substandard samples due to e.g. defects or contaminants [12, 99]. In fact, both the additively and multiplicatively mixed Weibull models can typically describe a given data set equally well [141], thanks to their increased mathematical flexibility. In this thesis, additively mixed 2-p Weibull distributions were utilized for which the cumulative distribution function is of form [12, 109]:

$$F(x) = \sum_{i=1}^{S}\frac{N_i}{N}F_i(x) = \sum_{i=1}^{S}\frac{N_i}{N}\left[1 - \exp\left\{-\left(\frac{x}{\alpha_i}\right)^{\beta_i}\right\}\right] \tag{3.5}$$

where $F_i(x)$ is the 2-p Weibull distribution from Equation (3.2), S is the number of subpopulations, N_i/N is the portion of subpopulation i and α_i and β_i are the Weibull scale and shape parameters of subpopulation i, respectively. Moreover it is defined that $N_i \geq 0$ and $\sum_{i=1}^{S} N_i/N = 1$. In the typical case two subpopulations are utilized ($S = 2$), one for describing the material-inherent breakdown distribution and another to describe the low-probability breakdowns deviating from the inherent breakdown distribution.

Statistical analysis was performed with Weibull++ and MATLAB software. In accordance to IEEE Std 930-2004 [113], the breakdown data were sorted from smallest to largest and each data point was assigned a rank from $i = 1$ to $i = n$ where n is the total amount of breakdown data points. The failure probabilities $F(i, n)$ of each event were then estimated using Median Rank method in Weibull++ software (which can be approximated as e.g. $F(i, n) \approx (i - 0.44)/(n + 0.25)$ as in [113]). For the Weibull distribution parameter estimation, maximum-likelihood estimation (MLE) and non-linear regression (NLR) methods were used. Linear correlation or statistical tests such as the Kolmogorov-Smirnov (K-S) test can then be utilized for evaluating the goodness-of-fit of the chosen theoretical distribution. A more detailed description of parameter estimation methods and goodness-of-fit tests is out of the scope of this thesis and can be found elsewhere (e.g. [109, 142]).

Weibull area-scaling can be utilized to extrapolate breakdown results measured with a smaller active area A_1 to represent a larger active area A_2. Assuming that a set of breakdown data measured with an active area A_1 is Weibull-distributed with a scale parameter α_1 and that the shape parameter β and the film thickness stay constant, the scale parameter α_2 of another (larger) area A_2 may be expressed as [109]:

$$\alpha_2 = \alpha_1 \left(\frac{A_2}{A_1} \right)^{-1/\beta} \tag{3.6}$$

However, the assumption of constant Weibull β may not always hold true and can lead to false conclusions [15]. Weibull area-scaling and the issues thereof are discussed in more detail later.

3.1.7 Comparative small-area single-breakdown measurement

In addition to the large-area multi-breakdown measurements, comparative small-area single-breakdown measurements were also performed in order to study the relationship between small- and large-area measurement methods. Small-area single-breakdown measurements were performed by using a steel rod-rod electrode configuration with thin graphite plates in between the rods and the sample film in order to smoothen the contact and to prevent electrode pitting. The active area was approximately $1\,\mathrm{cm}^2$ and the measurements were performed in mineral oil with a $400\,\mathrm{V\,s^{-1}}$ DC voltage ramp rate in accordance to the IEC-60243 standard [13, 14]. The method was equivalent to the one previously used in [64, 90, 143].

3.1.8 Application of inter-layer pressure

In one of the associated publications, the effect of inter-layer pressure on the breakdown characteristics of various capacitor-grade metallized films was analyzed using the self-healing multi-breakdown approach [P3]. A film arrangement comprising of two sheets of metallized film and a dielectric spacer film (polyimide, $100\,\mu\mathrm{m}$ in thickness) was used to form a test capacitor with an active area of $A = 16\,\mathrm{cm}^2$ similarly as described above

in Section 3.1.1. In addition, a 1 mm rubber sheet and a 16 cm^2 square piece of thin acrylic plastic plate were inserted between the films and the top plate of the test capacitor in order to smoothly focus the pressure on the active area of the test capacitor. A bolt-adjustable clamping device was used to exert axial compressive force on the active area of the test capacitor. An ACBES-3t load cell mounted beneath the clamping plates allowed measurement of the total compressive force F_{tot} by means of a Kyowa WGI-400A instrumentation amplifier. The inter-layer pressure P exerted on the active area was then calculated as $P = (F_{tot} - mg)/A$ where m is the total mass of the test capacitor and the lower steel plate and g is the gravitation constant (9.81 m/s^2).

3.2 Measurement method evaluation

3.2.1 Breakdown progression and discharge event characterization

Figure 3.7 presents freeze-frames extracted from breakdown measurement videos depicting typical self-healing breakdown progression over time at various breakdown voltage ranges (or film thickness range). The capacitor-grade PP-4 and the laboratory-stretched PP-1 film samples presented in Figures 3.7a–b were measured in insulating oil [P5]. A 6 µm BOPP film sample measured in atmospheric air is presented Figure 3.7c. For the films with a negligible thickness deviation over the active area, the breakdowns seemed to occur in a geometrically random manner at the active film area. However, in the case of laboratory-stretched film samples which exhibited more distinct thickness profiles, the breakdown progression more or less followed the film thickness profile. Due to the electrode de-metallization associated to the preceding breakdown events, the electrical contact with the thickest areas of the laboratory-stretched films was often lost before the voltage ramp reached their breakdown voltage (see e.g. Figure 3.7b, the last event). The self-segmentation effect was more profound in the case of the laboratory-stretched films but it was occasionally observed with the capacitor-grade and pilot-scale films too. It is also noticeable from Figure 3.7c that with decreasing film thickness, and hence with decreasing breakdown voltage level, the self-healing discharge energy decreases in accordance with Equation (2.3) and results in smaller de-metallized area. In principle, this increases the "resolution" of the method, i.e. a larger amount of breakdowns from a wider breakdown voltage range can be measured from the given active area.

The discharge events occurring during the multi-breakdown measurement could generally be categorized into [P1, P5]:

1. Breakdown events
2. Consecutive breakdown events close to or at previous breakdown sites
3. Non-shorting partial discharges
4. Flashovers across the metallized electrode edges

The breakdown events were characterizable by a major (50–70 %) voltage drop in the test capacitor terminals and a rapid flow of discharge current over the µs time scale, similarly as shown earlier in Figure 3.4b, and visually, as distinct self-healing breakdowns with approximately circular de-metallized areas (see Figure 3.7). In general, the observed breakdown events could be described similarly as the single-hole breakdowns described by Klein [126–128, 131]. At the breakdown voltage range <6 kV most of the measured discharge events were typically characterizable as single breakdown events [P1, P2, P3].

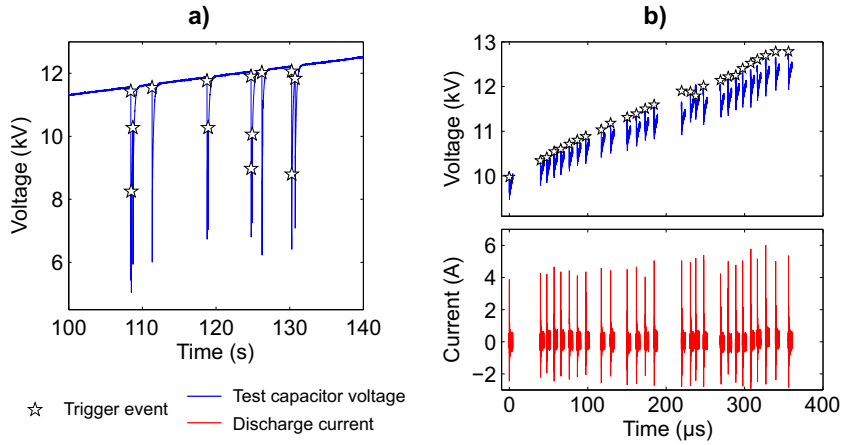

Figure 3.6. Examples of **a)** consecutive self-healing breakdowns and **b)** sequential non-shorting partial discharges measured from a laboratory-stretched PP-1 film [P5]. In a), the main breakdowns are followed by rapid consecutive breakdown events with breakdown voltages lower than that of the preceding main breakdown. The data in a) is a zoomed-in portion of Figure 3.4a within time interval of 100–140 s. In b), oscilloscope data of a rapidly occurring sequence of non-shorting partial discharges is shown (top: test capacitor voltage, bottom: discharge current). The leftmost event in b) occurred 225.17 s after the voltage ramp initiation in Figure 3.4a.

However, at higher voltage levels of >6–8 kV, the main breakdown events were often followed by rapid bursts of consecutive breakdown events, as exemplified in 3.6a. The breakdown voltages and the calculated discharge energies of the consecutive breakdowns were typically lower than that of the main breakdown event as they occurred during the voltage recharge period of the main breakdown. Visual analysis of consecutive discharge events confirmed that they often occurred close to or at previous breakdown sites and resulted in smaller and more deformed de-metallized patterns in comparison to the main breakdown events. Previously, consecutive self-healing breakdowns have been attributed to graphite formation and incomplete self-healing process [44]. Also, a thermally activated conduction wave originating from the heat release of the main breakdown can increase the local electric field at the surrounding colder regions [144], thus aiding the generation of consecutive breakdowns close to a previous breakdown site. In addition, non-shorting partial discharges were also observed at high voltage levels, especially after multiple discharge events and major de-metallization of the electrode surfaces had occurred closer to the end of the measurement, see Figure 3.6b. The partial discharges were characterized by a negligible voltage drop (<100 V), rapid current pulse of a few A magnitude and a significantly lower discharge energy in comparison to the actual breakdown events. The partial discharges were attributed to short-distance arcs visually observed on the metallized electrode surface and close to the electrical contacts with the electrode films. Lastly, on very rare occasions, flashovers across the metallized electrode edges were sometimes observed. The test capacitor voltage, discharge current and the discharge energy during flashover events were found to be very similar to those of the actual breakdown events occurring in the active area, and hence it was hard to distinguish them from the measurement data alone. The first breakdowns were however always checked against flashovers from the breakdown video recordings.

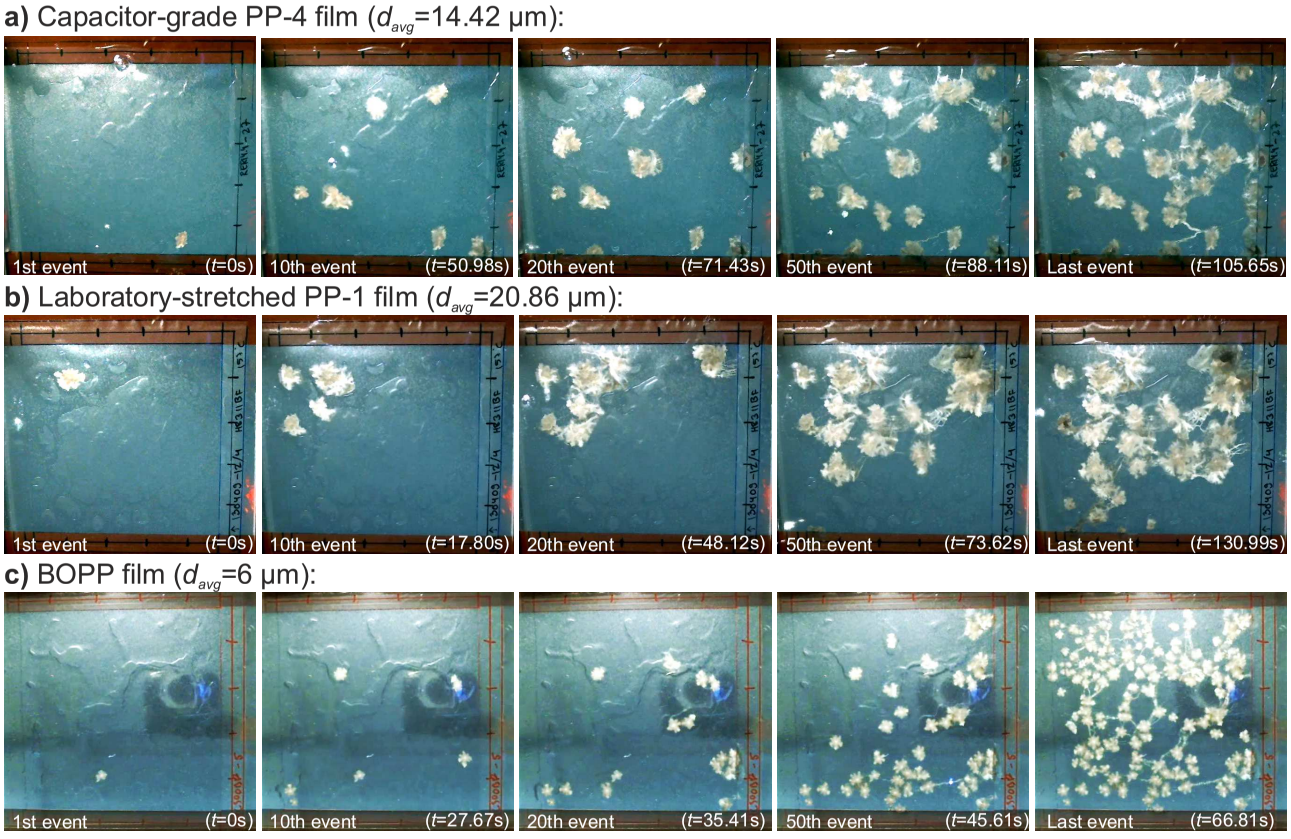

Figure 3.7. Breakdown evolution of **a)** a capacitor-grade PP-4 film sample (d_{avg}=14.42 µm) [P5], **b)** a laboratory-stretched PP-1 film sample (d_{avg}=20.86 µm) [P5] and **c)** a 6 µm BOPP film sample (dry measurement). The frames were extracted from the breakdown videos at the instants of the 1st, 10th, 20th, 50th and the last discharge event. The time values in brackets correspond to the time since the first breakdown. Active area is 81 cm^2 and the voltage was ramped at a 30 $V\,s^{-1}$ rate. The test capacitor voltage of the laboratory-stretched PP-1 film (b) was presented earlier in Figure 3.4a. The thickness profiles of the first two films are presented in [P5].

3.2.2 Self-healing discharge energy characteristics

Self-healing breakdown characteristics of the measurement system using Zn-Al-metallized 12 µm BOPP electrode films (Tervakoski PSX 12) are presented in Figure 3.8. The data are taken from 746 large-area multi-breakdown measurements of various non-metallized BOPP and BOPP-SiO_2 PNC sample films in the ∼4–25 µm range, mostly from [P4, P5, P6] but also from a number of previously unpublished measurement trials. Active area was $A = 81\,\mathrm{cm}^2$ and only the first measured breakdowns were considered from each sample film as they certainly represented independent breakdowns. Here, the exact nature of the sample film is not of interest; instead the purpose is to analyze the self-healing breakdown characteristics over a wide breakdown voltage range, as this serves as a foundation for the data qualification process described in the following sub-chapter.

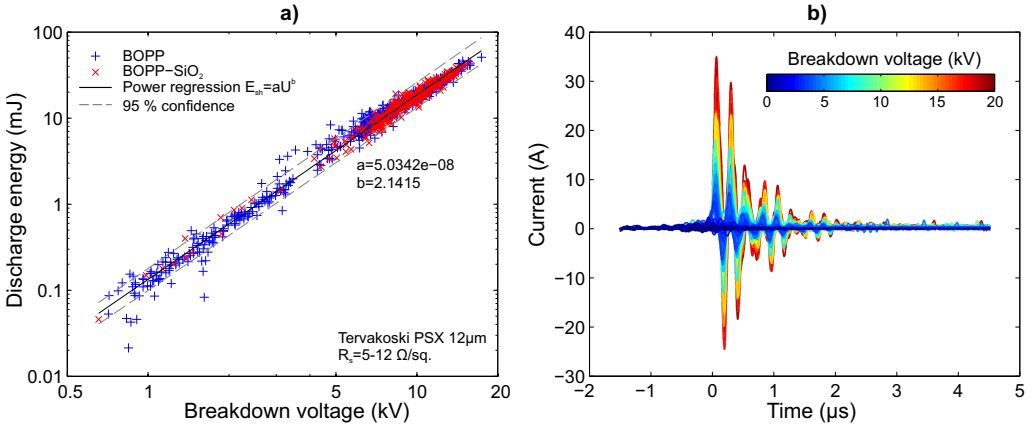

Figure 3.8. a) Self-healing discharge energy characteristics of the measurement system using Zn-Al-metallized 12 µm BOPP electrode films. The data are taken from the large-area multi-breakdown measurements of various BOPP- and BOPP-SiO_2 PNC films in the ∼4–25 µm range (a total of 746 measurements). Active area was $A = 81\,\mathrm{cm}^2$. Only the first self-healing breakdown event from each sample film was considered. Power dependence $E_{sh} = aU_{bd}^b$ in accordance with Equation (2.3) was fitted to the data (dashed lines show 95 % confidence). It is remarked that the studied BOPP-SiO_2 PNC films exhibited permittivities similar to that of BOPP. **b)** Overlay plot of discharge current waveforms corresponding to the data presented in (a) as a function of time and breakdown voltage, showing a typical under-damped RLC-circuit response. Gentle Savitzky-Golay filtering was applied in MATLAB in order to remove noise from the waveforms.

As is evident from Figure 3.8a, the calculated discharge energies show a clear power dependence $E_{sh} = aU^b$ in accordance with Equation (2.3) over the whole studied breakdown voltage range. The obtained constant $b = 2.1415$ is in the expectable experimental range of 2–6 [43, 124], although it is much lower than $b \approx 4$ originally reported by Heywang [19] and Shaw *et al.* [4]. However, the result here indicates that the discharge energy is approximately proportional to U_{bd}^2, in accordance with Equation (2.4). Figure 3.8a also suggests that E_{sh} is not strongly dependent on the sample capacitance variation[1]. This was also further confirmed in [P1] in which Zn-Al-metallized 6 µm BOPP film samples (R_s = 5–12 Ω/sq.) were found to show no difference in discharge energy characteristics when the active area was varied between 2–42 cm^2. Assuming simply that $E_{sh} = aU_{bd}^b = {}^1\!/_2 C_{eff} U_{bd}^2$, the effective capacitance partaking in the self-healing process can be approximated from

[1] In the ∼4–25 µm thickness range, C_{dut}∼41.2–6.6 nF ($A = 81\,\mathrm{cm}^2$, $\varepsilon_r = 2.3$).

Figure 3.8a as $C_{eff} \approx 101$ nF. Overall, in analogy to PD-measurement, these observations suggest that the measured (apparent) discharge energy characteristics largely reflect the response of the measurement system to a discharge event occurring in the test capacitor unit. Moreover, Figure 3.8b presents the captured discharge current waveforms of the above self-healing breakdown events as a function of time and breakdown voltage. Interestingly, the discharge current pulse duration is independent of the breakdown voltage which agrees well with the study of Sassoulas *et al.* [43] but not with the study of Qin *et al.* [119] in which $\tau_{sh} \propto U_{bd}^2$ has been suggested. It is reminded here that the self-healing breakdowns were non-confined, i.e. no inter-layer pressure was applied.

The effect of parallel capacitance on the self-healing breakdown characteristics was studied in [P1]. Figure 3.9 presents the discharge energy characteristics of 6 µm Zn-Al-metallized BOPP film as a function of parallel capacitance C_p (0.5–200 nF). As expected, varying capacitance has a strong effect on the self-healing discharge energy and duration. By decreasing the effective capacitance partaking in the breakdown process, the voltage drop magnitude across the test capacitor terminals is increased which leads to more effective arc constriction as the arc power density drops more rapidly. This reduces the discharge energy from several hundreds of mJ at $C_p = 200$ nF down to <10 mJ range at $C_p = 0.5$ nF, which accordingly also increases the number of discharge events measurable from the given active area.

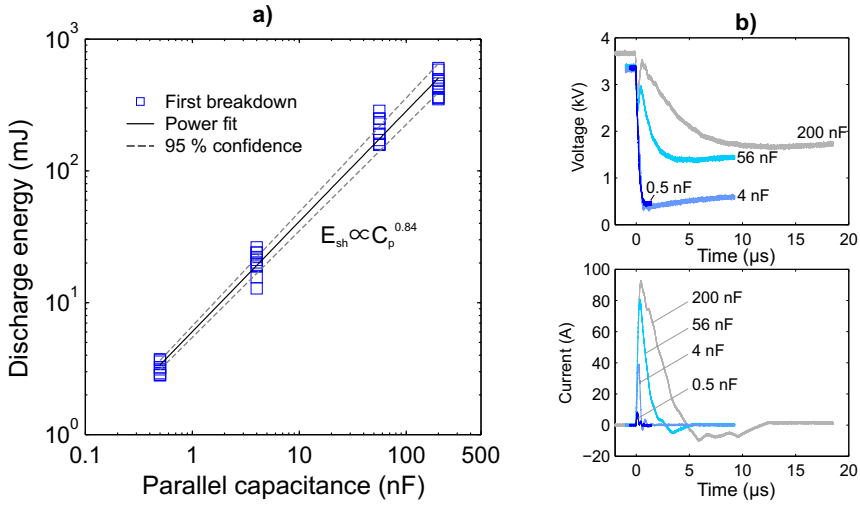

Figure 3.9. **a)** Discharge energy E_{sh} of 6 µm Zn-Al-metallized BOPP film ($A = 10\,\text{cm}^2$, $R_s = 5$–$12\ \Omega$/sq.) as a function of parallel capacitance C_p (0.5–200 nF) [P1]. Only the first self-healing breakdown from each sample was considered. **b)** Test capacitor voltage C_{dut} (top) and discharge current i_c (bottom) as a function of time and parallel capacitance C_p. With decreasing C_p, the voltage drop magnitude during self-healing breakdown increases which results in more effective arc constriction.

The effect of inter-layer pressure on the self-healing breakdown process was studied in [P3] and in other studies. Figure 3.10 presents discharge energy characteristics of Al-metallized 4 µm BOPP film ($R_s = 5\,\Omega$/sq.) as a function of inter-layer pressure and parallel capacitance (in the 0–4 MPa and 0–200 nF range, respectively). The current pulse duration was found to decrease strongly with inter-layer pressure, regardless of the fact that no major voltage drop occurred due to the added parallel capacitance. Already at $P = 0.5$ MPa the discharge energy decreased to <10 mJ range as the critical power

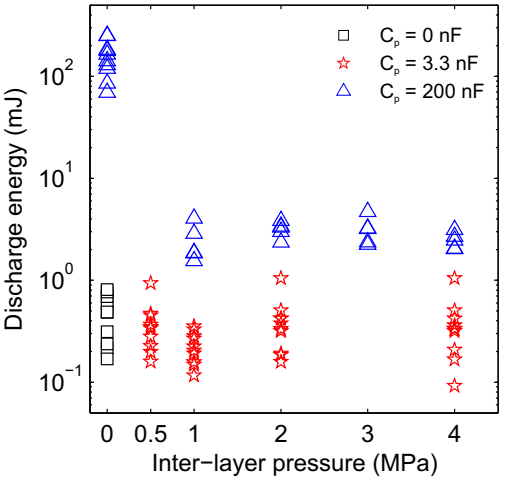

Figure 3.10. Effect of inter-layer pressure on the self-healing discharge energy characteristics of 4 µm Al-metallized BOPP film ($A = 16\,\mathrm{cm}^2$, $R_s = 5\ \Omega$/sq.). Only the first self-healing breakdown from each sample was considered. The average breakdown strength was in the ∼2 kV range at zero inter-layer pressure but decreased to ∼800 V range when inter-layer pressure was applied [P3].

density for sustaining the arc increased [117]. The results in Figure 3.10 are in line with the study of Chen *et al.* in which the discharge energy of Al-metallized 7.5 µm BOPP film was found to decrease strongly and saturate to <10 mJ range already at a relatively low inter-layer pressure of ∼200 kPa [123]. It is however notable that the breakdown strengths of the studied BOPP, PEN and PPS films in [P3] were also found to decrease significantly when inter-layer pressure was applied; this aspect is discussed in more detail in sub-chapter 4.3.

3.2.3 Breakdown data qualification

The purpose of the data selection procedure was to rule out non-breakdown events from the measurement data prior to the statistical analysis. This was seen as a crucial phase, as the non-breakdown events described above and in [P1, P5] would otherwise distort the breakdown distribution if all the data were used. The importance of careful data qualification prior to further analysis when subsequent self-healing breakdowns are included in the data set is also supported by e.g. Klein [126]. The foundations of the data qualification process was set on the self-healing discharge energy characteristics described in the previous sub-chapter. The data selection was based on two criteria, namely by selecting only the discharge events (i) for which the corresponding discharge energies follow the trend preset by the first measured self-healing breakdowns and (ii) for which the breakdown voltages are higher than that of the previously selected breakdown [P4, P5, P6, P7, P8]. Alternatively, data qualification can be based solely on the discharge energy criterion as in [P1, P2, P3]. The data qualification step was performed in MATLAB with a custom-made program which allowed convenient control and visualization of the data selection process (see Figure A.4).

The selection procedure is described graphically in Figure 3.11. Firstly, the calculated discharge energies of all the discharge events measured from six samples of laboratory-stretched PP-1 film from [P5] are shown as a function of the breakdown voltage in a log–log scale in Figure 3.11a, with the 50 first discharge events and the first measured breakdowns of each sample shown separately. The power dependence of the discharge energy on the breakdown voltage can be readily distinguished from Figure 3.11a, especially when considering e.g. the 50 first discharge events measured from each sample (compare with Figure 3.8a). The discharge events measured later on show larger scattering in

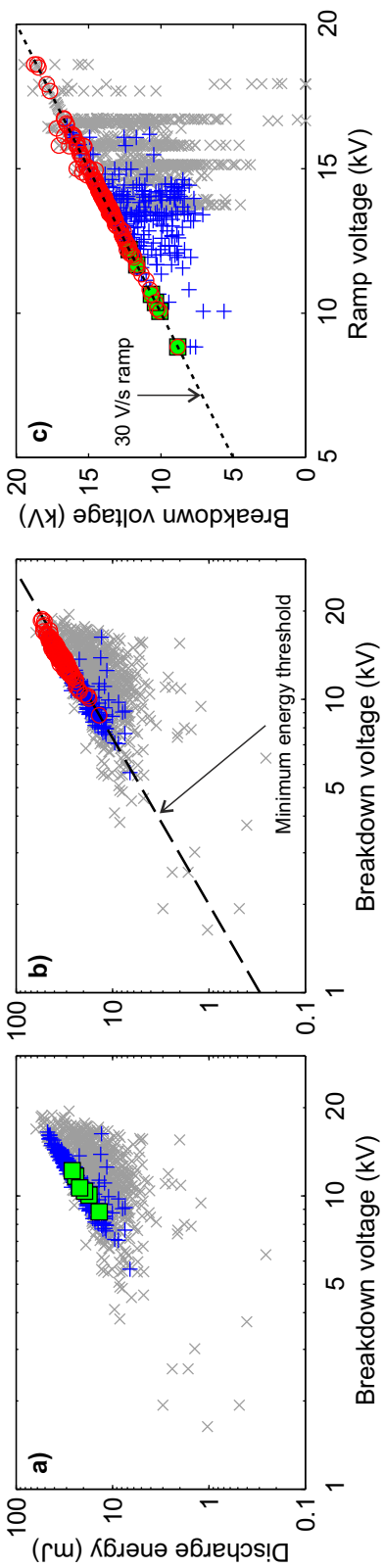

Figure 3.11. Data selection procedure applied to the data measured from six 81 cm^2 samples of laboratory-stretched PP-1 film for excluding non-breakdown events prior to the statistical analysis [P5]. **a)** The calculated discharge energies of all the discharge events as a function of breakdown voltage. The 50 first discharge events (blue) and the first measured breakdowns (green) of each sample are shown separately. **b)** Determination of the minimum discharge energy threshold and data selection. Only the discharge events above the energy threshold and with breakdown voltages higher than that of the previously selected breakdown are qualified (red). **c)** Measured breakdown voltages as a function of the 30 $V\,s^{-1}$ ramp voltage, depicting the time-dependence of the selected breakdowns.

terms of breakdown voltage and discharge energy which can be attributed to consecutive self-healing breakdowns and non-shorting partial discharges occurring closer to the end of the measurement.

The MATLAB program performed the following actions. By utilizing the first measured breakdowns, the slope b of the power regression line $E_{sh} = aU^b$ is calculated. For very homogeneous dielectric films, the first breakdown voltages can be close to each other and the calculated power regression line may not follow the discharge energy trend in a satisfactory way. In such a case, the discharge events subsequent to the first one may also be included in the power regression calculation in order to guide the slope b properly. Then, by taking into account the discharge energy deviation of the first breakdowns (as the points do not necessary fall on the calculated regression line precisely), the minimum energy threshold a_{min} is determined. In graphical terms (see Figures 3.11a–3.11b) the power regression line with a constant slope b is shifted vertically along the y-axis so that it passes through the lowest data point; this is set as a_{min}. Finally, by considering the data of each sample film separately, the program qualifies only the discharge events with discharge energies above the minimum energy threshold a_{min} and with breakdown voltages higher than that of the previously qualified event from the same sample film. First breakdowns are always qualified and are used as a basis for the data selection process. Figure 3.11c shows the measured breakdown voltages as a function of ramp voltage ($30\,\mathrm{V\,s^{-1}}$), depicting the time-dependence of the selected breakdowns. It is evident that the selection procedure described above only qualifies the events which follow the applied voltage ramp.

3.2.4 Statistical analysis and error assessment due to film thickness deviation

The associated publications [P1]–[P8] exemplify the statistical analysis of qualified multi-breakdown data measured from a wide variety of different polymer films. Single 2-p Weibull distributions were utilized always when possible. However, it was often found necessary to utilized additively mixed 2-p Weibull distributions in order to achieve mathematically and visually adequate fits to the multi-breakdown data sets [P1]–[P8]. As direct comparison of distributions with varying structures is not possible, 5 %, 63.2 % and 95 % breakdown percentiles were always calculated in order to enable convenient comparison between all the distributions. Figure 3.12 presents the large- and small-area breakdown distributions of the laboratory-scale, pilot-scale and capacitor-grade BOPP films from [P5] along with the 90 % confidence bounds. Both the average and manual thickness determination approaches were utilized for the breakdown field calculation and are presented separately. Regardless of the stringent data qualification step the large-area multi-breakdown method yields a large amount of breakdown data and results in detailed, fingerprint-like breakdown distributions. The calculated breakdown fields at the 63.2 % breakdown probability are well in the range of 600–700 V/µm which is typically considered as the dielectric strength of a good-quality BOPP film [15, 16]. The 5 % percentiles reside in the 500–600 V/µm range, similarly as measured by an automatic breakdown tester in [16].

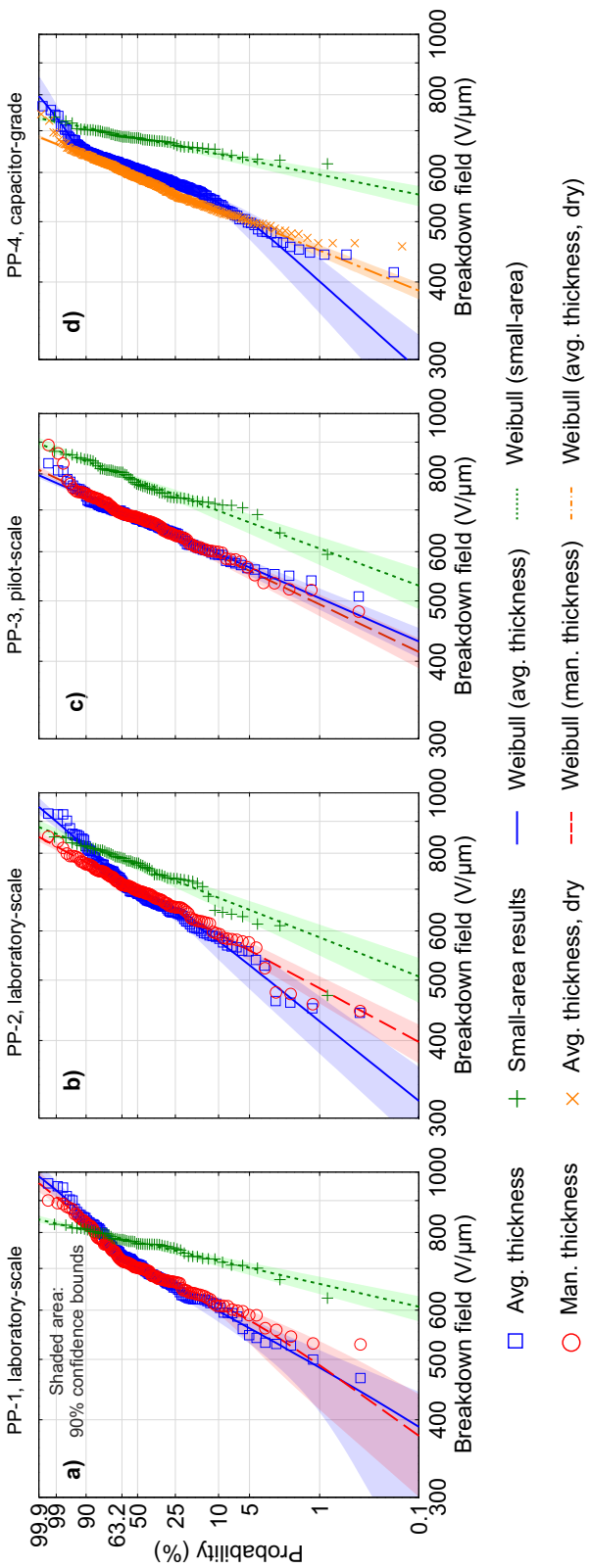

Figure 3.12. Large- and small-area breakdown distributions of laboratory-scale **a)** PP-1 and **b)** PP-2 films, **c)** pilot-scale PP-3 film and **d)** capacitor-grade PP-4 film [P5]. For the large-area multi-breakdown distributions, both the average (blue) and the manual thickness approach (red) were used for calculating the breakdown fields. Small-area results (1 cm^2 per sample, green) were measured with the conventional single-breakdown method. The shaded areas represent the 90 % confidence bounds. An additional large-area breakdown distribution of PP-4 measured in atmospheric air is also presented (orange). See [P5] for the distribution structures and Weibull parameters

Figure 3.12 shows that the breakdown distribution curvature is partly due to the film thickness determination method; when average sample film thickness is used, the distribution tends to spread at the low and high probability regions which can naturally be attributed to the thinnest and the thickest parts of the sample films. However, the overall difference between the average and manual thickness approaches was found to be surprisingly small in [P5] and it certainly cannot be the main reason why single 2-p Weibull distributions were found insufficient for describing some of the breakdown data sets. The film thickness deviation effect was studied in more detail by considering all the studied film types from [P4, P5, P6, P7] (and some unpublished data) for which both the average thickness and the manual point-by-point thickness determination approaches were utilized (in total 37 different film types). Comparing the average thickness approach with the manual point-by-point approach, Figure 3.13 presents the relative error in the 5, 63.2 and 95 % breakdown percentiles and the weakest measured point for the above films as a function of film thickness standard deviation (SD). The trends in Figure 3.13 support the conclusion above; with increasing film thickness deviation the average thickness approach tends to result in slightly lower 5 % and slightly higher 95 % breakdown percentiles in comparison to the manual approach. Understandably the weakest point shows the largest scatter while the 63.2 % percentile is very close to that calculated by the manual approach. The results here suggest that breakdown field determination based on the average film thickness approach is sensible, given that a sufficient thickness uniformity is maintained over the active area (SD $\leq 1\,\mu m$ based on Figure 3.13). For example, regarding the study discussed in sub-chapter 4.1 in which the film thickness standard deviations were $\sim$1 µm or less, the mean relative errors in the 5, 63.2 and 95 % breakdown percentiles due to the average sample thickness approach were found to be only $\pm$3.1 %, $\pm$0.83 % and $\pm$2.0 %, respectively. Due care has to be taken though when analyzing sample films with considerable thickness deviation, especially in the analysis of weak points.

3.3 Area-dependence and applicability of Weibull area-scaling

Area dependence of the breakdown properties in polymer films was studied in [P1, P2, P5]. Figure 3.14 presents the dielectric strength distributions of Zn-Al-metallized 6 µm BOPP film measured with $A = 2$–42 cm^2 active areas along with a multi-breakdown distribution representing the total measured area of 1950 cm^2 [P1]. Area dependence of the breakdown strength distributions is clearly distinguishable in the higher probability region ($> 10\%$) which is also supported by the decreasing Weibull α and relatively constant Weibull β with increasing electrode area. However, significant deviation from single 2-p Weibull distribution was observed in the low-probability region with all the electrode areas, similarly as reported for e.g. BOPP, PI and PTFE films [26, 39, 115]. Comparing with the large-area multi-breakdown distribution, Figure 3.14 exemplifies the fact that with a small active area, it is likely that most of the measured breakdowns only represent the very high breakdown probability region of the film. The large-area multi-breakdown distribution of the studied 6 µm BOPP film clearly shows a distinct defect population ("S-curvature") in the low-probability region; this was also further confirmed at a later stage in [145].

Weibull area scaling was studied in more detail in [P5], in which the large-area multi-breakdown method was compared with a conventional single-breakdown method. Figure 3.12 presented earlier shows that the small-area measurements reside in a higher breakdown field region in comparison to the large-area measurements but may still be projected vertically along the probability axis to match portions of the corresponding

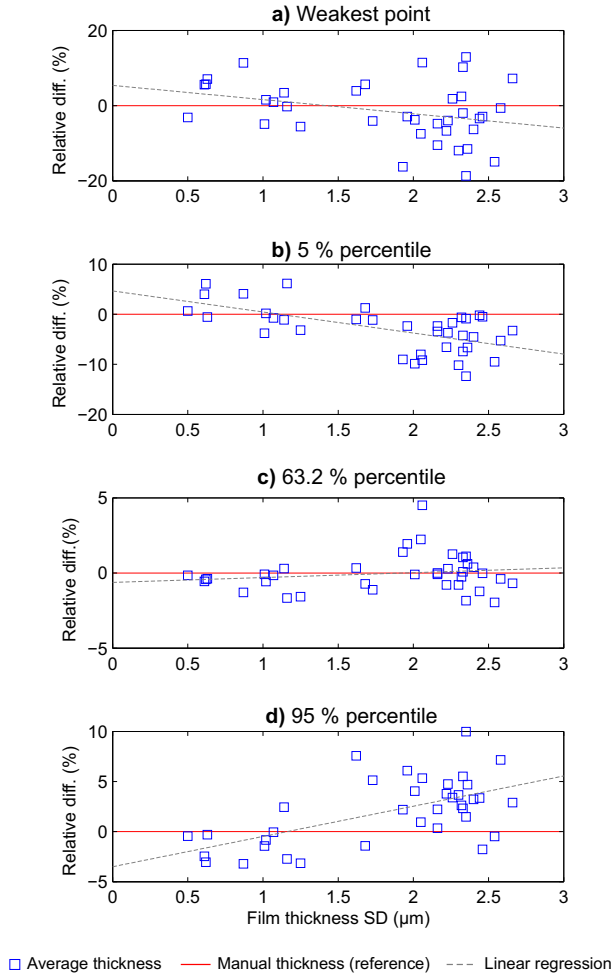

Figure 3.13. Relative error in breakdown field calculation due to the average sample film thickness approach in comparison to the manual point-by-point thickness determination. The data are taken from the large-area multi-breakdown measurements of 37 different BOPP- and BOPP-SiO_2 film types from [P4, P5, P6, P7]. The film thickness standard deviations (SD) represent 6–10 sample films per film type (486–810 cm^2 total area). The **(a)** weakest point and the **(b)** 5 %, **(c)** 63.2 % and **(d)** 95 % breakdown percentiles are presented. Dashed lines show linear regression.

large-area breakdown distributions, similarly as in Figure 3.14. However, the small-area single-breakdown distributions were found to exhibit higher Weibull β parameters in comparison to the large-area multi-breakdown distributions; while probably related to the area-effect, this could also be due to the differences in the breakdown measurement technique (see sub-chapter 3.1.7). Therefore, Weibull area-scaled small-area breakdown results in accordance with Equation (3.6) were found to be generally in poor agreement with the large-area dielectric strength results; if the distribution does not contain sufficient information about the large-area performance in the first place, area-scaling, which merely shifts the small-area breakdown distribution along the breakdown field axis, cannot extrapolate to larger areas correctly.

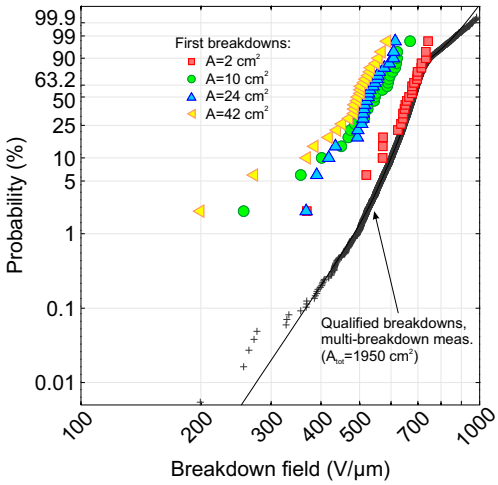

Figure 3.14. Dielectric strength distributions of Zn-Al-metallized 6 µm BOPP film measured with $A = 2$–42 cm^2 active areas along with a multi-breakdown distribution representing the total measured area of 1950 cm^2 [P1]

3.4 Statistical aspects of multi-breakdown measurement

The fundamental differences between the large-area multi-breakdown and the small-area single-breakdown measurement methods and the statistical aspects thereof are considered in more detail in the following. Essentially, the studied total sample film area A_0 can be represented as a parallel network of Weibull distributed components. In principle, one can determine the breakdown characteristics of the total film area by first cutting the sample film into smaller pieces and by then measuring their dielectric strengths piece-by-piece by the single-breakdown measurement approach, with the chosen active area essentially determining the "resolution" of the measurement. If the film area is covered completely, the obtained empirical distribution should represent even the weakest point of the total film area in a satisfactory way. By contrast, however, if the whole sample area is measured by the large-area multi-breakdown approach at one sweep, the breakdowns are measured in a bottom-up manner with each consecutive breakdown reducing the active area by a small de-metallized area A_{sh} related to the electrode vaporization around the breakdown site during self-healing. In this sense, the de-metallized area A_{sh} determines the "resolution" (or apparent active area) of the multi-breakdown measurement, and with a small enough "resolution" a comparable (or even more detailed) end-result as obtainable by the piece-by-piece small-area single-breakdown measurement is acquired.

In practical terms however, the above two methods rarely yield as detailed breakdown characteristics as described in the ideal case above. The disadvantage of the single-breakdown method is that in order to measure the breakdown characteristics of large film areas in fine detail a considerable amount of small-area samples has to be measured which is tedious, time-consuming and often impractical to realize. On the other hand, while the large-area multi-breakdown approach enables convenient measurement of relatively large film areas in a bottom-up approach, it is often not possible to cover the sample film area completely[2] due to the electrode de-metallization and self-segmentation effects, hence resulting in truncation of the empirical breakdown distribution. In this regard, a large-area multi-breakdown distribution should be differentiated from a conventional dielectric strength distribution based on small-area single-breakdown measurement with a constant active area.

[2]This is however also the case with small-area single-breakdown measurement as a sufficient film margin has to be left around the active area to prevent flashover across the electrodes.

The above scenarios were studied further by employing the Monte Carlo simulation technique in MATLAB. During each Monte Carlo simulation iteration, a 2500 cm^2 total film area was simulated by generating random numbers from a theoretical distribution representing the breakdown field distribution of a typical BOPP film. The chosen distribution was an additively mixed 2-p Weibull distribution in accordance with Equation (3.5):

$$F(x) = \frac{N_1}{N}\left[1 - \exp\left\{-\left(\frac{x}{\alpha_1}\right)^{\beta_1}\right\}\right] + \frac{N_2}{N}\left[1 - \exp\left\{-\left(\frac{x}{\alpha_2}\right)^{\beta_2}\right\}\right] \tag{3.7}$$

- Sub-population 1: $N_1/N = 1\%$, $\alpha_1 = 500\,\mathrm{V\,\mu m^{-1}}$ and $\beta_1 = 8$; representing a small amount of weak points deviating from the main distribution.
- Sub-population 2: $N_2/N = 99\%$, $\alpha_2 = 700\,\mathrm{V\,\mu m^{-1}}$ and $\beta_2 = 15$; representing a typical BOPP film as measured with a 1 cm^2 active area [16]

Random samples were then selected from the film area and the resulting sample distribution was compared against the true distribution representing the whole 2500 cm^2 surface. Thus, by varying the sample dimensions and quantity the area-effect could be studied. In each case 10000 simulations were calculated in order assure high statistical significance. The simulation scheme is detailed further in Appendix B.

Figure 3.15a exemplifies one typical iteration of the above simulation case when the total simulated film area is represented at 1 cm^2 resolution and selections of (i) 20 small-area single-breakdown samples (1 cm^2 active area) and (ii) 6 large-area multi-breakdown samples (81 cm^2 active area) were performed at random locations from the film area. Figure 3.15b presents the resulting sample distributions from Figure 3.15a, assuming that all the cells enclosed by the sample boundaries could be measured. It is evident already from Figure 3.15 that a large amount of breakdowns covering a relatively large film area is

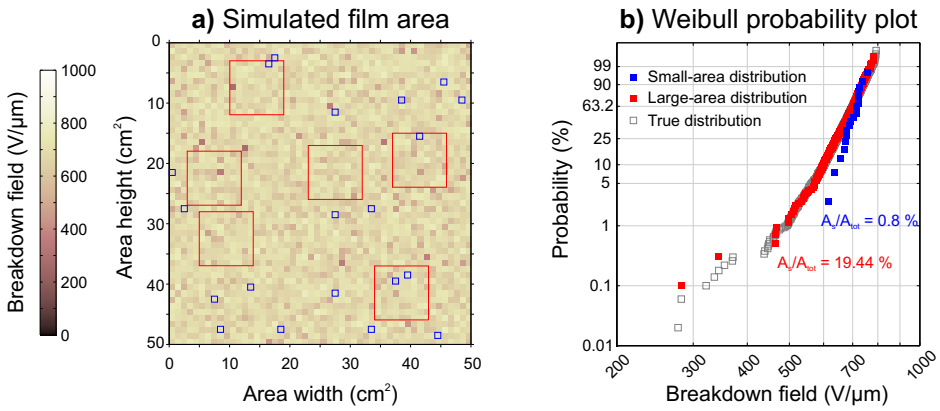

Figure 3.15. Example iteration of the Monte Carlo simulation technique employed in MATLAB. **a)** Simulated film area with each unit cell representing 1 cm^2 area of BOPP film. 20 small-area samples (1 cm^2 active area) and 6 large-area samples (81 cm^2 active area) were randomly selected from the film area. **b)** Resulting breakdown distributions from a), assuming that all the cells enclosed by the sample boundaries could be measured. The sample area fractions A_s/A_{tot} denote the percentage of total film area covered by the samples. The true distribution represents the whole simulated film area measured with 1 cm^2 active area.

required for reliable breakdown strength assessment; the 20 small-area single-breakdown samples, which cover only 0.8 % of the total film area, provide poor estimate of the true breakdown distribution shape and structure.

The above-described area-effect was studied in more detail by running a series of Monte Carlo simulations as a function of sample area fraction, see Figure 3.16. Two-sample Kolmogorov-Smirnov (K-S) test was performed to compare the sample distribution against the true distribution during each iteration, with the null hypothesis H_0 that the two were from the same population [109]. The results suggest that at very low sample area fractions the calculated p-values (Figure 3.16a) and the two-sample K-S test statistic values (Figure 3.16b) show large scatter which indicates high uncertainty in approximating the true distribution when only a small sample area is covered. However, with increasing sample area fraction, the p-value and the K-S test statistic distributions show decreasing scatter and they tend towards 1 and 0, respectively, thus indicating that the sample

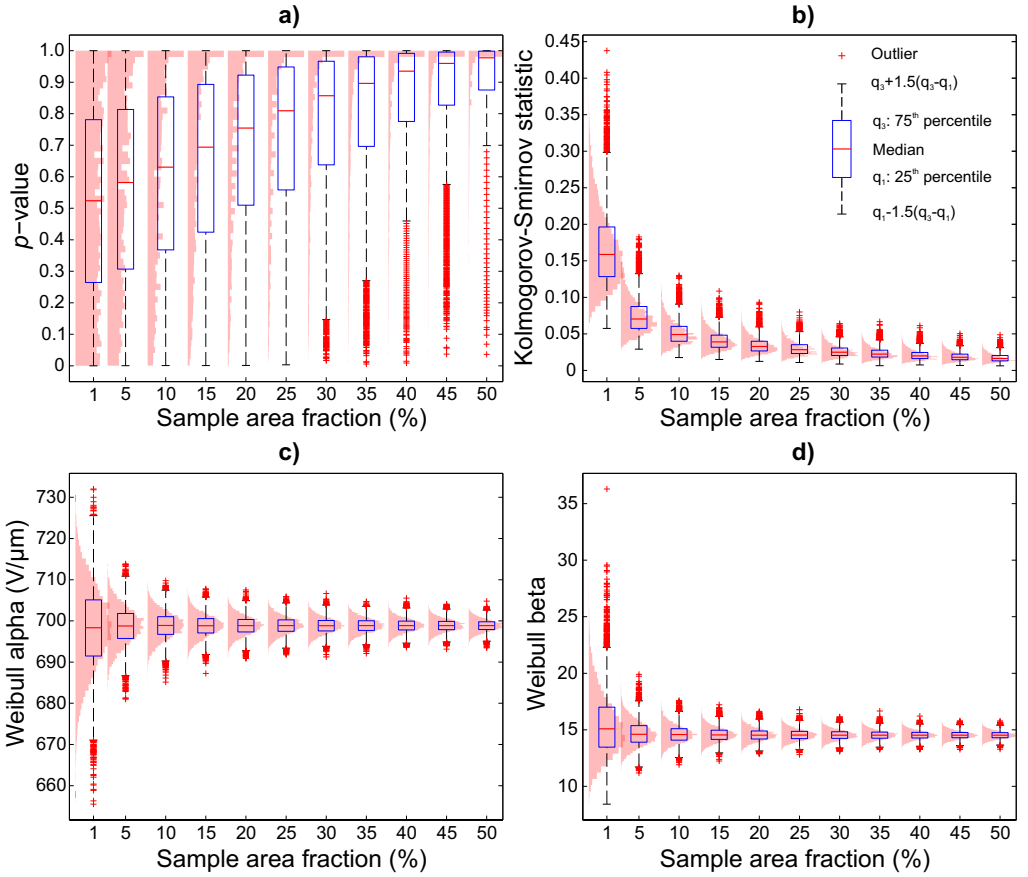

Figure 3.16. Monte Carlo simulation of the area-effect as a function of sample area fraction. Two-sample Kolmogorov-Smirnov (K-S) test was used for comparing the sample distribution against the true distribution during each iteration. In addition, 2-p Weibull distribution was fitted to the sample distribution during each iteration. The box plots and the underlying data histograms present: **a)** p-value and **b)** K-S test statistic distributions from the 2-sample K-S test and the 2-p Weibull **c)** α and **d)** β parameter distributions as a function of sample area fraction. 10000 iterations were calculated for each area fraction.

distribution better represents the true distribution when a larger area is covered. The 2-p Weibull α and β parameters fitted to the sample distributions (Figures 3.16c–d) also reflect the above aspects; particularly notable is the large scatter in Weibull β parameter at low sample area fractions which, in coherence with sub-section 3.3, also indicates high uncertainty in Weibull area-scaling if the small-area sample distribution were to be extrapolated to represent larger film area by using Equation (3.6). It is remarked here that in the above scenario all the elements enclosed by sample boundaries were considered in the analysis; Appendix B presents further simulation results as a function of active area when only the weakest point of each sample is considered in the analysis.

The Monte Carlo simulation scheme was expanded further by taking into account the self-segmentation effect during large-area multi-breakdown measurement. The resolution of the simulation was increased so that the simulated 2500 cm^2 film area was represented at 1 mm^2 resolution. This was done by area-scaling the assumed theoretical BOPP breakdown distribution from the initial $A_1 = 1\,\mathrm{cm}^2$ area to a new area $A_2 = 0.01\,\mathrm{cm}^2$ in accordance with Equation (3.6); see Figure 3.17a for a graphical description. Figure 3.17b exemplifies the simulated self-segmentation behavior when de-metallized area of $A_{sh} = 0.25\,\mathrm{mm}^2$ area is assumed to be removed with each self-healing breakdown; as more and more self-healing breakdowns occur in a bottom-up manner, sections of the remaining sample area are gradually isolated from the rest of the active area as the connection to the left- and right-hand sample boundaries simulating electrical contact edges are lost (compare with Figure 3.7). As a result, the isolated high-strength film regions cannot be measured which essentially restricts the empirical distribution to a smaller range. Figure 3.17c exemplifies the resulting multi-breakdown distribution from one Monte Carlo iteration when 6 samples of 81 cm^2 area were randomly chosen from the 2500 cm^2 total area; the right-truncation of the empirical distribution due to the self-segmentation effect is apparent in the high probability region. The general (doubly) truncated form of an additively mixed 2-p Weibull distribution is [133, 146]:

$$G(x) = \frac{F(x) - F(a)}{F(b) - F(a)} \quad 0 \leq a \leq x \leq b < \infty \tag{3.8}$$

where $F(x)$ is the additively mixed 2-p Weibull distribution given by Equation (3.5) and a and b define the left- and right-truncation points, respectively. Right-truncated distribution form is obtained when $a = 0$ and $b < \infty$, and an exemplifying fit to self-segmented sample distribution data is shown in Figure 3.17c. Further results on the Monte Carlo simulation of the self-segmentation effect are presented in Appendix B.

Although the simulated self-segmentation effect in Figure 3.17 suggests right-truncation of the sample distribution, this was rarely the case in practical measurements. Quite the contrary, the measured multi-breakdown distributions were often found to show rightward curvature in the high field/probability region, with this effect being most noticeable with thin films such as the 6 µm Zn-Al metallized BOPP film presented in [P1] (see also Figure 3.14). Although it can be speculated that these high-field breakdowns may represent another breakdown mechanism, further work is needed to clarify this. It is also remarked here that perhaps a more exact statistical evaluation of successive breakdown data could be adopted from the field of microelectronics reliability. Assuming uniform occurrence of K uncorrelated breakdown events over the given surface area, Suñé and co-workers have derived successive breakdown statistics based on the Poisson model, implying that only the first $K = 1$ breakdowns are Weibull distributed and result in a straight line in Weibull plot, whereas the successive $K \neq 1$ breakdowns are not necessarily Weibull distributed (although they can be approximated reasonably well with Weibull distributions) [147–149].

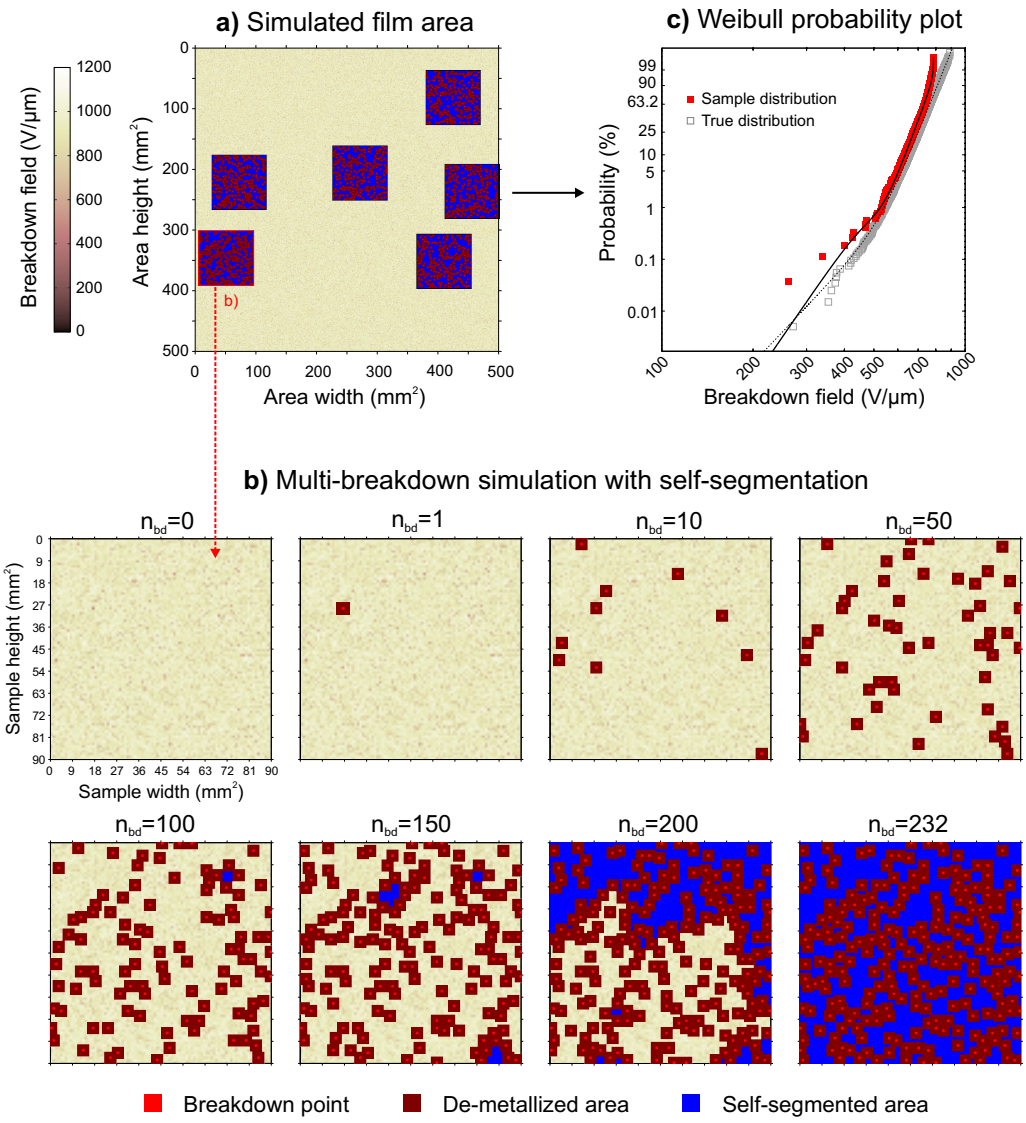

Figure 3.17. Example iteration of the Monte Carlo simulation of multi-breakdown measurement when the self-segmentation effect is considered. **a)** Simulated 2500 cm^2 film area represented at a 1 mm^2 resolution. A random selection of 6 multi-breakdown samples of 81 cm^2 has been performed. **b)** Series of snapshots as a function of breakdown number n_{bd} depicting the breakdown progression and eventual self-segmentation when the area de-metallized per each breakdown is $A_{sh} = 0.25\,\mathrm{mm}^2$. The cells break down in a bottom-up manner. The left- and right-hand sample boundaries represent the electrical contact edges. **c)** Resulting large-area multi-breakdown distribution (6 samples) compared against the true distribution measured with 0.25 mm^2 active area. The solid fit is the right-truncated additively mixed 2-p Weibull distribution fit, Equation (3.8), with $S = 2$, $N_1/N = 99.51\,\%$, $\alpha_1 = 738\,\mathrm{V\,\mu m^{-1}}$, $\beta_1 = 15.63$, $\alpha_2 = 450\,\mathrm{V\,\mu m^{-1}}$, $\beta_2 = 8.56$, $a = 0$ and $b = 787\,\mathrm{V\,\mu m^{-1}}$.

Utilization of such a model was not found justified though, as the more simple and convenient 2-p Weibull and additively mixed 2-p Weibull distributions were found to fit well to the qualified multi-breakdown data sets and they have also been previously applied to self-healing breakdown data [133–136].

3.5 Considerations and implications

Some final remarks on the multi-breakdown measurement method are presented in the following. In regard the data qualification step, although it is not possible to unambiguously claim that the data selection procedure is infallible (as it is possible that some of the excluded discharge events are actual breakdowns and conversely, that the set of qualified breakdowns contains non-breakdown events), the described approach was found to produce sensible results in a simple and convenient way. The ever increasing voltage criterion was found justified as it leads to more strict qualification of breakdown events. It is emphasized that simply by decreasing the sample film thickness, and hence the voltage range required for the measurement, many of the non-breakdown events can be avoided, and possibly, the data qualification step would not be required at all.

The active area can also be increased in order to cover even larger film areas. It should be noted however that the increase in the sample capacitance with the active area also increases the discharge energy level in accordance with the Equation (2.3). This effect is limited by the properties of the metallization layer though, as the sheet resistance (or thickness) of the metallization layer resists the current flow into the fault spot from the active areas further away from the fault spot. It should be also noted that with very large active areas, special measures may have to be taken in order to ensure a clear trigger condition during a discharge event in the test capacitor. By improving the sample film processing and by aiming towards lower overall film thickness and deviation, most of the problems associated to high-energy self-healing can be readily mitigated and the need for insulation oil is omitted.

The effect of ramp rate on the resulting breakdown distribution is an important factor to consider [109]. As detailed in sub-chapter 3.1.3, depending on the specimen thickness, either (i) a linear ramp or (ii) a slow rate-of-rise ramp profile in accordance with IEC-60243-1 standard [13] was chosen for the majority of the measurements conducted within this thesis. It is remarked here that the ramp rate effect was studied in more detail in [P8]. While the breakdown distributions of the conventional BOPP films measured in [P8] were found to be more or less unaffected by the ramp rate condition, those of the measured 4.5 wt-% SiO_2-BOPP nanocomposite films were found to exhibit strong ramp-rate-dependence with decreasing ramp rate leading to lower breakdown performance; these results will be discussed in more detail later on in sub-chapter 5.3. It is however concluded here that instead of using a fast rate-of-rise as proposed in e.g. IEC-60243-1 for thin films, breakdown measurement with moderate to slow ramp rate is more likely to reveal such unexpected behavior as that noticed in [P8].

In summary, the large-area multi-breakdown measurement method developed as a part of this thesis was thoroughly evaluated in this chapter and in the associated publications. The fundamental differences between the large-area multi-breakdown and the small-area single-breakdown measurement methods and the statistical aspects thereof were analyzed by the Monte Carlo simulation method. As opposed to conventional small-area single-breakdown measurement techniques (as described in e.g. IEC-60234 standard), the obvious advantage of the self-healing multi-breakdown approach is the ability to acquire a large amount of breakdown data from a relatively large total film area in a bottom-up

approach by utilizing a progressive voltage ramp test. The ability to obtain detailed breakdown fingerprints representing areas more relevant from the practical point-of-view is appealing, especially when considering e.g. research and development of novel dielectric films.

Chapter 4

Dielectric breakdown and structure-property relationships in polymer capacitor films

The main focus of this chapter is on the effect of film processing, structure and morphology on the large-area multi-breakdown characteristics of iPP-based capacitor films. The first part of the chapter covers a laboratory trial in which iPP-based non-oriented and bi-axially oriented films were manufactured by various small-scale film processing equipment in order to study the role of PP-grade, film structure, morphology and bi-axial orientation on the breakdown performance[1]. The latter part of the chapter is focused on the breakdown response and weak point characteristics of various commercial capacitor-grade BOPP, PEN and PPS films. Lastly, the effect of inter-layer pressure on the breakdown characteristics of capacitor-grade polymer films is discussed [P3].

4.1 Film structure, morphology and breakdown of cast and bi-axially oriented isotactic polypropylene

4.1.1 Polypropylene fundamentals: Crystal structure, morphology and film production

Polypropylene (PP) is a semicrystalline polymer with a repeat unit of –[CH_2–$CH(CH_3)$]– typically polymerized by Ziegler-Natta or metallocene catalysts [150, 151]. The macromolecular structure of PP homopolymer is illustrated in Figure 4.1 at different characteristic levels. Crystallization of PP, and hence the resulting morphology, is largely governed by the stereoregularity of the CH_3 (methyl) group in the PP chain as it determines the overall order (or tacticity) of the chain. As shown in Figure 4.1, PP can exist in isotactic (iPP) or syndiotactic (sPP) forms, which are both crystallizable but result in differing unit cells and melting temperatures; or in atactic (aPP) form which in the extreme case (zero tacticity) exhibits no crystallinity [152]. In general, high crystallinity necessitates high tacticity. Isotactic PP, which is the typical form of PP utilized in BOPP capacitor films, exhibits polymorphism; depending on the crystallization conditions it can crystallize into monoclinic α-, hexagonal β- or orthorhombic γ-forms which exhibit different crystallographic symmetries and unit cells [150]. Monoclinic α-form (see Figure 4.1) is the predominant form in most PP systems with a melting point of 160–165 °C. The less

[1] Based on a journal article manuscript still under preparation at the time of completion of this thesis (I. Rytöluoto, A. Gitsas, S. Pasanen & K. Lahti, "Effect of film structure and morphology on the dielectric breakdown characteristics of cast and bi-axially oriented polypropylene," *European Polymer Journal*).

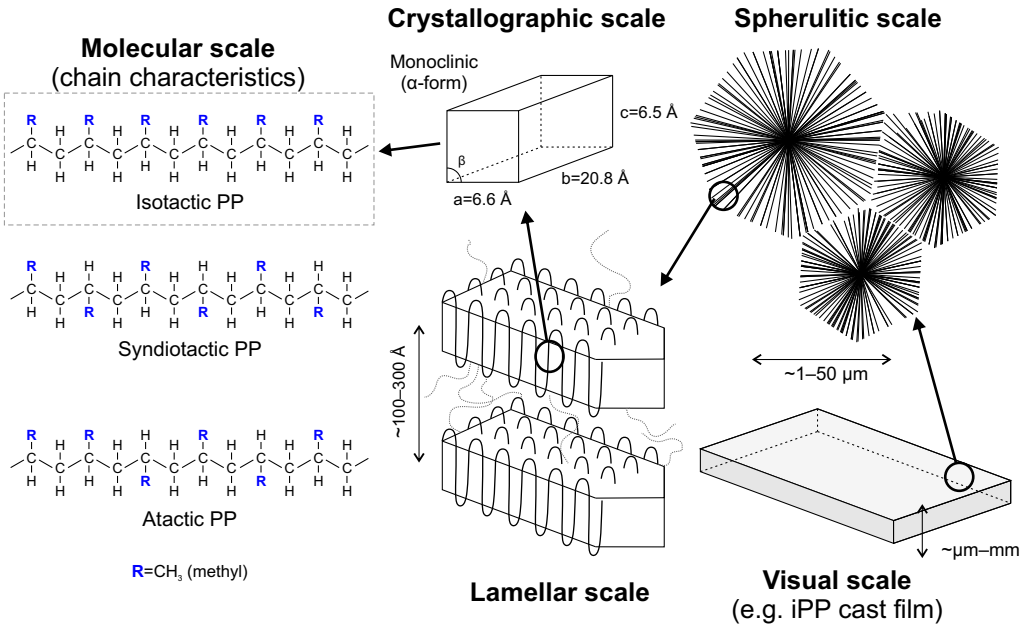

Figure 4.1. Schematical illustration of different levels of macromolecular structure in polypropylene. The size scales are adapted from [150].

stable and lower density hexagonal β-form is formed only under favorable crystallization conditions (suitable temperature gradient during cooling) or when selective β-nucleation agents are used, and it has a melting point of typically 12–15 °C lower than that of α-form [153]. Orthorhombic γ-iPP crystallites are only formed under high pressure which makes them relatively uncommon for samples formed under typical film processing conditions. Lastly, under rapid cooling conditions, iPP can also exist in non-crystalline mesomorphic (smectic) form which is an intermediate form between amorphous and crystalline forms. iPP polymorphism is discussed in more depth in e.g. [150, 151, 154].

On a larger scale, crystallizable iPP chains tend to form plate-like or ribbon-like lamella structures in which the polymer chains fold repeatedly over on themselves, as exemplified by the folded-chain model in Figure 4.1 [150]. Single polymer chains may form intercrystalline links between neighbouring lamellae through the amorphous volume [12]. α-form lamellar structures in iPP may also exhibit "cross-hatching" patterns in which tangential lamella branch from radially grown lamella [151]. Yet on a larger morphological scale, spherulitic structures may be formed under favorable crystallization conditions as cross-hatched lamellae grow radially outward from nucleation centers (Figure 4.1) [151]. As long as the conditions are kept favorable for crystallization, spherulites keep growing in a volume-filling manner until they impinge on their neighbours. Spherulitic morphology has a strong impact on the electrical properties [100], as will be discussed more later on.

Industrial-scale BOPP film manufacturing is essentially based on bubble (blown-film) or tenter-frame processes as described in e.g. [155, 156]. Both the processes begin by melt-extruding and quenching pre-stabilized PP pellets into a tube (bubble process) or a cast film (tenter-frame process) form. In the following step the PP tube or cast film is re-heated to a partly-molten state and thereafter bi-axially oriented. In the bubble process bi-axial orientation is achieved by inflating the polymer tube with air while simultaneously stretching it in the machine direction (MD) by film rolls. In sequential tenter-frame

process the re-heated cast-film is first stretched in the MD-direction by film rolls and thereafter conveyed to a tenter section in which it is stretched in the transverse direction (TD) by pulling the film by clips attached to the film edges. Alternatively, simultaneous tenter-frame processes in which MD/TD-directional orientation is achieved in one step are also available (see e.g. the LISIM® technology by Brückner Maschinebau GmbH & Co. KG [155]). In the final stage, the bi-axially oriented film is cooled and wound on rolls after which it can be metallized in a separate process if desired. Bi-axial orientation similar to that obtainable by sequential or simultaneous tenter-frame process can be mimicked in laboratory scale by using appropriate laboratory sheet-stretching equipment such as Brückner KARO IV laboratory-stretcher (as in this thesis). The bubble and tenter processes differ mainly in e.g. production speed and cost, but differences between them in terms of dielectric properties, such as high-field conduction and breakdown properties [157], have also been reported. Overall, although high-purity base polymer is a prerequisite for capacitor film production [17], many of the mechanical and dielectric properties of the final BOPP film are ultimately governed by the film manufacturing process [20]. PP film processing, morphology and breakdown characteristics are discussed more in the following.

4.1.2 Laboratory-scale film preparation, characterization and breakdown measurement

The general film processing steps for the laboratory-scale iPP-based cast and BOPP films are depicted in Figure 4.2. Two different commercial capacitor-grade iPP homopolymer pellets were used, PP1 and PP2, out of which PP2 was of high isotacticity grade. The polymers pellets were supplied already stabilized by the manufacturer. Melt flow rates (MFR), as measured under load of 2.16 kg at 230 °C in accordance with ISO 1133, were 2.2 and 3.3 g/10 min for PP1 and PP2, respectively. The crystalline melting temperatures T_m determined by DSC in accordance with ISO 11357-3 were 161 °C and 163 °C for PP1 and PP2, respectively. The polymers were dried at 70 °C prior to processing. The polypropylene pellets were melted and extruded into cast films. In order to study the effect of extrusion process on the cast film morphology and dielectric breakdown performance, three different extruders were utilized for the cast film manufacturing:

- **Extruder A**: Small-scale single-screw extruder (Brabender Plasticorder, 19/25 Z) with a flat die, melt pump and a screen pack with a three-layer filter pack (type H&B, 18 µm). Extruder A was operated in a semi-clean room environment. The compression ratio of the screw was high (4:1) and the extrusion pressure was set to 80 bar. Target cast film thickness d_{cast} for Extruder A was 500 µm.

- **Extruder B**: Large-scale single-screw extruder (Dolci 1) with a screen pack and a filter. The screw compression ratio was lower than that of Extruder A (approximately 1.5:1). Extruder B was operated without clean room facilities for manufacturing cast films with the target thickness of 400 µm.

- **Extruder C**: Small-scale extruder (Barmag). Extruder C had a low screw compression rate (1.5:1) and a dense filter pack (mesh size 400/900/2500/900/400). Extruder C was operated without clean room facilities for manufacturing both thick (200 and 400 µm) and thin (15 and 20 µm) cast films.

Cylinder temperature profile (T_{cylinder}), die temperature (T_{die}), chill-roll temperature (T_{cr}) and target cast film thickness (d_{cast}) are given in Table 4.1 for each extruder type.

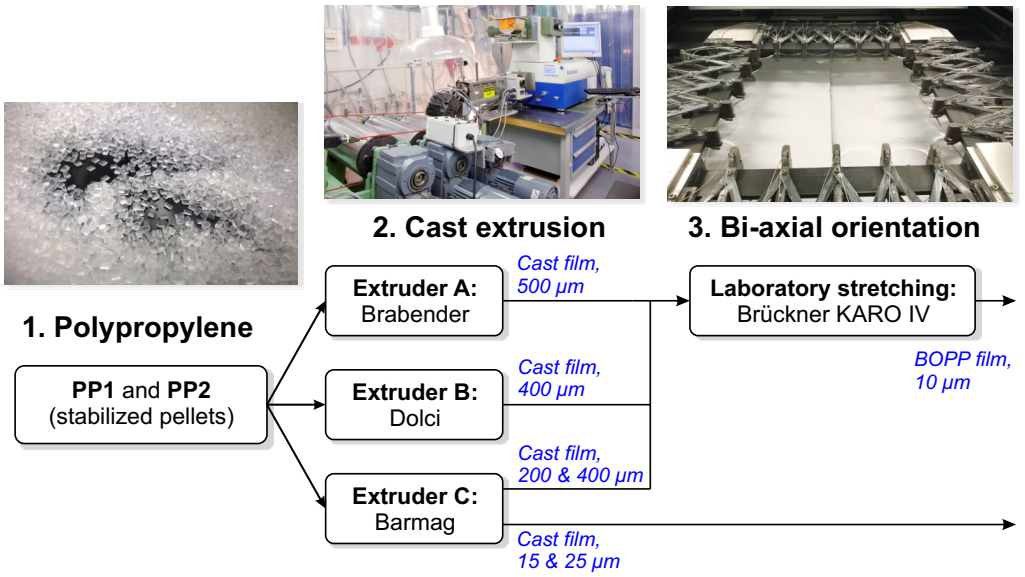

Figure 4.2. General iPP film manufacturing steps. Cast films were manufactured from two different polypropylenes by three different extruders. The thicker (200–500 µm) cast films we bi-axially oriented. The photographs from left to right showing PP-pellets, the Brabender Plasticorder extruder and bi-axial orientation of a cast film specimen with Brückner Karo IV are courtesy of VTT.

The extruders were cleaned prior to processing. The thick cast films (200–500 µm) were bi-axially oriented by Brückner KARO IV laboratory stretching machine (pre-heating time $t_{\mathrm{pre}} = 100$–120 s, fan power 60 %, set temperature $T_{\mathrm{set}} = 157\,^{\circ}\mathrm{C}$, constant strain speed of 417 %/s) with equibiaxial stretching ratios of either 3.5 x 3.5 (200 µm cast films) or 5.6 x 5.6 (400–500 µm cast films). The resulting BOPP films were ∼10–15 µm in thickness. The thin cast films (15–20 µm) were not bi-axially oriented. The naming convention of the samples is: polypropylene type – extruder – cast thickness – stretch-ratio (if bi-axially oriented), e.g. PP1-A-500-5.6 or PP2-C-15, see Table 4.1.

Cast-PP- and BOPP-film crystalline structures were studied by wide-angle X-ray scattering (WAXS). Bruker Discover D8 diffractometer operated in reflection mode with Ni-filtered CuKα X-rays (wavelength $\lambda = 1.5418$Å) was utilized to carry out the diffraction measurements. A two dimensional General Area Detector Diffraction System (GADDS) detector was used to record scattering data, in the 2θ interval of 10–32 degrees. The diffractometer was equipped with an Anton Paar DCS 350 heating stage with PEEK dome and a PT100 thermocouple. Three measurements were performed on each film sample in reflection geometry to determine the degree of crystallinity and phase content. The X-ray diffraction data were analyzed by first subtracting the amorphous halo from the diffraction profiles and by then using a multi-peak fitting procedure to fit the remaining crystalline peaks. β-form crystal indices depicting relative β-contents were calculated from the crystalline curves as [158]:

$$k_\beta = \frac{I^\beta_{300}}{I^\beta_{300} + I^\alpha_{110} + I^\alpha_{040} + I^\alpha_{130}} \tag{4.1}$$

Table 4.1. iPP cast film manufacturing and bi-axial orientation parameters. Numbers in parenthesis denote measured values (if available). Extruders A: Brabender, B: Dolci, C: Barmag. T_{cylinder} is the extruder cylinder temperature profile, T_{die} is the die temperature, T_{cr} is the chill-roll temperature, d_{cast} is the target cast thickness, t_{pre} is the pre-heating time prior to bi-axial orientation and T_{set} is the bi-axial orientation (set) temperature.

Code	PP	Cast film manufacturing					Bi-axial orientation		
		Extruder	T_{cylinder} (°C)	T_{die} (°C)	T_{cr} (°C)	d_{cast} (µm)	t_{pre} (s)	T_{set} (°C)	Stretch-ratio
PP1-A-500-5.6	PP1	A	220-230-230-230	230	90 (83)	500	120	157	5.6 x 5.6
PP1-B-400-5.6	PP1	B	160-195-220-230	230	88 (82.7)	400	120	157	5.6 x 5.6
PP1-C-400-5.6	PP1	C	220-230-260-260	270	80 (80)	400	120	157	5.6 x 5.6
PP1-C-200-3.5	PP1	C	220-230-260-260	270	80 (79)	200	100	157	3.5 x 3.5
PP1-C-15	PP1	C	220-230-260-260	270	80 (80)	15	-	-	-
PP1-C-20	PP1	C	220-230-260-260	270	80 (79)	20	-	-	-
PP2-A-500-5.6	PP2	A	220-230-230-230	230	90 (83)	500	120	157	5.6 x 5.6
PP2-B-400-5.6	PP2	B	160-195-220-230	230	88 (82.7)	400	120	157	5.6 x 5.6
PP2-C-400-5.6	PP2	C	220-230-260-260	270	80 (77)	400	120	157	5.6 x 5.6
PP2-C-200-3.5	PP2	C	220-230-260-260	270	80 (79)	200	100	157	3.5 x 3.5
PP2-C-15	PP2	C	220-230-260-260	270	80 (79)	15	-	-	-
PP2-C-20	PP2	C	220-230-260-260	270	80 (80)	20	-	-	-

where I^{α}_{hkl} and I^{β}_{hkl} are the intensities of the corresponding α- and β-form diffraction peaks with (hkl) defining the Miller's indices of each crystallographic plane.

Figures 4.3a–c present WAXS-profiles of iPP-cast films manufactured by Extruders A, B and C. The crystalline phases were predominantly of monoclinic α-form, however, the cast films also contained varying amounts hexagonal β-phase and negligible amounts of γ-form [158]. The β-phase contents were clearly linked to the cooling gradient induced upon transferring the cast film from the extruder die to the chill-roll. Overall, the cast film crystallinities were in the range of 68–70 %. Figure 4.3d presents WAXS-profiles of PP2-based BOPP films; only monoclinic α-form was present in the BOPP films and the crystallinities were 68 ± 1 %. Noticeable is also the (almost) complete disappearance of the $(111)/(041)(\bar{1}31)$ peak doublet at $2\theta \approx 21°$ angle upon bi-axial orientation which, according to Capt [156], is due to the anisotropic nature of the $(111)/(041)(\bar{1}31)$ crystal planes. Reflection mode WAXS-data only describe the (hkl) crystal planes oriented in the MD-TD plane, however, upon bi-axial orientation the $(111)/(041)(\bar{1}31)$ crystal planes are oriented in the TD-ND plane (as is seen in the transmission mode data in [156]).

Large-area multi-breakdown measurements and data analysis were performed in accordance with Chapter 3. Sample film thickness mapping (25 point-measurements per sample film) was performed for both PP-cast and BOPP film samples. The samples were immersed in insulating oil and DC voltage across the samples was ramped in accordance with the slow-rate-of-rise test at room temperature. Six sample films (81 cm^2 active area) were measured per each material. The breakdown fields were calculated based on the average film thickness which was found justifiable as the overall cast- and BOPP film thickness deviation was low. However, in order to study the effect of BOPP film thickness deviation in more detail, the breakdown fields of the BOPP films were also calculated based on the event-by-event manual thickness determination approach.

4.1.3 Observations on the breakdown behavior of BOPP and non-oriented cast PP films

Figure 4.4 exemplifies the breakdown behavior of BOPP and non-oriented cast iPP film samples during the multi-breakdown measurement. Figure 4.4a presents an overlay plot of the test capacitor voltages as a function of time during the breakdown measurements of a PP1-based BOPP film sample and a PP1-based non-oriented cast-PP sample. The initial fast voltage ramp phase ($400\,\mathrm{V\,s^{-1}}$) followed by a slower voltage ramp phase ($30\,\mathrm{V\,s^{-1}}$) in accordance with the slow-rate-of-rise test method are readily apparent in the Figure 4.4a. Discharge events occurring during the breakdown measurement are distinguishable as transitory drops in test capacitor voltage.

BOPP films

Regarding the BOPP film samples, as the voltage was ramped beyond the first breakdown voltage, discharge events began to occur at an increasing frequency, hence gradually reducing the active area and the capacitance of the sample. Figure 4.4b exemplifies typical test capacitor voltage and discharge current waveforms during a discharge event in a BOPP film sample; these are similar as described earlier in sub-chapter 3.1.3. Figure 4.4d shows a freeze-frame image of a BOPP test capacitor after the breakdown measurement, with the self-healing breakdown spots being recognizable as approximately circular de-metallized regions. The multi-breakdown activity of the BOPP sample film presented in Figure 4.4d lasted for 64.59 s, after which the electrical contact to the remaining active

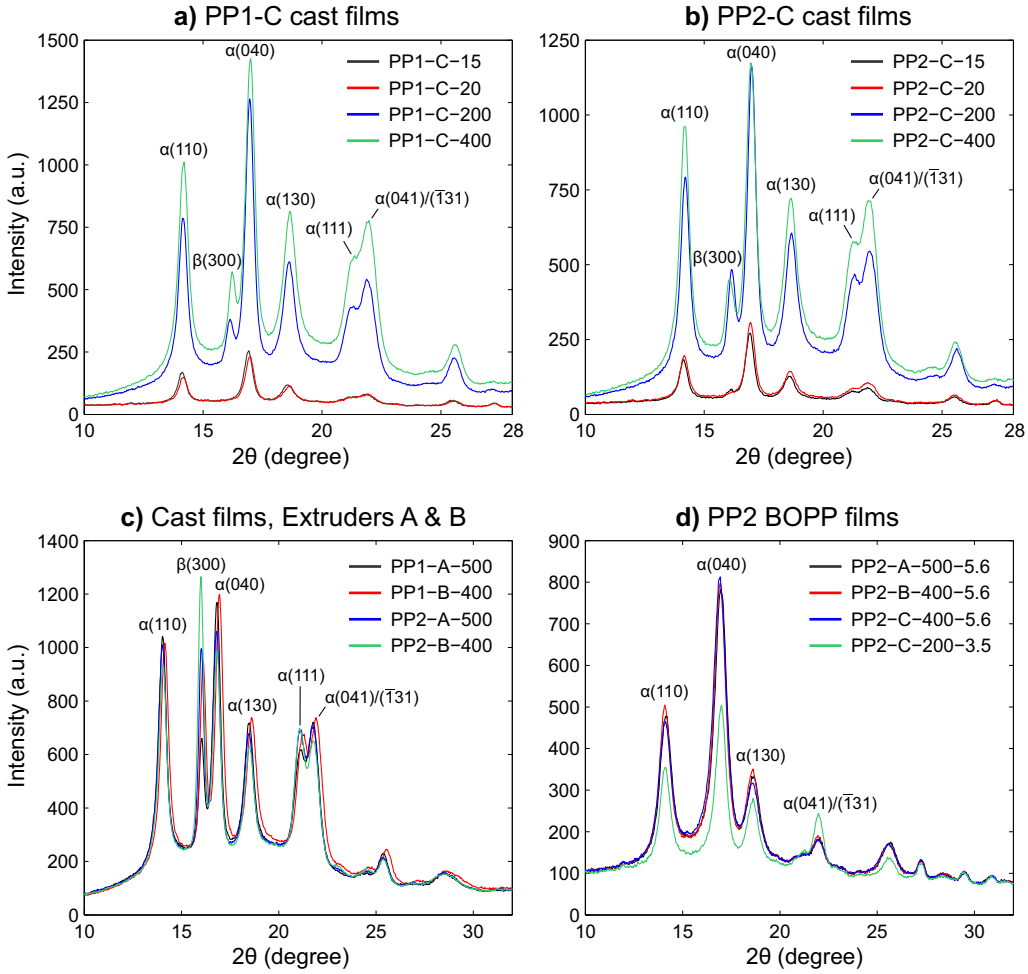

Figure 4.3. Wide-angle X-ray diffraction intensity vs. 2θ profiles of **a)** PP1-C cast films (15–400 µm), **b)** PP1-C cast films (15–400 µm), **d)** PP1 and PP2 cast films (Extruder A and B) and **d)** PP2 BOPP films. α- and β-crystal form diffraction peaks are marked in the figures [158]. Three measurements were performed on each sample in reflection mode; one representative curve is shown for each sample.

area was lost. Altogether, the multi-breakdown behavior of the BOPP film samples was found to be similar as observed in [P4, P5, P6, P7].

Non-oriented cast films

In contrary to the BOPP samples, the non-oriented PP cast films exhibited drastically different multi-breakdown behavior. Instead of occurring gradually with the slow ramp voltage, the cast films exhibited rapid avalanche-like breakdown behavior as soon as the first breakdown occurred, see Figure 4.4c and Figure 4.4d. Instead of occurring in an individual manner, the consecutive discharges typically propagated from the initial breakdown site onwards, with the maximum test capacitor voltage saturating to a level lower than the initial breakdown voltage and not being able to recover back to follow the

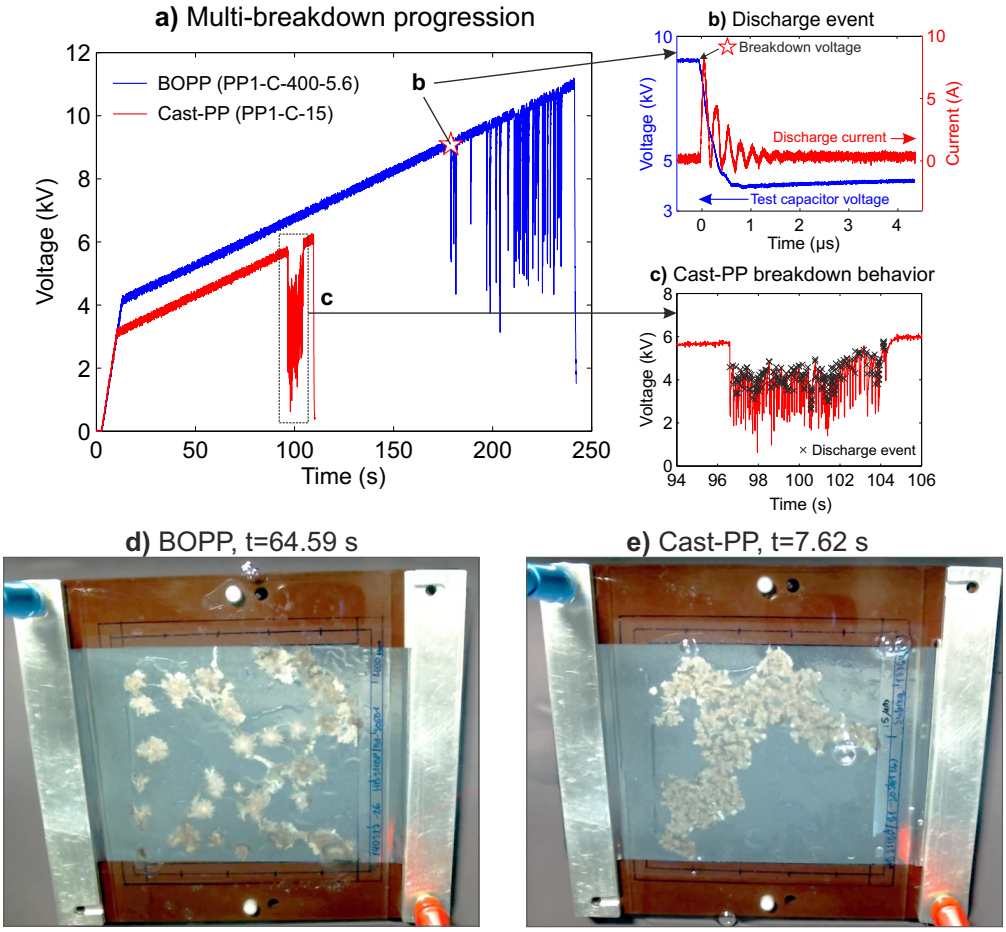

Figure 4.4. **a)** Overlay plot of test capacitor voltages during the multi-breakdown measurements of a BOPP sample and a non-oriented cast-iPP sample. Discharge events are distinguishable as sudden voltage drops. **b)** High-resolution acquisition of test capacitor voltage and discharge current during the first discharge event measured from the BOPP sample. **c)** A closer view of the test capacitor voltage during a rapid avalanche-like breakdown progression in the cast-PP sample. The superimposed markers correspond to the measured discharge events. **d)** & **e)** Freeze-frames of the BOPP and cast-PP test capacitors (top view) extracted from the video recordings at the time of last discharge event, respectively. The time values (t_d) indicate the time (s) since the first measured discharge event. The average film thicknesses were 13.42 µm and 14.81 µm for the BOPP sample and the cast-PP film sample, respectively.

set voltage ramp until electrical contact to the active area was lost (Figure 4.4c). The observed behavior was similar to the propagating-type breakdown previously observed by Klein [126, 131]. Typical duration of the propagating-type breakdown process was only a few seconds (7.62 s in Figure 4.4c). In a few cases the cast sample films also showed individual weak points at lower electric fields prior to the onset of the major propagating-type breakdown. The observed propagating breakdown behavior may be attributed to the inter-spherulitic regions of the non-oriented PP cast films which facilitate breakdown progression from the initial breakdown site along the damaged inter-spherulitic

regions; this aspect will be discussed in more depth later. It is remarked that in the case of a few PP cast sample films the initial breakdown event was not captured by the oscilloscope, as in the case presented in Figure 4.4c, which could be due to the trigger threshold level of the oscilloscope not being exceeded or due to the abrupt nature of the propagating-type breakdown process. Nevertheless, the onset breakdown voltage of the propagating-type breakdown process could then be extracted from the general voltage monitoring data recorded in LabVIEW.

Klein argues that the propagating-type breakdown is triggered by a single-hole breakdown event and, provided that replacing energy is supplied at a sufficient rate from the power supply, the hot periphery and damage of the previous breakdown site aid the occurrence of new breakdowns at adjacent sites [126, 127]. By increasing the series resistance R_{ser} in the measurement circuit (see Figure 3.3), the voltage recharge period between breakdown events can be elongated which should promote cooling between breakdowns and mitigate breakdown propagation. In order to study this, a few additional measurements were performed for the 15 µm PP2 cast-iPP films with increased series resistance. However, although a reduction in breakdown frequency was noticed, propagating-type breakdown progression was still observed even with $R_{\mathrm{ser}} = 100\,\mathrm{M\Omega}$; this suggests that the breakdowns process in the cast films is indeed different to that in BOPP films. It is noted that $R_{\mathrm{ser}} = 0\,\mathrm{M\Omega}$ was used for all the measurements presented in the following.

4.1.4 Large-area multi-breakdown distributions

Large-area multi-breakdown distributions of the studied BOPP- and non-oriented PP-cast films are presented in Figure 4.5 on the Weibull probability scale along with the

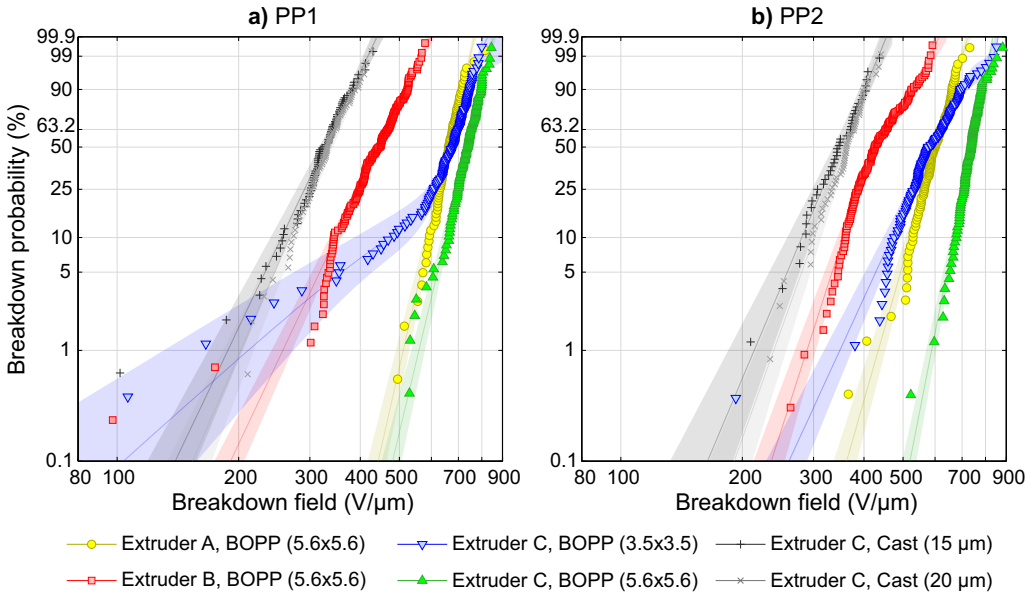

Figure 4.5. Large-area multi-breakdown distributions of the **a)** PP1- and **b)** PP2-based BOPP- and non-oriented iPP-cast films on the Weibull probability scale. Solid lines and shaded areas represent the Weibull distributions fitted to the empirical breakdown data and the 90 % confidence bounds, respectively. Either single or additively mixed 2-p Weibull distributions (2 sub-populations) were fitted to the breakdown data sets on the basis of best goodness-of-fit.

calculated 90 % confidence bounds (shaded areas). Regarding the results presented here, event-by-event breakdown field calculation approach was utilized for the BOPP films while the average film thickness approach was utilized for the non-oriented PP-cast films. Single 2-p Weibull distributions were found to fit well to most of the qualified breakdown data sets, with this being also evident from Figure 4.5 as most of the breakdown data sets fall on straight lines on the Weibull scale. However, some of breakdown distributions in Figure 4.5 clearly show curvature (see e.g. PP1-C-200-3.5 in Figure 4.5a) which suggests towards several breakdown mechanisms being active in those films. In such a case it was assumed that the breakdown mechanisms were Weibull distributed and additively mixed 2-p Weibull distributions (Equation (3.5) with $S = 2$) were utilized in order to obtain a satisfactory fit to breakdown data. In order to enable convenient comparison between all the distributions regardless of the distribution structure, 5, 63.2 and 95 % breakdown percentiles were calculated and are given in Table C.1. The lowest breakdown field measured and the mean sample film thicknesses along with the standard deviations are also presented in Table C.1 for each material. The onset electric fields of the propagating-type breakdown process observed in the PP cast films are given in Table C.2.

While not presented here, the breakdown fields of the BOPP films were also calculated based on the average sample film thickness approach. Compared with the event-by-event manual thickness approach, the calculated mean relative errors in the 5, 63.2 and 95 % breakdown percentiles due to the average sample thickness approach were found to be only ±3.1 %, ±0.83 % and ±2.0 %, respectively.

4.1.5 Link between film morphology and breakdown performance

Non-oriented cast films

Overall, the non-oriented thin cast films showed very similar breakdown responses with the mean onset breakdown fields of the observed propagating-type breakdown in the range of ∼360–400V/µm (Table C.2). The observed breakdown behavior may be attributed to the spherulitic morphology of iPP cast films as is widely known in the literature [12, 100, 101]. Upon crystallization of iPP, relatively large spherulites form, which are separated by defective inter-spherulitic regions, where the concentration of defective species, impurities and free volume is increased. As the inter-spherulitic regions exhibit higher charge mobility due to impurities and longer mean free paths in free volume, electron avalanching and eventually dielectric breakdown are facilitated along the spherulite boundaries which in thin samples can join the electrodes (the breakdown process of the amorphous inter-spherulitic regions has been argued to be due to a thermal process [159]). Consequently, dielectric breakdown strength has been shown to be strongly dependent on the crystallization rate, mean spherulite diameter and film thickness. Kolesov [160] performed isolated impulse breakdown measurements on both the spherulites and inter-spherulitic space of 60–70 µm thick PP and HDPE films as a function of spherulite size. While spherulites themselves showed much higher breakdown strength independent of their size, he found the breakdown strength of the inter-spherulitic space to decrease with increasing spherulite size until saturating to a certain level when the spherulite diameter was approximately equal to the specimen thickness or higher. Interestingly, by greatly decreasing the spherulite size in proportion to film thickness, improved breakdown strength can be achieved due to shorter mean free paths along the spherulite boundaries, as reported e.g. by Kim *et al.* in the case of non-oriented syndiotactic PP-films which inherently exhibit very small and irregular-shaped spherulites [161]. In fact, in a more

recent study by Diaham *et al.* on the thickness-dependence of DC breakdown strength of parylene HT films [162], an optimum film thickness was found to reside slightly below a certain film thickness critical for spherulite development, at which a thickness-confined growth of high-crystalline lamellar stacks and absence of spherulites was observed.

Reflecting the above to the cast-iPP breakdown results here, the fact that the films showed only weak thickness-dependence (see Tables C.1 and C.2) suggests that the 15 and 20 µm cast films exhibited only minor morphological differences. This is supported by the fact that the crystallization conditions (Table 4.1) and the overall crystalline structures (Figure 4.3) were similar for all the thin cast films. It is remarked however that thorough imaging of the initial cast film micro-structure would be required in order to characterize and ascertain the nature of crystallization and possible spherulite growth (i.e. if the spherulite growth was thickness-confined as in [162]). Nevertheless, the above aspects and the observed propagating-type multi-breakdown behavior underline the fact that non-oriented iPP cast films are of little use in film capacitor applications as is.

BOPP films

Upon bi-axial orientation of iPP-cast films, the initially spherulitic morphology is transformed into a highly ordered fibrillar network structure of densely packed lamellar crystallites aligned parallel to the film surface [163, 164], and consequentially, a substantial increase in dielectric breakdown strength is achieved [17, 165]. While this was also the case for the BOPP films studied here, significant differences in the large-area dielectric breakdown responses were observed among the studied BOPP films which can be linked to the differences between the iPP-grades and cast film extrusion and bi-axial orientation processes (see Figure 4.5 and Tables 4.1 and C.1).

Considering the studied cast extrusion processes (Extruders A, B and C), an evident link between the cast extrusion parameters, in particular the cylinder, die and chill-roll temperatures, and the final BOPP film breakdown response was observed for both the studied iPP grades. The initial cast film morphology is largely dictated by the cooling gradient induced upon transferring the cast film from the extruder die to the chill-roll, with a higher cooling gradient leading to a faster crystallization rate and thus to a decrease in spherulite size, β-form crystal content and crystallite size [156, 166, 167]. Upon bi-axial drawing of iPP cast film in partly molten state, a strain-induced crystal transformation of the β-form into the more stable α-form occurs [156, 168], with this also being evident from Figure 4.3d which shows that the BOPP films contained only monoclinic α-phase despite the initial β-phase in the corresponding cast films. In fact, $\beta \rightarrow \alpha$ transformation begins to occur already during the pre-heating stage at temperatures of 125–140 °C or above when the cast film is heated to the desired drawing temperature prior to bi-axial stretching [156, 166]. Interestingly, the $\beta \rightarrow \alpha$ crystal transformation has been previously linked to the formation of microvoids in the oriented film due to the volume contraction effect as the density of β-form crystals is lower than that of α-form crystals [169, 170]. Microvoids (porosity) contribute to structural inhomogeneities and free volume in the film and can thus directly influence and the dielectric strength of the BOPP film [12, 103, 171, 172]. Hence, the initial iPP cast film morphology, in particular the initial degree of β-form, is seemingly linked to the morphology and breakdown response of BOPP films. This is evident from Figure 4.6 in which the BOPP film $E_{63.2\%}$ breakdown percentiles plotted as a function of the corresponding cast film β-phase contents clearly show a decreasing trend with increasing β-content. Comparing the studied iPP-grades (PP1 and PP2), it is also clear that the high-isotacticity PP2 grade exhibits slightly higher initial cast film β-content, which is coherent with e.g. the study of Tamura *et al.* [168], and is

accordingly reflected as differences between the studied iPP-grades in terms of breakdown response (see Figure 4.6 and Table C.1). The differences between the iPP-grades and the corresponding large-area breakdown responses diminished when the initial cast film β-phase contents were low (Extruder C). PP-grade, initial cast film morphology and cast film thickness were also found to affect the bi-axial stretching behavior, as seen in Figure 4.7 in which the average MD/TD-directional (peak) stretch forces measured during the bi-axial orientation step are presented. For example, comparing the cast films manufactured by Extruders B and C (both with equal target cast thickness of 400 µm), it is seen from Figure 4.7 that higher β-content also results in lower MD/TD stretching forces (or "softer" film) during bi-axial orientation.

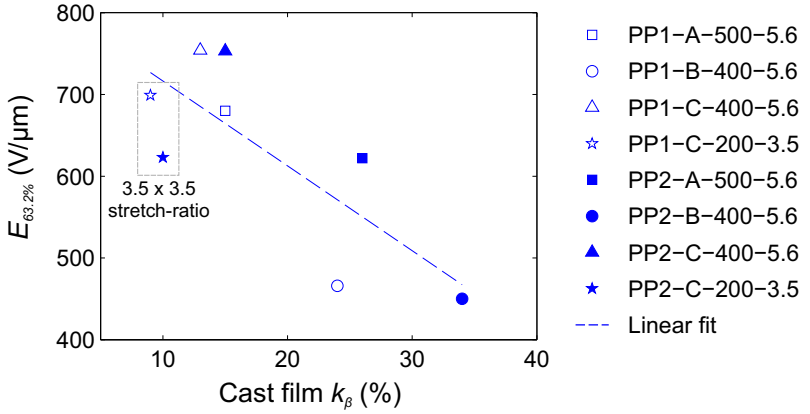

Figure 4.6. Dependence of BOPP film $E_{63.2\%}$ breakdown percentile on the initial cast film β-content. β-form crystalline indices (k_β) were determined from the WAXS-data in accordance with Equation (4.1).

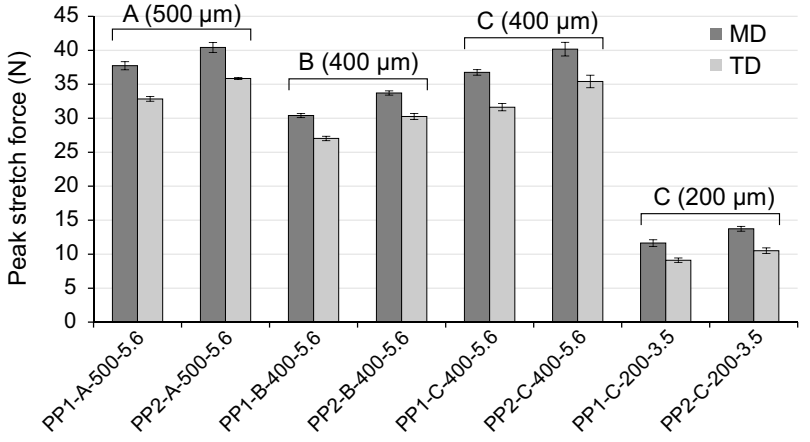

Figure 4.7. Average MD- and TD-directional (peak) stretch forces during the bi-axial orientation of the iPP cast films manufactured by Extruders A, B and C (cast film thickness is indicated in parenthesis). Error bars denote standard deviation (six sample films per material).

The breakdown responses of the 200 µm PP1- and PP2-based films (Extruder C) bi-axially oriented with the 3.5 x 3.5 stretch-ratio are particularly interesting. The initial

β-phase contents of the 200 µm cast films were lower than those of the thicker 400 µm cast films, which is presumably due to the more effective cooling of the film volume on the chill roll when the film thickness is decreased, similarly as previously reported by Tamura *et al.* [168, 173]. Yet, the 3.5 x 3.5 BOPP films exhibited lower breakdown performance in comparison to the 400 µm films oriented with the 5.6 x 5.6 stretch-ratio. This indicates that higher orientation ratio is linked to improved dielectric strength, in coherence with previous studies on e.g. PP-films [17, 165] and LDPE-PP copolymer films [174]. In general, increasing bi-axial stretch-ratio has been previously demonstrated to increase BOPP film crystallinity, crystalline melting temperature T_m and (040) in-plane orientation degree [156] and it may increase the amount of trapping sites on the amorphous-crystalline boundaries [100, 175]. Further, at a constant stretching temperature and with increasing bi-axial stretch-ratio, the apparent crystallite sizes have been reported to decrease [166], which has been linked to improved impulse breakdown strength [175]. Interestingly, the 3.5 x 3.5 BOPP films also showed differences in weak point behavior, with the PP1-based film showing a distinct defect population in the low probability region (see Figure 4.5a). While the actual origin of the defect population is unknown, weak point formation may be related to bi-axial deformation behavior at the relatively low 3.5 x 3.5 stretch ratio, which is barely above the critical area stretching ratio of 10 above which a finely oriented fibrous structure is obtained [156]. Weak points may also form due to thermal instability, mechanical vibration or internal stress occurring during the manufacturing process [41].

4.2 Breakdown characteristics of commercial capacitor-grade BOPP films

Various commercial capacitor-grade metallized and non-metallized BOPP films were studied throughout the thesis work (some of the results have been published in [P1, P2, P3, P5, P8]). The BOPP films were either obtained directly from their respective manufacturers (Tervakoski Films Group, DuPont Teijin Films, Bolloré Inc. and Shin-Etsu Film Co., Ltd.) or kindly provided by Alstom Grid Oy, Finland. Table 4.2 lists a set of metallized and non-metallized BOPP films in the 4–16 µm thickness range which are considered in the following. The non-metallized films were intended for oil-impregnated film-foil capacitors and exhibited varying degrees of surface roughness (for instance, the space factors of A-5, A-6 and A-7 films were in the range of 6–12 %) whereas the metallized films had smooth surfaces. Large-area multi-breakdown measurements were performed in accordance with Table 4.2 and Chapter 3. Regarding the metallized films, it is remarked that the active areas were not constant due to differences in film roll widths.

Figures 4.8a and 4.8b present the multi-breakdown distributions of non-metallized and metallized capacitor-grade BOPP films on Weibull probability scale (top) along with the weakest measured point $E_{\min}$ and the $E_{5\%}$, $E_{63.2\%}$ and $E_{95\%}$ breakdown percentiles as a function of film thickness (bottom), respectively. The breakdown results are also listed in Table C.3. Additively mixed 2-p Weibull distributions (Equation (3.5)) were utilized in order to achieve good fits to the breakdown data sets. Firstly, in contrast to the laboratory-scale BOPP films analyzed in the previous sub-chapter (see e.g. Figure 4.5), it is clearly seen that the commercial BOPP film breakdown distributions in Figure 4.8 show more profound curvature in the low probability region. In the high-probability region the distributions reside in the 500–700 V/µm range which is typical for BOPP [15, 16]. Overall, the fingerprint-like BOPP breakdown distributions in Figure 4.8 are similar to those previously observed in over 50 different capacitor-grade PP-films by Laihonen *et. al* using an automatic breakdown measurement system [15, 20, 39].

Table 4.2. Specifications of the commercial capacitor-grade BOPP films (manufacturers A, B, C and D). The films were manufactured by either bubble or tenter processes. Breakdown measurements were made either in insulating oil or in atmospheric air (dry). d_n is the nominal thickness given by the film manufacturer. N is the number of sample films, A is the active area and A_{total} is the resulting total measured film area.

Code	Metallization	d_n (µm)	Oil/dry	N	A (cm^2)	A_{total} (cm^2)	Publication
A-1	Zn-Al, 5–12 ohm/sq.	4.8	Dry	10	58	580	-
A-2	Zn-Al, 5–12 ohm/sq.	6.0	Dry	25	42	1050	[P1]
A-3	Zn-Al, 5–12 ohm/sq.	9.0	Oil	10	38	380	-
A-4	Zn-Al, 5–12 ohm/sq.	12.0	Dry	25	24	600	[P2]
A-5	-	13.8	Oil	6	81	486	[P2]
A-6	-	14.4	Oil	12	81	972	[P5]
A-7	-	9.0	Oil	10	81	810	-
B-1	-	9.0	Dry	10	81	810	-
B-2	-	10.1	Oil	10	81	810	-
B-3	-	16.2	Oil	10	81	810	-
C-1	-	7.4	Dry	10	81	810	-
C-2	-	8.3	Dry	10	81	810	-
D-1	Al, 5 ohm/sq.	4.0	Dry	10	16	160	[P3]

It is widely acknowledged in the literature that dielectric strength of polymer films is more strongly dependent on the film thickness than on the area [176]. The thickness dependence is commonly expressed by an inverse power law relationship $E_{bd}(d) = kd^{-n}$, where E_{bd} is the breakdown field, d the thickness and k and n are material-specific constants [27, 176–178]. While the inverse power law proposes a decrease in breakdown strength with increasing film thickness, this is not easily seen in Figure 4.8. Comparison of the films presented in Figure 4.8 is not straightforward though, as they most likely differ in e.g. film morphology. Interestingly however, it is noticeable that the low-probability trends in Figure 4.8 seemingly exhibit some degree of thickness dependence, with decreasing film thickness gradually resulting in more weak points and stronger "S-curvature". This trend is most notable with the non-metallized films (Figure 4.8a, bottom) while the smooth-surfaced metallized films exhibit only minor differences despite the 4–12 µm thickness range (Figure 4.8b, bottom). Nash [17] has previously observed similar thickness-dependent large-area dielectric strength (or weak point behavior) in rough-surfaced BOPP films; it was argued that with thinner films the surface roughness becomes more significant in relation to the film thickness and may lead to local stress-enhancement, electromechanical thinning and breakdown in the thinnest film regions. It is however noted that a sufficient degree of BOPP film surface roughness is mandatory in film-foil capacitor applications in order to facilitate more efficient oil-impregnation for preventing partial discharges at the electrode edges and electrode/film interfaces [4, 42]. In industrial BOPP film manufacturing the film roughness is mainly controlled by the degree of β-crystallinity in the surface layers of the initial cast film which is subsequently transformed to crater-like surface roughness (haziness) through the $\beta \rightarrow \alpha$ transformation during the bi-axial orientation phase [168, 173, 179]. This is mainly achieved by adjusting the cast film thickness and the chill roll temperature accordingly in order to support β-crystallization and by keeping the bi-axial orientation temperature between the melting

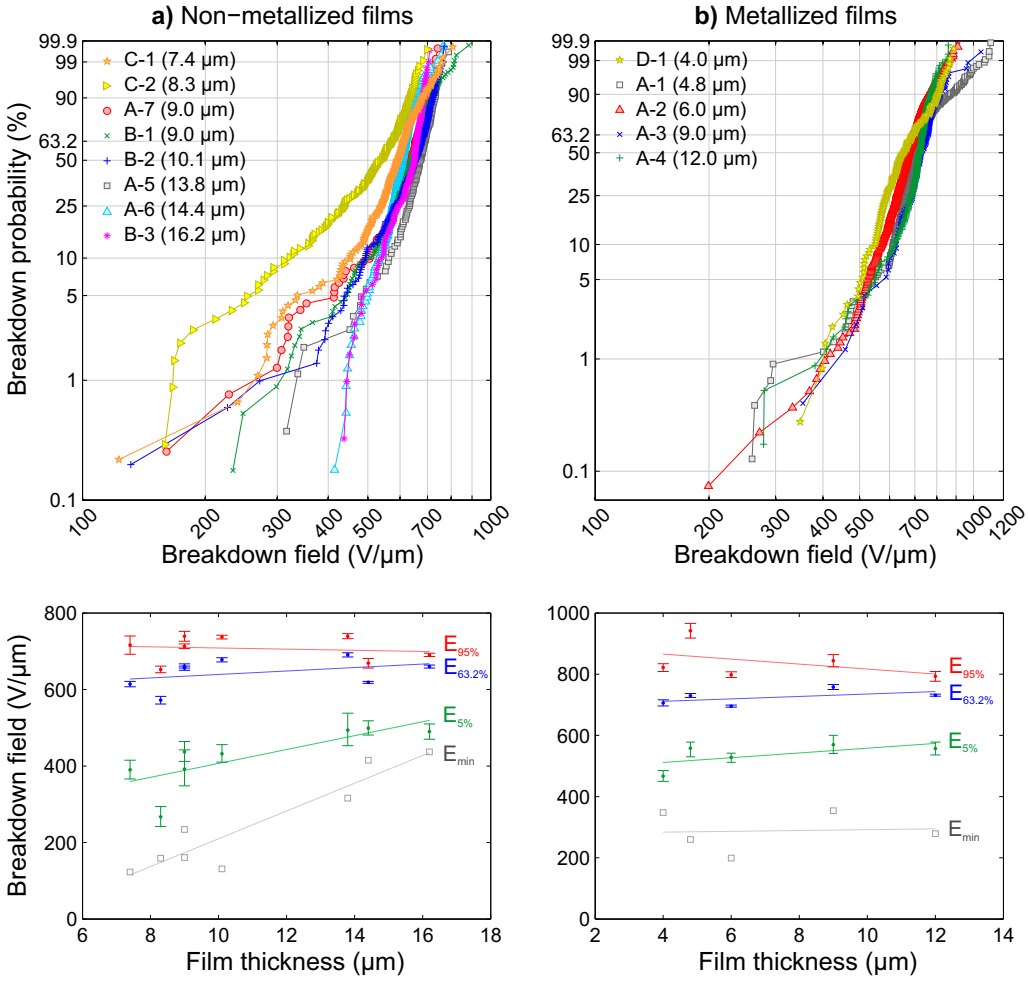

Figure 4.8. Large-area multi-breakdown responses of various **a)** non-metallized and **b)** metallized commercial capacitor-grade BOPP films in the 4–16 µm thickness range. Top figures show the measured breakdown distributions on the Weibull probability scale (Weibull fits are omitted for clarity). The bottom figures show the weakest measured point $E_{\min}$ and the $E_{5\%}$, $E_{63.2\%}$ and $E_{95\%}$ breakdown percentiles as a function of film thickness (error bars denote 90 % confidence; solid lines are linear fits to the data). See Table 4.2 for sample codes, film thicknesses and breakdown measurement details.

points of β- and α-form crystals (145–165 °C) [179]. Thereby, an interesting connection to the results discussed in the previous sub-chapter (4.1.5) arises, in which the initial cast film β-crystallinity was found to be linked to BOPP film breakdown performance. A further study, preferably in co-operation with the film manufacturers, is however needed to ascertain the exact role of film processing and β-crystallinity in the breakdown process of commercial BOPP films.

While the exact nature of the PP material, additives and film processing parameters used by the BOPP film manufacturers are unknown, the overall differences observed between the commercial capacitor-grade BOPP films (Figure 4.8) and the laboratory-scale BOPP films (Figure 4.5) are assumed to be related to differences in film processing steps,

thermal history, bi-axial stretching conditions and film morphology. For instance, in industrial-scale tenter process the film is rarely oriented simultaneously with equibiaxial stretch ratio, but rather the MD/TD stretching is done in a sequential manner with a stretch-ratio of 4.5 : 8.0 or similar [151], thus resulting in differences in the oriented film morphology [163, 164] and possibly in breakdown behavior. It is also likely that the deformation homogeneity during bi-axial orientation is not constant over the whole film area but rather the local true stretching stresses relate to fluctuations in e.g. cast film thickness and temperature [156], which in turn can affect local BOPP film orientation, crystallinity, thickness, and possibly, be linked to weak point formation. Other affecting factors may include e.g. impurities and residual antioxidants mainly contained in the amorphous phase in PP which have previously been reported to influence dielectric breakdown properties and losses in BOPP films [17, 42, 105, 180, 181].

4.3 Effect of inter-layer pressure on the breakdown characteristics of metallized capacitor films

In cylindrically wound metallized film capacitors, the adjacent film layers experience inter-layer (or interfacial) pressure originating mainly from the winding tension and shrinkage of the film during the heat treatment [119, 125]. The inter-layer pressure inside a wound capacitor element is relatively low at the outer layers of the capacitor winding but due to the radial compressive force from the surrounding layers it increases cumulatively towards the inner winding layers where it may reach tens of MPa [123, 125, 182]. As already discussed in sub-chapter 3.2.2, inter-layer pressure has a profound effect on the self-healing breakdown process; as the pressure confines the breakdown plasma, more efficient self-healing, reduced discharge energy, and consequently, reduced size of the de-metallized area results, see Equation (2.3). Consequently, a relatively high level of inter-layer pressure is often promoted for wound film capacitors in order to reduce the capacitance loss during self-healing and hence to extend the capacitor operation life [4, 42, 123, 183]. While this approach is focused on ”fine-tuning” the self-healing process, the effect of inter-layer pressure on polymer film breakdown properties is however less frequently considered. In general, breakdown strength of polymers has been shown to exhibit positive pressure dependence under hydrostatic or uniaxial compressive stresses up to a certain threshold, beyond which the breakdown strength collapses [12, 184–186]. It is suggested that cavities or low-density regions (free volume) with increased probability for impact ionization or electron avalanche may be formed in the polymer bulk under high electric field stress and that external pressure should hinder the formation of such regions, thus leading to increased dielectric strength [187]. However, only a very limited amount of studies on the effect of inter-layer pressure on the dielectric breakdown strength of thin metallized polymer films has been published. In [125, 188], the effect of inter-layer pressure on the dielectric breakdown strength of 9 µm metallized BOPP film was studied in the pressure range of 0–5.0 MPa by using brass electrodes. Intermediate pressure levels were found to decrease the dielectric strength first but at 4.7 MPa the dielectric strength recovered to a level almost equal to that when no pressure was applied. It is noted however that the statistical relevance of the results presented in [125, 188] is poor as only a very limited amount of breakdown data were presented.

The effect of inter-layer pressure on the DC breakdown characteristics of 4–6 µm capacitor-grade metallized BOPP, PET and PPS films was studied in [P3] by utilizing the multi-breakdown measurement approach and pressure application methodology detailed in sub-chapter 3.1.8. Figure 4.9 presents the qualified multi-breakdown distributions on

Weibull probability scale and with inter-layer pressure varying in the range of 0–8 MPa. Overall, the results indicate that the breakdown responses of all the studied materials exhibited negative dependence on the applied mechanical pressure in the whole studied pressure range. However, marked differences in breakdown performance were observed between the materials. Both the 4 µm and the 6 µm BOPP films were found to be superior in comparison to the 4 µm PET and PPS films in the whole studied pressure range. Inter-layer pressure was found to have a devastating effect particularly on the breakdown characteristics of PPS, and in the inter-layer pressure range of 0.5–1.0 MPa, all the PPS samples eventually suffered a permanent insulation resistance failure when the voltage was increase above a certain threshold (rapid consecutive self-healing). Similar behavior occurred with PEN samples above 2 MPa. At 2 MPa some of the PPS samples suffered a permanent failure as soon as the first breakdown occurred, see Figure 4.9d. It was also notable that with increasing inter-layer pressure, distinctive weak point populations evolved (PEN-4 and PPS-4) or became more prominent (BOPP-6) in the low breakdown probability region, see Figure 4.9 and [P3]. It is noted that polymer chemistry has been previously linked to the self-healing efficiency, with the amount of C, O and H atoms (or more precisely the ratio $q = (\mathrm{C} - \mathrm{O})/\mathrm{H}$)) in the polymer structure determining the amount of graphite formed in polymer decomposition [42, 44, 122]. As graphite deposition at the clearing site may lead to conductive paths and reduce the self-healing efficiency, some polymers (such as BOPP) clear better than others (such as PPS and PEN).

The fact that all the studied materials exhibited decreased breakdown performance with increasing axial compression is seemingly in contradiction with some of the previously published studies. One probable reason for the observed behavior could be the pressure application methodology; even though utmost care was taken to avoid damaging the film during test capacitor assembly and pressure application, thin films are particularly prone for damage under mechanical stress. It is however remarked that the multi-breakdown measurement approach counteracts this effect as the measurement is continued beyond the weakest point of the active sample area. Moreover, most of the previous studies in which increasing DBS with pressure was observed were made with thicker polymer films in the 9–300 µm range, with different electrode geometries and rarely with bi-axially oriented films. Nevertheless, although further study is seen necessary, the results here point towards the fact that breakdown characteristics of metallized polymer films should be determined carefully also under authentic operation stresses in order to ensure proper design and operation in practical applications.

4.4 Considerations and implications

In summary, the results presented in this chapter and the associated publications emphasize the determining effect of film processing in large-area dielectric breakdown characteristics of capacitor films. The results presented in sub-chapter 4.1 showed particularly well that even when starting with the exact same iPP raw material the breakdown response of the end-product is effectively dictated by how the film is prepared. While the morphological transformation from non-oriented iPP cast film morphology to bi-axially oriented film morphology was shown to be the prime factor in achieving high dielectric breakdown performance, the results presented in this chapter emphasize the complexity of interrelations involved in the bi-axial orientation process. The connection between initial iPP cast film β-crystallinity and the resulting BOPP film breakdown performance established in sub-chapter 4.1.5 is particularly intriguing, and its relation to industrial-scale BOPP film breakdown performance and weak point behavior should be studied further in the future.

It is however remarked here that BOPP samples prepared in laboratory conditions most likely differ from industrially manufactured BOPP films to some extent in terms of e.g. thermal history, morphology and breakdown performance; therefore, co-operation with industrial film manufacturers is seen necessary. Lastly it should be emphasized that the large-area multi-breakdown measurement approach itself was found to be a beneficial tool in studying the link between film morphology, practical operation stresses and breakdown.

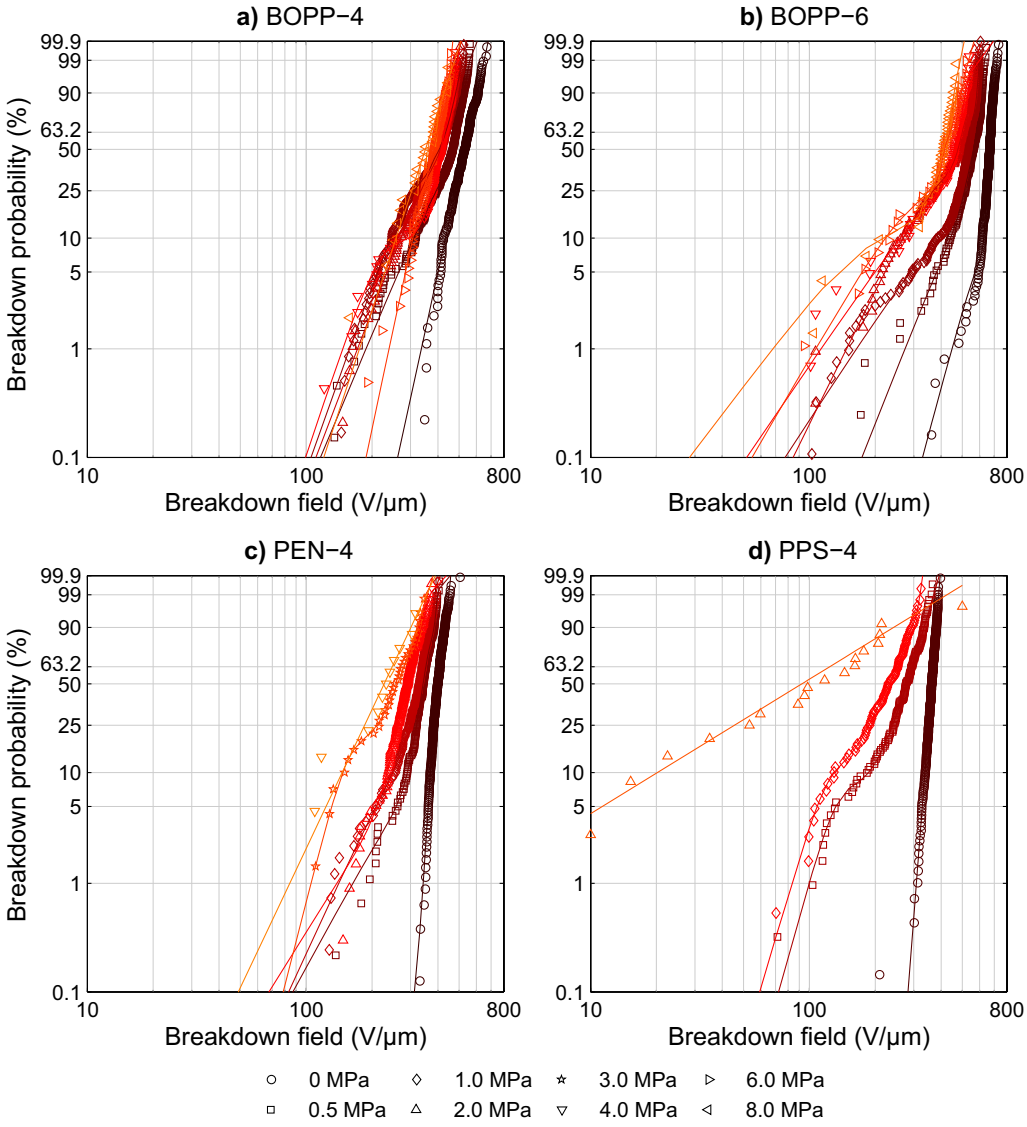

Figure 4.9. Characteristic breakdown probability distributions of the metallized BOPP, PET and PPS films as a function of inter-layer pressure [P3]. Solid lines represent Weibull fits in accordance with Equation (3.5).

Chapter 5

Large-area multi-breakdown response of BOPP-nanocomposite films

This chapter summarizes the main results from publications [P4, P6, P7, P8] in which the breakdown characteristics of BOPP-based polymer nanocomposites were studied. Particular emphasis is put on the effects of various compositional, structural and film processing factors on the breakdown behavior of laboratory- and pilot-scale melt-compounded BOPP nanocomposite films with silica and/or calcium carbonate nanofillers. The chapter also provides perspective on the importance of careful breakdown assessment when dielectric films of more complex internal structure are studied.

5.1 Material details and characterization

5.1.1 Composition and film processing

A number of film production trials were carried out during the NANOPOWER project in order to study the effects of various compositional, structural and film processing factors on the breakdown behavior of laboratory- and pilot-scale melt-compounded BOPP nanocomposite films. The studied processing trials reported in this thesis are:

- Effect of hydrophobic SiO_2 nanofillers [P4, P6, P7, P8]
- Effect of precipitated $CaCO_3$ nanofillers [P4]
- Effect of pre-mixing technique [P6, P7]
- Effect of compounder output and screw speed [P7]
- Effect of bi-axial orientation temperature [P6]
- Pilot-scale film production [P6, P7, P8]

Figure 5.1 presents an overview of the film processing steps together with the processing parameters which were varied along the production chain. The film processing was conducted at the VTT Technical Research Centre of Finland and at a Brückner pilot film line in Denmark. A detailed listing of all the materials, processing parameters and film specifications can be found from the related publications listed above. The purpose of the following is to summarize the main processing features.

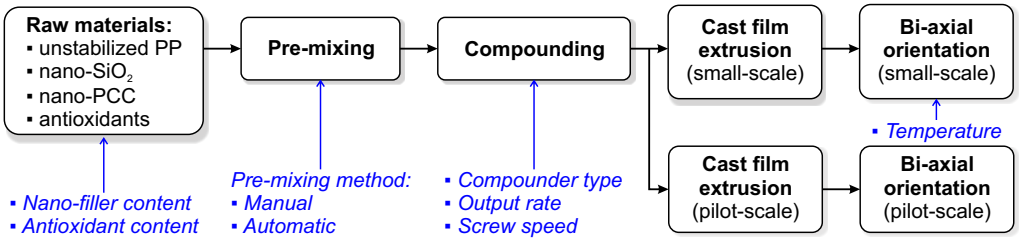

Figure 5.1. General BOPP PNC film processing steps and studied variables (italic).

Unstabilized isotactic polypropylene (iPP) homopolymer HC318BF in powder form (a non-commercial product from Borealis N.V.) was used as the matrix polymer. Nanofiller content of 4.5 wt–% of hexamethyldisilazane (HMDS)-treated hydrophobic fumed nano-silica (Aerosil R 812 S by Evonik) was used in most of the compounds. Lower fill-fractions of 1.0 and 2.0 wt–% of hydrophobic silica and/or stearine-coated precipitated calcium carbonate (PCC) nanofillers (Socal 322 by Solvay) were also studied in one of the trials. Antioxidant package comprising of main process stabilizer Irganox 1010 (0.47 wt–%) and co-stabilizer Irgafos 168 (0.35 wt–%) was added to the compounds in order to prevent thermo-oxidative degradation of PP during melt-processing. The main stabilizer Irganox 1010 (pentaerythritol tetrakis(3-(3,5-di-tert-butyl-4-hydroxyphenyl)propionate)) is a sterically hindered phenolic antioxidant intended to stabilize free radicals while the co-stabilizer Irgafos 168 (tris(2,4-ditert-butylphenyl)phosphite) is a phosphite antioxidant intended to work in synergy with Irganox 1010 for peroxide decomposition [189]. The co-stabilizer content was varied in one of the trials (0–0.35 wt–%).

For the laboratory-scale films, the general film processing steps were as follows. Initially, the raw materials (in powder form) were pre-mixed either manually in polyethylene bag or by using various automatic mixers and thereafter compounded mainly by a Berstorff ZE 25/48D twin screw compounder with high-shear screw geometry, two separate kneading sections and a melt filter (screen size 42 µm). The screw speed and output of the Berstorff ZE 25/48D compounder were 300 rpm and 9 kg/h, respectively, except for one trial in which the output was varied (3–15 kg/h at 300 rpm). Additionally, a high-speed twin screw Berstorff ZE 25 x 49D UTX compounder with 300–1200 rpm screw speed was also used in one of the trials (output 8 kg/h). Polymers and fillers were dried at 70 °C for 1.5 h in oven and vacuum-dried for 0.5 h prior to compounding. The compounded strands were cooled, pelletized and dried and thereafter extruded into ∼500 µm cast films by Brabender Plasticorder single-screw extruder with a three-layer screen pack. The pelletized compounds were dried before cast film extrusion. Finally, the cast films were bi-axially oriented with a Brückner KARO IV film stretching machine (set temperature mainly 157 °C, equibiaxial stretching ratio of 5.4 x 5.4), resulting in BOPP films ∼ 15–23 µm in thickness. Detailed compounder and cast extrusion temperatures, film thicknesses etc. can be found from the associated publications.

Some of the compounds were chosen for pilot-scale film manufacturing trial. The compounds (100–140 kg) were prepared similarly as described above. Automatic pre-mixing and the Berstorff ZE 25/48D compounder were used for the compounds. Pilot-scale films were produced at a Brückner pilot film line in Denmark consisting of a single screw extruder with a flat die, a casting station, machine- and transverse direction orientation (MDO and TDO) units and a winder. The polymer compound was first melted in the extruder, quenched on the casting roll and then transferred to the MDO where it was reheated and stretched in the machine direction. Thereafter, the film was reheated in the TDO unit before transverse stretching and cooled down before winding.

5.1.2 Quantitative assessment of nanocomposite structure

The importance of nano-scale imaging and dispersion assessment by quantitative techniques are largely emphasized in dielectric PNC development [9]. Both scanning electron microscopy (SEM) and transmission electron microscopy (TEM) were utilized for the structural characterization of the studied compounds. Cross-sectional surface morphologies of cryo-broken BOPP-PNC film samples were imaged by JEOL JSM-6360LV scanning electron microscope [P6, P7]. TEM imaging was performed for ultrathin cast film sections by JEOL JEM-1400EX electron microscope [P4, P6]. The SEM/TEM images were converted to binary particle-matrix images and the particle area distributions were determined by using ImageJ software [P7]. In [P6, P7] quantitative dispersion assessment was performed for the binary images by determining the free-space length L_f, a parameter describing the characteristic length of the unreinforced polymer domains [190, 191]. L_f is defined as the width of the largest randomly placed square for which the most probable number of intersecting particles is zero. The MATLAB code for calculating L_f was retrieved and used according to the literature [190].

Figure 5.2 presents exemplifying TEM-micrographs of ultrathin sections of PP-cast films with varying SiO_2 or PCC filler contents and pre-mixing methods. Figure 5.3 presents exemplifying SEM cross-sectional images of cryo-broken 4.5 wt-% SiO_2-BOPP films. The dispersion state of the nanoparticles in all the composites was found to be

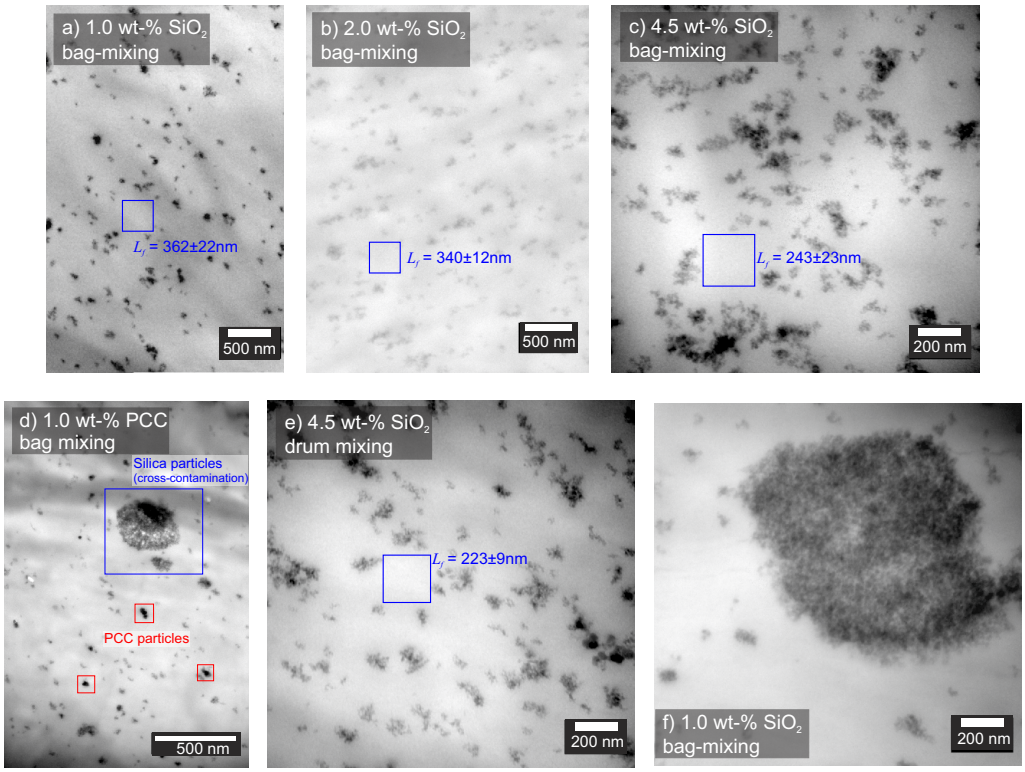

Figure 5.2. TEM-micrographs of ultrathin sections of PP PNC cast films: **a**–**d)** 1.0–4.5 wt-% of SiO_2 or PCC nanofillers (manual pre-mixing) and **e)** 4.5 wt-% of SiO_2 pre-mixed automatically by drum mixer. The calculated free-space lengths (L_f) characterizing the size of the unreinforced polymer domains are presented in the figures. **f)** SiO_2-agglomerate observed in 1.0 wt-% SiO_2-PP PNC cast film.[P6]

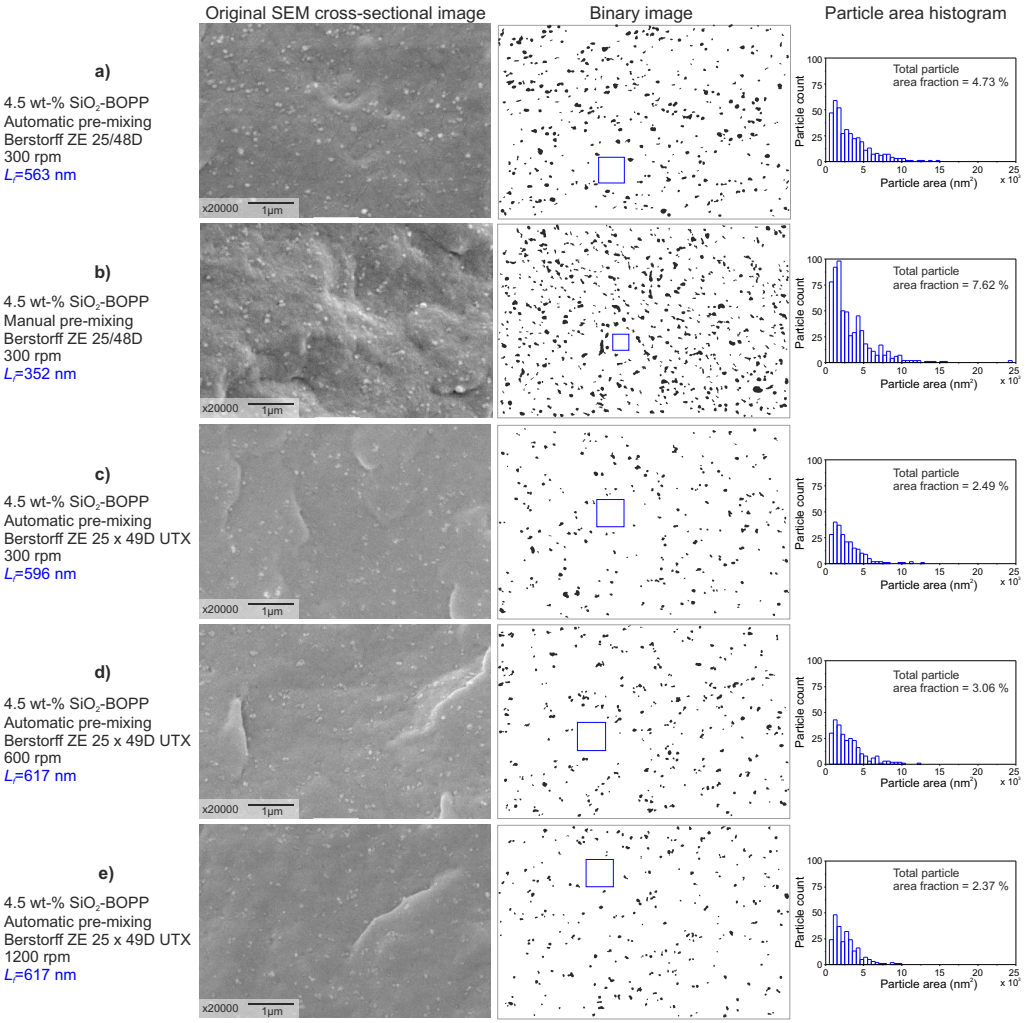

Figure 5.3. SEM cross-section images (left), nanodispersion analysis (middle) and particle area histograms (right) of various 4.5 wt-% SiO_2-BOPP films [P7]. The pre-mixing method, compounder details and analysis results are given in the figure. The blue boxes (middle) denote the free-space length L_f used for the dispersion quality quantification. L_f determination was performed iteratively in MATLAB (manual mode) by gradually increasing the amount of random tests up to 100000 in order to obtain high statistical accuracy. From the particle area histograms (right), the most probable particle diameter was approximated to be ∼41 nm (assuming circular shape).

similar and of heterogeneous nature. At the nanoscale, the filler material was partially well-dispersed in nanosized clusters but >100 nm agglomerates were also observed (see e.g. Figure 5.2c). TEM-imaging also revealed that PP-PCC-1 and PP-PCC-2 compounds contained silica (see Figure 5.2d), presumably due to a cross-contamination from the previously compounded silica-composites. Upon closer investigation of the 1.0 wt-% silica-composite, micron-sized agglomerates were observed (Figure 5.2f), and even though they were relatively scarce, they contained substantially high amounts of filler material. Considering the calculated free-space lengths L_f as a function of filler content, the

differences in unreinforced polymer domain lengths are relatively small when considering the increase in the silica content; if the filler material was well-dispersed, the free-space length should decrease markedly with increasing filler content [190]. This suggests that the dispersion state can be qualified as agglomerated and considering the densities of the nanoscale particle dispersions presented in Figure 5.2a–e, it is likely that all the compounds contain micro-agglomerates.

5.2 Interdependence of BOPP PNC composition, processing and breakdown performance

The following sub-chapters present various compositional, structural and film processing features which were found to significantly affect the SiO_2-BOPP PNC film breakdown response. Other processing features with less prominent effects (such as the compounder output rate) were also studied during the NANOPOWER project but are not presented here.

5.2.1 Effect of SiO_2 and PCC filler content

Comparing to the unfilled reference BOPP, Figure 5.4a shows that increasing silica content reduces the DC breakdown performance in the >5 % breakdown probability region, but also leads to a concurrent improvement in the breakdown distribution homogeneity [P6]. The compounds with 1.0 wt-% and 2.0 wt-% of PCC (Figure 5.4b) were found to show a similar trend [P8]. The decrease in the breakdown performance with increasing filler content is consistent with the previous reports on various amorphous polymer-silica nanocomposites [92], polystyrene-silica nanocomposites [93] and BOPP-PCC nanocomposites [90]; see also Figure 2.3a. Interestingly, the Weibull lines of the 1.0 wt-% SiO_2-BOPP PNC and the unfilled BOPP intersect in the 5–10 % breakdown probability range with the 1.0 wt-%

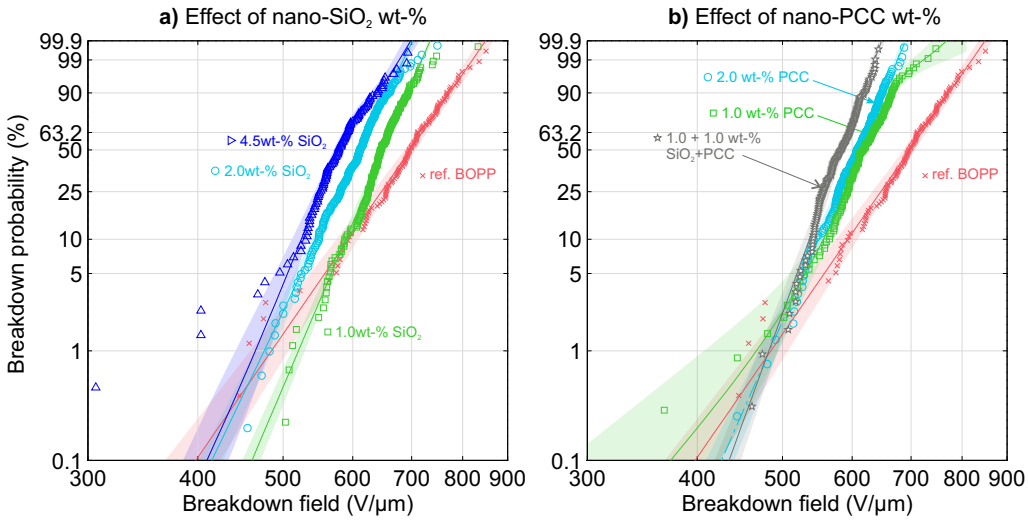

Figure 5.4. Effect of **a)** SiO_2 and **b)** PCC nano-fillers on the large-area multi-breakdown performance of BOPP [P4, P6]. Solid lines and shaded areas represent Weibull fits and 90 % confidence bounds, respectively. Manual pre-mixing method was utilized for all the compounds. [P4, P6]

SiO_2-BOPP PNC showing higher strength in the low probability region. This is promising, as considering film capacitors, for which the operative electric field is mandated by the electrical weak points in the polymer film, both the increase of breakdown distribution homogeneity (Weibull β) and the improvement in the low-probability breakdown behavior are substantially more relevant than the breakdown behavior in the higher (>10 %) breakdown probability region. In coherence with [92], this behavior may be attributed to nano-silica introducing a lower energy failure mode into the polypropylene matrix, but due to the relatively uniform nanodispersion, the breakdown variability is concurrently reduced in comparison to the neat polymer.

5.2.2 Effect of pre-mixing method

Effect of pre-mixing method on the large-area multi-breakdown performance was studied in [P6]. Although TEM/SEM-imaging analysis indicates that pre-mixing technique somewhat affects the silica nanodispersion (see Figure 5.2 and Figure 5.3), the multi-breakdown measurements suggested that the pre-mixing technique had little or no effect on the breakdown behavior [P6]. This, conversely, also confirms that automatic pre-mixing of larger batches is applicable for up-scaling purposes. Drum mixer was seen as the most potential pre-mixing method when manufacturing larger batches of SiO_2-PP compound.

5.2.3 Effect of compounder screw speed

Figure 5.5 presents breakdown results from another trial in which a high-speed twin screw Berstorff ZE 25 x 49D UTX compounder with a varying screw speed (300, 600 and 1200 rpm) was used for compounding 4.5 wt-% SiO_2-PP [P7]. SEM cross-sectional images and the corresponding particle analysis results are presented above in Figure 5.3c–e. Surprisingly, the 4.5 wt-% SiO_2-BOPP compounded with the slowest (300 rpm) screw speed was found to exhibit a considerable shift towards higher dielectric strength while the 600 and 1200 rpm variants resided in the same range as the 4.5 wt-% SiO_2-BOPP presented earlier in Figure 5.4a. For further comparison, Figure 5.5 also presents the 1.0 wt-% SiO_2-BOPP from Figure 5.4a, which exhibits a breakdown distribution strikingly similar to that of the 4.5 wt-% SiO_2-BOPP compounded with the 300 rpm screw speed.

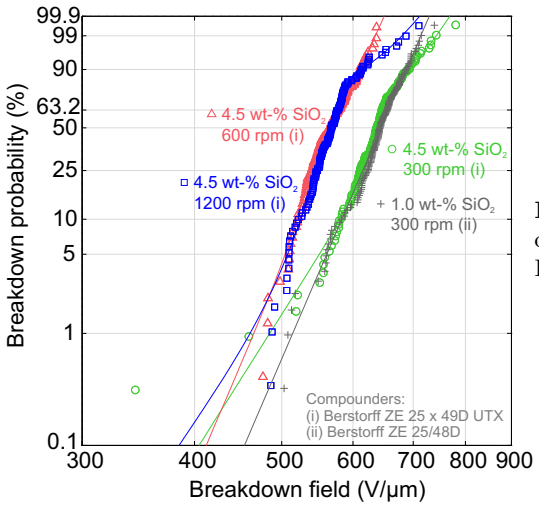

Figure 5.5. Effect of compounder screw speed on the breakdown behavior of 4.5 wt-% SiO_2-BOPP films [P7].

This result suggests that the silica content alone is not the only determining factor for SiO_2-BOPP PNC breakdown performance. Speculative explanations for the exceptional behavior could be e.g. improvement in silica dispersion and distribution at the nanoscale or reduction of silica micro-agglomeration with slower (or longer lasting) compounding, in a similar fashion as in [192]. Although Figures 5.3c–e suggest no major differences in the nano-scale dispersion qualities or particle sizes, it is reminded that a large number of SEM images would be required to obtain a statistically reliable estimate of the whole particle size distribution in the materials. While probably scarce in quantity, larger agglomerates may hinder the otherwise beneficial effect of good nanodispersion [90]. Indeed, a few agglomerates ~500 nm in diameter were observed in some of the SEM cross-sectional images of the 1200 rpm 4.5 wt-% SiO_2-BOPP compound, similarly as observed with TEM (Figure 5.2f). On the other hand, another explanation for the results could be related to differences in antioxidant depletion rate with different compounding rates. It is remarked that residual antioxidant content in BOPP films (e.g. the main process stabilizer Irganox 1010) has been shown to impair the breakdown strength [105, 181] and increase dielectric losses [180].

5.2.4 Effect of co-stabilizer content

The effect of varying co-stabilizer (Irgafos 168) content on the breakdown performance is presented in Figure 5.6. The unfilled BOPP shows a drastic difference in breakdown distribution homogeneity depending on whether Irgafos 168 was used or not, indicating that Irgafos 168 has a detrimental effect on the breakdown performance of the end-product. Interestingly, the dependence on Irgafos 168 content is less prominent with the 4.5 wt-% SiO_2-BOPP variants [P6]. A similar result was also observed in another trial with 1.0 wt-% SiO_2-BOPP films with 0–0.35 wt-% of Irgafos 168. These results point towards possible interaction mechanism between the HMDS-treated SiO_2 nanoparticles and antioxidants. In a study by Nawaz *et al.* [193] a substantial amount of phenolic antioxidant (Irganox 1010) was found to be adsorbed on filler surfaces in Al_2O_3-poly(ethylene-*co*-butyl-acrylate) nanocomposites, thus altering both the short- and long-term antioxidant activity. Similar results have also been reported by Chen *et al.* [194] and Gao *et al.* [195] for PP-SiO_2 nanocomposites with reactive antioxidants. These nanocomposites have been shown to exhibit larger oxidation induction times (OIT) in comparison to neat polymers, indicating

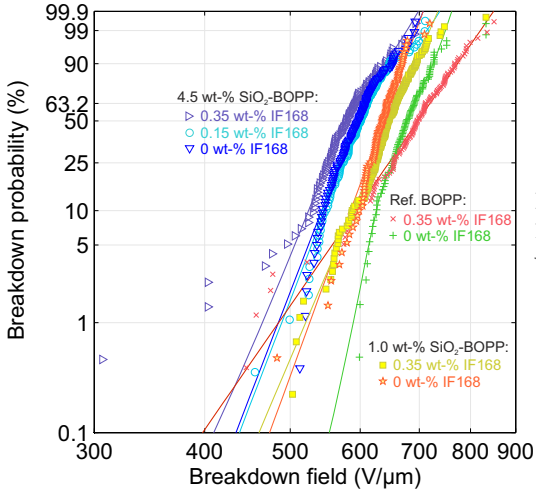

Figure 5.6. Effect of co-stabilizer (Irgafos 168) content on the breakdown behavior of 4.5 wt-% SiO_2-BOPP films [P6].

slow release of antioxidant from the adsorption sites and improved antioxidant efficiency and thermal stability. Nawaz *et al.* also found the antioxidant adsorption to be strongly dependent on the nanofiller surface functionalization (silane treatment) and dispersion quality. Assuming that phosphite antioxidant Irgafos 168 could adhere to HMDS-treated nanosilica in a similar fashion as discussed above, initial antioxidant immobilization and slow-release over time may well have an influence on both the short-term breakdown and aging properties of SiO_2-BOPP PNC films. This aspect should be investigated more thoroughly in the future.

5.2.5 Effect of bi-axial orientation temperature

Figure 5.7 presents SEM cross-sectional images of various cryo-broken SiO_2-BOPP films. In general, the fracture surface morphologies were found to vary from a finely oriented structure to a more coarse and circular structure. As opposed to un-filled reference films, the SiO_2-BOPP films bi-axially oriented at 157 °C were found to exhibit randomly distributed wide voids and fracture lines perpendicular to the film surface. Voids were observed especially in the manually pre-mixed compounds (Figure 5.7a) but also in the automatically pre-mixed compounds (Figure 5.7b). The dependence of void formation on the orientation temperature was therefore studied in [P6]. Upon increasing the orientation temperature of the silica nanocomposites, the amount of voids and fracture lines decreased until at 165 °C (Figure 5.7c) a fine oriented structure was obtained and no voids were observed (the threshold temperature was approximated to be ∼163 °C). The pilot-scale films, for which the bi-axial orientation temperature was higher than that in the laboratory-scale manufacturing [P6], were found to exhibit finely oriented cross-sectional morphology (Figure 5.7d). The corresponding large-area multi-breakdown

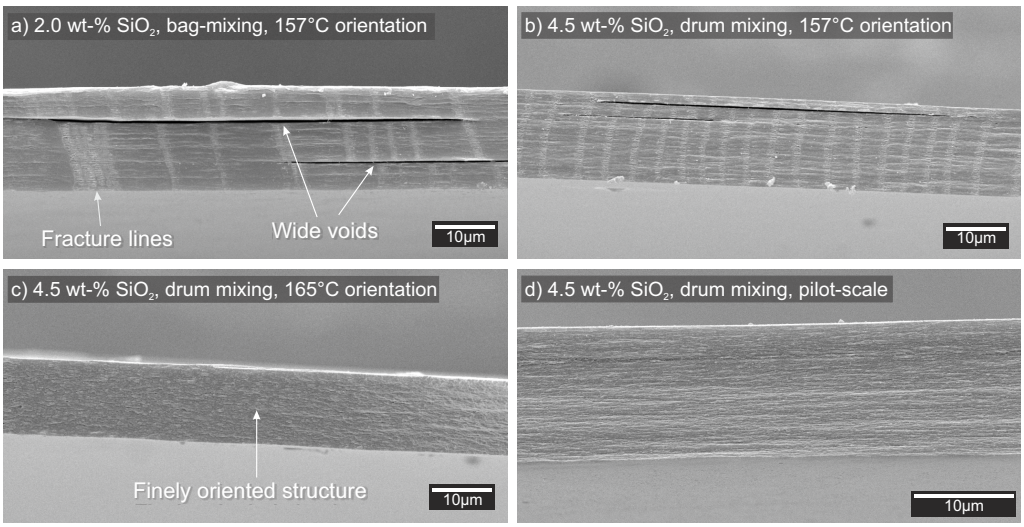

Figure 5.7. Effect of bi-axial orientation temperature on the SiO_2-BOPP film morphology [P6]. Laboratory-scale films: **a)** 2.0 wt-% SiO_2 (157 °C), **b)** 4.5 wt-% SiO_2 (157 °C) and **c)** 4.5 wt-% SiO_2 (165 °C). Large voids were systematically observed in films oriented at 157 °C (more profoundly in the bag-mixed compounds) whereas no voids were observed at the (set) temperature of 165 °C. **d)** presents a pilot-scale 4.5 wt-% SiO_2-BOPP film (MD and TD stretching temperatures in the range of 142–155 °C and 170–183 °C, respectively).

results are presented in Figure 5.8, showing a slight increase in breakdown performance with increasing orientation temperature for both the SiO_2- and un-filled BOPP. With increasing bi-axial orientation temperature, the MD/TD-directional stretching forces and film thickness were found to decrease and DSC characterization indicated a slight increase in BOPP film melting peak temperature and crystallinity, similarly as observed by Capt *et al.* [138, 156, 166]. It is remarked however that it is critical not to exceed the film melting point; with orientation temperatures above 167 °C the films were poorly oriented which was manifested as a collapse of MD/TD-stretching forces, film thickness and breakdown strength. Overall it was concluded that silica nanoparticles may act as the origin of the voids and fracture lines during the orientation process and optimization of the orientation temperature is required. The slight increase in large-area multi-breakdown performance with temperature could be due to the voids and fracture lines acting as weak points in SiO_2-BOPP films [P6], but also due to the slightly increased film crystallinity.

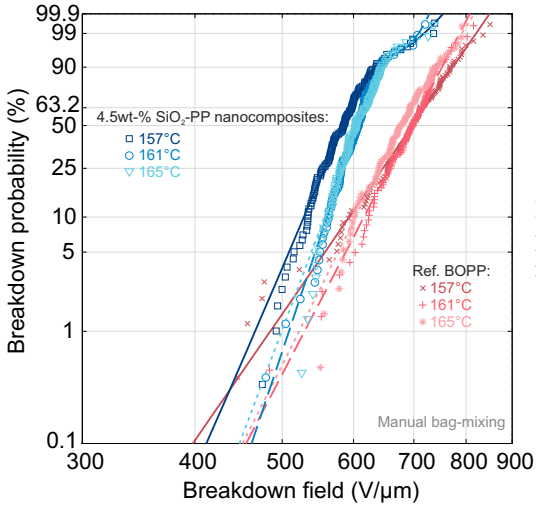

Figure 5.8. Effect of bi-axial orientation temperature on the nano-SiO_2- and un-filled BOPP film breakdown behavior [P6].

5.3 Area- and ramp-rate-dependencies in BOPP-nanocomposites

Area-dependence of the breakdown performance of BOPP PNC films from [P4, P6] was studied by utilizing both the small-area (1 cm^2) single-breakdown and the large-area (81 cm^2) multi-breakdown measurement approaches; exemplifying results are presented in Figure 5.9. While the small- and large-area breakdown behavior of the un-filled BOPP films could be explained by the area-effect (as already discussed in sub-chapter 3.3), the BOPP PNC films were found to exhibit anomalous breakdown responses which could not be explained solely by the area-effect. Therefore, additional large-area multi-breakdown measurements were performed for the laboratory- and pilot-scale films by utilizing a fast rate-of-rise voltage ramp in [P6]. Intriguingly, these initial measurements revealed that the breakdown responses of the 4.5 wt-% SiO_2-BOPP films were strongly dependent on the ramp-rate. When measured with the slow rate-of-rise, the 4.5 wt-% SiO_2-BOPP films were found to show lower breakdown fields but higher breakdown distribution homogeneity in comparison to the unfilled reference BOPP films (see sub-chapter 5.2.1). However, with a fast rate-of-rise the same films exhibited breakdown responses very similar to those of the un-filled BOPP films. The small- and large-area breakdown distributions measured

with the fast rate-of-rise were found to relate logically to each other. Interestingly, the pilot-scale 4.5 wt-% BOPP-silica film gave the highest small-area breakdown performance in comparison to the other studied films (Weibull α=842 V/µm), suggesting that inclusion of nano-silica may improve the short-term small-area breakdown strength of BOPP films.

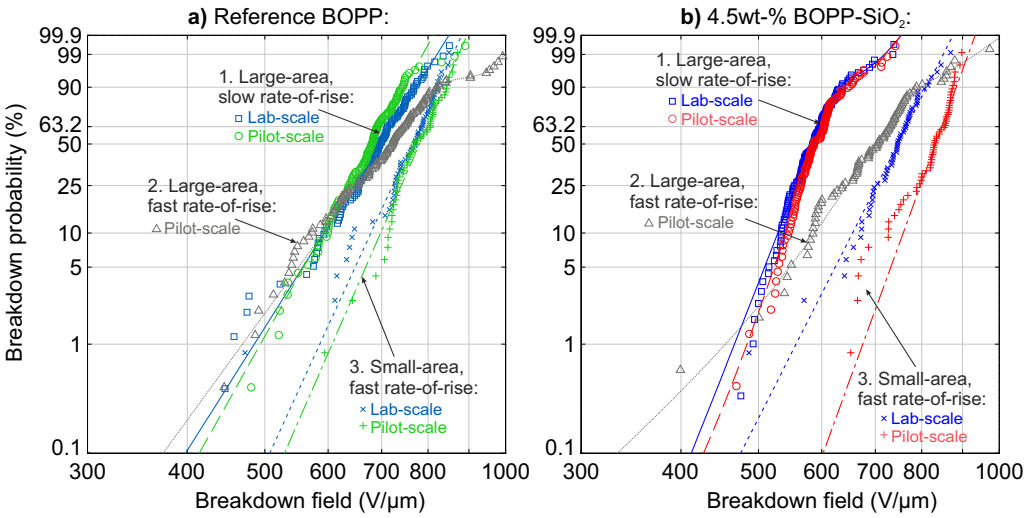

Figure 5.9. Area- and voltage-ramp-rate dependent breakdown responses of laboratory- and pilot-scale **a)** BOPP-silica (4.5 wt-%) and **b)** unfilled reference BOPP films. The large-area (81 cm^2) multi-breakdown measurements were performed using both the slow rate-of-rise method and a fast rate-of-rise of 400 $V\,s^{-1}$ voltage ramp profiles. The small-area single-breakdown measurements (60 samples per material) were made with a fast rate-of-rise (400 $V\,s^{-1}$). [P6]

The effect of DC field ramp rate on the large-area breakdown performance of pilot-scale 4.5 wt-% SiO_2-BOPP film was examined more thoroughly in [P8], in which a linearly rising ramp profile with DC field ramp-rates of 0.25, 1, 5, 10, 25 and 50 $V\,s^{-1}\,\mu m^{-1}$ were used; the large-area multi-breakdown responses are presented in Figure 5.11 on Weibull probability scale. The analysis of the ramp-rate-dependence was based on the work by Hill, Dissado and co-workers [12, 133, 137] and Equation (3.4) which, in terms of breakdown field E, can be written as:

$$F(E) = 1 - \exp\left\{-C\frac{a}{a+b}\dot{E}^{-a}E^{a+b}\right\} \tag{5.1}$$

where $\dot{E}$ is the field ramp rate, constants a and b correspond to the Weibull shape parameters of time and electric field, respectively, and C is the constant of proportionality (as already discussed in sub-chapter 3.1.6). Moreover, Equation (5.1) can be written in a form analogous to a 2-p Weibull distribution with shape parameter $\beta = a + b$. Thus, if several tests are performed at different field-ramp-rates, a log-log graph of the field ramp rate as a function of characteristic field (Weibull α) will result in a graph of slope $(a+b)/a$, thus allowing the constants a, b and C to be determined. If a mixed 2-p Weibull distribution was utilized (Equation (3.5), $S = 2$), the second sub-population was used as a basis for the above calculation, similarly as in [134].

[P8] confirmed the results obtained in [P6]; the studied 4.5 wt-% BOPP-SiO_2 film showed a strong dependence on the DC field ramp rate, with the breakdown field at 63.2 % probability systematically decreasing from 695 to 498 V/µm as the ramp rate was

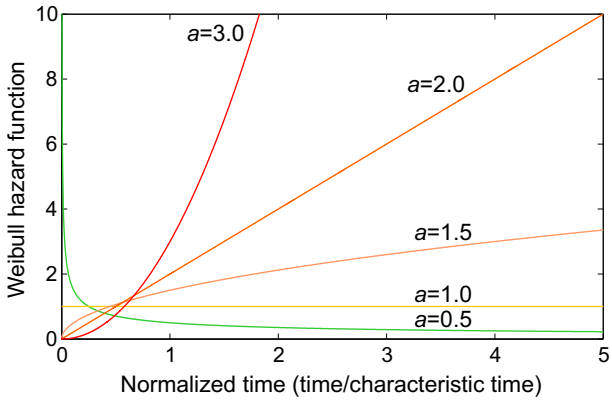

Figure 5.10. Weibull hazard function $h(t) = F'(t)/(1 - F(t))$ where $F(t)$ is the 2-p Weibull distribution of time. Five cases with the Weibull shape parameter a in the range of 0.5–3.0 are presented. The time scale has been normalized similarly as in [12] so that normalized time of one indicates a time equal to the characteristic time to breakdown.

decreased from 50 to 0.25 $\mathrm{V\,s^{-1}\,\mu m^{-1}}$. The un-filled BOPP films did not show as drastic ramp-rate-dependencies, which is in line with previous studies on e.g. BOPP [39] and parylene F films [111]. On average, the calculated Weibull shape parameters of time were $a < 1$ for the un-filled BOPP films, which indicates monotonically decreasing Weibull hazard function (see Figure 5.10) and thus decreasing failure rate over time [12, 139], hence suggesting that breakdowns occurring at high fields and/or long times can be associated to inherent defects in the material rather than electric-field-induced defects [134]. On the other hand, when $1 < a < 2$, as in the case of the studied SiO_2-BOPP film, the Weibull hazard rate increases over time but its rate of increase decreases (Figure 5.10), implying that breakdown probability increases and appears to stabilize to a certain level over time [12, 139].

While the underlying reason for the stronger DC ramp-rate-dependence in the SiO_2-BOPP film remains uncertain, the increase in a upon incorporation of nanofillers could be attributable to altered space charge behavior due to PP-silica interfaces [94, 178], micron-sized agglomerates [P6] and/or morphological changes in the initial cast films [196]. It is speculated that as the rate-of-rise decreases there is more time for space charge to accumulate at the interfaces which is manifested by an increase in a and a concurrent decrease in breakdown performance.

5.4 Considerations and implications

As a whole, publications [P4, P6, P7, P8] indicate that BOPP PNC breakdown properties are determined by a complex interplay between various compositional and film-processing-related features. The trends observable in the large-area breakdown responses are not merely attributable to the filler contents but rather they reflect the filler-matrix interaction, nanodispersion and the degree of micro-aggregation over large film volumes. While the optimum filler content presumably resides at the low fill-fraction range (∼1 wt-%), it is not the only determining factor, as compounds with equal silica content but with differences in e.g. compounder screw speed were found to exhibit large differences in the breakdown response. Although electron microscope imaging of the PNC structure is certainly required for evaluating the dispersion quality, the results indicate that nano-structural features cannot solely explain the observed large-area breakdown behavior — this aspect points towards large-area approach being necessary for the imaging techniques as well in order to reliably establish a link between structural properties and engineering breakdown strength. Overall, the results suggest that up-scaling of PNC production is sensible with

conventional melt-blending technology, although further development and optimization of nanocomposite formulations and processing are necessary. It is also remarked that in addition to short-term breakdown properties, the long-term aging properties of BOPP PNC films should be studied further by the large-area multi-breakdown approach; the first steps towards this direction have already been taken [197].

Above all, the presented results exemplify not only the importance of optimized film processing in achieving improved breakdown performance, but also the importance of careful breakdown strength assessment when dielectric films of more complex internal structure are studied. Breakdown assessment of polymer nanocomposites based solely on short-term test (as defined e.g. in IEC 60243 and ASTM D149 standards) may not reveal the breakdown properties of PNC films inclusively and, in the worst case, can lead to over-optimistic conclusions.

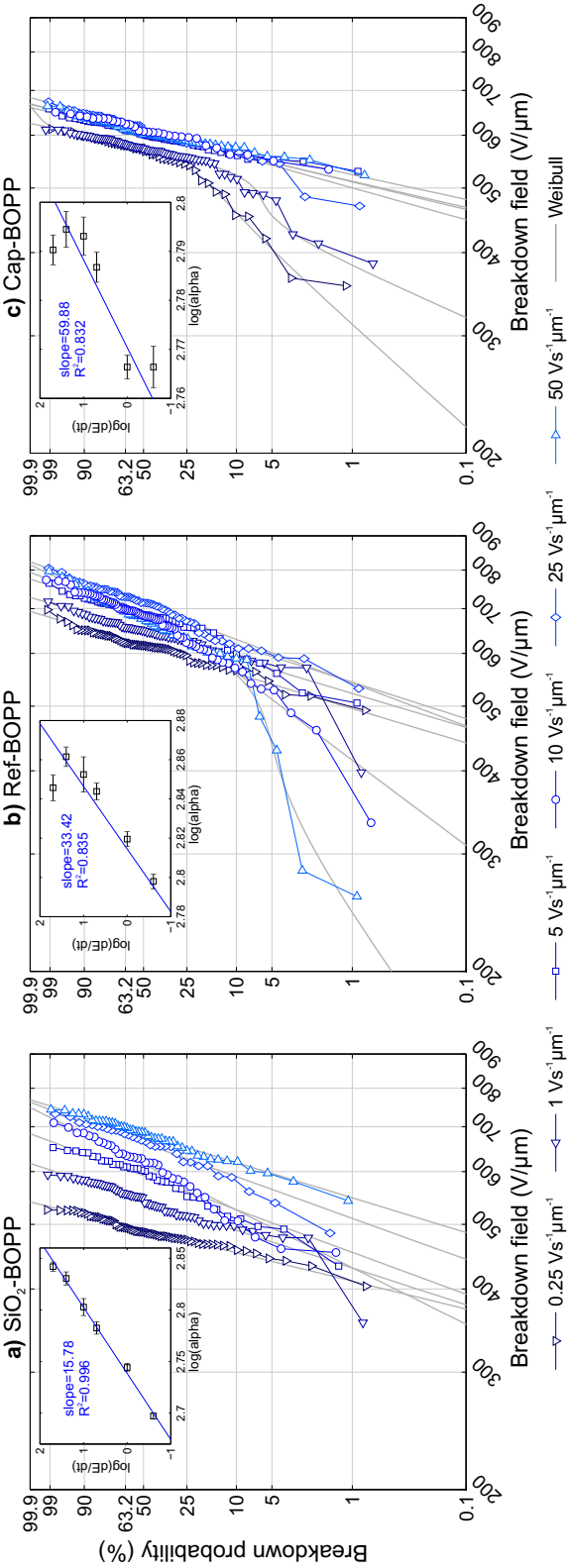

Figure 5.11. Large-area multi-breakdown distributions of **a)** SiO_2-BOPP, **b)** Ref-BOPP and **c)** Cap-BOPP films with varying DC-field ramp rate ($0.25–50\ \mathrm{V\,s^{-1}\,\mu m^{-1}}$) on Weibull probability scale. The insets present log-log graphs of the rate of field increase as a function of the characteristic breakdown field (Weibull α). The error bars represent 90 % confidence limits.

Chapter 6

Conclusions

The ever-growing need for high-energy density and high operation temperature capacitive energy storage for next-generation applications has necessitated research and development on new dielectric materials for film capacitors. Consequently, various new approaches offering unique ways to tailor dielectric properties of polymers have recently emerged, and new materials such as dielectric polymer nanocomposites are envisioned as potential next-generation dielectrics. Establishment of optimized formulation and processing conventions is however necessary in order to achieve improvement in dielectric breakdown properties. Importantly, such material development puts dielectric breakdown strength assessment of polymer films in a central role in guiding material formulation and processing towards highly optimized functional materials. However, the current state-of-the-art breakdown strength measurement techniques rarely provide statistically sufficient amounts of breakdown data from the application point-of-view, thus leading to impaired evaluation of the practical breakdown performance in film capacitors.

In response to these challenges, one of the main objectives of this thesis was to develop a new large-area multi-breakdown measurement method enabling dielectric breakdown characterization of polymer films with high statistical accuracy. Thereafter, by utilizing the large-area multi-breakdown methodology, the objective was to carry out a comprehensive analysis on structure–processing–breakdown relationships in polymer and polymer nanocomposite films. The main conclusions and scientific contributions of this thesis are presented in the following along with some recommendations for future research topics.

6.1 Main conclusions and scientific contributions of the thesis

The current state-of-the-art and challenges of existing polymer film dielectrics and various potential future technologies to overcome their limitations were reviewed in Chapter 2 with a particular emphasis on AC and DC dielectric breakdown properties of nano-silica-filled polymer nanocomposites. It was pointed out that although many of the reviewed material candidates show much potential for next-generation film capacitors, they also pose many research challenges. With polymer nanocomposites the major challenges are centered around preventing nanoparticle agglomeration, optimizing filler-matrix compatibilization and finding proper material processing conventions. The latter part of Chapter 2 reviewed dielectric breakdown process and its statistical nature in polymer films; the discussion underlined the complexity and stochastic nature of dielectric breakdown process and breakdown measurement and also indicated the necessity for obtaining large amount

of breakdown data from a large total film area. Lastly, Chapter 2 covered the self-healing breakdown process of metallized polymer films which forms the foundation for the large-area multi-breakdown characterization approach utilized in this thesis.

The large-area multi-breakdown measurement method developed as a part of this thesis was thoroughly evaluated in Chapter 3, in which various aspects encompassing the sample film preparation, measurement procedure, breakdown progression, discharge event characterization, breakdown field determination, data validation and statistical analysis were systematically and critically discussed. As opposed to conventional small-area single-breakdown measurement techniques (as described in e.g. IEC-60234 standard), the obvious advantage of the self-healing multi-breakdown approach is the ability to acquire a large amount of breakdown data from a relatively large total film area in a bottom-up approach by utilizing a progressive voltage ramp test. A data qualification process based on the self-healing discharge energy and breakdown voltage characteristics was developed and it was shown to be a sensible and convenient way to exclude non-breakdown events from the measurement data prior to Weibull statistical analysis. The measurement method was shown to enable high-statistical-accuracy breakdown characterization of both metallized and non-metallized polymer films of different nature, including a large variety of different laboratory-scale, pilot-scale and commercial-grade capacitor films. Overall, the method was shown to result in detailed, logical and fingerprint-like breakdown responses. Chapter 3 also covered statistical aspects on the area dependence and exemplified the problematic nature of Weibull area-scaling of small-area breakdown data. Moreover, the fundamental differences between the large-area multi-breakdown and the small-area single-breakdown measurement methods and the statistical aspects thereof were analyzed in more detail by the Monte Carlo simulation method.

The results presented in Chapter 4 on the effects of film processing, structure and morphology on the large-area multi-breakdown characteristics of iPP-based cast- and bi-axially oriented films emphasized the determining effect of film processing in large-area dielectric breakdown response of PP films. It was shown that even when starting with the exact same iPP raw material the breakdown response of the end-product is effectively dictated by how the film is prepared. While the morphological transformation from non-oriented to bi-axially oriented film morphology was shown to be in key role in achieving high dielectric breakdown performance, a strong dependence of the BOPP film breakdown response on the morphology and crystalline structure of the initial cast film was also pointed out. In particular, it was shown that the β-form crystal content in the initial iPP cast film is most likely linked to the resulting BOPP film breakdown performance, with a higher cast film β-content leading to a decrease in BOPP film breakdown performance. Overall, the analysis on the laboratory-scale iPP cast- and BOPP-film breakdown characteristics exemplified the vast amount of interrelated factors affecting PP breakdown performance. Chapter 4 also presented large-area multi-breakdown characteristics of various commercial capacitor-grade metallized and non-metallized polymer films; these films were found to exhibit differences in breakdown distribution structure and weak point behavior in comparison to the laboratory-scale BOPP films, presumably due to differences in raw material, additives, thermal history and processing. The studied non-metallized (hazy) capacitor BOPP films were also shown to exhibit increasing amount of electrical weak points with decreasing film thickness, an effect which is assumed to be linked to the film manufacturing process. Lastly, the results on the inter-layer-pressure-dependence of breakdown characteristics of capacitor films emphasized the importance of careful breakdown characterization also under authentic operation stresses in order to ensure proper design and operation in practical applications.

The results presented in Chapter 5 on the large-area breakdown characteristics of

laboratory- and pilot-scale melt-compounded BOPP nanocomposite films with silica and/or calcium carbonate nanofillers indicated a complex interplay between film composition, structure, processing and breakdown response. Although the optimum nano-silica content was found to reside at the low fill-fraction range (∼1 wt-%), the fill-fraction itself was found to be not the only determining factor, as compounds with equal nanoparticle content but with differences in e.g. compounder screw speed were found to exhibit large differences in breakdown response. Indications of possible silica-antioxidant interaction were also observed. The structural TEM/SEM imaging of the films showed that nanostructural features cannot solely explain the observed large-area breakdown behavior — this aspect points towards large-area approach being necessary for the imaging techniques as well in order to reliably establish a link between structural properties and engineering breakdown strength. The results pointed that up-scaling of PNC production is sensible with conventional melt-blending technology, although further development and optimization of nanocomposite formulations and processing were seen necessary. The study on the ramp-rate-dependence of the large-area multi-breakdown performance revealed that the 4.5 wt-% SiO_2-BOPP nanocomposite exhibits a systematic decrease in dielectric strength and increase in Weibull shape parameter of time in comparison to the un-filled BOPP films. The observed behavior was speculated to be attributable to highly altered internal charge dynamics of the silica-BOPP nanocomposite. The presented results exemplified not only the importance of optimized film processing in achieving improved breakdown performance, but also the importance of careful breakdown strength assessment when dielectric films of more complex internal structure are studied.

6.2 Future research topics

This thesis presented a comprehensive study on large-area multi-breakdown characterization of polymer- and polymer-nanocomposite films and their processing–structure–breakdown relationships. However, as this thesis strongly focused on the development, evaluation and application of the large-area multi-breakdown method, additional material characterization methods (other than those utilized in this work) which could provide further insight into the structure-property relationships were considered out of the scope of this thesis. Therefore, in a broader sense, the work presented here only covered a part of the full picture leaving many open question and possible future research topics yet to be studied. Some future research topics are proposed in the following:

1. In order to establish a deeper understanding of the interrelations involved in material composition, processing, structure and dielectric properties, more detailed and multidisciplinary material characterization in combination with the large-area multi-breakdown characterization is called-for. Dielectric spectroscopy as a function of frequency, electric field and temperature is seen as one of the most crucial characterization methods from the capacitor point-of-view. Further study on e.g. film crystallinity, morphology, antioxidants and impurities would also greatly benefit the research and development of dielectric polymer films. The effects of film composition, structure, manufacturing process and thickness on the dielectric properties should be studied further, preferably in co-operation with industrial film manufacturers.

2. While the work presented in this thesis showed that SiO_2-BOPP nanocomposites show some promising properties especially at low fill-fractions, further development and optimization of nanocomposite formulations and processing is seen

necessary. This could involve further optimization of the filler type, surface-functionalization, compounding and film processing. Expanding structural characterization to cover both nano- and micro-scale would greatly benefit the establishment of structure-property relationships in dielectric polymer nanocomposites. The possible nanoparticle-antioxidant interaction mechanisms and the underlying reason for the stronger DC ramp-rate-dependence in the SiO_2-BOPP nanocomposites should also be clarified.

3. Although the assessment of short-term breakdown response at room-temperature provides a good basic measure of the polymer film insulation capability, long-term breakdown properties at elevated temperatures are much more relevant from the application point-of-view. Analysis of the aging properties of BOPP-nanocomposites is also seen crucial. The large-area multi-breakdown measurement approach shows great potential for long-term aging study of polymer films, and the first steps towards this direction have already been taken [145, 197, 198]. Lastly, other voltage stress forms, in particular AC voltage, should be incorporated in the analysis.

References

[1] J. Ho, T. R. Jow, and S. Boggs, "Historical introduction to capacitor technology," *IEEE Electrical Insulation Magazine*, vol. 26, no. 1, pp. 20–25, 2010.

[2] W. J. Sarjeant, J. Zimheld, F. W. Macdougall, J. S. Bowers, N. Clark, I. W. Clelland, R. A. Price, M. Hudis, I. Kohlberg, G. McDuff, I. McNab, S. G. Parler, Jr, and J. Prymak, "Capacitors - Past, Present and Future," in *Handbook of Low and High Dielectric Constant Materials and Their Applications* (H. Nalwa, ed.), ch. 9, pp. 423–491, Academic Press, 1999.

[3] W. Sarjeant, J. Zirnheld, and F. MacDougall, "Capacitors," *IEEE Transactions on Plasma Science*, vol. 26, no. 5, pp. 1368–1392, 1998.

[4] D. Shaw, S. Cichanowski, and A. Yializis, "A Changing Capacitor Technology - Failure Mechanisms and Design Innovations," *IEEE Transactions on Electrical Insulation*, vol. EI-16, no. 5, pp. 399–413, 1981.

[5] M. Rabuffi and G. Picci, "Status quo and future prospects for metallized polypropylene energy storage capacitors," *IEEE Transactions on Plasma Science*, vol. 30, no. 5, pp. 1939–1942, 2002.

[6] T. A. Burress, S. L. Campbell, C. L. Coomer, C. W. Ayers, A. A. Wereszczak, J. P. Cunningham, L. D. Marlino, L. E. Seiber, and H. T. Lin, "Evaluation of the 2010 Toyota Prius hybrid synergy drive system," tech. rep., Oak Ridge Natonal Laboratory, 2011.

[7] L. Zhu, "Exploring Strategies for High Dielectric Constant and Low Loss Polymer Dielectrics," *The Journal of Physical Chemistry Letters*, vol. 5, no. 21, pp. 3677–3687, 2014.

[8] L. Zhu and Q. Wang, "Novel ferroelectric polymers for high energy density and low loss dielectrics," *Macromolecules*, vol. 45, pp. 2937–2954, 2012.

[9] J. K. Nelson, *Dielectric polymer nanocomposites*. Springer US, 2010.

[10] T. Tanaka and T. Imai, "Advances in nanodielectric materials over the past 50 years," *IEEE Electrical Insulation Magazine*, vol. 29, no. 1, pp. 10–23, 2013.

[11] Q. Wang and L. Zhu, "Polymer nanocomposites for electrical energy storage," *Journal of Polymer Science, Part B: Polymer Physics*, vol. 49, pp. 1421–1429, 2011.

[12] L. Dissado and J. Fothergill, *Electrical Degradation and Breakdown in Polymers*. London: Institution of Engineering and Technology (IET), 1992.

[13] "Electric strength of insulating materials - Test methods - Part 1: Tests at power frequencies, IEC standard 60243-1, 2013-03."

[14] "Electric strength of insulating materials - Test methods - Part 2: Additional requirements for tests using direct voltage, IEC standard 60243-2, 2001-02."

[15] S. J. Laihonen, U. Gäfvert, T. Schütte, and U. W. Gedde, "DC breakdown strength of

polypropylene films: Area dependence and statistical behavior," *IEEE Transactions on Dielectrics and Electrical Insulation*, vol. 14, no. 2, pp. 275–286, 2007.

[16] C. Xu, J. Ho, and S. A. Boggs, "Automatic breakdown voltage measurement of polymer films," *IEEE Electrical Insulation Magazine*, vol. 24, no. 6, pp. 30–34, 2008.

[17] J. L. Nash, "Biaxially oriented polypropylene film in power capacitors," *Polymer Engineering and Science*, vol. 28, no. 13, pp. 862–870, 1988.

[18] S. A. Boggs, J. Ho, and T. R. Jow, "Overview of laminar dielectric capacitors," *IEEE Electrical Insulation Magazine*, vol. 26, no. 2, pp. 7–13, 2010.

[19] H. Heywang, "Physikalische und chemische Vorgänge in selbstheilenden Kunststoff-Kondensatoren," *Colloid and Polymer Science*, vol. 254, no. 2, pp. 139–147, 1976.

[20] S. J. Laihonen, *Polypropylene: Morphology, Defects and Electrical Breakdown.* Phd thesis, Kungliga Tekniska Högskolan, 2005.

[21] M. A. Carter, "Is There a Substitute for Polycarbonate Film Capacitors?," *Power Electronics Technology*, vol. 28, no. 4, pp. 31–44, 2002.

[22] J. Ho and R. Jow, *Characterization of High Temperature Polymer Thin Films for Power Conditioning Capacitors, ARL-TR-4880.* U.S. Army Research Laboratory, Adelphi, MD 20783-1197, 2009.

[23] N. Zhang, J. Ho, J. Runt, and S. Zhang, "Light weight high temperature polymer film capacitors with dielectric loss lower than polypropylene," *Journal of Materials Science: Materials in Electronics*, pp. 1–6, 2015.

[24] Y. Wang, X. Zhou, Q. Chen, B. Chu, and Q. Zhang, "Recent development of high energy density polymers for dielectric capacitors," *IEEE Transactions on Dielectrics and Electrical Insulation*, vol. 17, no. 4, pp. 1036–1042, 2010.

[25] E. J. Barshaw, J. White, M. J. Chait, J. B. Cornette, J. Bustamante, F. Folli, D. Biltchick, G. Borelli, G. Picci, and M. Rabuffi, "High Energy Density (HED) Biaxially-Oriented Poly-Propylene (BOPP) Capacitors For Pulse Power Applications," *IEEE Transactions on Magnetics*, vol. 43, no. 1, pp. 223–225, 2007.

[26] S. Diaham, S. Zelmat, M. L. Locatelli, S. Dinculescu, M. Decup, and T. Lebey, "Dielectric breakdown of polyimide films: Area, thickness and temperature dependence," *IEEE Transactions on Dielectrics and Electrical Insulation*, vol. 17, no. June 2009, pp. 18–27, 2010.

[27] H. Kim and F. Shi, "Thickness dependent dielectric strength of a low-permittivity dielectric film," *IEEE Transactions on Dielectrics and Electrical Insulation*, vol. 8, no. 2, pp. 248–252, 2001.

[28] G. Maier, "Low dielectric constant polymers for microelectronics," *Progress in Polymer Science*, vol. 26, no. 1, pp. 3–65, 2001.

[29] B. Chu, X. Zhou, B. Neese, Q. M. Zhang, and F. Bauer, "Relaxor ferroelectric poly(vinylidene fluoride-trifluoroethylene- chlorofluoroethylene) terpolymer for high energy density storage capacitors," *IEEE Transactions on Dielectrics and Electrical Insulation*, vol. 13, no. 5, pp. 1162–1168, 2006.

[30] X. Zhou, B. Chu, B. Neese, M. Lin, and Q. M. Zhang, "Electrical energy density and discharge characteristics of a poly(vinylidene fluoride-chlorotrifluoroethylene) copolymer," *IEEE Transactions on Dielectrics and Electrical Insulation*, vol. 14, no. 5, pp. 1133–1138, 2007.

[31] X. Zhou, X. Zhao, Z. Suo, C. Zou, J. Runt, S. Liu, S. Zhang, and Q. M. Zhang, "Electrical breakdown and ultrahigh electrical energy density in poly(vinylidene

fluoride-hexafluoropropylene) copolymer," *Applied Physics Letters*, vol. 94, no. 16, p. 162901, 2009.

[32] Y. Wang, X. Zhou, M. Lin, and Q. M. Zhang, "High-energy density in aromatic polyurea thin films," *Applied Physics Letters*, vol. 94, no. 20, p. 202905, 2009.

[33] S. Wu, W. Li, M. Lin, Q. Burlingame, Q. Chen, A. Payzant, K. Xiao, and Q. M. Zhang, "Aromatic polythiourea dielectrics with ultrahigh breakdown field strength, low dielectric loss, and high electric energy density," *Advanced Materials*, vol. 25, no. 12, pp. 1734–1738, 2013.

[34] S. Wu, Q. Burlingame, Z.-X. Cheng, M. Lin, and Q. M. Zhang, "Strongly Dipolar Polythiourea and Polyurea Dielectrics with High Electrical Breakdown, Low Loss, and High Electrical Energy Density," *Journal of Electronic Materials*, vol. 43, no. 12, pp. 4548–4551, 2014.

[35] S. Wu, *High energy density, and low loss polymer dielectrics for energy storage capacitors and organic electronics*. Phd thesis, The Pennsylvania State University, 2014.

[36] S. Wu, M. Lin, Q. Burlingame, and Q. M. Zhang, "Meta-aromatic polyurea with high dipole moment and dipole density for energy storage capacitors," *Applied Physics Letters*, vol. 104, no. 7, p. 072903, 2014.

[37] X. Yuan and T. C. M. Chung, "Cross-linking effect on dielectric properties of polypropylene thin films and applications in electric energy storage," *Applied Physics Letters*, vol. 98, no. 6, pp. 2011–2014, 2011.

[38] X. Yuan, Y. Matsuyama, and T. C. M. Chung, "Synthesis of functionalized isotactic polypropylene dielectrics for electric energy storage applications," *Macromolecules*, vol. 43, no. 9, pp. 4011–4015, 2010.

[39] S. J. Laihonen, A. Gustafsson, U. Gäfvert, T. Schütte, and U. W. Gedde, "Area dependence of breakdown strength of polymer films: Automatic measurement method," *IEEE Transactions on Dielectrics and Electrical Insulation*, vol. 14, no. 2, pp. 263–274, 2007.

[40] S. Ul-Haq and G. Raju, "Weibull statistical analysis of area effect on the breakdown strength in polymer films," in *Annual Report Conference on Electrical Insulation and Dielectric Phenomena*, pp. 518–521, 2002.

[41] K. Wu, Y. Wang, Y. Cheng, L. A. Dissado, and X. Liu, "Statistical behavior of electrical breakdown in insulating polymers," *Journal of Applied Physics*, vol. 107, no. 6, p. 064107, 2010.

[42] C. W. Reed and S. W. Cichanowski, "Fundamentals of aging in HV polymer-film capacitors," *IEEE Transactions on Dielectrics and Electrical Insulation*, vol. 1, no. 5, pp. 904–922, 1994.

[43] P.-O. Sassoulas, B. Gosse, and J.-P. Gosse, "Self-healing breakdown of metallized polypropylene," in *ICSD'01. Proceedings of the 20001 IEEE 7th International Conference on Solid Dielectrics*, pp. 275–278, 2001.

[44] B. Walgenwitz, J.-H. Tortai, N. Bonifaci, and A. Denat, "Self-healing of metallized polymer films of different nature," in *Proceedings of the 2004 IEEE International Conference on Solid Dielectrics, 2004. ICSD 2004.*, pp. 27–30, 2004.

[45] M. A. Schneider, J. R. Macdonald, M. C. Schalnat, and J. B. Ennis, "Electrical breakdown in capacitor dielectric films: Scaling laws and the role of self-healing," in *Proceedings of the 2012 IEEE International Power Modulator and High Voltage Conference, IPMHVC 2012*, pp. 284–287, 2012.

[46] T. C. Mike Chung, "Functional polyolefins for energy applications," *Macromolecules*, vol. 46, no. 17, pp. 6671–6698, 2013.

[47] Z. M. Dang, J. K. Yuan, J. W. Zha, T. Zhou, S. T. Li, and G. H. Hu, "Fundamentals, processes and applications of high-permittivity polymer-matrix composites," *Progress in Materials Science*, vol. 57, no. 4, pp. 660–723, 2012.

[48] S. Wu, M. Lin, S. G. Lu, L. Zhu, and Q. M. Zhang, "Polar-fluoropolymer blends with tailored nanostructures for high energy density low loss capacitor applications," *Applied Physics Letters*, vol. 99, no. 13, p. 132901, 2011.

[49] K. Yao, S. Chen, M. Rahimabady, M. Mirshekarloo, S. Yu, F. Tay, T. Sritharan, and L. Lu, "Nonlinear dielectric thin films for high-power electric storage with energy density comparable with electrochemical supercapacitors," *IEEE Transactions on Ultrasonics, Ferroelectrics and Frequency Control*, vol. 58, no. 9, pp. 1968–1974, 2011.

[50] Y. Wang, X. Zhou, M. Lin, S. G. Lu, J. Lin, E. Furman, and Q. M. Zhang, "Nonlinear conduction in aromatic polyurea thin films and its influence on dielectric applications over a broad temperature range," *IEEE Transactions on Dielectrics and Electrical Insulation*, vol. 17, no. 1, pp. 28–33, 2010.

[51] Q. Chen, Y. Wang, X. Zhou, Q. M. Zhang, and S. Zhang, "High field tunneling as a limiting factor of maximum energy density in dielectric energy storage capacitors," *Applied Physics Letters*, vol. 92, no. 14, p. 142909, 2008.

[52] Y. Sun, S. Boggs, and R. Ramprasad, "The effect of dipole scattering on intrinsic breakdown strength of polymers," *IEEE Transactions on Dielectrics and Electrical Insulation*, vol. 22, no. 1, pp. 495–502, 2015.

[53] T. C. Mike Chung, "Functionalization of Polypropylene with High Dielectric Properties: Applications in Electric Energy Storage," *Green and Sustainable Chemistry*, vol. 2, no. 2, pp. 29–37, 2012.

[54] S. Gupta, X. Yuan, T. C. M. Chung, S. Kumar, M. Cakmak, and R. A. Weiss, "Effect of hydroxyl-functionalization on the structure and properties of polypropylene," *Macromolecules*, vol. 46, no. 14, pp. 5455–5463, 2013.

[55] S. Gupta, *Structure-property relationships in polymers for dielectric capacitors*. Phd thesis, The University of Akron, 2014.

[56] X. Qi and S. Boggs, "Electrothermal failure of metallized film capacitor end connections-computation of temperature rise at connection spots," *Journal of Applied Physics*, vol. 94, no. 7, pp. 4449–4456, 2003.

[57] J. Ho, T. R. Jow, and S. A. Boggs, "Implications of advanced capacitor dielectrics for performance of metallized film capacitor windings," *IEEE Transactions on Dielectrics and Electrical Insulation*, vol. 15, no. 6, pp. 1754–1760, 2008.

[58] S. Qin and S. Boggs, "Limits to the performance and design of high voltage metalized film capacitors," *IEEE Transactions on Dielectrics and Electrical Insulation*, vol. 17, no. 4, pp. 1298–1306, 2010.

[59] R. C. Smith, J. K. Nelson, and L. S. Schadler, "Electrical behavior of particle-filled polymer nanocomposites," in *Physical Properties and Applications of Polymer Nanocomposites* (S. Tjong and Y.-W. Mai, eds.), pp. 70–107, Cambridge: Woodhead Publishing Limited, 2010.

[60] E. David and M. Fréchette, "Polymer nanocomposites-major conclusions and achievements reached so far," *IEEE Electrical Insulation Magazine*, vol. 29, no. 6, pp. 29–36, 2013.

[61] K. Y. Lau, A. S. Vaughan, and G. Chen, "Nanodielectrics: Opportunities and Challenges," *IEEE Electrical Insulation Magazine*, vol. 31, no. 4, pp. 45–54, 2015.

[62] S. Virtanen, T. Krentz, J. Nelson, L. Schadler, M. Bell, B. Benicewicz, H. Hillborg, and S. Zhao, "Dielectric breakdown strength of epoxy bimodal-polymer-brush-grafted core functionalized silica nanocomposites," *IEEE Transactions on Dielectrics and Electrical Insulation*, vol. 21, no. 2, pp. 563–570, 2014.

[63] M. Roy, J. K. Nelson, R. K. MacCrone, and L. S. Schadler, "Candidate mechanisms controlling the electrical characteristics of silica/XLPE nanodielectrics," *Journal of Materials Science*, vol. 42, no. 11, pp. 3789–3799, 2007.

[64] M. Takala, H. Ranta, P. Nevalainen, P. Pakonen, J. Pelto, M. Karttunen, S. Virtanen, V. Koivu, M. Pettersson, B. Sonerud, and K. Kannus, "Dielectric properties and partial discharge endurance of polypropylene-silica nanocomposite," *IEEE Transactions on Dielectrics and Electrical Insulation*, vol. 17, no. 4, pp. 1259–1267, 2010.

[65] M. G. Danikas and T. Tanaka, "Nanocomposites - A review of electrical treeing and breakdown," *IEEE Electrical Insulation Magazine*, vol. 25, pp. 19–25, 2009.

[66] R. C. Smith, C. Liang, M. Landry, J. K. Nelson, and L. S. Schadler, "The mechanisms leading to the useful electrical properties of polymer nanodielectrics," *IEEE Transactions on Dielectrics and Electrical Insulation*, vol. 15, no. 1, pp. 187–196, 2008.

[67] P. Barber, S. Balasubramanian, Y. Anguchamy, S. Gong, A. Wibowo, H. Gao, H. J. Ploehn, and H. C. Z. Loye, "Polymer composite and nanocomposite dielectric materials for pulse power energy storage," *Materials*, vol. 2, pp. 1697–1733, 2009.

[68] T. Tanaka, M. Kozako, N. Fuse, and Y. Ohki, "Proposal of a multi-core model for polymer nanocomposite dielectrics," *IEEE Transactions on Dielectrics and Electrical Insulation*, vol. 12, no. 4, pp. 669–681, 2005.

[69] T. Tanaka, "Interface Properties and Surface Erosion Resistance," in *Dielectric Polymer Nanocomposites* (J. K. Nelson, ed.), pp. 229–257, Springer US, 2010.

[70] M. Roy, J. Nelson, R. MacCrone, L. Schadler, C. Reed, and R. Keefe, "Polymer nanocomposite dielectrics-the role of the interface," *IEEE Transactions on Dielectrics and Electrical Insulation*, vol. 12, no. 4, 2005.

[71] C. A. Grabowski, H. Koerner, J. S. Meth, A. Dang, C. M. Hui, K. Matyjaszewski, M. R. Bockstaller, M. F. Durstock, and R. A. Vaia, "Performance of Dielectric Nanocomposites: Matrix-Free, Hairy Nanoparticle Assemblies and Amorphous Polymer–Nanoparticle Blends," *ACS Applied Materials & Interfaces*, vol. 6, no. 23, pp. 21500–21509, 2014.

[72] T. J. Lewis, "Interfaces are the dominant feature of dielectrics at the nanometric level," *IEEE Transactions on Dielectrics and Electrical Insulation*, vol. 11, no. 5, pp. 739–753, 2004.

[73] T. Andritsch, *Epoxy Based Nanodielectrics for High Voltage DC-Applications – Synthesis, Dielectric Properties and Space Charge Dynamics.* Phd thesis, Delft University of Technology, 2010.

[74] T. Andritsch, R. Kochetov, P. H. F. Morshuis, and J. J. Smit, "Proposal of the polymer chain alignment model," in *Annual Report - Conference on Electrical Insulation and Dielectric Phenomena, CEIDP*, pp. 624–627, 2011.

[75] J. Seiler and J. Kindersberger, "Insight into the interphase in polymer nanocomposites," *IEEE Transactions on Dielectrics and Electrical Insulation*, vol. 21, no. 2,

pp. 537–547, 2014.

[76] J. Y. Li, L. Zhang, and S. Ducharme, "Electric energy density of dielectric nanocomposites," *Applied Physics Letters*, vol. 90, pp. 13–16, 2007.

[77] C. Calebrese, L. Hui, L. S. Schadler, and J. K. Nelson, "A review on the importance of nanocomposite processing to enhance electrical insulation," 2011.

[78] L. Hui, L. Schadler, and J. Keith Nelson, "The influence of moisture on the electrical properties of crosslinked polyethylene/silica nanocomposites," *IEEE Transactions on Dielectrics and Electrical Insulation*, vol. 20, no. 2, pp. 641–653, 2013.

[79] Z. M. Dang, Y. Q. Lin, H. P. Xu, C. Y. Shi, S. T. Li, and J. Bai, "Fabrication and dielectric characterization of advanced BaTiO 3/polyimide nanocomposite films with high thermal stability," *Advanced Functional Materials*, vol. 18, pp. 1509–1517, 2008.

[80] P. Kim, S. C. Jones, P. J. Hotchkiss, J. N. Haddock, B. Kippelen, S. R. Marder, and J. W. Perry, "Phosphonic acid-modified barium titanate polymer nanocomposites with high permittivity and dielectric strength," *Advanced Materials*, vol. 19, no. 7, pp. 1001–1005, 2007.

[81] L. A. Fredin, Z. Li, M. A. Ratner, M. T. Lanagan, and T. J. Marks, "Enhanced energy storage and suppressed dielectric loss in oxide core-shell-polyolefin nanocomposites by moderating internal surface area and increasing shell thickness," *Advanced Materials*, vol. 24, no. 44, pp. 5946–5953, 2012.

[82] K. Yu, Y. Niu, F. Xiang, Y. Zhou, Y. Bai, and H. Wang, "Enhanced electric breakdown strength and high energy density of barium titanate filled polymer nanocomposites," *Journal of Applied Physics*, vol. 114, no. 17, p. 174107, 2013.

[83] J. P. Calame, "Finite difference simulations of permittivity and electric field statistics in ceramic-polymer composites for capacitor applications," *Journal of Applied Physics*, vol. 99, no. 8, p. 084101, 2006.

[84] L. An, S. Boggs, and J. Calame, "Energy storage in polymer films with high dielectric constant fillers," *IEEE Electrical Insulation Magazine*, vol. 24, no. 3, pp. 5–10, 2008.

[85] P. Kim, N. M. Doss, J. P. Tillotson, P. J. Hotchkiss, M. J. Pan, S. R. Marder, J. Li, J. P. Calame, and J. W. Perry, "High energy density nanocomposites based on surface-modified BaTiO3 and a ferroelectric polymer," *ACS Nano*, vol. 3, no. 9, pp. 2581–2592, 2009.

[86] N. Guo, S. A. DiBenedetto, P. Tewari, M. T. Lanagan, M. A. Ratner, and T. J. Marks, "Nanoparticle, Size, Shape, and Interfacial Effects on Leakage Current Density, Permittivity, and Breakdown Strength of Metal Oxide-Polyolefin Nanocomposites: Experiment and Theory," *Chemistry of Materials*, vol. 22, no. 4, pp. 1567–1578, 2010.

[87] K. Yang, X. Huang, Y. Huang, L. Xie, and P. Jiang, "Fluoro-polymer@BaTiO3 hybrid nanoparticles prepared via RAFT polymerization: Toward ferroelectric polymer nanocomposites with high dielectric constant and low dielectric loss for energy storage application," *Chemistry of Materials*, vol. 25, no. 11, pp. 2327–2338, 2013.

[88] M. Zhu, X. Huang, K. Yang, X. Zhai, J. Zhang, J. He, and P. Jiang, "Energy Storage in Ferroelectric Polymer Nanocomposites Filled with Core–Shell Structured Polymer@BaTiO 3 Nanoparticles: Understanding the Role of Polymer Shells in the Interfacial Regions," *ACS Applied Materials & Interfaces*, vol. 6, no. 22, pp. 19644–

19654, 2014.

[89] M. Roy, J. K. Nelson, R. K. MacCrone, L. S. Schadler, C. W. Reed, R. Keefe, and W. Zenger, "Polymer nanocomposite dielectrics - The role of the interface," *IEEE Transactions on Dielectrics and Electrical Insulation*, vol. 12, no. 4, pp. 629–642, 2005.

[90] S. Virtanen, H. Ranta, S. Ahonen, M. Karttunen, J. Pelto, K. Kannus, and M. Pettersson, "Structure and dielectric breakdown strength of nano calcium carbonate/polypropylene composites," *Journal of Applied Polymer Science*, vol. 131, no. 1, p. 39504, 2014.

[91] L. Zhang, Y. Zhou, M. Huang, Y. Sha, J. Tian, and Q. Ye, "Effect of nanoparticle surface modification on charge transport characteristics in XLPE/SiO2 nanocomposites," *IEEE Transactions on Dielectrics and Electrical Insulation*, vol. 21, no. 2, pp. 424–433, 2014.

[92] C. A. Grabowski, S. P. Fillery, N. M. Westing, C. Chi, J. S. Meth, M. F. Durstock, and R. A. Vaia, "Dielectric breakdown in silica-amorphous polymer nanocomposite films: The role of the polymer matrix," *ACS Applied Materials and Interfaces*, vol. 5, no. 12, pp. 5486–5492, 2013.

[93] M. Praeger, A. S. Vaughan, and S. G. Swingler, "The breakdown strength and localised structure of polystyrene as a function of nanosilica fill-fraction," in *Proceedings of IEEE International Conference on Solid Dielectrics, ICSD*, pp. 863–866, 2013.

[94] K. Y. Lau, A. S. Vaughan, G. Chen, and I. L. Hosier, "Polyethylene nanodielectrics: The effect of nanosilica and its surface treatment on electrical breakdown strength," in *Annual Report - Conference on Electrical Insulation and Dielectric Phenomena, CEIDP*, pp. 21–24, 2012.

[95] A. Sami, E. David, M. Frechette, and S. Savoie, "Breakdown and surface discharge involving PE/SiO2 nanocomposites," in *Electrical Insulation (ISEI), Conference Record of the 2010 IEEE International Symposium on*, pp. 5–8, 2010.

[96] M. Hoyos, N. García, R. Navarro, A. Dardano, A. Ratto, F. Guastavino, and P. Tiemblo, "Electrical strength in ramp voltage AC tests of LDPE and its nanocomposites with silica and fibrous and laminar silicates," *Journal of Polymer Science, Part B: Polymer Physics*, vol. 46, no. 13, pp. 1301–1311, 2008.

[97] T. M. Krentz, Y. Huang, J. K. Nelson, L. S. Schadler, M. Bell, B. Benicewicz, S. Zhao, and H. Hillborg, "Enhanced charge trapping in bimodal brush functionalized silica-epoxy nanocomposite dielectrics," in *2014 IEEE Conference on Electrical Insulation and Dielectric Phenomena (CEIDP)*, pp. 643–646, 2014.

[98] G. Teyssedre and C. Laurent, "Advances in high-field insulating polymeric materials over the past 50 years," *IEEE Electrical Insulation Magazine*, vol. 29, no. 5, pp. 26–36, 2013.

[99] P. Fischer, "Dielectric breakdown phenomenon in polymers," in *Electrical properties of polymers* (D. A. Seanor, ed.), pp. 319–367, Academic Press, 1982.

[100] J. K. Nelson, "Breakdown Strength of Solids," in *Engineering Dielectrics Volume IIA Electrical Properties of Solid Insulating Materials: Molecular Structure and Electrical Behavior* (R. Bartnikas and R. Eichhorn, eds.), pp. 445–520, Philadelphia: ASTM International, 1983.

[101] M. Ieda, "Dielectric Breakdown Process of Polymers," *IEEE Transactions on Electrical Insulation*, vol. EI-15, no. 3, pp. 206–224, 1980.

[102] Y. Sun, C. Bealing, S. Boggs, and R. Ramprasad, "50+ Years of Intrinsic Breakdown," *IEEE Electrical Insulation Magazine*, vol. 29, no. 2, pp. 8–15, 2013.

[103] J. Artbauer, "Electric strength of polymers," *Journal of Physics D: Applied Physics*, vol. 29, no. 2, pp. 446–456, 1999.

[104] Q. Xiaoguang, Z. Zhong, and S. Boggs, "Computation of electro-thermal breakdown of polymer films," in *2003 Annual Report Conference on Electrical Insulation and Dielectric Phenomena*, pp. 337–340, IEEE, 2003.

[105] J. Ho, R. Ramprasad, and S. Boggs, "Effect of alteration of antioxidant by UV treatment on the dielectric strength of BOPP capacitor film," *IEEE Transactions on Dielectrics and Electrical Insulation*, vol. 14, no. 5, pp. 1295–1301, 2007.

[106] J. Ho and T. R. Jow, "Effect of crystallinity and morphology on dielectric properties of PEEK at elevated temperature," in *Proceedings of IEEE International Conference on Solid Dielectrics, ICSD*, pp. 385–388, 2013.

[107] J. K. Tseng, S. Tang, Z. Zhou, M. Mackey, J. M. Carr, R. Mu, L. Flandin, D. E. Schuele, E. Baer, and L. Zhu, "Interfacial polarization and layer thickness effect on electrical insulation in multilayered polysulfone/poly(vinylidene fluoride) films," *Polymer*, vol. 55, no. 1, pp. 8–14, 2014.

[108] J. Ho, *Effect of Alteration of Antioxidant on the Dielectric Strength of Biaxially-Oriented Polypropylene*. Ph.d. thesis, University of Connectricut, 2007.

[109] W. Hauschild and W. Mosch, *Statistical Techniques for High-Voltage Engineering*. Philadephia: Institution of Engineering and Technology, 1992.

[110] I. L. Hosier, A. S. Vaughan, and R. D. Chippendale, "Permittivity mismatch and its influence on ramp breakdown performance," in *Proceedings of IEEE International Conference on Solid Dielectrics, ICSD*, pp. 644–647, 2013.

[111] R. Khazaka, M. Bechara, S. Diaham, and M. L. Locatelli, "Parameters affecting the DC breakdown strength of parylene F thin films," in *Annual Report - Conference on Electrical Insulation and Dielectric Phenomena, CEIDP*, pp. 740–743, 2011.

[112] C. Daran-Daneau, E. David, M. F. Frechette, and S. Savoie, "Influence of the surrounding medium on the dielectric strength measurement of LLDPE/clay nanocomposites," in *Conference Record of IEEE International Symposium on Electrical Insulation*, pp. 654–658, 2012.

[113] "IEEE Guide for the Statistical Analysis of Electrical Insulation Breakdown Data," IEEE Std 930-2004 (Revision of IEEE Std 930-1987), 2005."

[114] J. Wei, Z. Zhang, J. K. Tseng, I. Treufeld, X. Liu, M. Litt, and L. Zhu, "Achieving High Dielectric Constant and Low Loss Property in a Dipolar Glass Polymer Containing Strongly Dipolar and Small Size Sulfone Groups," *ACS Applied Materials & Interfaces*, vol. 7, no. 9, pp. 5248–5257, 2015.

[115] G. Raju, A. Katebian, and S. Z. Jafri, "Breakdown voltages of polymers in the temperature range 23°-250°C," *IEEE Transactions on Dielectrics and Electrical Insulation*, vol. 10, no. 1, pp. 117–127, 2003.

[116] J. Tortai, N. Bonifaci, A. Denat, and O. Lesaint, "Self-healing of aluminium metallized polypropylene films: a spectroscopic investigation," in *Proceedings of 2002 IEEE 14th International Conference on Dielectric Liquids. ICDL 2002*, pp. 190–193, 2002.

[117] J. H. Tortai, N. Bonifaci, A. Denat, and C. Trassy, "Diagnostic of the self-healing of metallized polypropylene film by modeling of the broadening emission lines of

aluminum emitted by plasma discharge," *Journal of Applied Physics*, vol. 97, no. 5, p. 053304, 2005.

[118] J. Kammermaier, "Chemical Processes During Electrical Breakdown in an Organic Dielectric with Evaporated Thin Electrodes," *IEEE Transactions on Electrical Insulation*, vol. EI-22, no. 2, pp. 145–149, 1987.

[119] S. Qin, S. Ma, and S. A. Boggs, "The mechanism of clearing in metalized film capacitors," in *Conference Record of IEEE International Symposium on Electrical Insulation*, pp. 592–595, 2012.

[120] J. Tortai, A. Denat, and N. Bonifaci, "Predominance of joule heating effect on the electrode destruction due to a self-healing of a metallized film," in *2000 Annual Report Conference on Electrical Insulation and Dielectric Phenomena (Cat. No.00CH37132)*, vol. 2, pp. 674–677, 2000.

[121] V. O. Bel'ko, P. N. Bondarenko, and O. A. Emel'yanov, "The dynamic characteristics of self-healing processes in metal film capacitors," *Russian Electrical Engineering*, vol. 78, no. 3, pp. 138–142, 2007.

[122] J. Kammermaier, G. Rittmayer, and S. Birkle, "Modeling of plasma-induced self-healing in organic dielectrics," *Journal of Applied Physics*, vol. 66, no. 4, pp. 1594–1609, 1989.

[123] Y. Chen, H. Li, F. Lin, F. Lv, M. Zhang, Z. Li, and D. Liu, "Study on self-healing and lifetime characteristics of metallized-film capacitor under high electric field," *IEEE Transactions on Plasma Science*, vol. 40, no. 8, pp. 2014–2019, 2012.

[124] J. H. Tortai, A. Denat, and N. Bonifaci, "Self-healing of capacitors with metalized film technology: Experimental observations and theoretical model," *Journal of Electrostatics*, vol. 53, no. 2, pp. 159–169, 2001.

[125] S. Tandon, *Modeling of Stresses in Cylindrically Wound Capacitors: Characterization and the Influence of Stress on Dielectric Breakdown of Polymer Film*. Phd thesis, University of Massachusetts, 1997.

[126] N. Klein, "Electrical Breakdown in Solids," *Advances in Electronics and Electron Physics*, vol. 26, pp. 309–424, 1969.

[127] N. Klein, "The mechanism of self-healing electrical breakdown in MOS structures," *IEEE Transactions on Electron Devices*, vol. ED-13, no. 11, pp. 788–805, 1966.

[128] N. Klein, "ac Electrical Breakdown in Thin Silicon Oxide Films," *Journal of Applied Physics*, vol. 38, no. 9, p. 3721, 1967.

[129] N. Klein and E. Burstein, "Electrical pulse breakdown of silicon oxide films," *Journal of Applied Physics*, vol. 40, no. 7, pp. 2728–2740, 1969.

[130] R. Bartnikas, "High Voltage Measurements," in *Engineering Dielectrics Volume 2B - Electrical Properties of Solid Insulating Materials: Measurement Techniques* (R. Bartnikas, ed.), pp. 157–220, Philadelphia: ASTM International, 1987.

[131] N. Klein and H. Gafni, "The maximum dielectric strength of thin silicon oxide films," *IEEE Transactions on Electron Devices*, vol. ED-13, no. 2, pp. 281–289, 1966.

[132] Y. Inuishi and D. A. Powers, "Electric breakdown and conduction through mylar films," *Journal of Applied Physics*, vol. 28, no. 9, pp. 1017–1022, 1957.

[133] S. M. Rowland, R. M. Hill, and L. A. Dissado, "Censored Weibull statistics in the dielectric breakdown of thin oxide films," *Journal of Physics C: Solid State Physics*, vol. 19, no. 31, pp. 6263–6285, 1986.

[134] S. Haywood, M. Heyns, and R. De Keersmaecker, "The statistics of dielectric

breakdown in MOS capacitors under static and dynamic voltage stress," *Applied Surface Science*, vol. 30, no. 1-4, pp. 325–332, 1987.

[135] J. Suñé, I. Placencia, N. Barniol, E. Farrés, F. Martín, and X. Aymerich, "On the breakdown statistics of very thin SiO2 films," *Thin Solid Films*, vol. 185, no. 2, pp. 347–362, 1990.

[136] Z. Zhou, M. MacKey, J. Carr, L. Zhu, L. Flandin, and E. Baer, "Multilayered polycarbonate/poly(vinylidene fluoride-co-hexafluoropropylene) for high energy density capacitors with enhanced lifetime," *Journal of Polymer Science, Part B: Polymer Physics*, vol. 50, no. 14, pp. 993–1003, 2012.

[137] R. M. Hill and L. A. Dissado, "Examination of the statistics of dielectric breakdown," *Journal of Physics C: Solid State Physics*, vol. 16, no. 22, pp. 4447–4468, 1983.

[138] L. Capt, S. Rettenberger, H. Münstedt, and M. R. Kamal, "Simultaneous biaxial deformation behavior of isotactic polypropylene films," *Polymer Engineering And Science*, vol. 43, no. 7, pp. 1428–1441, 2003.

[139] L. Dissado, J. Fothergill, S. Wolfe, and R. Hill, "Weibull Statistics in Dielectric Breakdown; Theoretical Basis, Applications and Implications," *IEEE Transactions on Electrical Insulation*, vol. EI-19, no. 3, pp. 227–233, 1984.

[140] P. Fischer and K. Nissen, "The Short-Time Electric Breakdown Behavior of Polyethylene," *IEEE Transactions on Electrical Insulation*, vol. EI-11, no. 2, pp. 37–40, 1976.

[141] M. Cacciari and A. Contin, "Use of a mixed-Weibull distribution for the identification of PD phenomena," *IEEE Transactions on Dielectrics and Electrical Insulation*, vol. 2, no. 6, pp. 1166–1179, 1995.

[142] H. Rinne, *The Weibull Distribution: A Handbook*. Chapman and Hall/CRC, 2008.

[143] M. Takala, M. Karttunen, P. Salovaara, S. Kortet, K. Kannus, and T. Kalliohaka, "Dielectric properties of nanostructured polypropylene-polyhedral oligomeric silsesquioxane compounds," *IEEE Transactions on Dielectrics and Electrical Insulation*, vol. 15, no. 1, pp. 40–50, 2008.

[144] O. A. Emel'yanov, "Electrodynamic thermal breakdown of a capacitor insulator," *Technical Physics*, vol. 56, no. 11, pp. 1685–1688, 2011.

[145] M. Ritamäki, I. Rytöluoto, and K. Lahti, "Temperature Effect on Breakdown Performance of Insulating Polymer Thin Films," in *24th Nordic Insulation Symposium (NORD-IS 15)*, (Copenhagen, Denmark), pp. 75–79, 2015.

[146] D. N. P. Murthy, M. Xie, and R. Jiang, *Weibull Models*. Hoboken: John Wiley & Sons, 2003.

[147] J. Suñé and E. Y. Wu, "Statistics of successive breakdown events in gate oxides," *IEEE Electron Device Letters*, vol. 24, no. 4, pp. 272–274, 2003.

[148] J. Suñé and E. Y. Wu, "Statistics of successive breakdown events for ultra-thin gate oxides," in *Electron Devices Meeting, 2002. IEDM '02. International*, (San Francisco, CA, USA), pp. 147–150, 2003.

[149] J. Suné, E. Y. Wu, and W. L. Lai, "Successive oxide breakdown statistics: Correlation effects, reliability methodologies, and their limits," *IEEE Transactions on Electron Devices*, vol. 51, no. 10, pp. 1584–1592, 2004.

[150] R. A. Phillips and M. D. Wolkowicz, "Structure and Morphology," in *Polypropylene Handbook: Polymerization, Characterization, Properties, Applications* (E. P. Moore, ed.), pp. 113–176, Münich: Hanser Publishers, 1996.

[151] C. Maier and T. Calafut, *Polypropylene: The Definitive User's Guide and Databook*. Norwich: William Andrew Inc., 1998.

[152] L. Sperling, *Introduction to Physical Polymer Science*. Hoboken: John Wiley & Sons, Inc., 4th ed., 2005.

[153] P. Jacoby, *Beta Nucleation of Polypropylene: Properties, Technology, and Applications*. Waltham: William Andrew, PDL handbook series, 2013.

[154] S. Brückner and S. V. Meille, "Polymorphism in crystalline polypropylene," in *Polypropylene: An A-Z reference* (J. Karger-Kocsis, ed.), pp. 606–614, Springer Netherlands, 1999.

[155] J. Breil, "Biaxial Oriented Film Technology," in *Film Processing Advances* (T. Kanai and G. A. Campbell, eds.), pp. 193–229, Münich: Hanser, 2014.

[156] L. Capt, *Simultaneous biaxial stretching of isotactic polypropylene films in the partly molten state*. Phd thesis, McGill University, 2003.

[157] C. X. C. Xu and S. Boggs, "Measurement of resistive and absorption currents in capacitor films up to breakdown," in *Conference Record of the 2006 IEEE International Symposium on Electrical Insulation*, pp. 249–252, 2006.

[158] A. T. Jones, J. M. Aizlewood, and D. R. Beckett, "Crystalline forms of isotactic polypropylene," *Die Makromolekulare Chemie*, vol. 75, no. 1, pp. 134–158, 1964.

[159] M. Araoka, H. Yoneda, and Y. Ohki, "Dielectric breakdown of new type polymerized polyethylene using a single-site catalyst," *IEEE Transactions on Dielectrics and Electrical Insulation*, vol. 6, no. 3, pp. 326–330, 1999.

[160] S. N. Kolesov, "The Influence of Morphology on the Electric Strength of Polymer Insulation," *IEEE Transactions on Electrical Insulation*, vol. EI-15, no. 5, pp. 382–388, 1980.

[161] D. W. Kim, K. Yoshino, T. Inoue, M. Abe, and N. Uchikawa, "Influence of morphology on electrical properties of syndiotactic polypropylene compared with those of isotactic polypropylene," *Japanese Journal of Applied Physics*, vol. 38, no. 1, pp. 3580–3584, 1999.

[162] S. Diaham, M. Bechara, M.-L. Locatelli, R. Khazaka, C. Tenailleau, and R. Kumar, "Dielectric strength of parylene HT," *Journal of Applied Physics*, vol. 115, no. 5, p. 054102, 2014.

[163] T. Lüpke, S. Dunger, J. Sänze, and H. J. Radusch, "Sequential biaxial drawing of polypropylene films," *Polymer*, vol. 45, no. 20, pp. 6861–6872, 2004.

[164] H. Y. Nie, M. J. Walzak, and N. S. McIntyre, "Draw-ratio-dependent morphology of biaxially oriented polypropylene films as determined by atomic force microscopy," *Polymer*, vol. 41, no. 6, pp. 2213–2218, 2000.

[165] L. Gao, D. Tu, S. Zhou, and Z. Zhang, "The influence of morphology on the electrical breakdown strength of polypropylene film," *IEEE Transactions on Electrical Insulation*, vol. 25, no. 3, pp. 535–540, 1990.

[166] L. Capt, M. R. Kamal, H. Mündstedt, K. Stopperka, and J. Sänze, "Morphology Development during Biaxial Stretching of Polypropylene Films," in *17th Polymer Processing Society Annual Meeting*, pp. 1–9, 2001.

[167] M. Xu, S. Zhang, J. Liang, H. Quan, J. Liu, H. Shi, D. Gao, and J. Liu, "Influences of processing on the phase transition and crystallization of polypropylene cast films," *Journal of Applied Polymer Science*, vol. 131, no. 22, p. 41100, 2014.

[168] S. Tamura, K. Ohta, and T. Kanai, "Study of crater structure formation on the

surface of biaxially oriented polypropylene film," *Journal of Applied Polymer Science*, vol. 124, no. 4, pp. 2725–2735, 2012.

[169] F. Chu, T. Yamaoka, H. Ide, and Y. Kimura, "Microvoid formation process during the plastic deformation of β-form polypropylene," *Polymer*, vol. 35, no. 16, pp. 3442–3448, 1994.

[170] F. Chu, T. Yamaoka, and Y. Kimura, "Crystal transformation and micropore formation during uniaxial drawing of β-form polypropylene film," *Polymer*, vol. 36, no. 13, pp. 2523–2530, 1995.

[171] Z. H. Z. Hui, X. H. X. Hengkun, and L. Z. L. Ziyu, "Morphology and electrical breakdown of polypropylene," in *Proceedings of the 3rd International Conference on Properties and Applications of Dielectric Materials*, pp. 1161–1164, 1991.

[172] K. Wu, T. Okamoto, and Y. Suzuoki, "Simulation study on the correlation between morphology and electrical breakdown in polyethylene," *Journal of Applied Physics*, vol. 98, no. 11, pp. 1–5, 2005.

[173] S. Tamura, K. Takino, T. Yamada, and T. Kanai, "Crater formation mechanism on the surface of a biaxially oriented polypropylene film," *Journal of Applied Polymer Science*, vol. 126, no. S2, pp. 449–456, 2012.

[174] C. Zhang, T. Mori, T. Mizutani, M. Ishioka, and Y. Cheng, "Morphology and electrical breakdown properties of LDPE-polypropylene copolymer blends," *Journal of Polymer Science, Part B: Polymer Physics*, vol. 39, no. 15, pp. 1741–1748, 2001.

[175] K. Yahagi, "Dielectric Properties and Morphology in Polyethylene," *IEEE Transactions on Electrical Insulation*, vol. EI-15, no. 3, pp. 241–250, 1980.

[176] M. G. Danikas, "Comments, with reply, on 'Dependence of the electric strength on' thickness area and volume of polypropylene' by S. Cygan and J. R. Laghari," *IEEE Transactions on Electrical Insulation*, vol. 25, no. 4, pp. 762–763, 1990.

[177] B. Helgee and P. Bjellheim, "Electric breakdown strength of aromatic polymers: Dependence on film thickness and chemical structure," *IEEE transactions on electrical insulation*, vol. 26, no. 6, pp. 1147–1152, 1991.

[178] G. Chen, J. Zhao, S. Li, and L. Zhong, "Origin of thickness dependent dc electrical breakdown in dielectrics," *Applied Physics Letters*, vol. 100, no. 22, p. 222904, 2012.

[179] F. Mitsuyoushi, "Processing-induced morphology," in *Polypropylene: An A-Z reference* (J. Karger-Kocsis, ed.), pp. 668–677, Springer Netherlands, 1999.

[180] T. Umemura, T. Suzuki, and T. Kashiwazaki, "Impurity Effect of the Dielectric Properties of Isotactic Polypropylene," *IEEE Transactions on Electrical Insulation*, vol. EI-17, no. 4, pp. 300–305, 1982.

[181] A. Schneuwly, P. Gröning, L. Schlapbach, C. Irrgang, and J. Vogt, "Breakdown behavior of oil-impregnated polypropylene as dielectric in film capacitors," *IEEE Transactions on Dielectrics and Electrical Insulation*, vol. 5, no. 6, pp. 862–868, 1998.

[182] B. Peng, F. Lin, H. Li, Y. Chen, M. Zhang, and F. Lv, "Calculation and measurement of metalized film capacitor's inner pressure and its influence on self-healing characteristics," *IEEE Transactions on Dielectrics and Electrical Insulation*, vol. 17, no. 1, pp. 1612–1618, 2010.

[183] Y. Chen, H. Li, F. Lin, F. Lv, Z. Li, and M. Zhang, "Effect of interlayer air on performance of dry-type metalized film capacitor in DC, AC and pulsed applications," *IEEE Transactions on Dielectrics and Electrical Insulation*, vol. 18, no. 4, pp. 1301–

1306, 2011.

[184] C. Park, M. Hara, and M. Akazaki, "Effects of Temperature and Voltage on Dielectric Breakdown Strengths of PET and FRP under Mechanical Stresses," *IEEE Transactions on Electrical Insulation*, vol. EI-17, no. 6, pp. 546–553, 1982.

[185] C. H. Park, D. J. Kwak, and M. Hara, "Some Dielectric and Mechanical Properties of Heat Treated Biaxially Drawn Pet Films," *IEEE Transactions on Electrical Insulation*, vol. EI-20, no. 3, pp. 567–573, 1985.

[186] N. Zebouchi, R. Essolbi, D. Malec, H. T. Giam, B. Ai, and M. Bendaoud, "Electrical breakdown of polyethylene terephthalate under hydrostatic pressure," *Journal of Applied Physics*, vol. 76, no. 12, pp. 8218–8220, 1994.

[187] V. A. Zakrevskii, N. T. Sudar, A. Zaopo, and Y. A. Dubitsky, "Mechanism of electrical degradation and breakdown of insulating polymers," *Journal of Applied Physics*, vol. 93, no. 4, pp. 2135–2139, 2003.

[188] S. Tandon and R. J. Farris, "Metalized Polypropylene Film in Capacitors: Characterization and The Effect of Interfacial Pressure on the Dielectric Strength," in *MRS Proceedings*, pp. 147–153, 1997.

[189] M. Tolinski, *Additives for Polyolefins - Getting the Most out of Polypropylene, Polyethylene and TPO*. Elsevier Inc., 1st ed., 2009.

[190] H. S. Khare and D. L. Burris, "A quantitative method for measuring nanocomposite dispersion," *Polymer*, vol. 51, no. 3, pp. 719–729, 2010.

[191] J. Ye, H. S. Khare, and D. L. Burris, "Quantitative characterization of solid lubricant transfer film quality," *Wear*, vol. 316, no. 1-2, pp. 133–143, 2014.

[192] C. D. Green, A. S. Vaughan, G. R. Mitchell, and T. Liu, "Structure property relationships in polyethylene/montmorillonite nanodielectrics," *IEEE Transactions on Dielectrics and Electrical Insulation*, vol. 15, no. 1, pp. 134–143, 2008.

[193] S. Nawaz, P. Nordell, H. Hillborg, and U. W. Gedde, "Antioxidant activity in aluminium oxide - Poly(ethylene-co-butyl acrylate) nanocomposites," *Polymer Degradation and Stability*, vol. 97, no. 6, pp. 1017–1025, 2012.

[194] J. Chen, M. S. Yang, and S. M. Zhang, "Immobilization of antioxidant on nanosilica and the aging resistance behavior in polypropylene," *Composites Part A: Applied Science and Manufacturing*, vol. 42, no. 5, pp. 471–477, 2011.

[195] X. Gao, X. Meng, H. Wang, B. Wen, Y. Ding, S. Zhang, and M. Yang, "Antioxidant behaviour of a nanosilica-immobilized antioxidant in polypropylene," *Polymer Degradation and Stability*, vol. 93, no. 8, pp. 1467–1471, 2008.

[196] A. Pustak, P. Irina, M. Denac, I. Svab, J. Pohleven, V. Musil, and I. Smit, "Morphology of polypropylene/silica nano- and microcomposites," *Journal of Applied Polymer Science*, vol. 128, no. 5, pp. 3099–3106, 2013.

[197] M. Ritamäki, I. Rytöluoto, K. Lahti, and M. Karttunen, "Effects of Thermal Aging on the Characteristic Breakdown Behavior of Nano-SiO2-BOPP and BOPP Films," in *2015 IEEE 11th International Conference on the Properties and Applications of Dielectric Materials (ICPADM)*, 2015.

[198] M. Ritamäki, *Effects of thermal aging on polymer thin film insulations for capacitor applications*. Master's thesis, Tampere University of Technology, 2014.

Appendix A

Laboratory setup and data treatment

Figure A.1 presents photographs of sample capacitor assembly and multi-breakdown measurement in atmospheric air and in insulating oil. Figure A.2 presents a photograph of the test setup used for large-area multi-breakdown measurements. A more specific description of the utilized equipment and components is given in Chapter 3.

Figures A.3 and A.4 exemplify the MATLAB programs used for data treatment and analysis. The general steps of the large-area multi-breakdown data treatment and analysis are as follows:

1. Split sequential raw oscilloscope data into individual discharge events (discharge current and test capacitor voltage) and determine breakdown voltage E_{bd}, peak current I_{peak}, discharge energy E_{sh} and various pulse time parameters. The GUI-based MATLAB program used for carrying out the above process is exemplified in Figure A.3.

2. For a data set comprising of discharge event data of n sample films; append trigger time information to each discharge event and determine breakdown fields based on either (i) average sample film thickness or (ii) event-by-event manual thickness.

3. Perform data qualification process for the above data set in accordance with sub-chapter 3.2.3. The GUI-based MATLAB program enabling easy visualization and control of the data qualification process is exemplified in Figure A.4.

4. Perform statistical analysis for the qualified breakdown data (Weibull++ and/or MATLAB software).

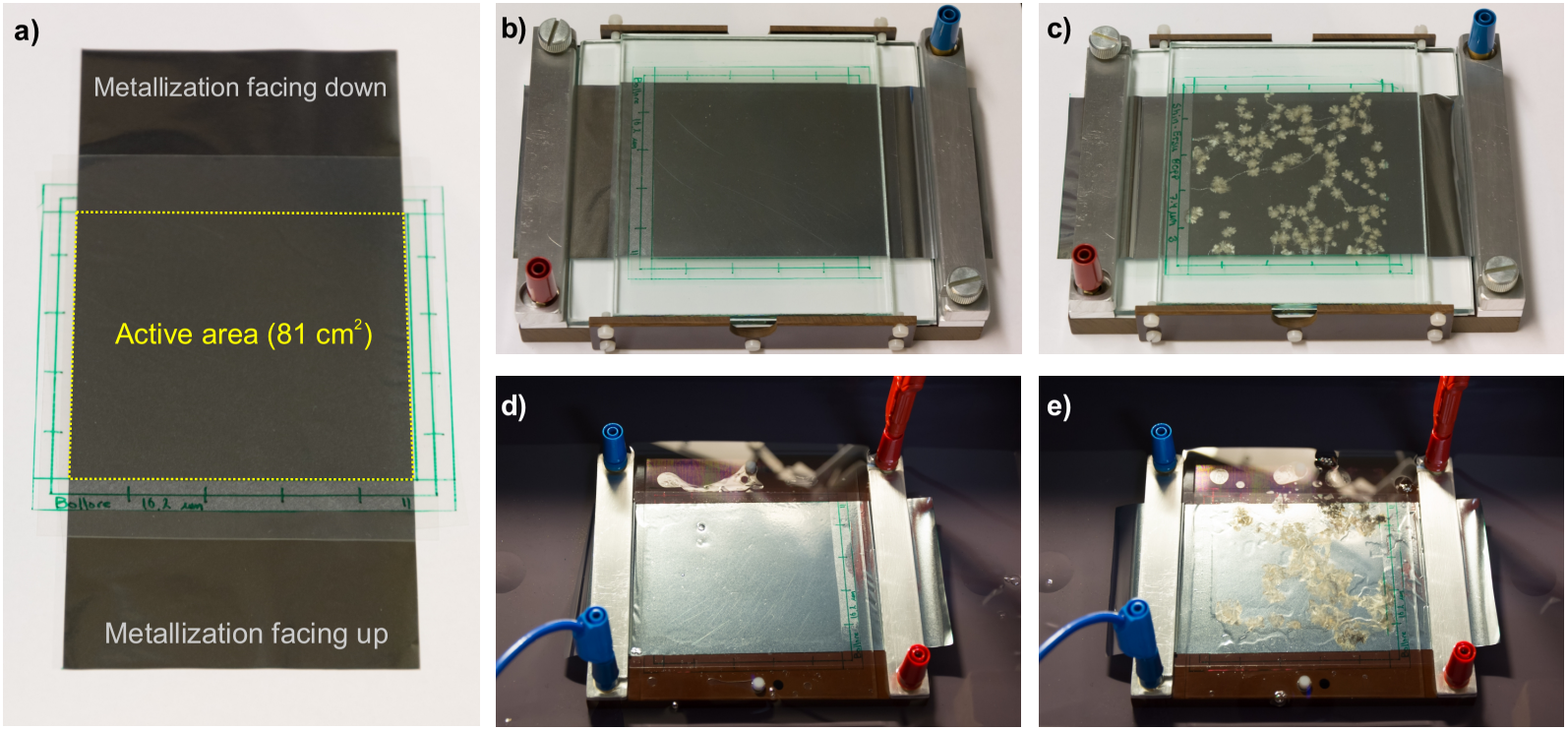

Figure A.1. Photographs of sample capacitor assembly and multi-breakdown measurement. **a)** shows an assembled test sample ready for multi-breakdown measurement ($A = 81\,\mathrm{cm}^2$. **b)** & **c)** show a test capacitor before (b) and after (c) multi-breakdown measurement in atmospheric air. **d)** & **e)** show a test capacitor before (d) and after (e) multi-breakdown measurement in insulating oil.

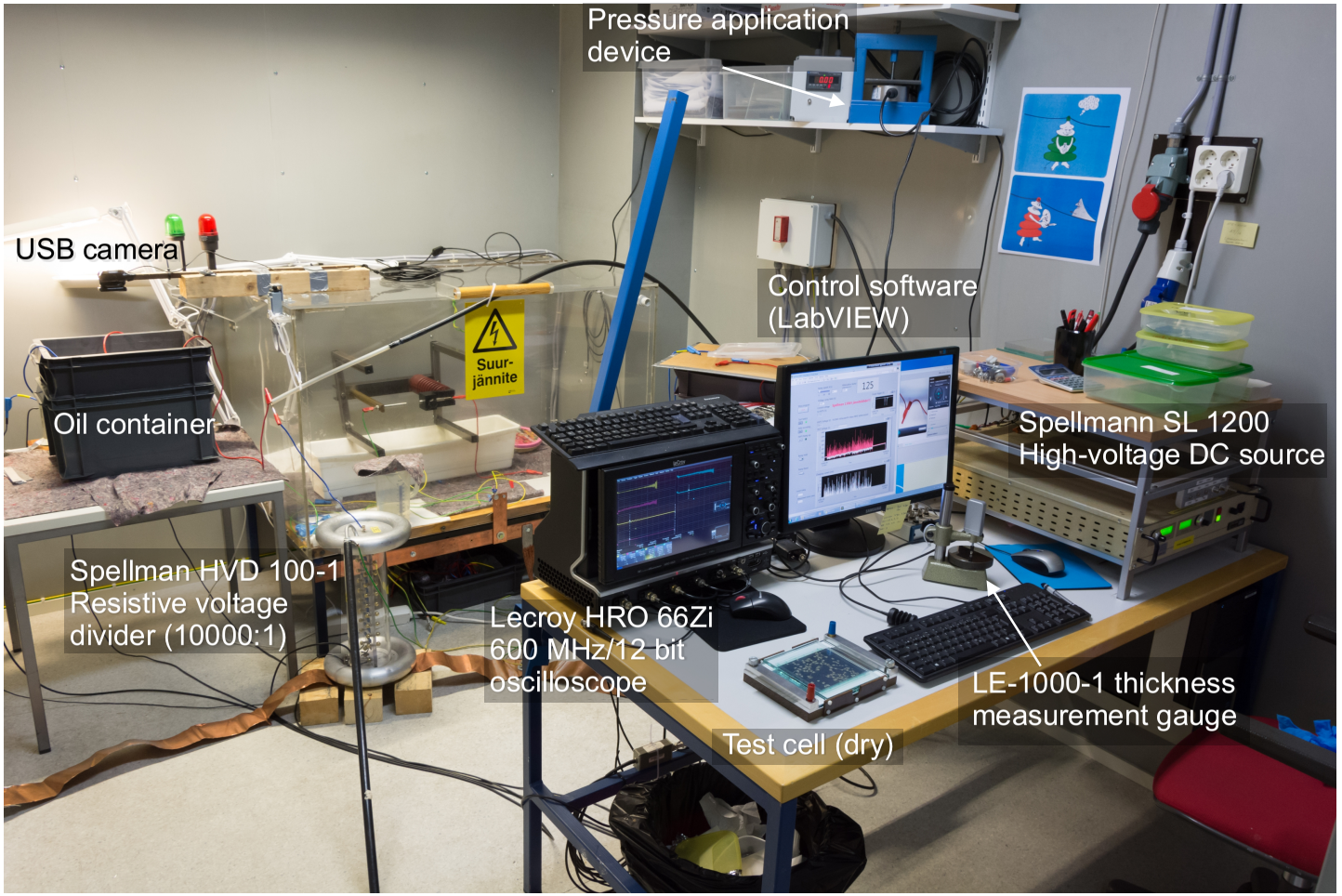

Figure A.2. Measurement setup used for large-area multi-breakdown measurements. The impulse current measurement resistor and the high-voltage probes used for measuring the discharge current and the test capacitor voltage, respectively, are not shown. See Chapter 3 for further information.

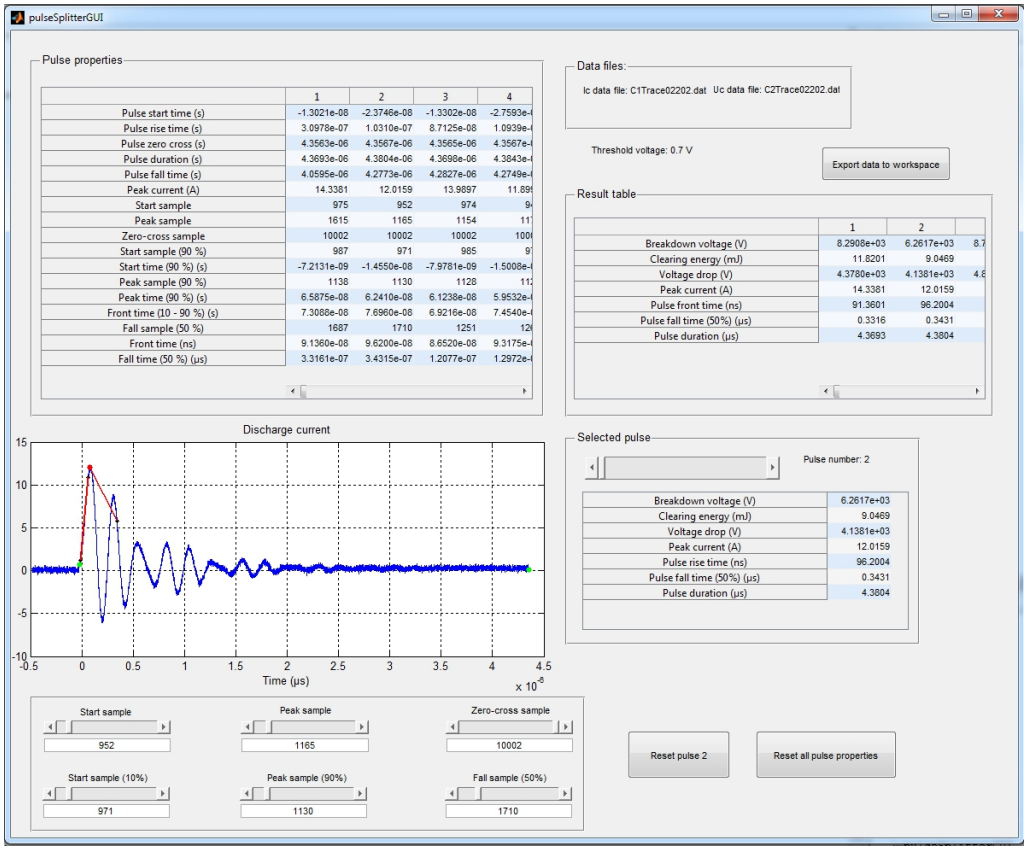

Figure A.3. MATLAB program for sequential oscilloscope data treatment and analysis. The program imports raw sequential data from the oscilloscope (test capacitor and discharge current), splits the data into individual events, and determines various properties such as breakdown voltage, discharge energy, voltage drop, peak current and various pulse time parameters. The user can visualize each discharge event individually and adjust the time parameters if necessary.

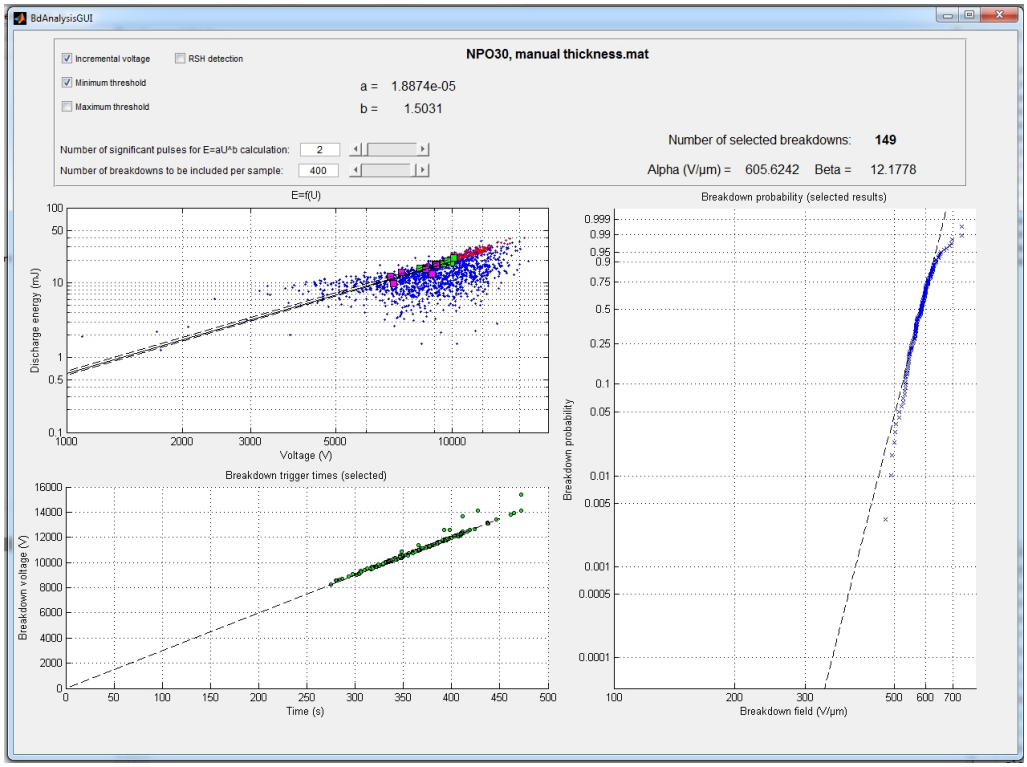

Figure A.4. MATLAB program for performing breakdown data qualification prior to statistical analysis. The program imports a material data set (comprising of individual discharge event data from multiple sample films) and carries out the data qualification process described in Chapter 3. The user can determine which selection criteria are utilized and how the data is utilized (e.g. how many discharge events are considered from each sample). The top-left sub-figure shows the discharge energy–breakdown voltage characteristics ($E_{sh} = aU^b$) while the bottom-left sub-figure shows the breakdown voltage–time dependence (assuming $30\,\mathrm{V\,s^{-1}}$ voltage ramp rate). The right-hand sub-figure shows the resulting breakdown distribution on the Weibull probability scale.

Appendix B

Monte Carlo simulation scheme and additional results

B.1 Description of the Monte Carlo simulation scheme

The fundamental differences between the large-area multi-breakdown and the small-area single-breakdown measurement methods and the statistical aspects thereof were analyzed by the Monte Carlo simulation method in MATLAB. For each simulated case, 10000 iterations were calculated in order assure high statistical significance. The simulation scheme is detailed in the following.

During each Monte Carlo simulation iteration, the program generated random numbers from the chosen theoretical Weibull distribution $F(x)$ and reshaped the data to a $m \times n$ -sized matrix to represent a film area with user-specified dimensions. Thus, as each element of the matrix represented a small section of the simulated total film area, the size of the data matrix essentially defined the resolution of the simulation (e.g. $1\,\mathrm{cm}^2$ or $1\,\mathrm{mm}^2$ per each element). Weibull area-scaling, Equation (3.6), was used accordingly to increase or decrease the base resolution of the theoretical distribution $F(x)$. For the simulation scenarios presented in sub-chapter 3.4, a total film area of $2500\,\mathrm{cm}^2$ was simulated. In order to simulate breakdown measurement, n randomly oriented $j \times k$ -sized sub-matrices (or film samples) were then selected from the simulated film area at random locations; thus, by varying the sample dimensions and quantity the area-effect could be studied. The elements of the sub-matrices (samples) were then treated in accordance with one of the following procedures:

1. Only the weakest point of each sub-matrix was considered (single-breakdown measurement).

2. All the elements of the sub-matrices were considered (multi-breakdown measurement).

3. The elements of the sub-matrices were considered in a bottom-up manner, taking into account the self-segmentation effect (multi-breakdown measurement).

The self-segmentation effect was simulated as follows. For each randomly chosen sub-matrix (sample), the elements were considered one by one in a bottom-up manner. With each selection of an element, a $j \times k$ -sized area (or de-metallized area A_{sh}) was removed around the chosen element to simulate self-healing breakdown, see Figure 3.17b for a graphical representation. After each simulated self-healing breakdown, the connectivity of the remaining active sample area was identified by using `bwconncomp` function in MATLAB; this allowed identification and exclusion of isolated film areas for which the connection to the left- and right-hand sample boundaries simulating electrical contact edges were lost. Thus, as sections of the remaining sample area were gradually isolated from the rest of the active area, the sample distribution was essentially restricted to a smaller range (right-truncation).

The resulting sample distribution was compared against the true distribution representing the whole simulated surface. The true distribution was represented either at (i) the base resolution of $F(x)$ or, if self-segmentation was studied, (ii) as $F(x)$ measured with $j \times k$ -sized active area. Non-parametric two-sample Kolmogorov-Smirnov (K-S) test was performed at $\alpha = 5\,\%$ significance level to compare the sample distribution against the true distribution during each iteration, with the null hypothesis H_0 that the two were from the same population [109]. Moreover, single 2-p Weibull distributions were fit to the distributions and the Weibull parameters were analyzed.

B.2 Small-area single-breakdown measurement: Area effect

Effect of active measurement area on the small-area single-breakdown measurement method was studied in more detail. In accordance with sub-chapter 3.4 and Equation (3.5), a 2500 cm^2 total film area was simulated at a base resolution of 1 mm^2. A series of Monte Carlo simulations were carried out to study the electrode areas of 0.25, 1, 4, 9 and 16 cm^2. In each case 20 film samples were randomly chosen from the simulated area and only the weakest point of each sample was considered. Single 2-p Weibull distributions were fitted to the selected breakdowns during each Monte Carlo iteration.

Figures B.1a–b present the single 2-p Weibull α and β parameter distributions as a function of electrode area, respectively. The area-effect is evident from Figure B.1a, with an increasing active area resulting in lower Weibull α parameter in accordance with Equation (3.6) (dashed line). The slight decrease in Weibull β values with increasing active area is also notable in Figure B.1b. Overall, the results area in line with [P1, P5] (see e.g. Figure 3.14) and [26, 39, 115].

B.3 Large-area multi-breakdown measurement: Self-segmentation effect

Effect of self-segmentation and de-metallized area on the large-area multi-breakdown measurement method was studied in more detail. In accordance with sub-chapter 3.4 and Equation (3.5), a 2500 cm^2 total film area was simulated at a base resolution of 1 mm^2. During each iteration, 6 multi-breakdown samples with 81 cm^2 area were randomly chosen from the simulated area. A series of Monte Carlo simulations were carried out to study the multi-breakdown behavior as a function of de-metallized area A_{sh}. De-metallized areas of 9, 25, 49, 81, 121, 169 and 225 mm^2 were simulated. The selected breakdowns from each sample film were considered as a single breakdown data set, in accordance with Chapter 3. Single 2-p Weibull distributions were fitted to the selected breakdowns during each Monte Carlo iteration.

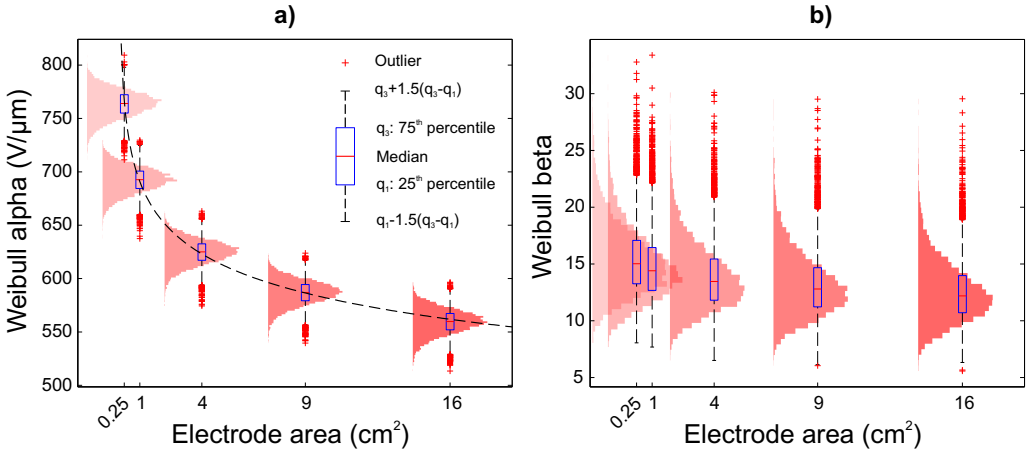

Figure B.1. Monte Carlo simulation of the effect of active area on the small-area single-breakdown measurement. The box plots and the underlying data histograms present the 2-p Weibull **a)** α and **b)** β parameter distributions as a function of electrode area. 10000 Monte Carlo iterations were calculated per each active area; during each iteration, 20 single-breakdown samples were randomly selected from the 2500 cm^2 simulated area. In a), the dashed power fit line is the Weibull area scaling law, Equation (3.6).

Figure B.2a presents a representative comparison of the multi-breakdown distribution and the true distribution after 10000 Monte Carlo iterations when the de-metallized area was 25 mm^2. The right-truncation of the multi-breakdown distribution is evident from Figure B.2a, as already discussed in sub-chapter 3.4. It however notable that the right-truncation is "soft", i.e., the truncation is not as discrete as suggested by Equation (3.8). This is understandable though, as the right-truncation point of each sample film is not constant, but rather there is a distribution of right-truncation points attributable to the random nature of the self-segmentation effect as shown in Figure B.2b.

Figures B.2c–d present the single 2-p Weibull α and β parameter distributions as a function of de-metallized area, respectively. It is noted here that the amount of breakdowns measurable from each sample naturally decreased with increasing de-metallized area. The connection between the de-metallized area and the "resolution" of the multi-breakdown measurement is evident Figures B.2c; with increasing de-metallized area the 2-p Weibull α parameters tend to decrease due to the self-segmentation effect. It is also notable that with increasing de-metallized area the calculated Weibull α values scale according to the Weibull area scaling (see the solid blue power fit in Figure B.2c), however, with a slightly higher Weibull area scaling exponent $-1/\beta$ (see Equation (3.6)) than in the case of area scaling of the true distribution (dashed line in Figure B.2c). The slight decrease in Weibull β values is seemingly related to the decreasing number of breakdowns obtainable with multi-breakdown method with increasing de-metallized area.

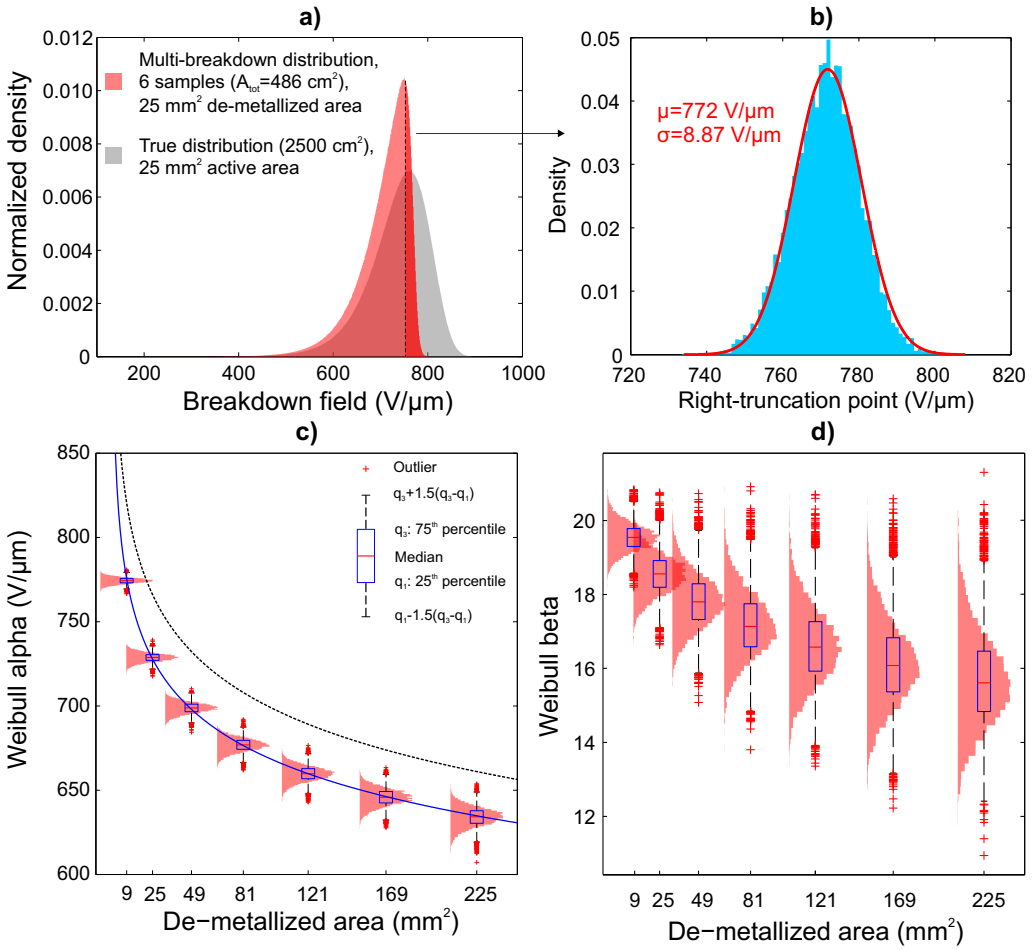

Figure B.2. Monte Carlo simulation of the effect of de-metallized area on the large-area multi-breakdown measurement. 10000 iterations were calculated per each active area; during each iteration, 6 multi-breakdown samples were randomly selected from the 2500 cm^2 simulated area. **a)** Representative comparison of the multi-breakdown distribution and the true distribution after 10000 Monte Carlo iterations when the de-metallized area was 25 mm^2. The histogram densities are normalized to 1. **b)** Distribution of the right-truncation points when de-metallized area was 25 mm^2. The parameters of the normal distribution fit (solid red line, correlation coefficient $\rho = 99.96\,\%$) are given in the figure. In **c)** and **d)** the box plots and the underlying data histograms present the 2-p Weibull α and β parameter distributions as a function of de-metallized area, respectively. In c), the solid line is the power fit to the median values of the Weibull α parameter distributions. The dashed line represents the ideal area-scaling of the true distribution.

Appendix C

iPP-based cast-, BOPP and PNC-film breakdown results

Table C.1. Sample film details and large-area multi-breakdown results. Mean sample film thicknesses and the corresponding standard deviations represent the 486 cm^2 total film area (6 sample films). k_β is the initial cast film β-crystallinity determined from the WAXS profiles. $E_{5\%}$, $E_{63.2\%}$ and $E_{95\%}$ are the calculated electric field values at 5, 63.2 and 95 % breakdown probabilities, respectively. The weakest point ($E_{\min}$) is the lowest breakdown field measured from the total film area. N_q denotes the number of qualified breakdowns after the data selection procedure.

Code	Film thickness (µm)		k_β (%)	N_q	Breakdown field (V µm^{-1})			
	Mean	SD			$E_{\min}$	$E_{5\%}$	$E_{63.2\%}$	$E_{95\%}$
PP1-A-500-5.6	15.58	1.02	15	91	495	566	680	728
PP1-B-400-5.6	12.54	0.61	24	213	98	317	466	537
PP1-C-400-5.6	13.36	1.25	13	131	106	360	699	765
PP1-C-200-3.5	13.37	0.50	9	122	529	621	754	810
PP1-C-15	14.92	0.58	1	80	102	232	342	395
PP1-C-20	20.62	0.60	3	82	211	245	350	398
PP2-A-500-5.6	15.21	0.87	26	124	366	493	622	678
PP2-B-400-5.6	12.05	0.62	34	164	263	334	450	554
PP2-C-400-5.6	12.62	1.16	15	135	193	428	623	741
PP2-C-200-3.5	12.32	0.63	10	126	522	642	753	798
PP2-C-15	15.03	0.51	1	42	210	258	364	413
PP2-C-20	20.57	0.79	2	60	234	281	375	418

Table C.2. Onset electric field strengths of the propagating-type breakdown process in the PP cast film samples. The onset fields were read from the general voltage monitoring data recorded in LabVIEW. Single 2-p Weibull distributions along with mean and standard deviation (normal distribution) are given. N denotes the number of data points.

Code	N	Propagating-type breakdown process			
		Weibull α (V µm^{-1})	Weibull β	Mean (V µm^{-1})	SD (V µm^{-1})
PP1-C-15	6	364	14.46	351	29
PP1-C-20	6	386	16.73	374	29
PP2-C-15	6	364	8.56	344	46
PP2-C-20	6	406	11.28	390	32

Table C.3. Large-area multi-breakdown results of the commercial capacitor-grade BOPP films (manufacturers A, B, C and D). Breakdown measurements were made either in insulating oil or in atmospheric air (dry). d_n is the nominal thickness given by the film manufacturer. N is the number of sample films, A is the active area, A_{total} is the resulting total measured film area, N_q is the number of qualified breakdowns, E_{min} is the weakest measured point and $E_{5\%}$, $E_{63.2\%}$ and $E_{95\%}$ are the 5%, 63.2% and 95% breakdown percentiles.

Code	d_n (µm)	Oil/dry	N	A (cm^2)	A_{total} (cm^2)	N_q	Breakdown field (V µm^{-1})			
							E_{min}	$E_{5\%}$	$E_{63.2\%}$	$E_{95\%}$
A-1	4.8	Dry	10	58	580	389	260	558	730	942
A-2	6.0	Dry	25	42	1050	679	199	528	695	798
A-3	9.0	Oil	10	38	380	124	354	570	758	844
A-4	12.0	Dry	25	24	600	287	279	557	731	793
A-5	13.8	Oil	6	81	486	133	316	494	691	739
A-6	14.4	Oil	12	81	972	280	415	499	619	669
A-7	9.0	Oil	10	81	810	197	161	392	656	713
B-1	9.0	Dry	10	81	810	283	234	437	661	739
B-2	10.1	Oil	10	81	810	253	131	432	678	737
B-3	16.2	Oil	10	81	810	154	437	490	660	690
C-1	7.4	Dry	10	81	810	229	123	390	614	716
C-2	8.3	Dry	10	81	810	172	159	267	572	652
D-1	4.0	Dry	10	16	160	182	348	467	706	822

Publications

Publication I

I. Rytöluoto and K. Lahti, "New approach to evaluate area-dependent breakdown characteristics of dielectric polymer films," *IEEE Transactions on Dielectrics and Electrical Insulation*, vol. 20, no. 3, pp. 937–946, 2013.

The following paper is the final version accepted for publication in IEEE Transactions on Dielectrics and Electrical Insulation. The published version of this paper is available at IEEE Xplore. DOI: 10.1109/TDEI.2013.6518963

New Approach to Evaluate Area-dependent Breakdown Characteristics of Dielectric Polymer Films

I. Rytöluoto and **K. Lahti**
Tampere University of Technology
Department of Electrical Engineering
P.O. Box 692
FI-33101 Tampere, Finland

ABSTRACT

A new dielectric breakdown measurement method for determining breakdown characteristics of polymer films has been developed and evaluated. The method is based on measurement of multiple breakdowns per sample area beyond the weakest point of the film by utilizing low-energy self-healing breakdown of metallized polymer film. A data selection process based on the discharge energy characteristics of each measured self-healing breakdown is utilized prior to the statistical analysis in order to validate the mutual independence of the results. Even with a relatively small sample area, the method yields a large amount of breakdown data from a wide voltage spectrum, thus enabling the formation of detailed material-specific breakdown fingerprints. The measurement system and the area dependence of the breakdown results have been evaluated with capacitor-grade metallized film. For the statistical analysis, additively mixed Weibull distributions are utilized as multiple breakdown mechanisms are found to be operative in the dielectric. Defects in the dielectric volume are found to have a profound effect on the structure of the mixed distribution with increasing area.

Index Terms — **Dielectric breakdown, metallized film, self-healing, statistical analysis, mixed Weibull distribution**

1 INTRODUCTION

BREAKDOWN strength measurement is a fundamental method for the evaluation of electrical insulation performance of dielectric polymer films. Analogous to the metaphor of the weakest link in the chain, dielectric breakdown strength is determined by the weakest points in the material volume and the measurement is typically realized as a short-term ramp-to-breakdown measurement [1-3]. Extreme-value statistics such as the Weibull distribution is typically then utilized for representing the gathered breakdown data [4]. In practice, a large amount of breakdown data is required though, as the knowledge of the breakdown strength at the low breakdown probability region with reasonably narrow confidence bounds is crucial e.g. for capacitor applications [5]. In return to this problem, various automatic breakdown strength measurement systems enabling convenient measurement of a large amount of breakdown data have been previously developed [6, 7].

However, in the absence of an automatic measurement system or a sufficient amount of sample material, the dielectric breakdown strength determined with only a small number of samples may be misleading, as the weakest points in the dielectric film may not be due to the inherent properties of the material itself but due to extrinsic factors such as defects, chemical impurities or voids in the material volume [1]. This may be crucial especially in the development phase of new dielectrics, and as in the case of nanodielectrics, poor material performance in terms of dielectric breakdown strength has been previously attributed to poor processing conditions and quality control during the manufacturing process [8]. Therefore, an alternative method for measuring dielectric breakdown characteristics beyond the weakest point of each sample film would provide a new insight into the true potential of the dielectric material.

On the other hand, prediction of large-area dielectric breakdown strength by extrapolation from a small-area empirical breakdown distribution has been shown to be problematic and experimental results contradictive with the area-scaling law have been previously presented [9, 10]. Theoretical studies based on field-assisted percolation model have shown that a small concentration of randomly distributed defects may cause deviation from a single Weibull distribution [11], implying that more sophisticated theoretical distributions and large-area breakdown measurement are required in order to achieve a reliable estimate of the breakdown strength for practical applications.

In the present work, a new dielectric breakdown measurement method for determining breakdown characteristics of polymer films is presented and evaluated. The method is based on measurement of multiple

Manuscript received on 24 January 2013, in final form 5 April 2013.

breakdowns per sample area beyond the weakest point of the film by utilizing low-energy self-healing breakdown of metallized polymer which minimizes the electrode loss during each self-healing breakdown. In order to validate the mutual independence of the results, a data selection procedure based on the self-healing discharge energy characteristics of each measured breakdown is utilized prior to further statistical analysis. Even with a relatively small sample area, the method yields a large amount of breakdown data from a wide voltage spectrum, thus enabling the formation of detailed material-specific breakdown fingerprints. The measurement system and the dependence of the breakdown results on the electrode area and total measured area have been evaluated with metallized bi-axially oriented polypropylene (BOPP) film. In addition to simple 2-parameter Weibull distributions, additively mixed Weibull distributions have been utilized for the statistical analysis, as the results strongly suggest the presence of multiple breakdown mechanisms in the dielectric.

2 THEORETICAL BACKGROUND

2.1 SELF-HEALING BREAKDOWN

Metallized film capacitors utilize dielectric films with thin metal electrodes evaporated directly on the film surface. This technology has a unique ability to undergo self-healing breakdown, a process which is shown schematically in Figure 1. When a breakdown occurs in the dielectric film, a portion of the stored energy is discharged through the breakdown channel, leading to a rapid increase in current density, temperature and pressure near the fault spot. As a consequence, a small area of the thin metallization layer surrounding the fault spot is vaporized (typically in the range of few mm^2), leading to the spontaneous isolation of the fault spot from the rest of the electrode and to the restoration of the insulation capability of the film. [12-14]

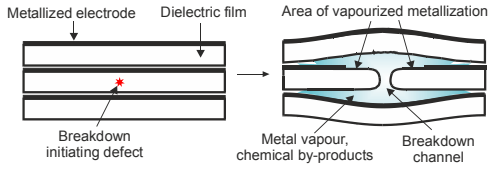

Figure 1. Self-healing breakdown of metallized polymer film.

Previous experimental investigations on the self-healing process suggest that the duration of the self-healing process, the peak value of the discharge current pulse and the area of the de-metallized layer may be characterized by the energy discharged during a self-healing breakdown [15-18]. Discharge energy E_{SH} has been shown to be a function of various parameters and it may be expressed conceptually as [14, 18]:

$$E_{SH} = \frac{kU^b C}{R_s^c \alpha(P)} = aU^b, \tag{1}$$

where U is the voltage, C is the capacitance, R_s is the metallization sheet resistance, $\alpha(P)$ is a function which relates the inter-layer pressure to the discharge energy and a, b, c and k are experimentally definable constants. An estimate for the coefficient b is often reported to be 4.7 although the coefficient may be rather varied from 2 up to 6 depending on aforementioned parameters [15]. For coefficient c, values in the range of 1.8 - 2 are often given in the literature [13, 16].

2.2 STATISTICAL ANALYSIS

The Weibull distribution belongs to the group of extreme-value distributions which are based on the principle that an extreme value, such as the weakest point in the dielectric, is the decisive factor for the operation of the whole system. The cumulative distribution function of a 2-parameter Weibull distribution is of form [3]:

$$F(x) = \begin{cases} 1 - \exp\left\{-\left(\frac{x}{\alpha}\right)^{\beta}\right\} & , x \geq 0 \\ 0 & , x < 0 \end{cases}, \tag{2}$$

where x is the measured variable (e.g. breakdown voltage), α is the scale parameter which corresponds to the value of x at 63.2% failure probability and β is the shape parameter depicting the slope of the theoretical distribution.

For the estimation of the Weibull parameters, various methods such as Maximum-likelihood estimation (MLE) and non-linear regression (NLR) may be used. Linear correlation or statistical tests such as the Kolmogorov-Smirnov (K-S) test may be then utilized for evaluating the goodness-of-fit of the chosen theoretical distribution. A detailed description of these methods is out of the scope of this paper and may be found elsewhere (e.g. [3, 19, 20]).

It is often of practical interest to estimate large-area breakdown probability based on the breakdown distribution measured with a smaller active area. If it is assumed that the breakdowns measured with the active area A_1 are Weibull-distributed with a scale factor α_1 and that the slope β and the film thickness stay constant, the scale factor α_2 of another area A_2 may be expressed as [3]:

$$\alpha_2 = \alpha_1 \left(\frac{A_2}{A_1}\right)^{-1/\beta}. \tag{3}$$

In some cases a single distribution is not sufficient for representing the whole breakdown data set as the breakdowns may be due to different failure mechanisms, each with their own distinct failure distribution $F_i(x)$. In such case, either additively or multiplicatively mixed distributions may be utilized. In this paper, additively mixed 2-parameter Weibull distributions are utilized, for which the cumulative distribution function is of form [3]:

$$F(x) = \sum_{i=1}^{S} \frac{N_i}{N} F_i(x) = \sum_{i=1}^{S} \frac{N_i}{N} \left[1 - \exp\left\{-\left(\frac{x}{\alpha_i}\right)^{\beta_i}\right\}\right], \tag{4}$$

where S is the number of subpopulations, N_i/N is the portion (%) of the subpopulation i and α_i and β_i are the Weibull parameters of subpopulation i.

3 EXPERIMENTAL DETAILS

3.1 SAMPLE DETAILS

The measurements were made with 6 µm thick BOPP film (Tervakoski PSX) with edge-reinforced zinc-aluminium metallization. The metallization sheet resistance was 5-12 Ω/□ for the main metallization body and 2-4 Ω/□ for the reinforced edge according to manufacturer's specifications. The relative permittivity of the film was ε_r=2.2. Samples were cut so that no heavy edge metallization region was used on the active area of the test capacitor.

3.2 FILM ARRANGEMENT AND STRUCTURE OF THE TEST CAPACITOR UNIT

A film arrangement comprising of two sheets of metallized film was utilized for the breakdown measurement (Figure 2a). Similarly as in [7] and [18], the test film was placed at the bottom with the metallized side facing down. The metallization of the test film acted as the bottom electrode and it was connected to the ground. Another metallized film with the metallization facing down was then laid on the test film and it was connected to high voltage source at the opposite end. Electrode films with different widths were used to achieve active areas of 2 - 42 cm^2. A dielectric spacer film (polyimide, 100 µm in thickness) was used to separate the films at the region where the top film overlaps with the edge of the bottom film in order to prevent a flashover across the electrode edges. Lastly, the aforementioned film arrangement was sandwiched between two additional sheets of polyimide film in order to support the arrangement mechanically. The whole film arrangement was then laid on the bottom plate of the test capacitor unit (Figure 2b). Electrical contacts to the metallized films were made by means of aluminium clamp electrodes at the both ends of the bottom plate. A lightweight top plate made of transparent acrylic plastic was then laid on the top of the structure for further mechanical support. Mechanical support was found to be very important when self-healing takes place in the test film, as the sudden pressure build-up during a self-healing breakdown event tends to shift and corrugate the films easily.

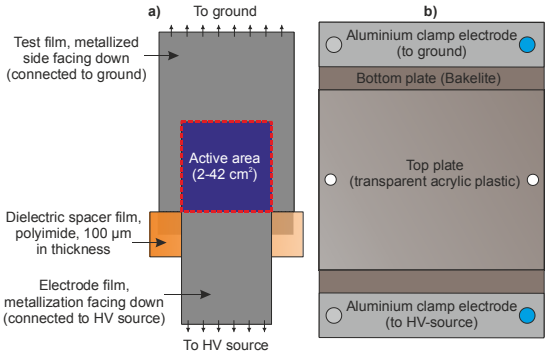

Figure 2. a) Film arrangement used for the test capacitor showing the active area of the test capacitor. Electrode films with different widths were used in order to achieve different active areas (2-42 cm^2). b) Test capacitor unit comprising of bottom and top plates and aluminium electrode clamps at the both ends for making electrical contact to the metallized films.

3.3 MEASUREMENT CIRCUIT AND TEST PROCEDURE

The experimental measurement setup used for the breakdown analysis is presented schematically in Figure 3 and a comprehensive list of used equipment is given in Appendix A (Table 4). In the test circuit, the test capacitor unit is depicted as the capacitance C_{DUT}. The purpose of the parallel capacitance C_P is to act as a fast charge storage buffer during a breakdown in the test capacitor. When a breakdown occurs in the test capacitor, a portion of the charge stored in the total capacitance C=C_P+C_{DUT} is rapidly discharged at the fault spot. The discharge current $i_d(t)$ is then measured with an impulse current measurement resistor R_M as voltage signal $u_{id}(t)$. Simultaneously, the voltage $u_{DUT}(t)$ across the test capacitor is measured with a high voltage probe. Discharge current and test capacitor voltage during each breakdown event were recorded with an oscilloscope operating in the sequence acquisition mode and triggered to the rising edge of the discharge current signal. The self-healing energy E_{SH} could then be calculated by integrating the test capacitor voltage and the discharge current over the whole discharge duration τ:

$$E_{SH} = \int_0^{\tau} u_{DUT}(t) i_d(t) dt. \quad (5)$$

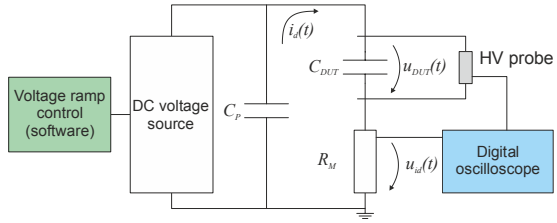

Figure 3. Experimental measurement setup used for the self-healing breakdown measurement.

The progression of the breakdown measurement is illustrated schematically in Figure 4. The voltage of the DC voltage source is ramped from zero (Figure 4a) with a constant speed of 30 V/s by means of a LabVIEW-based software until the voltage U_{DBS} corresponding to the dielectric breakdown strength of the film sample is reached and the first breakdown occurs in the film (Figure 4b). As the voltage ramp is continued beyond the first breakdown, more breakdowns begin to occur at an increasing frequency (Figure 4c) until finally, the electrical contact to the test sample is lost due to the vaporization of the metallized electrodes near the clamp electrodes (Figure 4d).

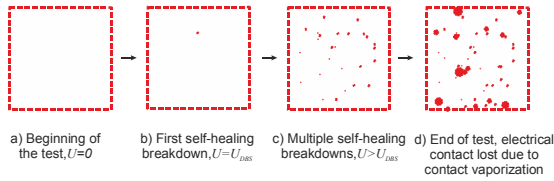

Figure 4. Progression of the breakdown measurement. The square area represents the active area of the test capacitor and the red spots depict breakdown evolution as the voltage is increased steadily.

3.4 UTILIZATION OF LOW-ENERGY SELF-HEALING FOR BREAKDOWN MEASUREMENT

Self-healing breakdown may be utilized for the determination of small area dielectric breakdown strength by progressively increasing the voltage until the first breakdown occurs in the film, as already reported in [7]. However, under typical measurement conditions and near the typical small-area breakdown fields of polymer films (for BOPP up to 700 V/µm or more [7]) the discharge energy and the corresponding discharge current pulse during self-healing are high, and severe deterioration of the metallized electrodes is likely to result. If the measurement is continued beyond the first breakdown, consecutive self-healing breakdowns will further deteriorate the metallized electrode, leading quickly to the isolation of the sample film. Furthermore, if multiple breakdowns are measured, the mutual independence of the results is also questionable.

3.4.1 REDUCTION OF THE DISCHARGE ENERGY DURING SELF-HEALING BREAKDOWN

In order to avoid excessive de-metallization during self-healing and to enable proper measurement of multiple breakdowns, the discharge energy level should be minimized. One approach for minimizing the discharge energy is to reduce the total capacitance C involved in the self-healing process, as also suggested by equation (1). In fact, early studies on self-healing [21] showed that a linear dependency of E_{SH} on C is realized with low capacitances (up to few hundred nF) while with higher capacitances (in the range of µF), E_{SH} shows dependence proportional to $C^{1/2}$. In this study, low-energy self-healing breakdown was achieved by reducing the total capacitance in the self-healing circuit.

The effect of total capacitance on the discharge energy level was analyzed by making ten measurements with metallized BOPP by using C_P in the range of 0.5-200 nF and an active test area of A=10 cm^2. Thus, the sample capacitance calculated as $C=\varepsilon_0\varepsilon_r A/d$ with ε_r=2.2 and d=6 µm was C_{DUT}=3.25 nF. Discharge energies of all the measured self-healing breakdowns were calculated according to (5) and they are shown in Figure 5 as a function of voltage and parallel capacitance with the first breakdowns shown separately. The total capacitance has clearly a major effect on the discharge energy level and when a parallel capacitance of 0.5 nF was used, the discharge energies of the self-healing breakdowns were reduced to less than 10 mJ. It is also notable that as the damage to the metallized layer is reduced with discharge energy, the amount of measured breakdowns increases considerably and most of the consecutive self-healing breakdowns shown in Figure 5 follow the power dependency $E_{SH}=aU^b$ as suggested by (1). Photographs of measured films are shown in Appendix B.

Figure 6 shows the typical behaviour of the discharge current and test capacitor voltage during a self-healing breakdown at ~3.5 kV as a function of time and parallel capacitance. As the parallel capacitance is decreased, the total charge available during the self-healing breakdown is decreased and a major voltage drop across the test capacitor will result. As the power density of the breakdown arc is reduced with the voltage drop, the breakdown arc constricts rapidly, thus minimizing the size of the de-metallized area and the damage to the surrounding metallized layer. Due to the fast nature of the self-healing phenomenon the voltage drop was not compensated by the DC voltage source during a breakdown; however, the voltage was quickly recovered soon after the breakdown event was finished and before a consequential breakdown occurred.

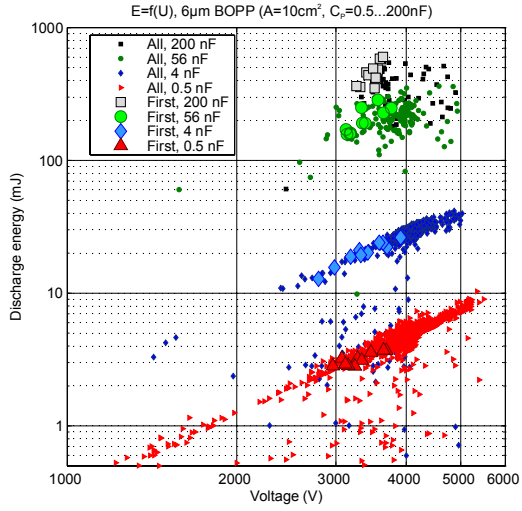

Figure 5. Measured discharge energies as a function of voltage and parallel capacitance C_P, showing a major reduction in the discharge energy level with decreasing parallel capacitance. The total amount of measured breakdowns were 67, 149, 665 and 1390 with C_P of 200, 56, 4 and 0.5 nF, respectively. Sample capacitance was 3.25 nF.

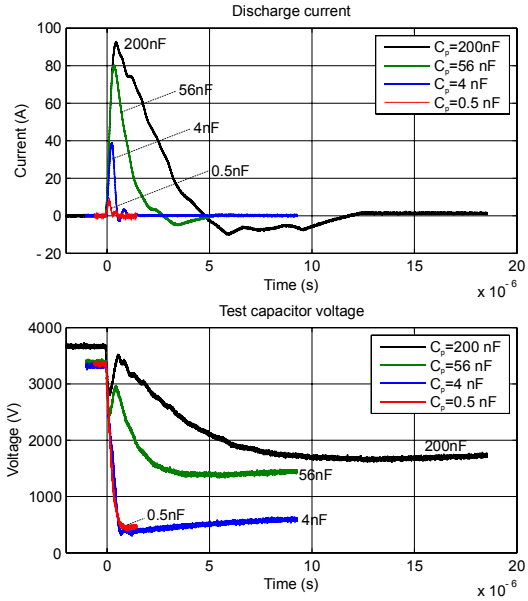

Figure 6. Discharge current pulse (top) and test capacitor voltage (bottom) as a function of time and parallel capacitance C_P. With decreasing C_P, the voltage drop during self-healing breakdown increases, leading to more effective decrease in power density and constriction of the breakdown arc. The peak current and discharge current duration drop from 92.9 A and 12 µs to 8.3 A and 535 ns with parallel capacitance of 200 and 0.5 nF, respectively. Sample capacitance was 3.25 nF.

3.4.2 Data selection procedure

Some of the breakdowns measured with the low-energy self-healing method are scattered in terms of breakdown voltage and discharge energy as also shown in Figure 5. In order to validate each measured breakdown and to ensure mutual independence of the results, a data selection procedure based on the power dependence of the discharge energy on the breakdown voltage was utilized prior to the statistical analysis. The concept of the procedure is best described graphically, as shown in Figure 7, in which the calculated discharge energies of all the breakdowns measured on 25 samples of metallized BOPP (A=10 cm^2, C_P=0.5 nF, C_{DUT}=3.25 nF) are shown as a function of the breakdown voltage. The hypothesis is that only those breakdown data points should be qualified for further analysis (i) for which the corresponding discharge energies follow the trend preset by the first measured self-healing breakdowns and (ii) for which the breakdown voltage is higher than that of the first breakdown of the sample. First self-healing breakdowns of each sample were used as a basis for the data selection criterion as they were certainly mutually independent. A block diagram describing the main aspects of the MATLAB-based program used for the selection procedure is shown in Figure 8.

A physical explanation for the lower-than-expected discharge energies or breakdown voltages is that those breakdowns may have occurred near previous breakdown sites, resulting in lower discharge energy as the electrode layer around the breakdown site is already deteriorated or demetallized. Moreover, these breakdowns may also be attributed to successive self-healing taking place at the same breakdown site, presumably due to graphite formation and incomplete self-healing as reported in [17]. Due to the questionable nature and mutual dependence of these breakdowns they are not chosen for further analysis.

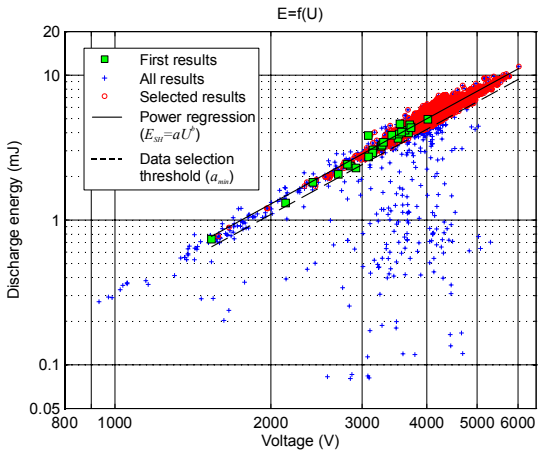

Figure 7. Example of the data selection procedure. The plot shows the calculated discharge energies of all the low-energy self-healing breakdowns measured on 25 samples of metallized BOPP with 10 cm^2 electrode area (blue). The first breakdowns (green) are used for the determination of the slope b of the power regression line (solid line, $E=aU^b$). By taking the energy variation of the first points into account, a_{min} is determined and used as a threshold (dashed line). Only the data points with discharge energies above the threshold and with breakdown voltages higher than the first breakdown of the sample are chosen (red).

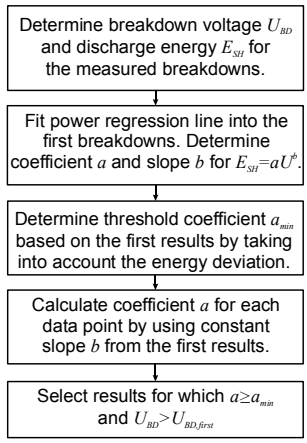

Figure 8. Block diagram describing the main aspects of the data selection procedure.

4 RESULTS AND DISCUSSION

4.1 BREAKDOWN MEASUREMENT RESULTS

Breakdown measurement was performed for four test series, each consisting of 25 samples with active electrode areas of 2, 10, 24 or 42 cm^2. Thus, the total measured areas for the individual test series were 50, 250, 600 and 1050 cm^2, respectively, resulting in total measured area of 1950 cm^2. Parallel capacitance of 0.5 nF was used in the measurement circuit for each measurement. The discharge energies of the measured breakdowns were calculated according to equation (5) and the data selection procedure was used for selecting the data for further analysis. Statistical analysis was then performed for the qualified data points using Weibull++ and MATLAB programs, which enabled convenient calculation and fitting of single 2-parameter Weibull distributions and additively mixed Weibull distributions into the breakdown data sets.

4.1.1 DEPENDENCE ON THE ELECTRODE AREA

The electrode area dependence was first approached by analyzing the first measured breakdowns of each sample film. Figure 9 shows the Weibull probability plots of the first measured breakdowns with active areas of 2, 10, 24 and 42 cm^2. The corresponding Weibull parameter estimates calculated with the MLE-method are given in Table 1. Figure 9 clearly shows the area dependence of the breakdown results at the higher probability region (> 10%) which is also supported by the decreasing Weibull α and relatively constant Weibull β with increasing electrode area (Table 1). However, significant deviation from the theoretical distributions can be seen at the low-probability region with all the electrode areas, as also indicated by the elevated K-S test quantities (Table 1). Similar deviation from a single Weibull distribution has been previously reported for e.g. BOPP, PI (polyimide) and PTFE (polytetrafluoroethylene) films [10, 22, 23]. This deviation suggests that the breakdowns may be due to more than one breakdown mechanisms and that a single 2-parameter Weibull distribution is in fact insufficient for representing the breakdown data.

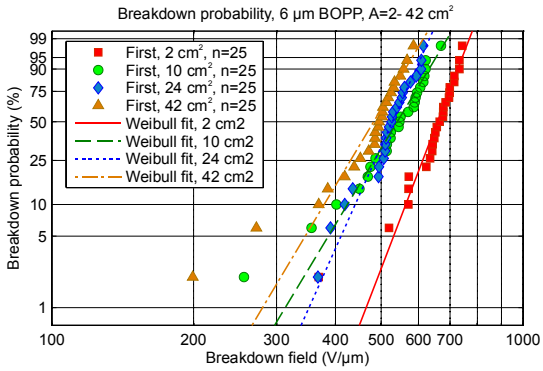

Figure 9. Weibull breakdown probability distributions of the first measured breakdowns with 2, 10, 24 and 42 cm^2 active electrode areas (25 samples per each area). The electrode area dependence can be clearly distinguished at the high probability region (>10%) whereas increasing deviation from the theoretical distributions is shown at the low-probability region.

Table 1. Parameters of the 2-parameter Weibull distributions fitted into the first breakdowns measured with different electrode areas. MLE method was used for the Weibull-parameter estimation.

Electrode area (cm^2)	α (V/µm)	β	Kolmogorov-Smirnov test (%)
2	679	12.15	3.49
10	567	7.74	8.19
24	547	10.4	8.32
42	505	7.80	58.42

Next, the electrode area dependence of the breakdown results obtained with the low-energy self-healing measurement method was analyzed. Figure 10 shows the selected breakdowns and the fitted theoretical distributions measured with active areas of 2, 10, 24 and 42 cm^2. The breakdown sets represent total measured areas of 50, 250, 600 and 1050 cm^2. Sample capacitances (0.65, 3.25, 7.80 and 13.64 nF for 2, 10, 24 and 42 cm^2 electrodes, respectively) were found to have no significant effect on the measurement.

As the amount of obtainable breakdown data is considerably higher with the new method than what could be easily achievable with conventional breakdown measurement methods, the shapes of the empirical distributions in Figure 10 are very detailed, showing a typical S-shaped curve which strongly suggests the presence of multiple breakdown mechanisms [19]. In practice, 3-subpopulation mixed Weibull distributions were fitted into the breakdown data, as they showed the best goodness-of-fit test results. The distribution parameters calculated with the NLR-method and the goodness-of-fit test results of the utilized mixed distributions are given in Table 2. The distributions showed a very good fit in the measurement data, although few data points deviate from the theoretical distribution at the very low probability region (<0.5%) as shown in Figure 10.

The physical meaning of the fact that three distinct Weibull distributions were found to fit in the data is complex and although a detailed analysis of the underlying breakdown mechanisms is out of the scope of this paper, few considerations are made in the following. Table 2 shows that the first and the second subpopulations for each data series measured with 2, 10 and 24 cm^2 electrode areas have nearly identical Weibull α values but different (low and high) β values. Similarly as reported in [23, 24], the first subpopulation with lower β value representing the low-field breakdowns can be attributed to a defect population present in the dielectric or to other extrinsic factors such as dust, foreign particles, film wrinkling or electrode edge effect. On the other hand, the second subpopulation with high β presumably represents the inherent, defect-independent breakdown distribution of the dielectric material.

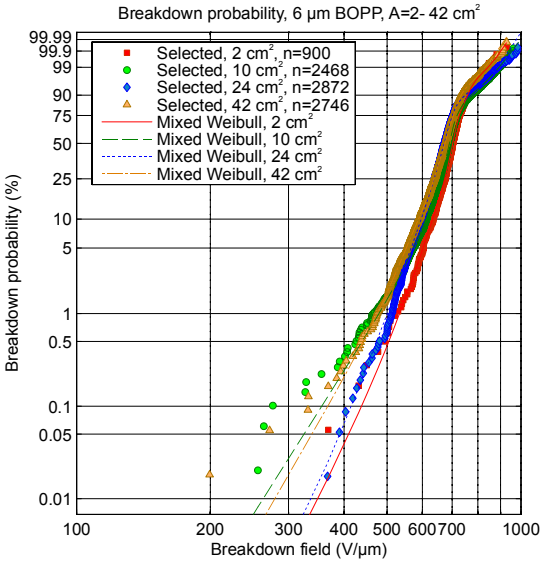

Figure 10. 3-subpopulation mixed Weibull breakdown probability distributions of the selected breakdown results measured with 2, 10, 24 and 42 cm^2 active electrode areas (25 film samples/electrode area).

Table 2. Parameters and goodness-of fit test results of the 3-subpopulation mixed Weibull distributions fitted into the selected breakdown results measured with 2, 10, 24 and 42 cm^2 active areas. NLR method was used for the Weibull-parameter estimation.

Subpopulation portion N_i/N (%)				
Electrode area (cm^2)	Total measured area (cm^2)	Sub 1	Sub 2	Sub 3
2	50	60.469	25.676	13.856
10	250	48.809	20.214	30.977
24	600	48.583	34.129	17.288
42	1050	2.469	70.638	26.893
Weibull α (V/µm)				
Electrode area (cm^2)	Total measured area (cm^2)	Sub 1	Sub 2	Sub 3
2	50	716	707	760
10	250	697	695	759
24	600	676	681	788
42	1050	562	687	719
Weibull β				
Electrode area (cm^2)	Total measured area (cm^2)	Sub 1	Sub 2	Sub 3
2	50	16.17	46.93	9.36
10	250	17.61	50.00	7.59
24	600	13.85	27.72	9.33
42	1050	17.46	19.77	8.36
Goodness-of-fit				
Electrode area (cm^2)	Total measured area (cm^2)	Correlation coefficient ρ (%)	Kolmogorov-Smirnov test (%)	
2	50	96.82	5.35×10^{-8}	
10	250	95.47	1.00×10^{-10}	
24	600	99.45	1.00×10^{-10}	
42	1050	95.81	4.05×10^{-7}	

Interestingly, for the breakdown series measured with the largest electrode area (42 cm^2), Table 2 shows that the structure of the mixed distribution is different in comparison to the structures of the distributions representing the smaller electrode areas. Table 2 shows that for the largest electrode area, the first and the second subpopulations are clearly separated in terms of Weibull α value and the subpopulation β values and portions have also changed accordingly. This is merely an indication that the Weibull parameter estimation algorithm results in a different distribution structure as the amount of low-field breakdown data increases.

Regarding to the third subpopulation, only speculations may be given in this paper. The distinct knee shown in each breakdown distribution at the high-field region in Figure 10 is most likely due to the excessive vaporization of the metallized electrode and the consequential decrease in active area during rapid self-healing. However, one would still anticipate for the high-field breakdowns to follow the material-inherent breakdown distribution (subpopulation 2) before the electrical contact to the sample film is lost (see Figure 4). In addition, the fact that a large portion of the breakdowns (~17-31%) are represented by the third subpopulation is significant and the possible presence of another breakdown mechanism at the high-field region cannot be disregarded completely.

It is very important to point out that direct comparison of the empirical and theoretical distributions shown in Figure 10 and Table 2 is not straightforward due to the differences in the number of data points. In fact, all the measured empirical distributions are merely approximations of the absolute breakdown distribution underlying in the dielectric and the differences in the electrode area are only reflected into the number of obtainable breakdown data points. Figure 10 clearly shows that as the number of measured breakdowns increases with electrode area, the empirical distribution shifts upwards in the probability axis and the amount of observed low-probability breakdowns increases.

4.1.2 COMBINED LARGE AREA BREAKDOWN RESULTS

The analysis of the dependence on the total measured area was extended by combining the breakdown sets measured with different electrode areas and by performing the data selection process for the combined series. This enabled the formation of breakdown result sets representing total measured areas of 1100 cm^2 (2 and 42 cm^2 sets combined), 1350 cm^2 (2, 10 and 42 cm^2 sets combined) and 1950 cm^2 (2-42 cm^2 sets combined). Figure 11 shows the combined breakdown results and the mixed Weibull distributions fitted into the breakdown data. The corresponding Weibull parameters and the goodness-of-fit test results are given in Table 3.

Table 3 shows the evolution of the Weibull parameters as the total measured area and the number of data points increase. In Table 3 it is noticeable that the Weibull α of the second subpopulation, which may be attributed to the inherent breakdown distribution of the material, shows only a slight change as the total measured area is increased. In fact, Tables 2 and 3 together show that the Weibull α of the second subpopulation stays is in the same range regardless of the electrode or total measured area, implying that the measurement method provides a good estimate of the inherent breakdown distribution of the dielectric material.

On the other hand, the evolution of the defect population (subpopulation 1) with increasing total measured area is evident based on Tables 2 and 3. Recently, the effect of small amount of randomly distributed defects on the breakdown distribution of polymers has been studied based on the field-assisted percolation model [11]. The study showed that the significance of the defect population was profound in large samples and resulted in deviation from a single Weibull distribution. This observation is coherent with the experimental results given in Tables 2 and 3.

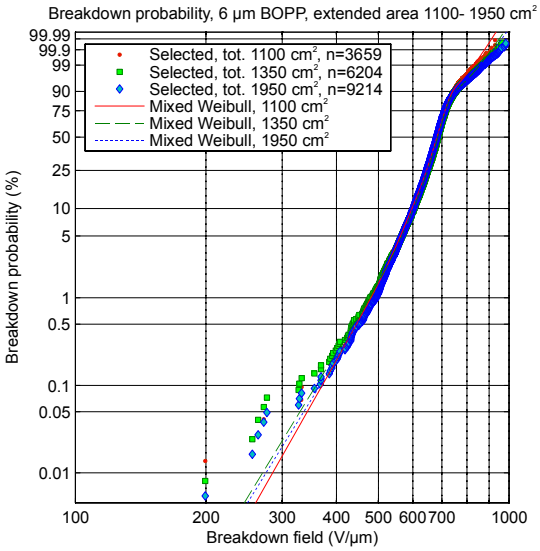

Figure 11. Breakdown results and the corresponding 3-subpopulation mixed Weibull distributions for the combined total areas of 1100, 1350 and 1950 cm^2.

Table 3. Parameters and goodness-of fit test results of the 3-subpopulation mixed Weibull distributions fitted into the breakdown results of 1100, 1350 and 1950 cm^2 combined total areas. NLR method was used for the Weibull-parameter estimation.

Subpopulation portion N_i/N (%)			
Total measured area, combined (cm^2)	Sub 1	Sub 2	Sub 3
1100	1.391	65.931	32.678
1350	2.148	64.936	32.916
1950	2.279	68.470	29.251
Weibull α (V/µm)			
Total measured area, combined (cm^2)	Sub 1	Sub 2	Sub 3
1100	578	694	718
1350	596	695	733
1950	586	690	743
Weibull β			
Total measured area, combined (cm^2)	Sub 1	Sub 2	Sub 3
1100	22.54	20.70	8.76
1350	21.90	22.80	8.11
1950	20.90	21.28	8.04
Goodness-of-fit			
Total measured area, combined (cm^2)	Correlation coefficient ρ (%)	Kolmogorov-Smirnov test (%)	
1100	96.55	1.60×10^{-8}	
1350	96.35	2.03×10^{-5}	
1950	97.01	7.60×10^{-9}	

Lastly, Figure 12 shows a comparison of the combined large area breakdown distribution (A_{tot}=1950 cm^2) and the first measured breakdowns in order to underline the problematic nature of making predictions based on small number of small-area measurements with conventional breakdown measurement methods. Figure 12 illustrates that when dielectric breakdown strength is determined, the electrode area defines the voltage range (or the "bandwidth") from where the results are likely to be obtained. With a small electrode area (2 cm^2), most of the results are obtained only from the high-field part of the absolute characteristic breakdown distribution and unless a large total area is measured, an over-optimistic estimate of the breakdown strength is likely to result. This is due to the fact that the defect concentration in the material is small and the probability for a small sample area to contain a defect is low. Therefore, application of the area scaling law may also be problematic as the small-area breakdown distribution does not contain sufficient information about the low-field breakdowns required for accurate extrapolation to larger areas. As the electrode area (or the total measured area) is increased, an improved estimate of the absolute breakdown distribution of the dielectric film is obtained. Figure 12 also underlines the reason why a single Weibull distribution is often not sufficient for representing the whole empirical breakdown distribution.

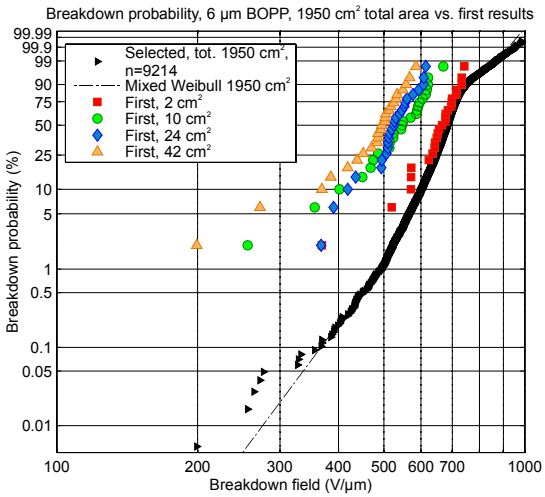

Figure 12. Comparison of the breakdown distribution of a large combined area (1950 cm^2) and the first measured breakdowns with electrode areas of 2, 10, 24 and 42 cm^2. With increasing electrode area or total measured area, an improved estimate of the absolute breakdown distribution of the dielectric may be obtained.

4.2 IMPLICATIONS

The area dependence analysis of the breakdown results indicates that increasing electrode or total measured area has an effect on the composition of the defect population and on the overall structure of the theoretical distribution (Table 2-3). However, all the measured breakdown distributions still exhibit a similar shape as shown by Figure 10 and 11. In fact, the breakdown distributions presented in this paper may be regarded as material-specific breakdown patterns or fingerprints, as also suggested in [9], in which unique breakdown patterns were measured for various BOPP films from different vendors. Moreover, different types of breakdown patterns are also presented in [7] for BOPP and in [22] for other polymer films. Differences between various BOPP films may explain why the metallized BOPP film used in this study showed a distinct defect-population especially when a large total measured area is considered.

As the amount obtainable breakdown data is large with the low-energy self-healing breakdown measurement method, the breakdown fingerprints obtained are very detailed, allowing accurate comparison to be made between different dielectric materials. It should also be highlighted that as the low-energy self-healing measurement method enables convenient breakdown measurement beyond the weakest point of the dielectric, detailed information about the dielectric performance of the material is obtained even with a small sample amount regardless of the defects present in the dielectric or other extrinsic factors such as dust, foreign particles, film wrinkling or electrode edge effect. Thus, the measurement method could be a valuable tool especially in the development phase of new dielectric materials.

In regard to the statistical analysis, additively mixed Weibull distributions were found to fit well into the breakdown data in this study. On the other hand, further improvement of the quality of fit could be possible by utilizing more complex mixed distributions comprising of combinations of e.g. Weibull, Gumbel and other types of single distributions. This aspect will be further analysed in a future publication. However, regardless of the type or structure of the chosen theoretical distribution, it should be emphasized that the role of the theoretical distribution is merely to approximate the empirical data and to enable convenient comparison between different data sets.

Certain limitations have to be considered when the self-healing breakdown mechanism is utilized for the measurement of multiple breakdowns. As the total capacitance involved in the self-healing circuit has a major effect on the discharge energy, the active area of the sample film should be chosen so that a reasonable discharge energy level is maintained. Moreover, film thickness is also reflected to the discharge energy level as it determines the voltage range needed for breakdown measurement. Measurement of thick films (in the range of >10 µm) will thus result in higher discharge energy level. High voltages may also lead to additional challenges such as flashovers along the film surfaces which may further complicate the breakdown measurement.

Lastly, it is also important to remark that even though the measurements presented in this paper were made with metallized films, the measurement method should be applicable to non-metallized sample films as well. As discussed in [7], dielectric breakdown of non-metallized films may be readily measured by using metallized films as electrodes above and under the test film with the metallized sides facing towards the test sample. So far, the breakdown measurement method has been found to be applicable for both metallized and non-metallized polymer films with thicknesses in the range of 4-12 µm.

5 CONCLUSION

A new dielectric breakdown measurement method for determining the breakdown characteristics of polymer films has been presented and evaluated. The measurement method is based on the low-energy self-healing breakdown of metallized polymer film which effectively reduces the de-metallized area around each breakdown site and the damage to the surrounding electrode layer. Discharge energy reduction was realized by reducing the total capacitance involved in the self-healing circuit and as a result, a large amount of breakdowns may be measured. A data selection procedure based on the discharge energy behaviour of metallized dielectric film was utilized for validating mutual independence of the breakdown results.

The measurement method yields a large amount of breakdown data which enables the formation of detailed breakdown patterns or characteristic breakdown fingerprints. With the metallized BOPP film used in this study, a single Weibull distribution was found to be insufficient for representing the whole breakdown data set and additively mixed Weibull distributions were utilized. The area dependence analysis of the breakdown data demonstrated the evolution of the breakdown distribution with increasing electrode or total measured area. Most importantly, the area dependence analysis underlined the importance of large-area breakdown measurement in order to obtain a realistic picture of the dielectric performance of the film for practical applications.

The possibility to continue breakdown measurement beyond the weakest point of each sample film enables detailed dielectric breakdown characterization regardless of the weak points present in the dielectric. Thus, the measurement method could be a valuable tool especially in the development phase of new dielectric materials. The measurement method was shown to provide very detailed information about the material-inherent breakdown distribution. On the other hand, by measuring a large total area, more detailed information about the low-probability breakdowns is also acquired.

APPENDIX A

Table 4. List of equipment used in the measurement system.

High-voltage source	Spellman SL 1200 DC voltage source (1200 W)
Parallel capacitance C_P	**0.5 nF**: Series connection of two Haefely 2000 pF/400kV coupling capacitors and one Haefely 1000 pF/120 kV coupling capacitor
	4 nF: Hipotronics 4 nF/100 kV coupling capacitor,
	56 nF: Nokian Capacitors 56 nF/ $36/\sqrt{3}$ kV surge capacitor
	200 nF: Nokian Capacitors 0,2 µF/ $24/\sqrt{3}$ kV surge capacitor
Measurement resistor R_M	T&M Research Products impulse current viewing resistor, R=0.971 Ω, low inductance
High-voltage probe	Tektronics P6015A
Digital oscilloscope	Lecroy HRO 66Zi, 600 MHz 12-bit oscilloscope
Voltage ramp control	National Instruments PCI-6221 data acquisition card + LabVIEW

APPENDIX B

Figure 13-14 show photographs of sample films (Zn-Al metallized 6 µm BOPP film, A=24 cm^2) after breakdown measurement as viewed from the metallized side. The size of the de-metallized region and the damage to the metallized layer is greatly reduced with low-energy self-healing breakdown method (Figure 13, C_P=0.5 nF) in comparison to regular self-healing (Figure 14, C_P=200 nF). With less damage to the metallized layer, the number of measured breakdowns increases.

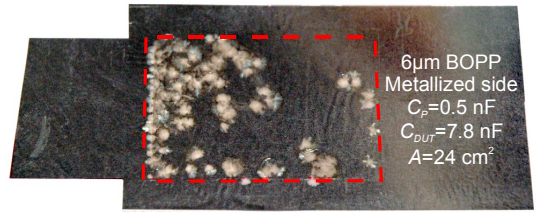

Figure 13. Photograph of a sample film after test (low-energy self-healing breakdown, C_P=0.5 nF, C_{DUT}=7.8 nF). 119 measured breakdowns.

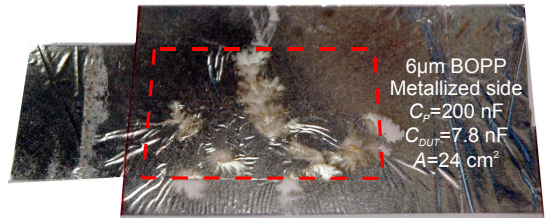

Figure 14. Photograph of a sample film after test (regular self-healing, C_P=200 nF, C_{DUT}=7.8 nF). 13 measured breakdowns.

REFERENCES

[1] L. A. Dissado and J. C. Fothergill, *Electrical Degradation and Breakdown in Polymers*, Philadelphia, USA, Peter Peregrinus Ltd., 1992.

[2] A.R. Blythe and D. Bloor, *Electrical Properties Of Polymers*, 2nd ed., Cambridge University Press, UK, 2005.

[3] W. Hauschild and W. Mosch, *Statistical Techniques for High-Voltage Engineering,* Philadephia, IET, UK, 1992.

[4] "IEEE Guide for the Statistical Analysis of Electrical Insulation Breakdown Data," IEEE Std 930-2004 (Revision of IEEE Std 930-1987), 2005.

[5] S. Ul-Haq and G.R.G. Raju, "Weibull statistical analysis of area effect on the breakdown strength in polymer films," IEEE Conf. Electr. Insul. Dielectr. Phenomena, pp. 518-521, 2002.

[6] S.J. Laihonen, U. Gafvert, T. Schutte, and U.W. Gedde, "Influence of electrode area on dielectric breakdown strength of thin poly(ethylene terephthalate) films," IEEE Conf. Electr. Insul. Dielectr. Phenomena, pp. 563- 567, 2004.

[7] C. Xu, J. Ho, and S.A. Boggs, "Automatic breakdown voltage measurement of polymer films," IEEE Electr. Insul. Mag., Vol. 24, No. 6, pp. 30-34, 2008.

[8] C. Calebrese, L. Hui, L.S. Schadler, and J.K. Nelson, "A review on the importance of nanocomposite processing to enhance electrical insulation," IEEE Trans. Dielectr. Electr. Insul., Vol. 18, No. 4, pp. 938-945, 2011.

[9] S.J. Laihonen, U. Gafvert, T. Schutte, and U.W. Gedde, "DC breakdown strength of polypropylene films: Area dependence and statistical behavior," IEEE Trans. Dielectr. Electr. Insul., Vol. 14, No. 2, pp. 275-286, 2007.

[10] S.J. Laihonen, A. Gustafsson, U. Gafvert, T. Schutte, and U.W. Gedde, "Area dependence of breakdown strength of polymer films: automatic measurement method," IEEE Trans. Dielectr. Electr. Insul.,

Vol. 14, No. 2, pp. 263-274, 2007.

[11] K. Wu, Y. Wang, Y.H. Cheng, L.A. Dissado, and X.J. Liu, "Statistical behavior of electrical breakdown in insulating polymers," J. Appl. Phys., Vol. 107, no. 6, 2010.

[12] D.G. Shaw, S.W. Cichanowski, and A. Yializis, "A Changing Capacitor Technology - Failure Mechanisms and Design Innovations," IEEE Trans. Electr. Insul., Vol. 16, No. 5, pp. 399-413, 1981.

[13] C.W. Reed and S.W. Cichanowski, "The fundamentals of aging in HV polymer-film capacitors," IEEE Trans. Dielectr. Electr. Insul., Vol. 1, No. 5, pp. 904-922, 1994.

[14] M. Rabuffi and G. Picci, "Status quo and future prospects for metallized polypropylene energy storage capacitors," IEEE Trans. Plasma Sci., Vol. 30, No. 5, pp. 1939-1942, 2002.

[15] J.H Tortai, A. Denat, and N. Bonifaci, "Self-healing of capacitors with metallized film technology: Experimental observations and theoretical model," J. Electrostatics, Vol. 53, No. 2, pp. 159-169, 2001.

[16] P.-O. Sassoulas, B. Gosse, and J.-P. Gosse, "Self-healing breakdown of metallized polypropylene," IEEE 7th Int'l. Conf. Solid Dielectrics (ICSD), pp. 275-278, 2001.

[17] B. Walgenwitz, J.-H. Tortai, N. Bonifaci, and A. Denat, "Self-healing of metallized polymer films of different nature," IEEE 7th Int'l. Conf. Solid Dielectrics (ICSD), pp. 29-32, 2004.

[18] Y. Chen, H. Li, F. Lin, F. Lv, M. Zhang, Z. Li, and D. Liu, "Study on Self-Healing and Lifetime Characteristics of Metallized-Film Capacitor Under High Electric Field," IEEE Trans. Plasma Sci., Vol. 40, No. 8, pp. 2014-2019, 2012.

[19] D. Kececioglu, *Reliability Engineering Handbook* Vol.1, DEStech Publications, Inc., 2002.

[20] H. Rinne, *The Weibull Distribution - A Handbook*, 1st ed., Chapman and Hall/CRC, 2008.

[21] H. Heywang, "Physikalische und chemische Vorgänge in selbstheilenden Kunststoff-Kondensatoren," Colloid Polymer Sci., Vol. 254, No. 2, pp. 139-147, 1976.

[22] G. Raju, A. Katebian, and S.Z. Jafri, "Breakdown voltages of polymers in the temperature range 23°-250°C," IEEE Trans. Dielectr. Electr. Insul., Vol. 10, No. 1, pp. 117-127, 2003.

[23] S. Diaham, S. Zelmat, M.-L. Locatelli, S. Dinculescu, M. Decup, and T. Lebey, "Dielectric breakdown of polyimide films: Area, thickness and temperature dependence," IEEE Trans. Dielectr. Electr. Insul., Vol. 17, No. 1, pp. 18-27, 2010.

[24] P.H.H. Fischer and K.W. Nissen, "The Short-Time Electric Breakdown Behavior of Polyethylene," IEEE Trans. Electr. Insul., Vol. 11, No. 2, pp. 37-40, 1976.

Ilkka Rytöluoto (S'13) was born in Tampere, Finland on 17 April 1985. He received the M.Sc. (Tech.) degree in electrical engineering from Tampere University of Technology (TUT), Tampere, Finland in 2011. Since 2012 he has been working as a Researcher in the high voltage research group of the Department of Electrical Engineering at TUT, with the aim towards the Ph.D. degree. His current research interests include dielectric characterization of polymer and polymer nanocomposite films and analysis of the self-healing performance of metallized dielectric films.

Kari Lahti (M'01) was born in Hämeenlinna, Finland, on 8 March 1968. He received the M.Sc. and Doctoral degrees in electrical engineering from Tampere University of Technology in 1994 and 2003, respectively. Since then he has worked at the Department of Electrical Engineering at TUT, currently as a Research Manager and Adjunct Professor. Since 2002 he has been responsible for the high voltage laboratory services at TUT. His research interests are in the area of high voltage engineering, especially surge arresters, environmental testing of high voltage materials and apparatus, high voltage testing methods and dielectric characterization of insulating materials.

Publication II

I. Rytöluoto and K. Lahti, "Effect of film thickness and electrode area on the dielectric breakdown characteristics of metallized capacitor films," in *23rd Nordic Insulation Symposium (NORD-IS 13)*, pp. 33–38, 2013.

Effect of Film Thickness and Electrode Area on the Dielectric Breakdown Characteristics of Metallized Capacitor Films

Ilkka Rytöluoto & Kari Lahti
Tampere University of Technology (TUT)
Department of Electrical Engineering (DEE)
P.O. Box 692
FI-33101 Tampere, Finland

Abstract
An alternative approach for measuring breakdown characteristics of metallized and non-metallized polymer films has been previously developed at TUT. The method enables measurement of multiple breakdowns beyond the weakest point of each sample film by utilizing low-energy self-healing breakdown of metallized film. The method yields a large amount of breakdown data even from a relatively small sample area which enables the formation of detailed material-specific breakdown fingerprints. In this paper, some preliminary results of an ongoing further research on the area and thickness dependence of the breakdown characteristics of various polymer films are presented.

1. Introduction
Dielectric polymer films utilized in film capacitors are subjected to very high electric field stresses and thus, accurate statistical knowledge of their breakdown characteristics at the low breakdown probability region is of utmost importance in order to ensure safe and reliable design and operation in practice [1-4]. Breakdown measurement is typically realized as a short-term ramp-to-breakdown measurement and Weibull or other extreme-value distributions are then utilized for statistical analysis of the breakdown data [5]. However, weak spots in the polymer film due to the internal morphology and inherent properties of the polymer itself or due to extrinsic factors such as defects, voids, chemical impurities and non-ideal processing conditions can lead to a large deviation in the breakdown strength [6]. Moreover, the area and volume dispersion of the weak points in the film further complicates the dielectric strength evaluation [7-9]. Therefore, a large amount of breakdown data is required from a relatively large test area in order to gain a sufficient statistical relevance for practical applications. One approach for obtaining a large amount of breakdown data is to utilize an automatic breakdown strength measurement system such as in [10-11].
However, especially when the development and optimization phase of new dielectric materials such as polymer nanocomposites is considered, weak spots due to non-ideal processing conditions or other external factors may have a deteriorating effect on the dielectric breakdown strength [12]. Moreover, as the amount of sample material available for breakdown measurement may be scarce, the dielectric breakdown strength determined with only a small number of parallel samples may be misleading as it may be more representative of the weak spots due to extrinsic factors rather than a measure of the inherent properties of the material. Consequently, the true potential of the new dielectric may not be revealed completely.
In return to this problem, an alternative approach for measuring breakdown characteristics of thin polymer films has been previously developed at TUT [13]. The method is based on the concept of measuring multiple breakdowns per sample film beyond the weakest point (or dielectric strength) of each film by utilizing low-energy self-healing breakdown of metallized polymer film which effectively reduces the damage inflicted to the electrode layer with each consecutive breakdown. A data selection procedure based on the discharge energy behavior during self-healing of metallized dielectric film is utilized for validating mutual independence of the breakdown results prior to the statistical analysis. As a result, the method yields a large amount of breakdown data which enables the formation of detailed material-specific breakdown fingerprints.
The aim of this paper is to present the measurement method and some preliminary results of an ongoing further study on the area and thickness dependence of the breakdown characteristics of bi-axially oriented polypropylene (BOPP) and other capacitor-grade polymer films.

2. Background
Metallized film capacitors, which comprise of dielectric polymer films with thin metal electrodes evaporated directly on the film surface, have a unique ability to undergo self-healing breakdown [4]. During a breakdown in the dielectric film, a portion of the stored charge is discharged through the breakdown channel and consequently, a small area of the thin metallization layer around the fault spot is vaporized (Fig.1). As a result, the fault spot is spontaneously isolated from the rest of the electrode and insulation capability of the film is restored.

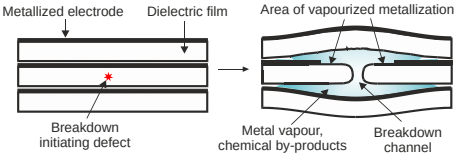

Fig.1. Self-healing breakdown in metallized polymer film.

Self-healing breakdown of metallized film has been extensively studied in the past literature and various factors have been found to affect the self-healing breakdown process [14-18]. The self-healing process may be characterized by the energy E_{SH} discharged during a self-healing event and it may be expressed as:

$$E_{SH} = \frac{kU^b C}{R_s^c \alpha(P)} = aU^b, \quad (1)$$

where U is the voltage, C is the capacitance, R_s is the metallization sheet resistance, $\alpha(P)$ is a function which relates inter-layer pressure to the discharge energy and a, b, c and k are experimentally definable constants.

2. Experimental

2.2. Test capacitor structure

A film arrangement comprising of two sheets of metallized film was used to form a test capacitor with an active area of A=2-42cm^2 (Fig. 2). The test film was placed at the bottom with the metallized side facing down. Another metallized film with the metallization facing down was then laid on the test film. A dielectric spacer film (polyimide, 100 µm in thickness) was used to separate the films at the region where the top film overlaps with the edge of the bottom film in order to prevent a flashover across the electrode edges. The film arrangement was then sandwiched between two sheets of thick transparent film in order to support the arrangement mechanically. The whole film arrangement was then laid on the bottom plate of the test capacitor unit and electrical contacts to the metallized films were made by means of aluminum clamp electrodes at the both ends of the bottom plate. Finally, a lightweight top plate made of transparent acrylic plastic was then laid on the top of the structure for further mechanical support (not shown in Fig. 2). Mechanical support was found to be very important when self-healing breakdown takes place in the test film, as the sudden pressure build-up during a self-healing breakdown event tends to shift and corrugate the films easily.

The measurement circuit used for the breakdown analysis is presented schematically in Fig. 3. In the test circuit, the test capacitor unit is depicted as the capacitance C_{DUT}. The purpose of the parallel capacitance C_P is to act as a fast charge storage buffer during a breakdown in the test capacitor. When a

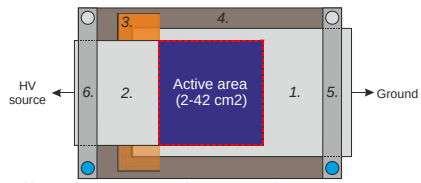

Fig.2. Film arrangement and test capacitor structure (top view). **1-2:** Metallized film (metallized surface facing down), **3:** Dielectric spacer film, **4:** Bottom plate, **5-6:** Aluminum clamp electrode (to high voltage source and ground).

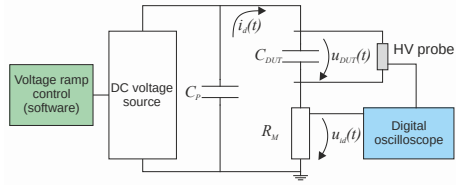

Fig.3. Measurement circuit for the breakdown measurement.

breakdown occurs in the test capacitor, a portion of the charge stored in the total capacitance $C=C_P+C_{DUT}$ is rapidly discharged at the fault spot. The discharge current $i_d(t)$ is then measured with an impulse current measurement resistor R_M as voltage signal $u_{id}(t)$. Simultaneously, the voltage $u_{DUT}(t)$ across the test capacitor is measured with a high voltage probe. Discharge current and test capacitor voltage during each self-healing event were recorded with an oscilloscope operating in sequence acquisition mode and triggered to the rising edge of the discharge current signal. The discharge energy E_{SH} could then be calculated by integrating the test capacitor voltage and the discharge current over the whole discharge duration τ:

$$E_{SH} = \int_0^\tau u_{DUT}(t) i_d(t) dt. \quad (2)$$

2.3. Measurement of multiple breakdowns

In order to enable convenient measurement of multiple self-healing breakdowns from the same sample area, a low level of discharge energy per each self-healing breakdown is desired, as it results in smaller de-metallized area around each breakdown site and reduced damage to the surrounding metallized layer. As also suggested by Eq. (1), there are various ways to affect the discharge energy during a self-healing breakdown. In this study, low-energy self-healing was realized by minimizing the total capacitance $C=C_P+C_{DUT}$ in the self-healing circuit. Thus, as the total charge available during the breakdown process is limited, a major voltage drop will occur across the test capacitor during each self-healing breakdown which effectively reduces the power density of the breakdown arc and leads to a rapid constriction of the breakdown arc. The effect of total capacitance on the discharge energy was studied in more detail in [13]. In this study, C_P=0-3.3nF was used in the measurement circuit in order to ensure that a sufficiently large discharge current pulse was measurable from the test capacitor terminals (clear trigger condition).

The progression of the breakdown measurement is illustrated schematically in Fig. 4. DC voltage is ramped from zero (Fig. 4a) with a constant speed of 30V/s until the voltage U_{DBS} corresponding to the dielectric breakdown strength of the film sample is reached and the first breakdown occurs in the film (Fig. 4b). As the voltage is increased beyond the first breakdown, more breakdowns begin to occur at an increasing frequency (Fig. 4c) until finally, the electrical contact is lost due to de-metallization at the active area and contact edges near the aluminum electrode clamps (Fig. 4d).

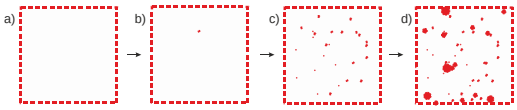

Fig.4. Progression of the breakdown measurement. The square area represents the active area of the test capacitor and the red spots depict the breakdown evolution as the voltage is increased. **a)** Beginning of test, U=0, **b)** first self-healing breakdown, U=U_{DBS}, **c)** multiple self-healings, U>U_{DBS}, **d)** end of test.

As multiple self-healing breakdowns are measured per sample area, only the breakdowns which appear independent should be chosen for further statistical analysis. One approach for the selection is to analyze the discharge energy behavior of the measured self-healing breakdowns on the basis of the power dependence E_{SH}=aU^b [13]. The concept of the procedure is best described graphically, as shown in Fig. 7, in which the calculated discharge energies E_{SH} of all breakdowns measured from 25 samples of metallized BOPP (thickness d=6µm, C_P=0.5nF, C_{DUT}=$\varepsilon_0\varepsilon_r A/d$=3.25nF) are shown as a function of the breakdown voltage U_{BD}. Only those breakdowns are chosen (i) for which the corresponding discharge energies follow the trend preset by the first measured self-healing breakdowns and (ii) for which the breakdown voltage is higher than the dielectric strength of the sample. A physical explanation for the lower-than-expected discharge energies or breakdown voltages is that those breakdowns may have occurred near previous breakdown sites, resulting in lower discharge energy as the electrode layer around the breakdown site is already deteriorated or de-metallized. These breakdowns may also be attributed to successive self-healing taking place at the same breakdown site, presumably due to graphite formation and incomplete self-healing [17]. Non-breakdown events (partial discharges, surface flashovers etc.) may also be easily distinguished and disregarded with the discharge energy analysis.

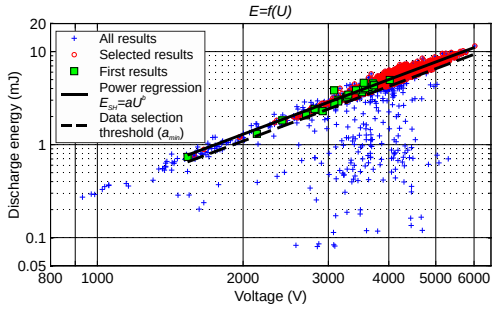

Fig. 7. Example of the data selection. The plot shows the calculated discharge energies of all the low-energy self-healing breakdowns measured from 25 samples of 6 µm metallized BOPP, A=10 cm^2 (blue). The first breakdowns (green) are used to determine the slope b of the power regression line (solid line, E=aU^b). By taking the energy variation of the first breakdowns into account, a_{min} is determined and used as a threshold (dashed line). Only the breakdowns with discharge energies above the threshold and with breakdown voltages higher than the first breakdown of the sample are chosen (red).

2.4. Statistical analysis

For the statistical analysis of the breakdown data in this study, 2-parameter Weibull distributions and additively mixed Weibull distributions were utilized. The cumulative distribution function of a 2-parameter Weibull distribution is of form [5]:

$$F(x) = 1 - \exp\left\{-\left(\frac{x}{\alpha}\right)^{\beta}\right\}, x \geq 0, \quad (3)$$

where x is the measured variable (e.g. breakdown voltage), α is the scale parameter which corresponds to the value of x at 63.2% failure probability and β is the shape parameter depicting the slope of the theoretical distribution. The cumulative distribution function of an additively mixed 2-parameter Weibull distribution is of form [5]:

$$F(x) = \sum_{i=1}^{S} \frac{N_i}{N} F_i(x), \quad (4)$$

where $F_i(x)$ is the Weibull distribution from Eq. (3), S is the number of subpopulations, N_i/N is the portion (%) of the subpopulation i and α_i and β_i are the Weibull parameters of subpopulation i. A more detailed description of the distributions, parameter estimation and goodness-of-fit tests is out of the scope of this paper and can be found elsewhere.

2.5. Sample details

A collection of preliminary results of an ongoing study on the area and thickness dependence of the breakdown characteristics of various polymer films is presented in this paper. Various commercial-grade metallized polymer films have been studied, including BOPP, PEN (polyethylene naphthalate) and PPS (polyphenylene sulfide) films in the thickness range of 4 to 13.8µm. Metallized films were tested in dry conditions with the film arrangement presented in sub-chapter 2.2. In addition, the measurement technique was applied to a non-metallized 13.8µm hazy BOPP film by using metallized BOPP-12 films as electrodes above and under the test film with the metallized sides facing towards the non-metallized test film. These preliminary measurements were performed in mineral oil in order to mitigate surface flashovers above the ~5kV voltage range. Specifications of the studied films are given in Table 1. Film thickness and relative permittivity values were taken from the film data sheets.

Table 1. Specifications of the sample films.

Dielectric	Thickness (µm)	ε_r (1 kHz)	Metallization	Sheet resistance (Ω/□)
BOPP-12	12	2.2	Zn-Al alloy	5-12
BOPP-6	6	2.2	Zn-Al alloy	5-12
BOPP-4	4	2.2	Al	5
PEN	4	3.1	Al	5
PPS	4	3.0	Al	5
BOPP-13.8	13.8	2.2	-	-

3. Results and discussion

The area dependence of the breakdown results was studied in more detail with BOPP-6 and BOPP-12 films. The studied active areas included 2, 10, 24 and 42cm^2 for BOPP-6 and 2 and 24cm^2 for BOPP-12 (25 samples per active area). BOPP-6 and BOPP-12 films were obtained from the same manufacturer and they were of the same film type. Regarding to the other studied films, results measured with only one active area per film type are presented in this paper (A=16 or 20cm^2). When considering the thickness range of all the studied films as a whole, some implications on the thickness dependence of the results may also be given.

3.2. Area and thickness dependence

3.2.1 Dielectric strength

Firstly, Weibull plots of the dielectric strengths (first measured breakdowns) of the studied films are presented in Fig. 8 and the corresponding Weibull parameters are given in Table 2. Regarding to BOPP-6, the area dependence may be clearly seen in Fig. 8 at the higher probability region (>10%) which is also supported by the decreasing α and relatively constant β values with increasing area (Table 1). On the other hand, BOPP-12 clearly shows high β value for small active area but with larger area, β decreases considerably which implies that Weibull area scaling law does not apply (β should stay constant [5, 10]). It is also interesting to notice that BOPP-4 shows lower α and β values in comparison to the thicker BOPP films. PEN and PPS films show lower dielectric strengths in comparison to the BOPP films, however, PEN-4 shows exceptionally homogeneous breakdown distribution (high β). Lastly, especially the breakdown data points of BOPP-6 and BOPP-12 show deviation from the single Weibull distributions at the low-probability region (see Fig. 8). Similar deviation from a single Weibull distribution has been previously reported for e.g. BOPP, PI (polyimide) and PTFE (polytetrafluoroethylene) films [11, 19-20]. This deviation suggests that the breakdowns may be due to more than one breakdown mechanisms and that a single 2-parameter Weibull distribution is in fact insufficient for representing such a breakdown data set.

3.2.2 Characteristic breakdown distributions

The characteristic breakdown probability distributions

Table 2. Weibull-parameters of the dielectric strengths of the studied films (first measured breakdowns).

BOPP-6					
Area (cm^2)	2*	10*	16**	24*	42*
α (V/µm)	679	567	596	547	505
β	12.15	7.74	11.16	10.40	7.80
BOPP-12					
Area (cm^2)	2*	24*			
α (V/µm)	709	607			
β	18.85	6.17			
	BOPP-4** (16cm^2)	**PEN-4**** (16cm^2)	**PPS-4**** (16cm^2)	**BOPP-13.8**** (20cm^2)	
α (V/µm)	555	365	341	613	
β	6.31	36.15	10.89	10.48	

*) 25 samples/area
**) 10 samples/area

obtained with the low-energy self-healing breakdown measurement method are shown in Fig. 9a and Fig. 9b for BOPP-6 and BOPP-12, respectively, and in Fig. 9c for the other films. Breakdown fields corresponding to 50% breakdown probabilities of the mixed distributions are shown in Fig. 10 as a function of electrode area for comparison. The number of breakdowns considered from each measured film sample was limited to 50 (if less breakdowns were obtained, all of them were taken into consideration). The data selection procedure was then applied to the selected breakdowns (see sub-chapter 2.3) and mixed Weibull distributions were fitted to the selected breakdowns on the basis of the best goodness-of-fit test result. Detailed description of the discharge energies, data selection procedure, Weibull parameter estimation, distribution fitting and the structure of the mixed distributions is out of the scope of this paper and will be covered in a future publication. In regard to BOPP-6, the aforementioned issues and the evolution of the structure of the mixed Weibull distribution with increasing active area have been previously analyzed in [13].

As the measurement method yields a large amount of breakdown data from a relatively small amount of samples, the empirical breakdown distributions shown in Fig. 9 are very detailed and various different types of breakdown patterns may be identified, similarly as in [7], [8], [11] and [20]. For example, BOPP-6 clearly shows a distinct defect population at the low-probability region which can be seen as the curvature (or S-shape) of the theoretical distributions (Fig. 9a). As the electrode area (or total measured area) is increased, the amount of low-field low-probability breakdowns increases whereas the

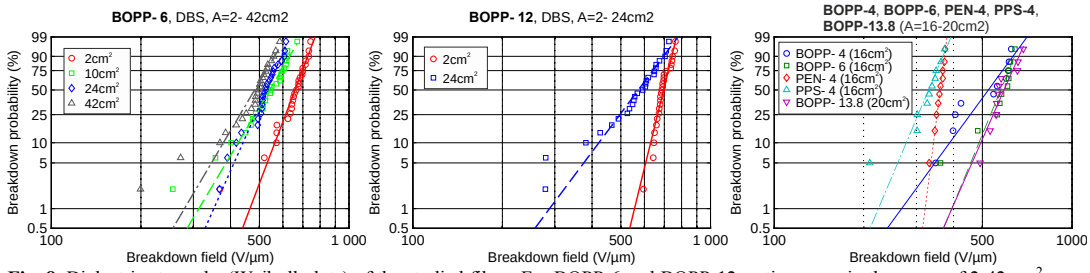

Fig. 8. Dielectric strengths (Weibull plots) of the studied films. For BOPP-6 and BOPP-12, active areas in the range of 2-42 cm^2 were used (25 measurements per area). For the other films, measurements were made with 16 or 20 cm^2 (10 measurements per area).

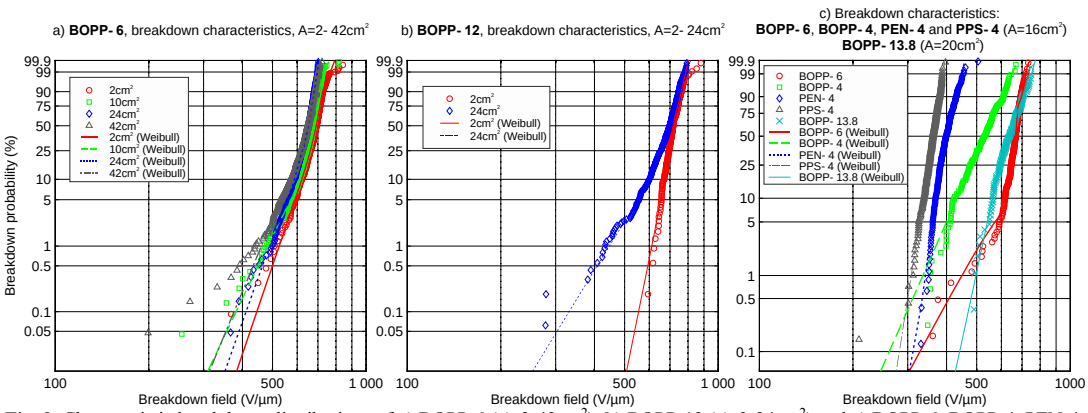

Fig. 9. Characteristic breakdown distributions of **a**) BOPP-6 (A=2-42cm^2), **b**) BOPP-12 (A=2-24cm^2) and **c)** BOPP-6, BOPP-4, PEN-4, PPS-4 and BOPP-13.8 (A=16-20cm^2). Multiple breakdowns were measured per each sample by utilizing low-energy self-healing breakdown. The number of breakdowns considered per each film sample was limited to 50. Mixed Weibull distributions were fitted to the breakdown data on the basis of the best goodness-of-fit test. The numbers of selected breakdowns were; **BOPP-6**: 546, 1103, 1040 and 1057 for 2, 10, 24 and 42cm^2 areas, respectively; **BOPP-12**: 271 and 811 for 2 and 24cm^2 areas, respectively; **BOPP-6**, **BOPP-4**, **PEN-4**, **PPS-4** (16cm^2) and **BOPP-13.8** (20cm^2): 225, 311, 396, 347 and 139, respectively.

high-probability parts (>10%) of the distributions, which may be attributed to the intrinsic breakdown strength of the polymer itself, exhibit only a slight shift towards lower dielectric strength but show no major change in distribution homogeneity. On the other hand, the results obtained from BOPP-12 samples clearly show that the breakdown distribution becomes more disperse with increasing area (Fig. 9b), as also suggested by the dielectric strength results (see Table 2 and Fig. 8.). In comparison to BOPP-6, the other studied materials do not show as clear defect populations and especially PEN and PPS films show very homogeneous distributions.

The breakdown results of the BOPP films (in the 4-13.8µm thickness range) also show that the breakdown distributions become more homogeneous with increasing thickness (Figs. 8-9). The effect is more profound with small areas (see 2cm^2 distributions for BOPP-6 and BOPP-12) and similar results have been previously reported for e.g. PI and BOPP films, for which the Weibull β increased with thickness [8, 19].

The breakdown distributions of the BOPP films also show a shift towards higher dielectric strength with increasing thickness. However, this is in contradiction to the inverse power law typically reported for solid dielectrics which proposes a decrease in dielectric strength with an increase in sample thickness [21].

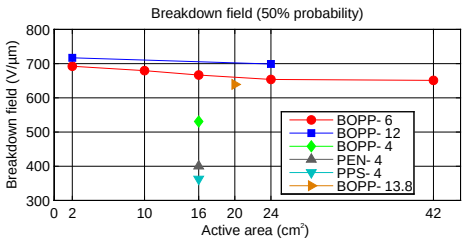

Fig. 10. Breakdown fields corresponding to the 50% breakdown probability for the studied materials as a function of electrode area. The values are based on the characteristic breakdown distributions presented in Fig. 9.

Recently, the statistical behavior of dielectric breakdown of polymers has been modeled based on the field-assisted percolation model which represents the amorphous, crystalline and free volume of polymer as a three-dimensional cubic lattice of randomly distributed traps with trap barriers in a certain range [22]. In the presence of an electric field the trap barriers are reduced which facilitates electron transfer and if the field is high enough, a percolation cluster leading to a dielectric breakdown can form across the material volume. The study showed that a small concentration of randomly distributed defects in the material volume can cause deviation from a single Weibull distribution and the defect population is more significant in large-area samples. This is coherent with the breakdown results obtained from BOPP-6 samples (Fig. 9a and Fig. 9c).

The field-assisted percolation model study also suggested the decrease of Weibull α and β values with decreasing simulated network size (sample volume) which is generally in a good agreement with the thickness dependence results obtained in this study. However, the fact that BOPP-12 first showed more homogeneous breakdown distribution in comparison to BOPP-6 with small active area, but that the effect was then mitigated when a larger sample area was measured, may be attributed to a defect population present in the BOPP-12 film. A more detailed analysis will be covered in a future publication.

4. Conclusion

A new dielectric breakdown measurement method for determining breakdown characteristics of polymer films was presented. The method is based on the measurement of multiple breakdowns per sample area beyond the weakest point of the film by utilizing low-

energy self-healing breakdown of metallized polymer film which effectively reduces the electrode loss during self-healing. The method yields a large amount of breakdown data which enables the formation of detailed material-specific breakdown fingerprints.

Breakdown characteristics of various metallized and non-metallized BOPP, PEN and PPS films in the thickness range of 4 to 13.8 µm were measured and analyzed with active areas in the range of 2 to 42 cm^2. Measurement of multiple breakdowns beyond the weakest point of each sample film enabled detailed dielectric breakdown characterization and comparison regardless of the weak points present in the films. Various types of breakdown patterns were observed and in most cases, single 2-parameter Weibull distributions were found to be insufficient for representing the breakdown data sets. Regarding to the studied BOPP films, the statistical analysis showed that defects in the films have a profound effect on the breakdown characteristics with increasing active area. Moreover, increase in film thickness was found to generally increase the breakdown strength and breakdown distribution homogeneity of BOPP films, especially with small active areas. The results obtained in this study underline the complex nature of the area and thickness dependence of dielectric breakdown characteristics of polymer films.

References

[1] M. Rabuffi and G. Picci, "Status quo and future prospects for metallized polypropylene energy storage capacitors," *Plasma Science, IEEE Transactions on*, vol. 30, no. 5, pp. 1939-1942, 2002.

[2] C.W. Reed and S.W. Cichanowski, "The fundamentals of aging in HV polymer-film capacitors," *Dielectrics and Electrical Insulation, IEEE Transactions on*, vol. 1, no. 5, pp. 904-922, 1994.

[3] W.J. Sarjeant, J. Zirnheld, and F.W. MacDougall, "Capacitors,", vol. 26, no. 5, pp. pp.1368-1392, 1998.

[4] S.A. Boggs, J. Ho, and T.R. Jow, "Overview of laminar dielectric capacitors," *Electrical Insulation Magazine, IEEE,* vol. 26, no. 2, pp. 7-13, 2010.

[5] Hauschild W. and Mosch W., *Statistical Techniques for High-Voltage Engineering*. Philadephia: Institution of Engineering and Technology, 1992.

[6] L. A. Dissado and J. C. Fothergill, *Electrical Degradation and Breakdown in Polymers*. Philadelphia: Peter Peregrinus Ltd., 1992.

[7] S.J. Laihonen, U. Gafvert, T. Schutte, and U.W. Gedde, "Influence of electrode area on dielectric breakdown strength of thin poly(ethylene terephthalate) films," in *Electrical Insulation and Dielectric Phenomena, 2004. CEIDP '04. 2004 Annual Report Conference on*, 2004, pp. 563- 567.

[8] S.J. Laihonen, U. Gafvert, T. Schutte, and U.W. Gedde, "DC breakdown strength of polypropylene films: Area dependence and statistical behavior," *Dielectrics and Electrical Insulation, IEEE Transactions on*, vol. 14, no. 2, pp. 275-286, 2007.

[9] S. Ul-Haq and G.R.G. Raju, "Weibull statistical analysis of area effect on the breakdown strength in polymer films," in *Electrical Insulation and Dielectric Phenomena, 2002 Annual Report Conference on*, 2002, pp. 518-521.

[10] Chunchuan Xu, Janet Ho, and S. Boggs, "Automatic breakdown voltage measurement of polymer films," *Electrical Insulation Magazine, IEEE*, vol. 24, no. 6, pp. 30-34, 2008.

[11] S.J. Laihonen, A. Gustafsson, U. Gafvert, T. Schutte, and U.W. Gedde, "Area dependence of breakdown strength of polymer films: automatic measurement method," *Dielectrics and Electrical Insulation, IEEE Transactions on*, vol. 14, no. 2, pp. 263-274, 2007.

[12] C. Calebrese, Le Hui, L.S. Schadler, and J.K. Nelson, "A review on the importance of nanocomposite processing to enhance electrical insulation," *Dielectrics and Electrical Insulation, IEEE Transactions on*, vol. 18, no. 4, pp. 938-945, 2011.

[13] I. Rytöluoto and K. Lahti, "New Approach to Evaluate Area-Dependent Breakdown Characteristics of Dielectric Polymer Films," *Dielectrics and Electrical Insulation, IEEE Transactions on*, 2013, in press.

[14] H. Heywang, "Physikalische und chemische Vorgänge in selbstheilenden Kunststoff-Kondensatoren," *Colloid & Polymer Science*, vol. 254, no. 2, pp. 139-147, 1976.

[15] J.H Tortai, A. Denat, and N. Bonifaci, "Self-healing of capacitors with metallized film technology: Experimental observations and theoretical model," *Journal of Electrostatics*, vol. 53, no. 2, pp. 159-169, 2001.

[16] P.-O. Sassoulas, B. Gosse, and J.-P. Gosse, "Self-healing breakdown of metallized polypropylene," in *Solid Dielectrics, 2001. ICSD '01. Proceedings of the 2001 IEEE 7th International Conference on* , 2001, pp. 275-278.

[17] B. Walgenwitz, J.-H. Tortai, N. Bonifaci, and A. Denat, "Self-healing of metallized polymer films of different nature," in *Solid Dielectrics, 2004. ICSD 2004. Proceedings of the 2004 IEEE International Conference on*, 2004, pp. 29-32.

[18] J.-H. Tortai, N. Bonifaci, A. Denat, and C. Trassy, "Diagnostic of the self-healing of metallized polypropylene film by modeling of the broadening emission lines of aluminum emitted by plasma discharge," *Journal of Applied Physics*, vol. 97, no. 5, 2005.

[19] S. Diaham et al., "Dielectric breakdown of polyimide films: Area, thickness and temperature dependence," *Dielectrics and Electrical Insulation, IEEE Transactions on*, vol. 17, no. 1, pp. 18-27, 2010.

[20] G. Raju, A. Katebian, and S.Z. Jafri, "Breakdown voltages of polymers in the temperature range 23°-250°C," *Dielectrics and Electrical Insulation, IEEE Transactions on*, vol. 10, no. 1, pp. 117-127, 2003.

[21] G. Chen, Z. Junwei, S. Li, and L. Zhong, "Origin of thickness dependent dc electrical breakdown in dielectrics," *Applied Physics Letters*, vol. 100, no. 22, 2012.

[22] K. Wu, Y. Wang, Y. Cheng, L.A. Dissado, and X. Liu, "Statistical behavior of electrical breakdown in insulating polymers," *Journal of Applied Physics*, vol. 107, no. 6, 2010.

[23] D.G. Shaw, S.W. Cichanowski, and A. Yializis, "A Changing Capacitor Technology - Failure Mechanisms and Design Innovations," *Electrical Insulation, IEEE Transactions on*, vol. EI-16, no. 5, pp. 399-413, 1981.

Publication III

I. Rytöluoto and K. Lahti, "Effect of inter-layer pressure on dielectric breakdown characteristics of metallized polymer films for capacitor applications," in *Proceedings of IEEE International Conference on Solid Dielectrics, ICSD*, pp. 682–687, 2013.

The following paper is the final version accepted for publication in IEEE International Conference on Solid Dielectrics. The published version of this paper is available at IEEE Xplore. DOI: 10.1109/ICSD.2013.6619787

Effect of Inter-Layer Pressure on Dielectric Breakdown Characteristics of Metallized Polymer Films for Capacitor Applications

I. Rytöluoto & K. Lahti
Department of Electrical Engineering
Tampere University of Technology
Tampere, Finland
ilkka.rytoluoto@tut.fi

Abstract— **Relatively high level of inter-layer pressure is often promoted for wound metallized film capacitors as it has been found to reduce the capacitance loss during self-healing breakdown. However, the effect of inter-layer pressure on the dielectric breakdown strength of metallized polymer films is not well documented and further analysis is needed. In this study, the effect of inter-layer pressure on the dielectric breakdown characteristics of various metallized polymer films is studied. By utilizing low-energy self-healing breakdown, multiple breakdowns can be measured per sample film. The results suggest that high inter-layer pressure has a negative impact on the breakdown characteristics of the metallized films studied and, in the worst case, may lead to insulation resistance failure.**

Keywords—dielectric breakdown, self-healing, metallized film, inter-layer pressure

I. INTRODUCTION AND BACKGROUND

Dielectric breakdown strength of polymer films is one of the limiting factors to be considered in film capacitors [1]. Generally, in order to ensure safe and reliable operation, the operation voltage level has to be chosen so that a sufficient safety margin from the breakdown field of the dielectric film is maintained. However, metallized film capacitors, which comprise of dielectric polymer films with thin metal electrodes evaporated directly on the film surface, have a unique ability to undergo self-healing breakdown, i.e. spontaneous isolation of the fault spot due to the vaporization of small amount of metallization layer around the breakdown channel [2-4]. Thus, self-healing capability enables metallized film capacitors to be operated safely with operation fields substantially closer to the dielectric strength of the film material [5, 6].

Self-healing breakdown of metallized film has been extensively studied in the past literature and various factors have been found to affect the self-healing breakdown process [6-11]. The self-healing process may be characterized by the energy E_{SH} discharged during a self-healing event and it may be expressed as:

$$E_{SH} = \frac{kU^b C}{R_s^c \alpha(P)} = aU^b, \quad (1)$$

where U is the voltage, C is the capacitance, R_s is the metallization sheet resistance, $\alpha(P)$ is a function which relates the inter-layer pressure to the discharge energy and a, b, c and k are experimentally definable constants. The focus of this study is on the inter-layer pressure which originates mainly from the winding tension and shrinkage of the film during the heat treatment [13]. Previous studies suggest that the pressure inside a wound capacitor element is relatively low at the outer layers of the capacitor but due to the radial compressive force from the surrounding layers it increases cumulatively towards the inner layers and may reach values of more than 10 MPa [14, 15]. Inter-layer pressure has a profound effect on the self-healing process as also suggested by Eq. (2). The pressure hinders the expansion of the breakdown plasma which results in more efficient self-healing, reduced discharge energy, and consequently, reduced size of the de-metallized area. Therefore, a relatively high level of inter-layer pressure is often promoted for wound film capacitors in order to reduce the capacitance loss due to self-healing [2, 4, 14].

However, only few studies on the effect of inter-layer pressure on the dielectric breakdown strength of metallized polymer films have been published. In [15, 16], the effect of inter-layer pressure on the dielectric breakdown strength of metallized bi-axially oriented polypropylene (BOPP) film was studied in the pressure range of 0–5.0 MPa by using brass electrodes. In the study, intermediate pressure levels were found to decrease the dielectric strength first but at 4.7 MPa the dielectric strength increased in comparison to the zero-pressure value. Unfortunately, the statistical relevance of the results remained poor as only a very limited amount of breakdown data was presented.

The aim of this study is to analyze the breakdown characteristics of various metallized capacitor-grade polymer films as a function of inter-layer pressure. A previously developed breakdown measurement method based on the measurement of multiple low-energy self-healing breakdowns per sample film is utilized [17]. A data selection procedure based on the discharge energy behavior of metallized dielectric film is utilized for validating mutual independence of the breakdown results prior to the statistical analysis. Compressive force is applied to the active area of the test samples by means of a bolt-adjustable clamping device. The method yields a large amount of breakdown data which enables the formation of detailed material-specific breakdown fingerprints as a function of inter-layer pressure.

II. EXPERIMENTAL

A. Test capacitor structure and pressure application

A film arrangement comprising of two sheets of metallized film and a dielectric spacer film (polyimide, 100 µm in thickness) was used to form a test capacitor with an active area of A=16 cm^2 (Fig. 1a). The film arrangement was sandwiched between two sheets of thick transparent film in order to support the arrangement mechanically. The whole film arrangement was then laid on the bottom plate of the test capacitor unit and electrical contacts to the metallized films were made by means of aluminum clamp electrodes at the both ends of the bottom plate. A thin rubber sheet (1 mm in thickness) was laid on the film arrangement to smoothen the contact and then a 16 cm^2 square piece of thin acrylic plastic plate was used on top of the rubber to focus the pressure on the active area of the test capacitor (Fig. 1b). Finally, a lightweight top plate made of transparent acrylic plastic was laid on the top of the structure.

In order to apply inter-layer pressure on the active area of the film arrangement, a bolt-adjustable clamping device shown schematically in Fig. 1b was used to exert compressive force on the active area of the test capacitor. The clamping device comprised of a heavy-duty steel frame and two steel plates. A fine threaded M10 bolt was fitted into the steel frame which allowed smooth adjustment of the compressive force F_{comp}. An ACBES-3t load cell was mounted beneath the clamping plates which allowed the measurement of the total force F_{tot} by means of a Kyowa WGI-400A instrumentation amplifier. The inter-layer pressure P could then be calculated as:

$$P = \frac{F_{comp}}{A} = \frac{F_{tot} - m_{setup} \cdot g}{A} \qquad (2)$$

where m_{setup} is the total mass of the test capacitor and the lower steel plate and g the gravitation constant (=9.81 m/s^2).

The measurement circuit used for the breakdown analysis is presented schematically in Fig. 2. In the test circuit, the test capacitor unit is depicted as the capacitance C_{DUT}. The purpose of the parallel capacitance C_P is to act as a fast charge storage

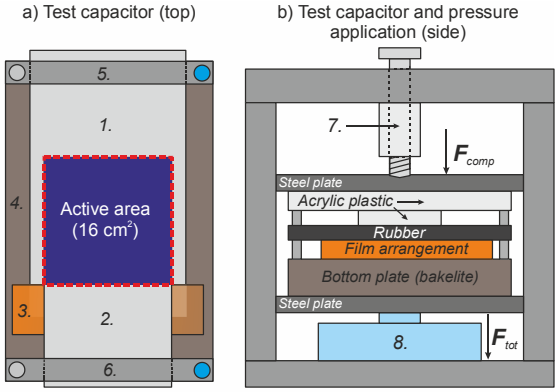

Fig. 1. **a)** Film arrangement and test capacitor structure. **b)** bolt-adjustable pressure clamping device for pressure application. **1-2**: Metallized film (metallization facing down), **3**: dielectric spacer film, **4**. bottom plate, **5-6**: aluminium clamp electrodes (to high voltage source and ground). **7**: fine-threaded M10 bolt, **8**: load cell for force measurement.

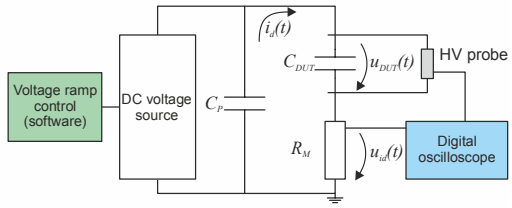

Fig. 2. Measurement circuit for the self-healing breakdown measurement.

buffer during a breakdown in the test capacitor. When a breakdown occurs in the test capacitor, a portion of the charge stored in the total capacitance C=C_P+C_{DUT} is rapidly discharged at the fault spot. The discharge current $i_d(t)$ is then measured with an impulse current measurement resistor R_M as voltage signal $u_{id}(t)$. Simultaneously, the voltage $u_{DUT}(t)$ across the test capacitor is measured with a high voltage probe. Discharge current and test capacitor voltage during each breakdown event were recorded with an oscilloscope operating in the sequence acquisition mode and triggered to the rising edge of the discharge current signal. The discharge energy E_{SH} could then be calculated by integrating the test capacitor voltage and the discharge current over the whole discharge duration τ:

$$E_{SH} = \int_0^{\tau} u_{DUT}(t) i_d(t) dt. \qquad (3)$$

B. Measurement of multiple breakdowns

Previously, a new measurement method for determining breakdown characteristics of polymer films has been developed and evaluated [17]. In summary, the measurement method is based on the concept of low-energy self-healing breakdown of metallized polymer film which effectively reduces the de-metallized area around each breakdown site and the damage to the surrounding electrode layer. Low-energy self-healing is realized by minimizing the total capacitance C=C_P+C_{DUT} in the self-healing circuit, which, according to Eq. (1), reduces the discharge energy. In practice, as the total charge available for the breakdown process is then limited, a major voltage drop will occur during each self-healing breakdown which effectively reduces the power density of the breakdown arc and leads to the rapid constriction of the breakdown arc. Therefore, as the damage to the metallized layer is minimized, a large amount of breakdowns may be measured from the same sample area which enables the formation of detailed material-specific breakdown fingerprints.

The progression of the breakdown measurement is illustrated schematically in Fig. 3. The voltage of the DC voltage source is ramped from zero (Fig. 3a) with a constant speed of 30 V/s by means of a LabVIEW-based software until the voltage U_{DBS} corresponding to the dielectric breakdown strength of the film sample is reached and the first breakdown occurs in the film (Fig. 3b). As the voltage ramp is continued beyond the first breakdown, more breakdowns begin to occur at an increasing frequency (Fig. 3c) until finally, either electrical contact is lost (due to de-metallization) or insulation resistance failure occurs (Fig. 3d).

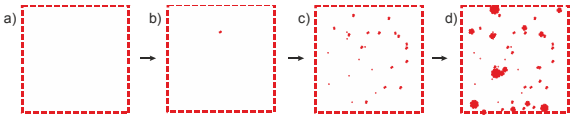

Fig. 3. Progression of the breakdown measurement. The square area represents the active area of the test capacitor and the red spots depict breakdown evolution as the voltage is increased steadily. **a)** beginning of test, $U=0$, **b)** first self-healing breakdown, $U=U_{DBS}$, **c)** multiple self-healings, $U>U_{DBS}$, **d)** end of test.

As multiple self-healing breakdowns are measured per sample area, only the breakdowns which appear independent should be chosen for further statistical analysis. One approach for the selection is to analyze the discharge energy behavior of the measured self-healing breakdowns on the basis of the power dependence $E_{SH}=aU^b$ [14]. The concept of the procedure is best described graphically, as shown in Fig. 4, in which the calculated discharge energies of 50 first breakdowns measured from 10 samples of metallized BOPP (thickness d=6 µm, C_P=3.3 nF, C_{DUT}=5.20 nF) are shown as a function of the breakdown voltage. Only those breakdowns are chosen (i) for which the corresponding discharge energies follow the trend preset by the first measured self-healing breakdowns and (ii) for which the breakdown voltage is higher than that of the first breakdown of the sample. A physical explanation for the lower-than-expected discharge energies or breakdown voltages is that those breakdowns may have occurred near previous breakdown sites, resulting in lower discharge energy as the electrode layer around the breakdown site is already deteriorated or de-metallized. Moreover, these breakdowns may also be attributed to successive self-healing taking place at the same breakdown site, presumably due to graphite formation and incomplete self-healing [10].

C. Statistical analysis of the breakdown data

For the statistical analysis of the breakdown data in this study, 2-parameter Weibull distributions and additively mixed Weibull distributions are utilized. The cumulative distribution function of a 2-parameter Weibull distribution is of form [18]:

$$F(x)=1-\exp\left\{-\left(\frac{x}{\alpha}\right)^{\beta}\right\},\ x\geq 0, \tag{4}$$

where x is the measured variable (e.g. breakdown voltage), α is the scale parameter which corresponds to the value of x at 63.2% failure probability and β is the shape parameter depicting the slope of the theoretical distribution. The cumulative distribution function of an additively mixed 2-parameter Weibull distribution is of form [18]:

$$F(x)=\sum_{i=1}^{S}\frac{N_i}{N}F_i(x), \tag{5}$$

where $F_i(x)$ is the Weibull distribution from Eq. (4), S is the number of subpopulations, N_i/N is the portion (%) of the subpopulation i and α_i and β_i are the Weibull parameters of subpopulation i. A more detailed description of the distributions, parameter estimation and goodness-of-fit tests is out of the scope of this paper and can be found elsewhere.

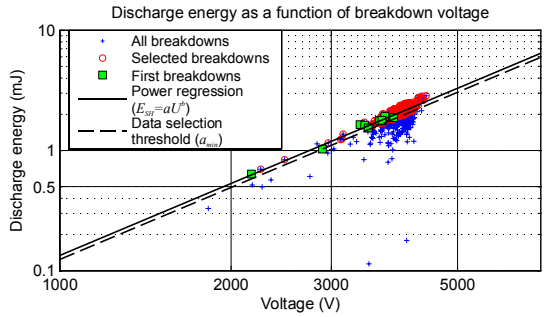

Fig. 4. Breakdown data selection procedure. The discharge energies of all the measured self-healing breakdowns are shown in blue. The first breakdowns (green) are used for the determination of the slope b of the power regression line (solid line, $E=aU^b$). By taking the energy variation of the first points into account, a_{min} is determined and used as a threshold (dashed line). Only the data points with discharge energies above the threshold and with breakdown voltages higher than the first breakdown of the sample are chosen (red).

D. Sample details and test series specifications

Various commercial-grade metallized polymer films were chosen for the breakdown measurements including BOPP, PEN (polyethylene naphthalate) and PPS (polyphenylene sulfide) films. The specifications of the sample films and test series are shown in Tables 1 and 2, respectively. Measurements at zero inter-layer pressure were made without C_p in order to minimize the capacitance involved in the self-healing circuit. The sample capacitances calculated as $C_{DUT}=\varepsilon_0\varepsilon_r A/d$ were 5.20 nF, 7.80 nF, 10.98 nF and 10.63 nF for BOPP-6, BOPP-4, PEN and PPS, respectively. It should be noticed that the sample capacitance decreases gradually during the test with each self-healing breakdown. When inter-layer pressure is increased, the level of discharge energy decreases, and subsequently, the discharge current pulse measurable from the test capacitor terminals decreases in amplitude. Thus, C_p of 3.3 nF was used for the measurements with inter-layer pressure in order to ensure a clear trigger condition for the measurement. As shown in Table 2, ten samples of each material were measured up to 2.0 MPa. Beyond 2.0 MPa, only the materials which still performed to satisfaction were measured.

TABLE I. SPECIFICATIONS OF THE SAMPLE FILMS

Dielectric	Film thickness (µm)	ε_r (1 kHz)	Metallization	Sheet resistance (Ω/□)
BOPP-6	6	2.2	Zn-Al alloy	5-12
BOPP-4	4	2.2	Al	5
PEN	4	3.1	Al	5
PPS	4	3.0	Al	5

TABLE II. SPECIFICATIONS OF THE TEST SERIES

C_p (nF)	Inter-layer pressure (MPa)	Number of samples measured			
		BOPP-6	BOPP-4	PEN	PPS
0	0	10	10	10	10
3.3	0.5	10	10	10	10
3.3	1.0	10	10	10	10
3.3	2.0	10	10	10	10
3.3	3.0	-	-	3	-
3.3	4.0	5	5	3	-
3.3	6.0	3	3	-	-
3.3	8.0	3	3	-	-

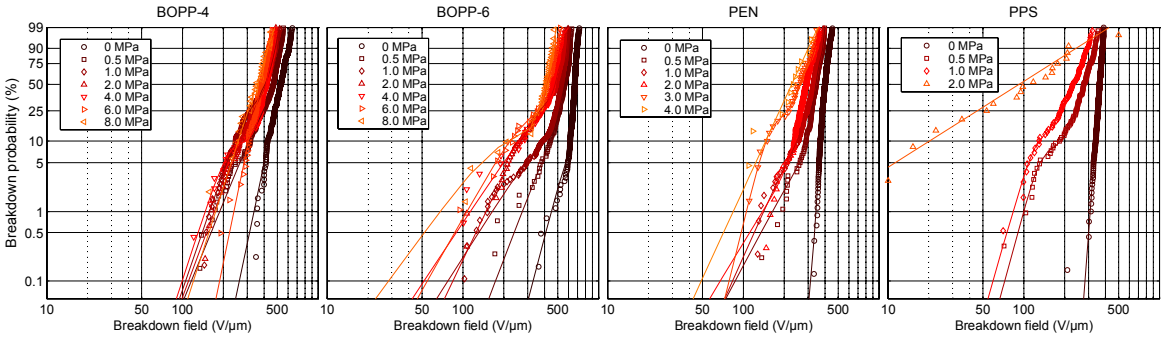

Fig. 5. Characteristic breakdown probability distributions of the metallized films as a function of inter-layer pressure. Multiple breakdowns were measured from each sample film and the data selection criterion based on the discharge energy was applied to 50 first breakdowns. Theoretical Weibull and mixed Weibull distributions fitted to the breakdown data are shown as solid lines. Note that the number of breakdowns for each empirical distribution is not constant.

III. Results and Discussion

A. Breakdown characteristics as a function of pressure

The measured characteristic breakdown probability distributions of the metallized films are shown in Fig. 5 as a function of inter-layer pressure. The number of breakdowns considered from each measured film sample was limited to 50 (if less breakdowns were obtained, all of them were taken into consideration). The data selection procedure was then applied to the breakdowns. The amount of selected breakdowns is shown in Table 3 for each material and inter-layer pressure condition. As the measurement method yields a large amount of breakdown data from a relatively small amount of samples, the empirical breakdown distributions shown in Fig. 5 are very detailed. Single Weibull and mixed Weibull distributions (with 2 to 4 subpopulations) were then fitted to the selected breakdowns on the basis of the best goodness-of-fit test result.

The results were analyzed as follows. The breakdown strength, as determined by the first measured breakdowns of each sample film, was determined separately for each material as a function of inter-layer pressure. Single Weibull distributions were then fitted to the first measured breakdowns and Fig. 6 shows the effect of inter-layer pressure on the Weibull α parameter corresponding to the dielectric breakdown strength of each material. Moreover, the electric fields corresponding to 5% and 50% probabilities of the characteristic breakdown probability distributions (from Fig. 5) are shown in Fig. 7 as a function of inter-layer pressure.

TABLE III. Number of selected breakdowns prior to statistical analysis for each dielectric and inter-layer pressure condition.

Pressure (MPa)	Number of selected breakdowns			
	BOPP-6	BOPP-4	PEN	PPS
0	311	225	396	347
0.5	203	328	230	156
1.0	465	295	205	94
2.0	159	239	167	17
3.0	-	-	35	-
4.0	72	116	11	-
6.0	47	102	-	-
8.0	36	26	-	-

Figures 5-7 together indicate that inter-layer pressure has clearly a negative effect on the breakdown characteristics of the studied dielectric materials. Firstly, when inter-layer pressure is increased to 1.0 MPa, the calculated dielectric breakdown strengths of all the materials are reduced to the range of 146 V/µm (PPS) to 257 V/µm (PEN) (see Fig. 6). With further increase in inter-layer pressure, the dielectric breakdown

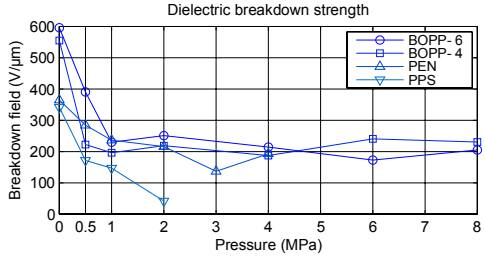

Fig. 6. Dielectric breakdown strength of the materials as a function of inter-layer pressure (Weibull α of the first breakdowns).

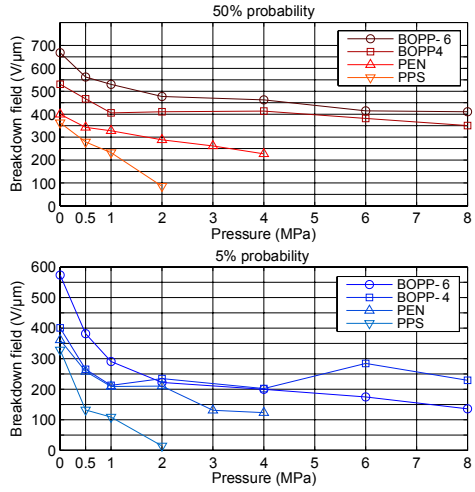

Fig. 7. Electric field stresses corresponding to the 50% and 5% breakdown probabilities of the characteristic breakdown distributions as a function of pressure.

strengths decrease more or stay at a relatively same level. However, as the first breakdowns are self-healing (except for some PPS samples at high pressure in this study), the dielectric breakdown strength (first breakdowns) itself is not as critical when considering practical applications. Instead, the 50% and 5% characteristic breakdown probabilities (Fig. 7) are more relevant. The 50% probabilities may be attributed to the intrinsic pressure-dependent breakdown characteristics of the polymers. Fig. 7 shows that the breakdown characteristics of both 4 and 6 µm BOPP films are superior in comparison to PEN and PPS in the whole pressure range from 0 to 8.0 MPa. The electric field values corresponding to 5% probabilities (Fig. 7) are essential for practical applications in metallized film capacitors as some breakdowns may be tolerated due to the self-healing capability. The 5% probability values show larger deviation in comparison to 50% values due to the smaller amount of breakdowns at the low-probability region. It should also be pointed out that the 5% probability point is only taken as an example in this study and it should be chosen according to the practical application.

Regarding to the electrical insulation capability of the films as a function of pressure, the operation limits of both PEN and PPS were encountered in this study. Inter-layer pressure was found to have a devastating effect especially on the breakdown characteristics of PPS. In the inter-layer pressure range of 0.5 to 1.0 MPa, all the samples of PPS suffered a permanent insulation resistance failure when the voltage was increased beyond a certain threshold. Similar behavior occurred with PEN beyond 2.0 MPa. This behavior is illustrated in Fig. 8 for PPS at 1.0 MPa and for PEN at 3.0 MPa by showing the relation between the first breakdowns and the point of insulation resistance failure. Clearly, as the electric field was increased beyond the first breakdown of each sample, more and more breakdowns occurred rapidly until a permanent failure resulted. At 2.0 MPa some of the PPS samples suffered a permanent failure as soon as the first breakdown occurred. However, neither of the BOPP films suffered permanent failures regardless of the inter-layer pressure.

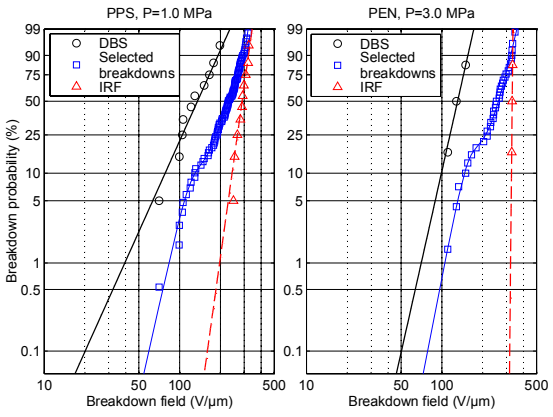

Fig. 8. Breakdown behavior of ten PPS film samples at 1.0 MPa inter-layer pressure (left) and of three PEN film samples at 3.0 MPa inter-layer pressure (right). Dielectric breakdown strength (DBS), the characteristic breakdown distribution and the points of insulation resistance failure (IRF) are shown separately.

B. Implications

Some remarks should be made regarding to the shapes of the characteristic breakdown distributions shown in Fig. 5. The distinct curvature (or "S-shape") in some of the empirical breakdown distributions implies that multiple breakdown mechanisms may be operative in the metallized films [18, 19]. For example, BOPP-6 shows clearly a distinct defect population at the low probability region which is coherent with the results obtained with the same film type in a previous study [17]. The defect population can be attributed to the combination of various factors such as defects and voids in the material volume or to other extrinsic factors such as dust, foreign particles, film wrinkling, electrode edge effect or mechanical stress due to the pressure application. In Fig. 5 it is especially interesting that the defect population in BOPP-6 samples becomes more significant as the inter-layer pressure is increased whereas BOPP-4 does not show as drastic behavior. This behavior may be related to small amounts of random defects distributed in the material volume which can cause deviation from a single Weibull distribution [20]. Moreover, PEN and PPS at zero inter-layer pressure show very homogeneous breakdown distributions but as inter-layer pressure is increased, distinct defect populations begin to evolve (see Fig. 5). A more detailed analysis of the underlying factors is out of the scope of this paper and will be covered in the future work.

It should also be considered that the pressure application methodology has almost certainly an effect on the breakdown behavior of the films, as even the smallest particles or other non-idealities in the measurement setup may distort the breakdown behavior. However, the fact that the measurement is continued beyond the weakest point of the film counteracts this effect and especially the 50% probability values shown in Fig. 7 should give a detailed picture of how the polymers perform as a function of pressure. The fact that inter-layer pressure was found to have a negative effect on the breakdown characteristics of the metallized films at the whole pressure range studied differs from the previous experimental results reported for various polymer films [16, 21]. Generally, it is suggested that cavities or low-density regions with increased probability for impact ionization or electron avalanche may be formed in the polymer bulk under high electric field stress and that external pressure should hinder the formation of such regions, thus leading to increased dielectric strength [22]. It may be speculated that the relatively low thickness range of the films used in this study (4 to 6 µm), bi-axial orientation of the films or the metallization layer may have an influence on the pressure-dependent breakdown characteristics of films. However, a more detailed analysis is out of the scope of this paper.

Lastly, it should be emphasized that the analysis presented in this study is only related to the breakdown behavior of the studied metallized films. This is due to the fact that the total capacitance in the self-healing circuit was set deliberately as small. For the analysis of the self-healing performance of metallized dielectric films, the capacitance should be set so that it simulates the situation in a real capacitor element in order to achieve realistic discharge energy behavior. Such analysis will also be covered in the future work.

IV. Conclusions

Dielectric breakdown characteristics of Al-metallized BOPP, PEN and PPS films were studied as a function of inter-layer pressure in the range of 0 to 8.0 MPa. Multiple breakdowns were measured from each film sample by utilizing the concept of low-energy self-healing breakdown and a discharge energy based data selection process. Inter-layer pressure was found to have a negative effect on the breakdown characteristics of all the films at the whole pressure range studied. The breakdown characteristics of the metallized BOPP films were found to be superior beyond the inter-layer pressure level of 2.0 MPa. PPS and PEN films were found to suffer permanent insulation resistance failure beyond 2.0 MPa. The results underline the fact that the breakdown characteristics of various metallized polymer films should be determined carefully in order to ensure proper design and operation in practical applications.

Acknowledgment

DuPont Teijin Films (Luxembourg) and Tervakoski Films Group (Finland) are greatly acknowledged for the collaboration and for providing the metallized films used in this study.

Appendix

Fig. 9 shows a photograph of the pressure distribution achievable with the test setup. Fujifilm Prescale pressure sensitive film was placed on the bottom plate of the test capacitor and compressive force of F_{Comp}=3.20 kN corresponding to 2.0 MPa of inter-layer pressure was applied. The red color intensity corresponds to the pressure intensity (pressure charts and more information are available from the film manufacturer). The force was measured by means of a load cell mounted under the setup (see Fig. 1). Although some local deviation in the pressure distribution may be seen, the distribution is still relatively homogeneous. In practice, it is very demanding to achieve a perfect pressure distribution for active in the range of several or tens of cm^2 which may have an effect on the measurement results.

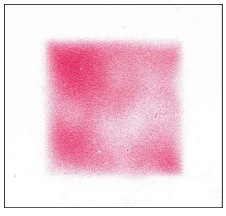

Fig. 9. A photograph showing of the pressure distribution of the test setup. P=2.0 MPa, A=16 cm^2. The red color intensity corresponds to the pressure intensity.

References

[1] L. A. Dissado and J. C. Fothergill, *Electrical Degradation and Breakdown in Polymers*. Philadelphia: Peter Peregrinus Ltd., 1992.

[2] D.G. Shaw, S.W. Cichanowski, and A. Yializis, "A Changing Capacitor Technology - Failure Mechanisms and Design Innovations," *Electrical Insulation, IEEE Transactions on*, vol. EI-16, no. 5, pp. 399-413, 1981.

[3] M. Rabuffi and G. Picci, "Status quo and future prospects for metallized polypropylene energy storage capacitors," *Plasma Science, IEEE Transactions on*, vol. 30, no. 5, pp. 1939-1942, 2002.

[4] C.W. Reed and S.W. Cichanowski, "The fundamentals of aging in HV polymer-film capacitors," *Dielectrics and Electrical Insulation, IEEE Transactions on*, vol. 1, no. 5, pp. 904-922, 1994.

[5] Sarjeant, W.J.; Zirnheld, J.; MacDougall, F.W.; , "Capacitors," *IEEE Transactions on Plasma Science,* vol. 26, no. 5, pp. 1368-1392, 1998

[6] Boggs, S. A.; Ho, J.; Jow, T. R.; , "Overview of laminar dielectric capacitors," *IEEE Electrical Insulation Magazine*, vol. 26, no. 2, pp. 7-13, 2010

[7] H. Heywang, "Physikalische und chemische Vorgänge in selbstheilenden Kunststoff-Kondensatoren," *Colloid & Polymer Science*, vol. 254, no. 2, pp. 139-147, 1976.

[8] J.H Tortai, A. Denat, and N. Bonifaci, "Self-healing of capacitors with metallized film technology: Experimental observations and theoretical model," *Journal of Electrostatics*, vol. 53, no. 2, pp. 159-169, 2001.

[9] P.-O. Sassoulas, B. Gosse, and J.-P. Gosse, "Self-healing breakdown of metallized polypropylene," in *Solid Dielectrics, 2001. ICSD '01. Proceedings of the 2001 IEEE 7th International Conference on* , 2001, pp. 275-278.

[10] B. Walgenwitz, J.-H. Tortai, N. Bonifaci, and A. Denat, "Self-healing of metallized polymer films of different nature," in *Solid Dielectrics, 2004. ICSD 2004. Proceedings of the 2004 IEEE International Conference on*, 2004, pp. 29-32.

[11] J.-H. Tortai, N. Bonifaci, A. Denat, and C. Trassy, "Diagnostic of the self-healing of metallized polypropylene film by modeling of the broadening emission lines of aluminum emitted by plasma discharge," *Journal of Applied Physics*, vol. 97, no. 5, 2005.

[12] V. O. Bel'ko, P. N. Bondarenko, and O. A. Emel'yanov, "The Dynamic Characteristics of Self-Healing Processes in Metal Film Capacitors," *Russian Electrical Engineering*, vol. 78, no. 3, pp. 138-142, 2007.

[13] Shanshan, Q.; Shilei, M.; Boggs, S. A.; , "The mechanism of clearing in metalized film capacitors," *Conference Record of the 2012 IEEE International Symposium on Electrical Insulation (ISEI),* pp. 592-595, 2012.

[14] Yaohong Chen et al., "Study on Self-Healing and Lifetime Characteristics of Metallized-Film Capacitor Under High Electric Field," *Plasma Science, IEEE Transactions on*, vol. 40, no. 8, pp. 2014-2019, 2012.

[15] S. Tandon, "Modeling of stresses in cylindrically wound capacitors: Characterization and the influence of stress on dielectric breakdown of polymeric film," University of Massachusetts Amherst, Massachusetts, Ph.D. Thesis 1997.

[16] S. Tandon and R.J. Farris, "Metallized Polypropylene Film in Capacitors: Characterization and The Effect of Interfacial Pressure on the Dielectric Strength," in *MRS Proceedings*, vol. 476, 1997.

[17] I. Rytöluoto and K. Lahti, "New Approach to Evaluate Area-Dependent Breakdown Characteristics of Dielectric Polymer Films," *Dielectrics and Electrical Insulation, IEEE Transactions on*, 2013, in press.

[18] Hauschild W. and Mosch W., *Statistical Techniques for High-Voltage Engineering*. Philadephia: Institution of Engineering and Technology, 1992.

[19] Kececioglu D., *Reliability Engineering Handbook Vol.1*.: DEStech Publications, Inc., 2002.

[20] K. Wu, Y. Wang, YH Cheng, L.A. Dissado, and XJ Liu, "Statistical behavior of electrical breakdown in insulating polymers," *Journal of Applied Physics*, vol. 107, no. 6, 2010.

[21] N. Zebouchi, T. G. Hoang, and Bui Ai, "Thermoelectronic breakdown with pressure and space charge effects in polyethylene,", *Journal of Apllied Physics*, vol. 81, no. 5, 1997.

[22] V. A. Zakrevskii, N. T. Sudar A. Zaopo and Yu. A. Dubitsky, "Mechanism of electrical degradation and breakdown of insulating polymers," *Journal of Apllied Physics*, vol. 93, no. 4, 2003.

Publication IV

I. Rytöluoto, K. Lahti, M. Karttunen, M. Koponen, S. Virtanen, and M. Pettersson, "Influence of low amounts of nanostructured silica and calcium carbonate fillers on the large-area dielectric breakdown performance of bi-axially oriented polypropylene," in *2014 IEEE Conference on Electrical Insulation and Dielectric Phenomena (CEIDP)*, pp. 655–658, 2014.

The following paper is the final version accepted for publication in IEEE Conference on Electrical Insulation and Dielectric Phenomena. The published version of this paper is available at IEEE Xplore. DOI: 10.1109/CEIDP.2014.6995848

Influence of Low Amounts of Nanostructured Silica and Calcium Carbonate Fillers on the Large-Area Dielectric Breakdown Performance of Bi-axially Oriented Polypropylene

I. Rytöluoto[1], K. Lahti[1], M. Karttunen[2], M. Koponen[2], S. Virtanen[3], M. Pettersson[3]
[1]Tampere University of Technology, Department of Electrical Engineering, Tampere, Finland
[2]Technical Research Centre of Finland, Tampere, Finland
[3]Nanoscience Center, Department of Chemistry, University of Jyväskylä, Jyväskylä, Finland

Abstract — **Influence of low amounts (1.0-2.0wt-%) of nanostructured silica and calcium carbonate fillers on the large-area dielectric breakdown performance of bi-axially oriented polypropylene (BOPP) is analyzed. A multi-breakdown measurement method based on the self-healing breakdown capability of metallized film is utilized for the breakdown characterization in order to cover relatively large total film areas, thus leading to results of higher relevance from the practical point-of-view. The dispersion and distribution qualities of filler particles at the nanoscale are evaluated with transmission electron microscopy (TEM) imaging. Weibull statistical analysis suggests that the breakdown distribution homogeneity can be improved with both the filler types. The 1.0wt-% silica-BOPP composite also shows a shift of the weakest points towards higher dielectric strength in comparison to the neat BOPP. However, with increasing filler content, new failure modes are introduced into the nanocomposites, hence decreasing the overall breakdown performance in the >5% breakdown probability region in comparison to the un-filled reference BOPP film.**

Keywords—Polymer nanocomposite film, polypropylene, silica, calcium carbonate, dielectric breakdown performance

I. INTRODUCTION

In recent years, an increasing amount of research on dielectric polymer nanocomposite films for next-generation capacitor applications has emerged and improvements in properties such as dielectric breakdown strength are aspired [1]. In general, potential improvements in the short-term breakdown performance may be achieved with polymer nanocomposites of permittivity-matching constituents and preferably with low nanoparticle fill-fractions, as demonstrated e.g. with nano-silica filled cross-linked polyethylene (XLPE) [2], core functionalized nano-silica filled epoxy [3] and nano-silica filled bi-axially oriented polypropylene (BOPP) films [4], [5], [6]. However, filler dispersion and distribution in the polymer matrix as well as the film processing conditions [6], [7] strongly affect the dielectric properties of the end-product and the potential advantageous effect of a smooth nanodispersion on the breakdown performance can be overwhelmed if micro-aggregates are present in the material, as reported e.g. in the case of nano-calcium-carbonate-filled BOPP films in [8]. Apart from the material composition and processing alone, accurate statistical knowledge of the breakdown performance is of fundamental importance during the development and optimization phase of novel dielectric films [9]. However, the current state-of-the-art dielectric breakdown measurement methods often result only in a limited amount of data, leading to poor statistical relevance and impaired evaluation of the breakdown performance [10]. In this paper, the influence of low amounts of nanostructured silica and calcium carbonate filler particles on the large-area dielectric breakdown performance of BOPP is studied. A multi-breakdown measurement method based on the self-healing breakdown capability of metallized film is utilized for the breakdown characterization in order to cover relatively large total sample areas with a slow rate-of-rise approach, thus leading to results of higher relevance from the practical point-of-view [10], [11]. The dispersion and distribution qualities of the filler particles at the nanoscale are evaluated with transmission electron microscopy (TEM) imaging.

II. EXPERIMENTAL

A. Film processing and sample details

The sample details along with the measured average film thicknesses and standard deviations are presented in Table 1. Unstabilized polypropylene homopolymer HC318BF in powder form (a non-commercial product from Borealis N.V.) was used as the matrix polymer. The filler loadings of 1.0wt-% and 2.0wt-% of Aerosil R812 S (hydrophobic fumed silica by Evonik) and Socal 322 (precipitated calcium carbonate (PCC) by Solvay) were studied. One of the compounds included both 1.0wt-% of silica and 1.0wt-% of PCC. Process stabilizer

TABLE I. SAMPLE FILM DETAILS.

Sample code	Filler loading (wt-%)			*N* samples / total film area (cm^2)	Film thickness (µm)	
	Planned		*Realized*		*Avg.*	*SD*
	Silica	PCC				
PP-Sil-1	1.0	-	1.14	10 / 810cm^2	18.85	2.36
PP-Sil-2	2.0	-	2.24	10 / 810cm^2	18.06	2.22
PP-PCC-1	-	1.0	0.80	10 / 810cm^2	23.19	2.44
PP-PCC-2	-	2.0	1.87	10 / 810cm^2	22.94	2.66
PP-Sil+PCC	1.0	1.0	1.62	10 / 810cm^2	25.22	2.32
PP-Ref	-	-	-	6 / 486cm^2	21.33	2.58

Irganox 1010 (0.47wt-%) and co-stabilizer Irgafos 168 (0.35wt-%) were added to the compounds. The processing was conducted at the VTT Technical Research Centre of Finland.

The raw powder materials were first pre-mixed manually in a polyethylene bag (approximate mixing time of 2 min) and thereafter compounded by a Berstorff ZE 25/48D twin screw compounder with high-shear screw geometry, two separate kneading sections and a melt filter (screen size 42µm). The compound was cooled in a water bath under a laminar air flow hood over the cooling section. Polymers were dried at 70°C for 1.5 hours in an oven and for 0.5 hour in a vacuum oven before the compounding. Cast films were then extruded by a Brabender Plasticorder single screw extruder with a three-layer screen pack. The single screw had three stages with a mixing zone and the compression was 4:1. The films (500-700µm) were cast through a 120mm slot die onto a chill roll at +90°C. Screw speed was 100rpm and cylinder temperatures were between 220°C and 230°C. Compounds were also dried before the cast film extrusion. Finally, the cast films were bi-axially oriented with a Brückner KARO IV film stretching machine (set temperature 157°C, stretching ratio 5.4x5.4). The realized filler amounts were determined by burning the organic polymer and additives in an oven at 600°C for 30min+10min (see Table 1) according to the ISO 3451-1 standard.

For the multi-breakdown measurement, sample films were cut to 110mm x 110mm dimensions from the bi-axially oriented film sheets. Sample film thicknesses were measured systematically at 25 points covering a 100mm x 100mm area with an LE1000-1 high-precision thickness measurement gauge (accuracy 0.1µm, resolution 0.05µm). The average film thicknesses with the standard deviations are presented in Table 1. Thickness deviation of the sample films was taken into account during the breakdown field calculation. In order to realize the self-healing breakdown capability, Zn-Al-metallized BOPP film (12µm Tervakoski PSX) was used as the electrode film. The sample film was sandwiched between two electrode films (metallized surfaces facing towards the sample film), thus forming a test capacitor with an active area of 81cm^2.

B. Large-area multi-breakdown measurement

The large-area breakdown measurement was based on the self-healing breakdown capability of metallized film which enables the measurement of multiple breakdowns from the sample area [6], [10], [11]. During the self-healing process, the fault spot is spontaneously isolated from the rest of the electrode due to the vaporization of small amount of metallization layer around the breakdown channel. The measurements were conducted in oil (Shell Diala DX) in accordance with IEC-60243 standard in order to mitigate surface flashovers. The DC voltage across the test capacitor was first raised to approximately 40-60% of the probable short-time breakdown voltage with a fast ramp speed of 400V/s, after which a slow ramp speed of 30V/s was used for measuring the self-healing breakdown events, roughly in accordance to the slow rate-of-rise test defined in the IEC-60243-1. The test setup and the procedure are discussed in more detail in [10].

During each discharge event in the test capacitor, the discharge current, test capacitor voltage and the time-signature of the event were recorded with a high-resolution oscilloscope operated in the sequence-acquisition mode and triggered to the positive rising edge of the discharge current signal. This allowed a detailed determination of the breakdown voltage, voltage drop, peak current, discharge energy and various pulse time parameters for each event. A video was recorded from the top of the test capacitor unit for the whole duration of the breakdown measurement, allowing detailed chronological analysis of the breakdown progression of the sample after the measurement. Breakdown fields were determined manually by rigorously determining the average thickness around the discharge spot (by means of the video recording) and by calculating the average breakdown field event-by-event in MATLAB.

C. Breakdown data selection procedure

A data selection procedure based on the discharge energy characteristics of the self-healing breakdown process was utilized for excluding non-breakdown events from the measurement data. It has been hypothesized that discharge events with the discharge energies and breakdown voltages not following the trend set by the first breakdowns may be attributed to successive breakdowns occurring close to or at previous breakdown sites or to other non-breakdown events (partial discharges, surface flashovers). The data selection was based on two criteria, namely by selecting only the discharge events (i) for which the corresponding discharge energies followed the trend preset by the first measured self-healing breakdowns and (ii) for which the breakdown voltages were higher than that of the previously selected breakdown. First breakdowns were used as a basis for the data selection procedure. The procedure is discussed in detail elsewhere [6], [10], [11].

D. Statistical analysis

For the statistical analysis of the breakdown data, 2-parameter Weibull distributions and additively mixed Weibull distributions were utilized:

$$F(x) = \sum_{i=1}^{S} \frac{N_i}{N} F_i(x) = \sum_{i=1}^{S} \frac{N_i}{N} \left[1 - \exp\left\{ -\left(\frac{x}{\alpha_i} \right)^{\beta_i} \right\} \right]. \quad (1)$$

In (1), $F_i(x)$ is the 2-parameter Weibull distribution, S is the number of subpopulations, N_i/N is the portion (%) of the subpopulation i and α_i and β_i are the Weibull parameters of subpopulation i. The scale parameter α corresponds to the value of x at the 63.2% failure probability and the shape parameter β depicts the slope or homogeneity of the theoretical distribution. For a single 2-parameter Weibull distribution, S and the portion N_i/N in (1) are equal to 1 and 100%, respectively. Maximum-likelihood estimation (MLE) and non-linear regression (NLR) methods were used for the parameter estimation and the analysis was performed with Weibull++ and MATLAB software. 90% confidence bounds were calculated based on the Fisher Matrix (FM) method.

III. Results and Discussion

A. Structural characterization

Figure 1 presents TEM-micrographs of ultrathin sections of the studied PP-composites. The ultrathin sections of the cast film samples were obtained using a Diatome 35° diamond

knife at room temperature with a Leica Reichert Ultracut ultramicrotome. The 90nm thick sections were collected on a 400 mesh copper grid and imaged with a JEOL JEM-1400EX electron microscope. The dispersion state of the nanoparticles in all the composites was found to be similar and of heterogeneous nature. At the nanoscale, the filler material was partially well-dispersed in nanosized clusters but >100nm agglomerates were also observed. The TEM-images also revealed that PP-PCC-1 and PP-PCC-2 compounds contained silica, presumably due to a cross-contamination from the previously compounded silica-composites. Upon closer investigation of the 1.0wt-% silica-composite, micron-sized agglomerates were observed, and even though they were relatively scarce, they contained substantially high amounts of filler material. Thus, considering the densities of the nanoscale particle dispersions presented in Figure 1, all the compounds may contain micro-agglomerates.

B. Large-area breakdown performance

Large-area multi-breakdown distributions of the studied composites are presented in Figure 2 along with the 90% confidence bounds (shaded areas). If applicable, single 2-parameter Weibull distributions were fitted to the breakdown data; otherwise mixed Weibull distributions (2-3 subpopulations) were utilized on the basis of the best goodness-of-fit test result. In order to enable convenient comparison between all the distributions regardless of the distribution structure, 5%, 63.2% and 95% breakdown percentiles and the weakest points measured from the total film areas are presented in Table 2.

Figure 2 and Table 2 together indicate that in comparison to the unfilled BOPP film, the inclusion of 1.0 and 2.0wt-% of either silica or PCC filler decreases the breakdown performance in the >5% breakdown probability region but also leads to a concurrent improvement of the breakdown distribution homogeneity. In the case of silica filler, the difference between 1.0wt-% and 2.0wt-% fill-fractions is distinguishable (Figure 2a) whereas the compounds with 1.0wt-% and 2.0wt-% of PCC together show a very similar breakdown performance (Figure 2b). The compound PP-Sil+PCC with both silica and PCC fillers shows the highest breakdown distribution homogeneity with the Weibull β of 22.14 in comparison to the 11.65 of the reference BOPP, however, its breakdown performance in the >5% breakdown probability region is the lowest of all the studied compounds. The 1.0wt-% silica composite (PP-Sil-1) stands out from the rest of the composites as it shows both the improvement of breakdown distribution homogeneity and the shift of weak points towards higher dielectric strength in comparison to the

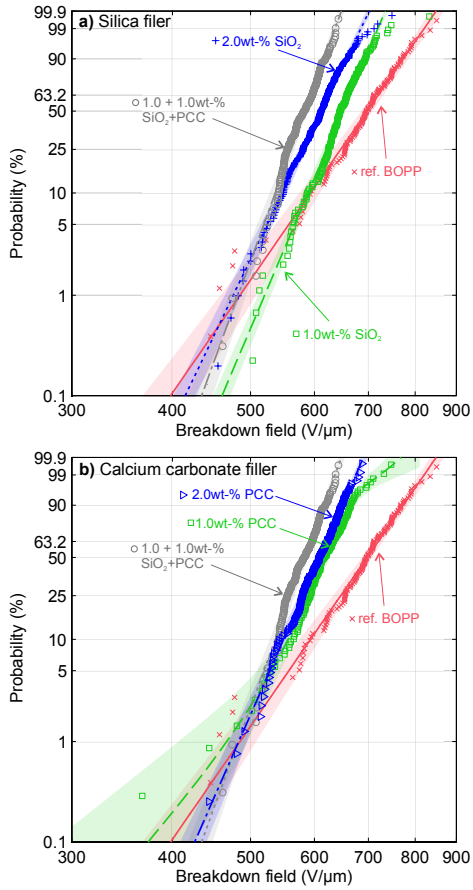

Fig. 2. Effect of **a)** silica and **b)** calcium carbonate fillers on the large-area multi-breakdown performance of BOPP. The shaded areas represent the 90% confidence bounds.

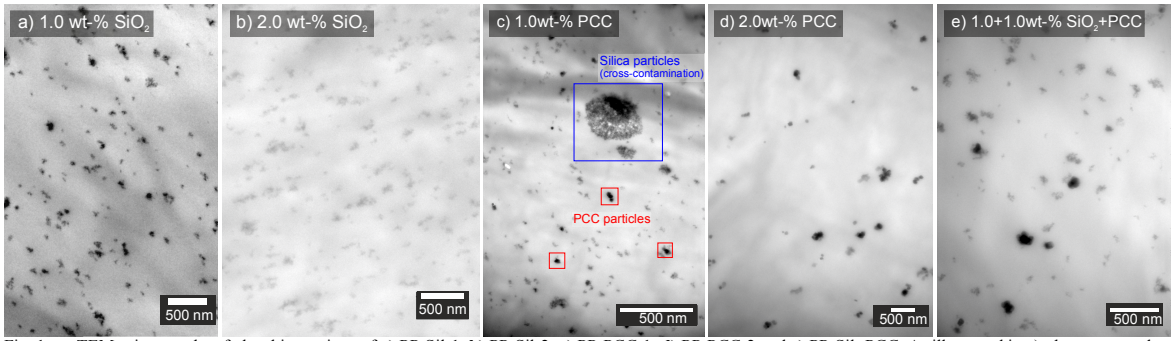

Fig. 1. TEM-micrographs of ultrathin sections of **a)** PP-Sil-1, **b)** PP-Sil-2, **c)** PP-PCC-1, **d)** PP-PCC-2 and **e)** PP-Sil+PCC. As illustrated in c), the compounds PP-PCC-1 and PP-PCC-2 showed small amounts of silica particles, presumably due to a cross-contamination from the previously compounded silica-materials.

neat BOPP film, see Figure 2a. It should be noted that from the practical point-of-view, both the increase of breakdown distribution homogeneity (Weibull β) and the improvement in the low-probability breakdown behavior are substantially more relevant than the breakdown behavior in the higher (>10%) breakdown probability region.

C. Discussion

The trends observable in the large-area breakdown responses are not merely attributable to the filler contents (see Table 1 for the realized filler contents) but rather they reflect the filler-matrix interaction, nanodispersion and the degree of micro-aggregation over large film volumes. The decrease in the breakdown performance with increasing filler content is consistent with previous reports on various amorphous polymer-silica nanocomposites [12], polystyrene-silica nanocomposites [13] and BOPP-PCC nanocomposites [8]. The composites studied here also exhibited improvements in the breakdown distribution homogeneity. In coherence with [12], the nano fillers seem to introduce a lower energy failure mode into the polypropylene matrix, but due to the relatively uniform dispersion at the nanoscale, the breakdown variability is concurrently reduced in comparison to the neat polypropylene.

The role of the antioxidants in the final breakdown performance should also be considered. Although not studied here, the co-stabilizer Irgafos 168 has been shown to have a detrimental effect on the breakdown distribution homogeneity of BOPP films [6] and likewise, residues of the main process stabilizer Irganox 1010 may also impair the breakdown strength of BOPP [14]. Further, the interaction between the antioxidants and the nanofillers should also be considered, as a substantial amount of antioxidant may be adsorbed on the filler surfaces as discussed e.g. in the case of poly(ethylene-*co*-butyl acrylate)-Al_2O_3 nanocomposites and Irganox 1010 in [15]. Initial antioxidant adsorption on the nanofiller surfaces, film processing and the possible slow-release of the antioxidant residue from the adsorption sites over time may have an influence on both the short- and long-term breakdown performance of the end-product, and should be investigated further in the future.

IV. Conclusions

Inclusion of low fill-fractions of silica and/or calcium carbonate nanoparticles in BOPP was found to decrease the large-area multi-breakdown performance in the >5% breakdown probability region but also lead to concurrent improvements in the breakdown distribution homogeneity in comparison to the unfilled reference. The 1.0wt-% silica composite (PP-Sil-1) stood out from the rest of the composites as it showed both the improvement of the breakdown distribution homogeneity and a shift of weak points towards higher dielectric strength. The results point that the optimum nanofiller content resides at the low fill fraction level where it is more probable to achieve good-quality nanodispersion without excess micro-agglomeration over large volumes. The study also exemplified the utilization of large-area multi-breakdown approach for measuring breakdown performance of relatively large film areas with high statistical accuracy.

TABLE II. Large-area breakdown percentiles.

Sample code	*n*	Breakdown field (V/µm)			Weakest point (V/µm)
		5%	*63.2%*	*95%*	
PP-Sil-1	224	567 (560…575)	664 (659…668)	703 (699…707)	503
PP-Sil-2	253	524 (515…533)	626 (621…630)	668 (664…671)	456
PP-PCC-1	174	531 (515…547)	634 (629…639)	679 (669…689)	367
PP-PCC-2	198	528 (519…538)	621 (617…625)	660 (655…664)	444
PP-Sil+PCC	161	519 (511…528)	594 (590…598)	624 (620…628)	462
PP-Ref	128	558 (539…578)	720 (711…729)	791 (780…802)	446

[a] *n* indicates the number of qualified breakdowns after the data selection procedure.
[b] Numbers in parenthesis denote the 90% confidence bounds.

References

[1] J. Keith Nelson, Dielectric Polymer Nanocomposites.: Springer US, 2010.
[2] M. Roy, J. K. Nelson, R. K. MacCrone, and L.S. Schadler, "Candidate mechanisms controlling the electrical characteristics of silica/XLPE nanodielectrics," *Journal of Materials Science*, vol. 42, no. 11, pp. 3789-3799, 2007.
[3] S. Virtanen et al., "Dielectric breakdown strength of epoxy bimodal-polymer-brush-grafted core functionalized silica nanocomposites," *IEEE Transactions on Dielectrics and Electrical Insulation*, vol. 21, no. 2, pp. 563-570, 2014.
[4] M. Takala et al., "Dielectric properties and partial discharge endurance of polypropylene-silica nanocomposite," *IEEE Transactions on Dielectrics and Electrical Insulation*, vol. 17, no. 4, pp. 1259-1267, 2010.
[5] M. Takala et al., "Effect of low amount of nanosilica on dielectric properties of polypropylene," in *10th IEEE International Conference on Solid Dielectrics (ICSD)*, 2010, pp. 1-5.
[6] I. Rytöluoto et al., "Large-Area Dielectric Breakdown Performance of Polymer Films – Part II: Interdependence of Filler Content, Processing and Breakdown Performance in Polypropylene-Silica Nanocomposites," *IEEE Transactions on Dielectrics and Electrical Insulation*, (under review), 2014.
[7] C. Calebrese, Le Hui, L.S. Schadler, and J.K. Nelson, "A review on the importance of nanocomposite processing to enhance electrical insulation," *IEEE Transactions on Dielectrics and Electrical Insulation*, vol. 18, no. 4, pp. 938-945, 2011.
[8] Virtanen S. et al., "Structure and dielectric breakdown strength of nano calcium carbonate/polypropylene composites," *Journal of Applied Polymer Science*, vol. 131, no. 1, 2014.
[9] M.A. Schneider, J.R. MacDonald, M.C. Schalnat, and J.B. Ennis, "Electrical breakdown in capacitor dielectric films: Scaling laws and the role of self-healing," in IEEE International Power Modulator and High Voltage Conference (IPMHVC), 2012, pp. 284-287.
[10] I. Rytöluoto, K. Lahti, M. Karttunen, and M. Koponen, "Large-Area Dielectric Breakdown Performance of Polymer Films – Part I: Measurement Method Evaluation and Statistical Considerations on Area-Dependence," *IEEE Transactions on Dielectrics and Electrical Insulation*, (under review), 2014.
[11] I. Rytöluoto and K. Lahti, "New Approach to Evaluate Area-Dependent Breakdown Characteristics of Dielectric Polymer Films," *IEEE Transactions on Dielectrics and Electrical Insulation*, vol. 20, no. 3, pp. 937-946, 2013.
[12] A. Grabowski Christopher et al., "Dielectric Breakdown in Silica–Amorphous Polymer Nanocomposite Films: The Role of the Polymer Matrix," *ACS Applied Materials & Interfaces*, vol. 5, no. 12, pp. 5486-5492, 2013.
[13] M. Praeger, A.S. Vaughan, and S.G. Swingler, "The breakdown strength and localised structure of polystyrene as a function of nanosilica fill-fraction," in *IEEE International Conference on Solid Dielectrics (ICSD)*, 2013, pp. 863-866.
[14] J. Ho, R. Ramprasad, and S. Boggs, "Effect of Alteration of Antioxidant by UV Treatment on the Dielectric Strength of BOPP Capacitor Film," *IEEE Transactions on Dielectrics and Electrical Insulation*, vol. 14, no. 5, pp. 1295-1301, 2007.
[15] S. Nawaz, P. Nordell, H. Hillborg, and U.W. Gedde, "Antioxidant activity in aluminium oxide – poly(ethylene-co-butyl acrylate) nanocomposites," *Polymer Degradation and Stability*, vol. 97, no. 6, pp. 1017-1025, 2012.

Publication V

I. Rytöluoto, K. Lahti, M. Karttunen, and M. Koponen, "Large-area dielectric breakdown performance of polymer films – Part I : Measurement method evaluation and statistical considerations on area-dependence," *IEEE Transactions on Dielectrics and Electrical Insulation*, vol. 22, no. 2, pp. 689–700, 2015.

The following paper is the final version accepted for publication in IEEE Transactions on Dielectrics and Electrical Insulation. The published version of this paper is available at IEEE Xplore. DOI: 10.1109/TDEI.2015.7076764

Large-area Dielectric Breakdown Performance of Polymer Films – Part I: Measurement Method Evaluation and Statistical Considerations on Area-dependence

I. Rytöluoto, K. Lahti
Tampere University of Technology
Department of Electrical Engineering
P.O. Box 692
FI-33101 Tampere, Finland

M. Karttunen and **M. Koponen**
Technical Research Centre of Finland
P.O. Box 1300
FI-33101 Tampere, Finland

ABSTRACT

A multi-breakdown measurement method for large-area dielectric breakdown characterization of polymer films is presented and evaluated. Based on the self-healing breakdown capability of metallized film, large amount of breakdown data can be obtained from a relatively large total film area, thus enabling the execution of detailed breakdown performance analysis. The studied films include non-metallized laboratory-scale, pilot-scale and commercial capacitor-grade bi-axially oriented polypropylene films in the thickness range of 14-25 µm. With the active measurement area of 81 cm^2 per sample, breakdown distributions covering total film areas of 486-972 cm^2 are presented. Various aspects encompassing the sample film preparation, measurement procedure, breakdown progression, discharge event characterization, breakdown field determination, data validation and statistical analysis are discussed. Comparative small-area breakdown measurements were performed in order to study the relationship between the large-area multi-breakdown measurement method and a conventional small-area (1 cm^2) manual breakdown measurement method. Implications of the area-dependence and the applicability of the Weibull area-scaling are also discussed.

Index Terms — **Dielectric breakdown, self-healing, large-area breakdown performance, area-dependence, statistical analysis, Weibull distribution**

1 INTRODUCTION

MEASUREMENT of dielectric breakdown strength is essential during the development and optimization phase of novel polymeric materials for capacitive energy storage purposes in film capacitors. The measurement is typically realized as a short-term ramp-to-breakdown measurement of small film samples by using cylindrical edge-rounded metal electrodes [1, 2] or, as is becoming more common recently, by utilizing metallized polymer films as the electrodes [3-6]. Weibull or other extreme-value distributions are then utilized for the statistical analysis [7]. However, due to the inherently stochastic nature of the breakdown process in polymer films, a large number of breakdowns has to be collected in order to gain a sufficiently high statistical significance for making comparisons among materials and for guiding the material optimization process [8]. Also, from the application point-of-view, knowledge of the breakdown strength at the low breakdown probability region with reasonably narrow confidence bounds is crucial [9]. Although a few automatic systems for the breakdown voltage measurement of polymer films have been developed [10, 11], manual breakdown measurement with small electrodes (in the mm^2-cm^2 range) still seems to be the generally prevailing method [4, 12-15] and a trade-off between the sample size and measurement convenience is often made.

The breakdown strength evaluation is further complicated by the area and volume dispersion of weak points in the film which may show as distinct defect distributions differing from the inherent breakdown distribution of the polymer itself [16]. Indeed, several experimental [17-21] and theoretical [22] studies on the area-dependence present breakdown results where significant deviation from a single

Manuscript received on 6 May 2014, in final form 13 August 2014, accepted 11 November 2014.

Weibull distribution is evident in the low breakdown probability region. In such a case, manual small-area breakdown measurement is likely to result in an over-optimistic breakdown strength estimate and extrapolation of the breakdown distribution to represent a larger active area becomes unreliable. Thus, it can be concluded that in addition to a sufficiently large number of breakdown points, a relatively large total film area should also be covered.

An alternative breakdown measurement technique based on the measurement of multiple self-healing breakdowns on metallized polymer films was reported earlier [21]. During the self-healing process, the fault spot is spontaneously isolated from the rest of the electrode due to the vaporization of small amount of metallization layer around the breakdown channel [23-25]. The obvious advantage of the multi-breakdown approach is the ability to measure large amount of breakdowns past the weakest point from a relatively large film area in a convenient way. In fact, the self-healing breakdown approach has been extensively applied to very thin metal-oxide-semiconductor (MOS) structures with AC, DC and impulse voltages but less frequently to polymer films for which the range of relative thickness and breakdown voltage is much higher (in the µm and kV range, respectively) [26-30]. It is the purpose of this paper (Part I) to present and evaluate the application of the self-healing multi-breakdown measurement technique on non-metallized polymer films ranging from commercial capacitor-grade to small-scale laboratory-stretched bi-axially oriented polypropylene (BOPP) films. The large-area breakdown performance of laboratory- and pilot-scale bi-axially oriented polypropylene-silica nanocomposite films is analysed in the accompanying paper (Part II).

2 EXPERIMENTAL DETAILS

2.1 SAMPLE DETAILS AND FILM PROCESSING

The sample details, processing and average film thicknesses with the standard deviations are presented in Table 1. The polypropylene homopolymers HB311BF (in pelletized form with stabilizers) and HC318BF (in powder form, unstabilized) were obtained from Borealis N.V. The film processing was conducted at the VTT Technical Research Centre of Finland and at a Brückner pilot film line in Denmark. The commercial capacitor-grade hazy BOPP film was obtained from Tervakoski Films Group.

The PP-2 and PP-3 materials were compounded similarly to the polypropylene-silica nanocomposites which are presented in the associated publication (Part 2). Firstly, the polypropylene powder and stabilizing agents were pre-mixed either manually in a polyethylene bag (approximate mixing time of 2 min) or automatically with a drum mixer (mixing time of 3 min), see Table 1. Then, Berstorff ZE 25/48D twin screw compounder with high-shear screw geometry and two separate kneading sections was used for compounding. Melt filter (screen size 42 µm) was used in the compounding unit. Compounding was made with a continuous nitrogen gas purge (flow 2.5 l/min). The compound was cooled in a water bath under a laminar air flow hood over the cooling section. Polymers were dried at 70 °C for 1.5 hours in an oven and for 0.5 hour in a vacuum oven before the compounding. Compounder output was 9 kg/h for all compounds.

Cast films were extruded by a Brabender Plasticorder single screw extruder with a three-layer screen pack. The single screw had three stages with a mixing zone and the compression was 4:1. The films were cast through a 120 mm slot die onto a chill roll at +90 °C. The cast film thickness was 500-700 µm. Screw speed was 100 rpm (revolutions per minute) and cylinder temperatures were between 220 °C and 230 °C. Compounds were also dried before the cast film extrusion as before compounding. Finally, the laboratory-scale PP-1 and PP-2 cast films were bi-axially oriented with a Brückner KARO IV film stretching machine (set temperature 157 °C, stretching ratio 5.4 x 5.4).

Pilot-scale film was produced from the PP-3 compound at a Brückner pilot film line. The pilot line consisted of a single screw extruder with a flat die, a casting station, MDO and TDO units and a winder. First, the polymer compound was melted in the extruder, quenched on the casting roll and then transferred to the MDO where it was reheated and stretched in the machine direction. Thereafter, the film was reheated in the TDO unit before transverse stretching and cooled down before winding. The temperature profile of the extruder was between 214 to 240 °C. Chill roll temperature was 62 °C. MD stretching roll temperatures were 142 °C to 155 °C and the stretching ratio was approximately 1:4. In TD-stretching the oven section temperatures were 170 °C to 183 °C and TD-stretching ratio was approximately 1:6.

2.2 SAMPLE PREPARATION AND TEST CAPACITOR STRUCTURE

All the sample films were cut to 110 mm x 110 mm dimensions as shown schematically in Figure 1a. In the case of the capacitor-grade and pilot-scale films, the samples were cut directly from the film rolls. In the case of the laboratory-stretched films, the oriented sheets of approximately 360 mm x 360 mm size were first divided into four quadrants and then cut into the actual film samples from the area next to the middle part of the full sheet. This was done in order to utilize the available film as efficiently as possible, as some of the sample material was limited in quantity. The thickness of each sample film was then measured systematically at 25 points covering a 100 mm x 100 mm area with an LE1000-1 high-precision thickness measurement gauge (accuracy 0.1 µm, resolution 0.05 µm)

Table 1. Sample film details, processing and average film thicknesses. Film thicknesses are assumed to be normal distributed. SD = standard deviation.

Code	Type	PP	Pre-mixing	Compounding	Cast extrusion	Bi-axial orientation	Film thickness (µm)	
							Average	SD
PP-1	Laboratory-scale	HB311BF, pellet	-	-	b	yes, c	20.40	2.30
PP-2	Laboratory-scale	HC318BF, powder	Bag mixing	a	b	yes, c	21.33	2.58
PP-3	Pilot-scale	HC318BF, powder	Drum mixer	a	d	yes, d	16.24	1.68
PP-4	Commercial film	Tervakoski RER (14.4µm)	-	-	-	yes	14.35	0.52

a: Berstorff ZE 25/48D twin screw compounder
b: Brabender Plasticorder single screw extruder
c: Brückner KARO IV laboratory-stretcher
d: Brückner pilot-line

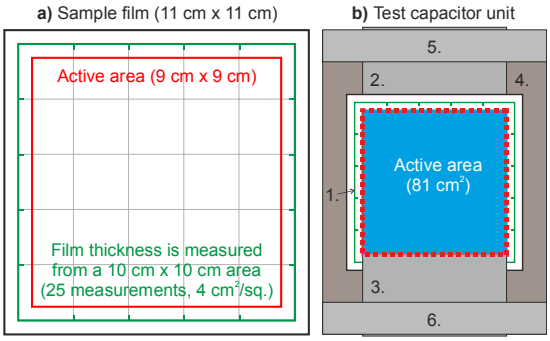

Figure 1. a) Test film dimensions and the active area. The film thickness is measured systematically from 25 measurement points covering a 100 cm^2 area. **b)** Test capacitor structure: **1**: Test film, **2-3**: Metallized electrode films (metallized sides facing towards test film), **4**: Bottom plate, **5-6**: aluminum clamp electrodes (to high voltage and ground).

using a ball-point measurement tip and a constant measurement force of 0.6-0.85 N. The measured sector thicknesses were then utilized for calculating the breakdown fields, as discussed later. The average film thicknesses with the standard deviations are presented in Table 1. It is evident from Table 1 that the laboratory-stretched films exhibited more thickness deviation in comparison to the pilot-scale and commercial films, as the middle region of a laboratory-stretched film is typically thinner in comparison to the outer regions. This aspect and its influence on the breakdown results are discussed in more detail later.

In order to realize the self-healing breakdown capability of non-metallized sample films, two sheets of edge-reinforced Zn-Al-metallized BOPP film (12 µm Tervakoski PSX) were used as the electrodes. According to the manufacturer, the metallization sheet resistivity was 5-12 Ω/sq. for the main metallization body and 2-4 Ω/sq. for the reinforced edge. The electrode films were cut straight from the roll to the dimensions of 92 mm x 130 mm (90 mm wide metallization and 2 mm free margin on one side). The electrode films were placed above and under the non-metallized test film with the metallized surfaces facing towards the test film, thus forming an active test area of 81 cm^2 (see Figure 1b). The film arrangement was sandwiched between two sheets of 100 µm thick transparent polyester film in order to provide mechanical support for the films during the breakdown measurement. The whole film arrangement was then laid on the bottom plate of the test capacitor unit and electrical contacts with the metallized films were made by means of aluminum clamp electrodes at the both ends of the bottom plate.

2.3 MEASUREMENT CIRCUIT

The measurement circuit used for the multi-breakdown measurement consisted of a Spellman SL 1200 DC high voltage source (1200 W nominal power) in parallel with the test capacitor unit. The control voltage used for ramping up the DC voltage source was generated with a National Instruments PCI-6221 DAQ card and LabVIEW software. A resistive voltage divider (Spellman HVD 100-1, 1:10000 division ratio) parallel to the test capacitor was used for general monitoring of the measurement voltage in LabVIEW. A video was recorded from the top of the test capacitor unit for the whole duration of the breakdown measurement, allowing a detailed chronological analysis of the breakdown progression of the sample after the measurement. A circuit diagram is presented in Appendix A.

For the high-resolution acquisition of the discharge events, the discharge current $i_d(t)$ and the voltage $u_{DUT}(t)$ across the test capacitor unit during each event were measured by means of a 1.0330 Ω impulse current measurement resistor and a Tektronix P6015A high voltage probe, respectively. The discharge current and test capacitor voltage signals along with the trigger time information of each discharge event were recorded with a high-resolution 12 bit oscilloscope (Lecroy HRO 66Zi) operated in the sequence-acquisition mode and triggered to the positive rising edge of the discharge current signal. This allowed a detailed determination of the breakdown voltage, voltage drop, peak current, discharge energy and various pulse time parameters for each event. The discharge energy E_{SH} during each event was calculated by integrating the product of the test capacitor voltage and discharge current over the discharge duration τ:

$$E_{SH} = \int_0^{\tau} u_{DUT}(t) i_d(t) dt. \quad (1)$$

2.4 TEST PROCEDURE

Due to the fact that the sample film thicknesses were approximately in the range of 14-25 µm (Table 1), the voltage range required for the breakdown measurement exceeded several kilovolts. Above 6-8 kV range, testing in atmospheric air becomes problematic as non-breakdown events such as surface flashovers across the metallized electrodes and partial discharges emerge. Therefore, the breakdown measurement was performed in mineral oil (Shell Diala DX) in accordance with the IEC-60243 standard [1, 2]. Before oil-immersion, a fast DC voltage ramp (U_{peak}=3.0 kV, ramp speed 400 V/s) was applied across the test capacitor in atmospheric air in order to pull the electrode films into contact with the test film by electrostatic force. This was done in order to remove excess air from between the films and to minimize the amount of oil penetrating in between the electrode films and the test film. The test capacitor was then immersed in mineral oil and thereupon, a lightweight transparent top-plate made of acrylic plastic was laid on the film arrangement. This was found to result in a smooth contact between the electrode films and the test film, as the oil displaced during the top-plate positioning gently pushed and smoothed out the films.

The voltage was first raised to approximately 40-60 % of the probable short-time breakdown voltage with a fast ramp speed of 400 V/s, after which a slow ramp speed of 30 V/s was used for measuring the breakdown events, roughly in accordance with the slow rate-of-rise test defined in the IEC-60243-1 [1] (Figure 2a). This ensured that most of the first breakdowns occurred between 120-240 s after initiating the voltage ramp. As the voltage was ramped beyond the first breakdown voltage, discharge events began to occur at an increasing frequency, hence gradually reducing the active area and the capacitance of the sample. The measurement

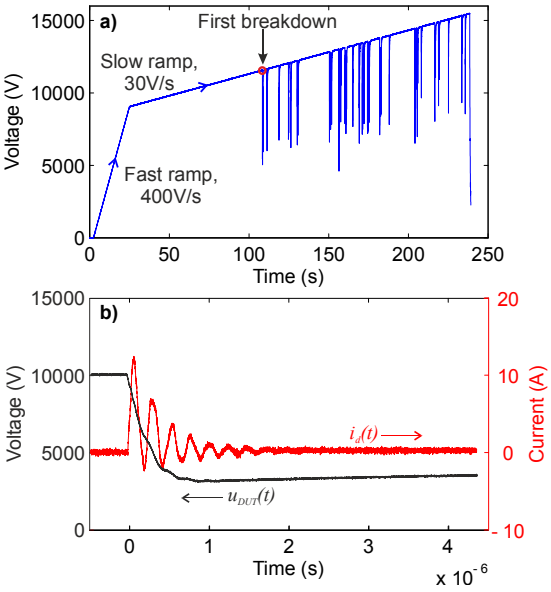

Figure 2. a) Test capacitor voltage during the breakdown measurement of a laboratory-stretched PP-1 film sample. Self-healing breakdown events can be distinguished as sudden voltage drops. **b)** Discharge current pulse $i_d(t)$ and test capacitor voltage $u_{DUT}(t)$ during the first self-healing breakdown event. Calculated breakdown field and discharge energy were 544 V/µm and 17.53 mJ, respectively.

was continued until no more discharge events could be measured from the sample area or until 400 events were recorded. Six samples were typically measured per material, resulting in 486 cm^2 of total measured area. A typical self-healing breakdown event measured from a laboratory-stretched PP-1 film sample is presented in Figure 2b showing a discharge current pulse with an oscillating component and an abrupt voltage drop at the instant of the breakdown followed by a voltage recharge period.

It should be noted here that as the data acquisition was triggered to the discharge current signal, not all the recorded discharge events were actual breakdowns. This was done deliberately though in order to gather all the events that occurred during the multi-breakdown measurement for more detailed analysis. Alternatively, triggering could also be based on the voltage drop during a breakdown (e.g. by AC coupling the capacitor voltage in order to remove the DC ramp component), thus avoiding non-shorting partial discharges to be recorded.

2.5 BREAKDOWN FIELD DETERMINATION

The basic approach to transform the measured breakdown voltages into breakdown fields was to form an average thickness $d_{i,avg}$ for each sample film i [1]. By utilizing the video recordings, $d_{i,avg}$ was calculated as an average of the sector thicknesses where breakdowns had occurred by the end of the breakdown measurement. The nth measured breakdown field $E_{n,i}$ of the sample i was then calculated as:

$$E_{n,i} = U_{n,i} / d_{i,avg}, \tag{2}$$

where $U_{n,i}$ is the nth measured breakdown voltage of the sample i.

The utilization of the average sample thickness approach is readily justified for films with low thickness deviation, i.e. for the capacitor-grade and pilot-scale films. However, as the laboratory-stretched films inevitably exhibit a certain degree of thickness deviation, an error in the breakdown field calculation may result if the deviation is large and the average film thickness is used. In order to study this effect, breakdown fields were also determined manually for each event. This was done with the aid of MATLAB by extracting the video frames at the time of each discharge event and by rigorously determining the average thickness around the discharge spot and by calculating the average breakdown field event-by-event. If a discharge event occurred in the middle part of a sector, the sector thickness was used; otherwise an average of the surrounding sector thicknesses was used.

2.6 BREAKDOWN DATA SELECTION PROCEDURE

As multiple self-healing breakdowns are measured from each sample, the measured data has to be validated, any non-breakdown events should be ruled out and only the breakdown events which appear independent of each other should be qualified for further analysis. In the previous work [21, 31, 32], a breakdown data selection procedure based on the discharge energy characteristics of the self-healing process has been utilized for this purpose. The self-healing process may be characterized by the energy E_{SH} discharged during a self-healing event and it can be expressed as [24, 33]:

$$E_{SH} = \frac{kU^b C}{R_s^c \alpha(P)} = aU^b, \tag{3}$$

where U is the voltage, C is the capacitance, R_s is the metallization sheet resistance, $\alpha(P)$ is a function which relates inter-layer pressure to the discharge energy and a, b, c and k are experimentally definable constants. It has been hypothesized that the discharge events with discharge energies and breakdown voltages not following the trend set by the first breakdowns may be attributed to successive breakdowns occurring close to or at previous breakdown sites or to other non-breakdown events. A similar data selection procedure is applied in this study and its applicability is evaluated and discussed in more depth in Chapter 3.

2.7 STATISTICAL ANALYSIS

For the statistical analysis of the breakdown data, 2-parameter Weibull distributions and additively mixed Weibull distributions were utilized. The cumulative distribution function of a 2-parameter Weibull distribution is of form [16]:

$$F(x) = \begin{cases} 1 - \exp\left\{-\left(\frac{x}{\alpha}\right)^{\beta}\right\} & , x \geq 0 \\ 0 & , x < 0 \end{cases}, \tag{4}$$

where x is the measured variable (e.g. breakdown voltage), α is the scale parameter which corresponds to the value of x at

the 63.2 % failure probability and β is the shape parameter depicting the slope of the theoretical distribution.

In some cases, a single distribution is not sufficient for representing the whole breakdown data set as the breakdowns may be due to different failure mechanisms, each with their own distinct failure distribution $F_i(x)$. The cumulative distribution function of an additively mixed 2-parameter Weibull distribution is of form [16]:

$$F(x) = \sum_{i=1}^{S} \frac{N_i}{N} F_i(x) = \sum_{i=1}^{S} \frac{N_i}{N} \left[1 - \exp\left\{ -\left(\frac{x}{\alpha_i} \right)^{\beta_i} \right\} \right], \qquad (5)$$

where $F_i(x)$ is the Weibull distribution from Equation (4), S is the number of subpopulations, N_i/N is the portion (%) of the subpopulation i and α_i and β_i are the Weibull parameters of subpopulation i.

Weibull area-scaling law can be utilized for extrapolating breakdown results measured with a smaller active area A_1 to represent a larger active area A_2. If it is assumed that the breakdowns measured with the active area A_1 are Weibull-distributed with a scale factor α_1 and that the slope β and the film thickness stay constant, the scale factor α_2 of another area A_2 may be expressed as [16]:

$$\alpha_2 = \alpha_1 \left(\frac{A_2}{A_1} \right)^{-1/\beta} . \qquad (6)$$

For the Weibull parameter estimation, maximum-likelihood estimation (MLE) and non-linear regression (NLR) methods were used. Linear correlation or statistical tests such as the Kolmogorov-Smirnov (K-S) test can then be utilized for evaluating the goodness-of-fit of the chosen theoretical distribution. A more detailed description of the distributions, parameter estimation and goodness-of-fit tests is out of the scope of this paper and can be found elsewhere (e.g. [16]). Statistical analysis was performed with Weibull++ and MATLAB software.

2.8 COMPARATIVE SMALL-AREA BREAKDOWN MEASUREMENT

In addition to the large-area multi-breakdown measurements, comparative small-area breakdown measurements were also performed in order to study the relationship between the small- and large-area measurement methods. The small-area breakdown measurements were performed by using a steel rod-rod electrode configuration with thin graphite plates in between the rods and the sample film in order to smoothen the contact and to prevent electrode pitting. The active area was approximately 1 cm^2 and the measurements were performed in mineral oil with a 400 V/s DC voltage ramp rate in accordance to the IEC-60243 standard [1, 2]. The method was equivalent to the one previously used in [12-14].

3 RESULTS AND DISCUSSION

3.1 BREAKDOWN PROGRESSION

Figure 3 presents extracted breakdown video frames depicting typical self-healing breakdown progressions as a function of time; presented are a capacitor-grade PP-3 film sample in Figure 3a and a laboratory-stretched PP-1 film sample in Figure 3b. Also, the measured thickness profiles of the both films are presented in Figure 4 with the profile orientations matching the film orientations in Figure 3. In the case of the capacitor-grade PP-3 film with a negligible thickness deviation, the breakdowns seemed to occur in a geometrically random manner in the active film area. However, in the case of the laboratory-stretched PP-1 samples which exhibited more distinct thickness profiles, the breakdown progression more or less followed the film thickness profile. Due to the electrode de-metallization associated to the preceding breakdown events, the electrical contact with the thickest areas in the laboratory-stretched films was often lost before the voltage ramp reached their breakdown voltage (see Figure 3b, the last event). The self-segmentation effect was more profound in the case of the laboratory-stretched films but it was occasionally observed with the capacitor-grade and pilot-scale films too.

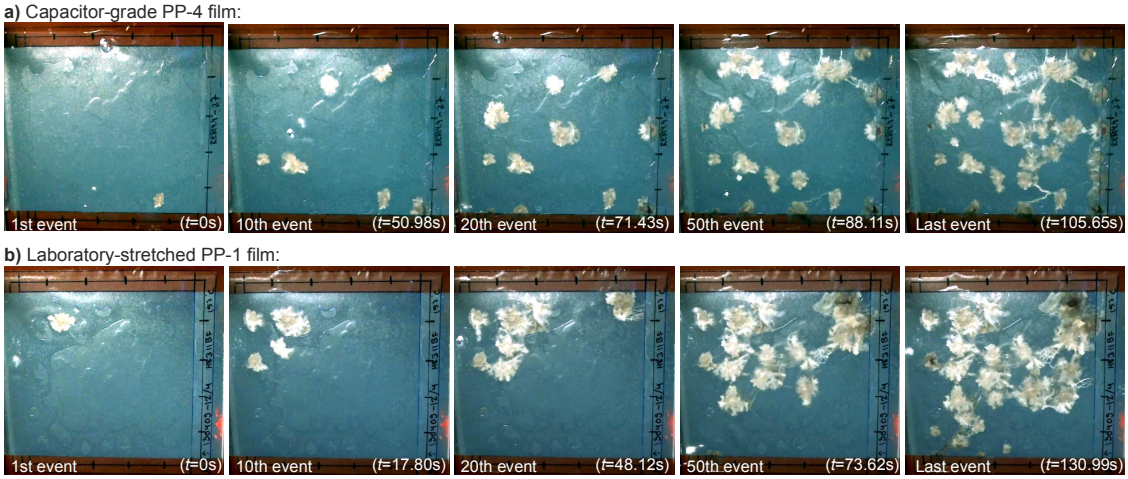

Figure 3. Breakdown evolution **a)** on a capacitor-grade PP-4 film sample and **b)** on a laboratory-stretched PP-1 film sample. The images were extracted from the breakdown videos at the instants of the 1st, 10th, 20th, 50th and the last discharge event. The time values in brackets correspond to the time since the first breakdown. Active area is 81 cm^2 and the voltage was ramped at a 30 V/s rate. The first breakdowns occurred at 6404 V and 11431 V for the capacitor-grade and the laboratory-stretched films, respectively. The test capacitor voltage of the laboratory-stretched PP-1 film (a) was presented eariler in Figure 2.

Film thickness profiles (µm):

a) Capacitor-grade PP-4 film:

14.12	14.28	14.22	14.62	15.00
14.18	14.50	15.05	15.04	14.29
14.73	14.32	13.81	14.51	14.51
14.40	14.28	14.40	15.07	14.80
13.76	13.75	14.10	14.34	14.36

b) Laboratory-stretched PP-1 film:

17.00	17.52	20.10	21.51	23.00
16.82	17.08	19.31	20.75	21.30
19.70	18.85	19.87	20.95	21.92
20.00	21.82	23.76	24.62	23.18
20.05	20.85	23.41	24.24	23.90

Figure 4. Measured thickness profiles of **a)** a capacitor-grade PP-4 film sample (see Figure 3a) and **b)** a laboratory-stretched PP-1 film sample (see Figure 3b). The measured thicknesses are in µm and the profile orientations match the video frames presented in Figure 3.

3.2 DISCHARGE EVENT CHARACTERIZATION

The discharge events occurring during the multi-breakdown measurement could generally be categorized into:

1. Breakdown events
2. Consecutive breakdown events close to or at previous breakdown sites
3. Non-shorting partial discharges
4. Flashovers across the metallized electrode edges.

Breakdown events were characterized by a major (50-70 %) voltage drop and a rapid flow of discharge current over the µs time scale, as already shown in Figure 2b, and visually, as distinct self-healing breakdowns resulting in approximately circular de-metallized areas (see Figure 3a-b, e.g. the first breakdowns). However, the main breakdown events were often followed by rapid bursts of consecutive breakdown events, as shown in Figure 5. The breakdown voltages and the calculated discharge energies of the consecutive breakdowns were typically lower than that of the main breakdown event as they occurred during the voltage recharge period of the main breakdown. The visual analysis of consecutive discharge events confirmed that they often occurred close to or at previous breakdown sites and resulted in smaller and more deformed de-metallized patterns in comparison to the main breakdown events. Previously, consecutive self-healing breakdowns have been attributed to graphite formation and incomplete self-healing process [34]. Also, a thermally activated conduction wave originating from the heat release of the main breakdown can increase the local electric field at the surrounding colder regions [35], thus aiding the generation of consecutive breakdowns close to a previous breakdown site. The relatively high discharge energy level due to the high breakdown voltage range undoubtedly resulted in challenging conditions for the self-healing process, as also suggested by Equation (3). Nevertheless, a complete loss of the self-healing capability was never observed during the breakdown measurements.

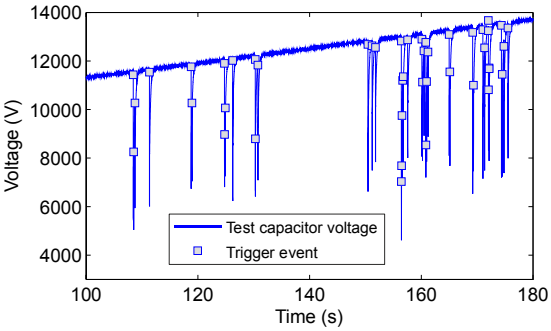

Figure 5. Example of consecutive self-healing breakdows measured on a laboratory-stretched PP-1 film, during which multiple trigger instances (i.e. detected discharge events) occur over a short period of time. The breakdown voltages of the consecutive breakdowns following the main breakdown are lower than that of the main breakdown.

In addition to the breakdown and consecutive breakdown events, non-shorting partial discharges were also observed, especially after multiple discharge events and major de-metallization of the electrode surfaces had occurred closer to the end of the measurement. An example of sequential non-shorting partial discharges measured on a laboratory-stretched PP-1 film is presented in Figure 6. The partial discharges were characterized by a negligible voltage drop (<100 V), rapid current pulse of a few A magnitude and a significantly lower discharge energy in comparison to the actual breakdown events. The partial discharges were attributed to short-distance arcs visually observed on the metallized electrode surface and close to the electrical contacts with the electrode films.

Lastly, on very rare occasions, flashovers across the metallized electrode edges were observed. The flashovers could be attributed to the possible imperfections of the test capacitor surfaces, dust particles in the insulation oil, small film wrinkles and quality of cut edge of the metallized electrode films. The test capacitor voltage, discharge current and the discharge energy during the flashover events were found to be very similar to those of the actual breakdown events occurring in the active area, and hence it was hard to distinguish them from the measurement data alone. The first breakdowns were however always checked against flashovers from the breakdown video recordings.

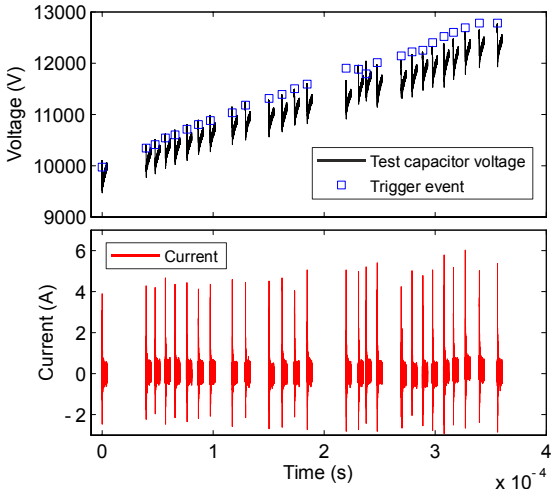

Figure 6. Example of sequential non-shorting partial discharges measured from a laboratory-stretched PP-1 film sample over a short time. The oscilloscope data of the test capacitor voltage (top) and discharge current (bottom) are shown separately for each pulse. The leftmost pulse was the 84th measured discharge and it occurret at 225.17 s after the initiation of the voltage ramp (see Figure 2-3).

3.3 EVALUATION OF THE DATA SELECTION PROCEDURE

The purpose of the data selection procedure is to rule out non-breakdown events from the measurement data prior to the statistical analysis. This was seen as a crucial phase, as the non-breakdown events would otherwise distort the breakdown distribution if all the data was used, as is evident when considering the cases presented in the Figure 5-6. The data selection was based on two criteria, namely by selecting only the discharge events (i) for which the corresponding discharge energies followed the trend preset by the first measured self-healing breakdowns and (ii) for which the breakdown voltages were higher than that of the previously selected breakdown. It has been observed that the discharge energies of the first few discharge events from each data set show a distinctive power dependency on the breakdown voltage $E_{SH}=aU^b$, a property well-known for self-healing breakdown, and a generally increasing trend in the breakdown voltage. In practice, the breakdown data selection was performed in MATLAB with a custom-made program. It is remarked that the presented approach is of empirical nature and just one approach to deal with multi-breakdown data including non-breakdown events.

The selection procedure is described graphically in Figure 7. Firstly, the calculated discharge energies of all the discharge events measured from six samples of laboratory-stretched PP-1 film are shown as a function of the breakdown voltage in a log-log scale in Figure 7a, with the 50 first discharge events and the first measured breakdowns of each sample shown separately. The power dependence of the discharge energy on the breakdown voltage can be readily distinguished from Figure 7a, especially when considering the 50 first discharge events measured from each sample. The discharge events measured later on show larger scattering in terms of breakdown voltage and discharge energy, and can be attributed to consecutive self-healing breakdowns and non-shorting partial discharges as described in the previous sub-chapter.

By utilizing the first measured breakdowns, the slope b of the power regression line $E_{SH}=aU^b$ is calculated. For very homogeneous dielectric films, the first breakdown voltages can be close to each other and the calculated power regression line may not follow the discharge energy trend in a satisfactory way. In such a case, the discharge events subsequent to the first one may also be included in the power regression calculation in order to guide the slope b properly. Then, by taking into account the discharge energy deviation of the first breakdowns (as the points do not necessary fall on the calculated regression line precisely), the minimum energy threshold a_{min} is determined. In graphical terms (see Figure 7a-7b) the power regression line with a constant slope b is shifted vertically along the y-axis so that it passes through the lowest data point; this is set as a_{min}. Finally, by considering the data of each sample film separately, the program qualifies only the discharge events with discharge energies above the minimum energy threshold a_{min} and with breakdown voltages higher than that of the previously qualified event from the same sample film. First breakdowns are always qualified and are used as a basis for the data selection process. Figure 7c shows the measured breakdown voltages as a function of ramp voltage (30 V/s), depicting the time-dependence of the selected breakdowns. It is evident that the selection procedure described above only qualifies the events which follow the applied voltage ramp.

Considering the different types of discharge events discussed in Chapter 3.2, the data selection procedure seems to exclude most of the unwanted discharge events from the data. It could also be a sensible alternative to consider only a part of the data in a chronological order from each sample (e.g. 50 first discharge events from each sample) in order to avoid most of the non-breakdown events (see Figure 7). However, it is not possible to unambiguously claim that the data selection procedure is infallible; it is still possible that some of the excluded discharge events were actual breakdowns and conversely, that the set of qualified breakdowns contains non-breakdown events. Nevertheless, the procedure described here was found to produce sensible results in a simple and convenient way. It is also worth mentioning here that simply by decreasing the overall thickness of the samples, and hence the breakdown voltage level, most of the challenges associated to high-energy self-healing, partial discharges and flashovers are readily mitigated.

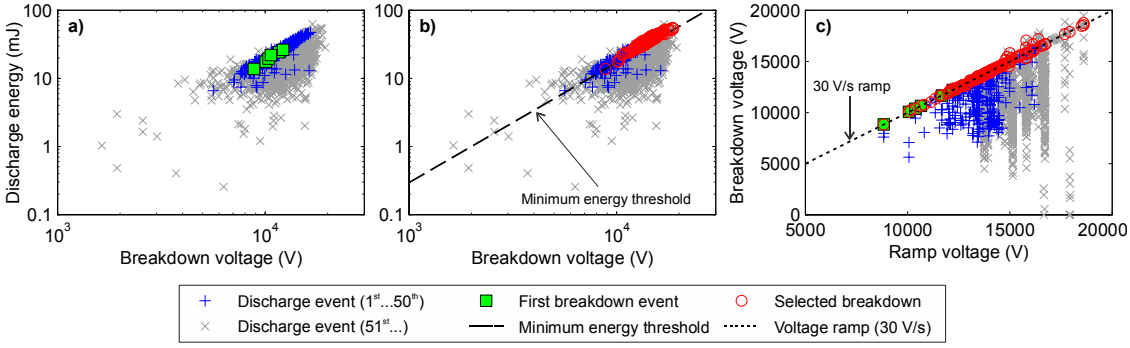

Figure 7. Data selection procedure applied to the data measured from six 81 cm^2 samples of laboratory-stretched PP-1 film for excluding non-breakdown events prior to the statistical analysis. **a)** The calculated discharge energies of all the discharge events as a function of breakdown voltage. The 50 first discharge events (blue) and the first measured breakdowns (green) of each sample are shown separately. **b)** Determination of the minimum discharge energy threshold and data selection. Only the discharge events above the energy threshold and with breakdown voltages higher than that of the previously selected breakdown are qualified (red). **c)** Measured breakdown voltages as a function of the 30 V/s ramp voltage, depicting the time-dependence of the selected breakdowns.

Table 2. Small- and large-area weibull parameters of the laboratory-scale PP-1 and PP-2, pilot-scale PP-3 and capacitor-grade PP-4 films. The parameters of the large-area multi-breakdown results are based on both the (i) average thickness and (ii) manual thickness field determination methods, except for PP-4 for which the thickness deviation was negligible. Subpop 1-2 and the portion (%) refer to the sub-populations of the mixed Weibull distributions; if only sub-population 1 is presented, the distribution is a single 2-parameter Weibull distribution. The calculated breakdown fields (E_{BD}) at 5 %, 63.2 % and 95 % breakdown probabilites can be used for comparing the different breakdown distributions. Number of samples indicates the number of sample films and the values in brackets the number of breakdowns qualified after the data selection procedure (multi-breakdown measurement).

Distribution structure		PP-1, laboratory-scale			PP-2, laboratory-scale			PP-3, pilot-scale			PP-4, capacitor-grade		
		Large-area		Small-area	Large-area		Small-area	Large-area		Small-area	Large-area		Small-area
		Avg. thickness	*Man. thickness*		*Avg. thickness*	*Man. thickness*		*Avg. thickness*	*Man. thickness*		*Avg. thickness*	*Avg. thickness**	
Subpop 1	Weibull α (V/µm)	697	694	782	676	720	781	696	701	798	626	*604**	689
	Weibull β	12.79	20.69	27.39	25.00	11.65	15.99	14.38	13.11	16.82	7.04	*15.55**	31.26
	Portion (%)	52	43	100	24	100	100	100	100	100	23	*100**	100
Subpop 2	Weibull α (V/µm)	805	778	-	746	-	-	-	-	-	618	-	-
	Weibull β	9.02	8.76	-	7.83	-	-	-	-	-	21.99	-	-
	Portion (%)	48	57	-	76	-	-	-	-	-	77	-	-
E_{BD} (V/µm)	5 %	561	578	702	529	558	649	566	559	669	499	*499**	627
	63.2 %	738	725	782	717	720	781	696	701	798	619	*604**	689
	95 %	881	861	814	848	791	836	751	762	852	669	*648**	714
Number of samples		6 (129)		60	6 (127)		60	6 (124)		60	12 (280)	*12 (339)**	60

*) Measured in atmospheric air.

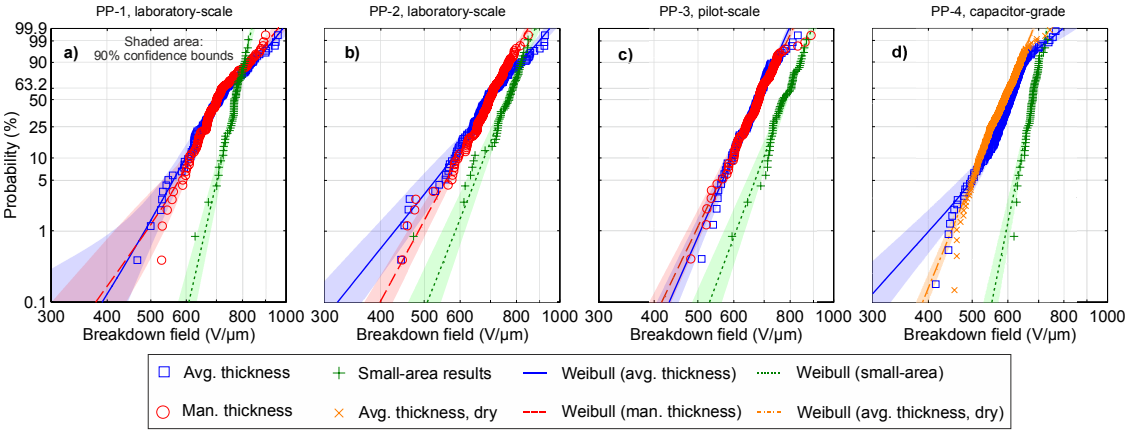

Figure 8. Large- and small-area breakdown perfromances of the laboratory-scale **a)** PP-1 and **b)** PP-2 films, **c)** pilot-scale PP-3 film and **d)** capacitor-grade PP-4 film. Both the average sample film thickness approach (blue) and the manual thickness determination (red) were used for calculating the breakdown fields of the large-area multi-breakdown distributions (81 cm^2 per sample). Small-area results (1 cm^2 per sample, green) were measured with the manual method. The shaded areas represent the 90 % confidence bounds. An additional large-area breakdown distribution of PP-4 measured in atmospheric air is also presented (orange). See Table **2** for the associated parameters.

3.4 STATISTICAL ANALYSIS OF THE BREAKDOWN DATA

Figure 8 presents the large- and small-area breakdown distributions of the laboratory-scale, pilot-scale and capacitor-grade films along with the 90 % confidence bounds. For the analysis of the large-area breakdown data, both the average sample film thickness and the manual thickness approaches were utilized for the breakdown field determination and the results are presented separately. If applicable, single 2-parameter Weibull distributions were utilized; otherwise mixed Weibull distributions with two sub-populations were used. It is emphasized that the statistical approach is of empirical nature. The distribution structures along with the sample film and selected breakdown quantities are given in Table 2. It should be remarked here that a direct comparison of the Weibull parameters presented in Table 2 is only possible if the distributions compared are of the same type (e.g. single 2-paremeter Weibull). Therefore, in order to enable convenient comparison between all the distributions, 5 %, 63.2 % and 95 % breakdown percentiles were calculated and are also given in Table 2. For all the studied BOPP films, the calculated breakdown fields at the 63.2 % breakdown probability (equal to the Weibull α parameter) are well in the range of 600-700 V/µm which is typically considered as the dielectric strength of a good-quality BOPP film [11, 19]. Regarding the confidence bounds, slightly wider bounds at the low-probability region are obtained if mixed distributions are utilized, as is evident from Figure 8.

It can be seen from Figure 8 and Table 2 that regardless of the stringent data selection procedure the large-area multi-breakdown method yields a large amount of breakdown data and results in detailed, fingerprint-like breakdown distributions. Interestingly, some of the distributions clearly show S-shaped curvature and mixed Weibull distributions had to be utilized in order to achieve a satisfactory goodness-of-fit, similarly as previously presented and analyzed in [21, 31, 32]. On the other hand, such behavior was not observed with the pilot-scale PP-3 film. Figure 8 shows that the curvature of the breakdown

distribution is partly due to the film thickness determination method; when average sample film thickness is used, the distribution tends to spread at the low and high probability regions which can naturally be attributed to the thinnest and the thickest parts of the sample films. However, regarding the distributions presented here, the overall difference between the average thickness and the manual thickness approaches seems to be surprisingly small. Due care has to be taken though with sample films with considerable thickness deviation, especially in the analysis of the weakest points.

The possible influence of the insulation oil on the breakdown distribution structure was also studied by performing additional large-area measurements with the capacitor-grade PP-4 film in atmospheric air. It can be seen from Figure 8d that the insulation oil may have a small influence on the breakdown distribution shape, but on the whole it seems to have a negligible effect on the final conclusion (see the breakdown percentiles presented in Table 2). It has to be emphasized that intense partial discharges and surface flashovers were observed during the dry measurements, especially above the ~7 kV voltage level and after several discharge events had occurred, hence possibly compromising the measurement reliability.

3.5 AREA DEPENDENCE AND APPLICABILITY OF THE WEIBULL AREA-SCALING

The area-effect is evident from Figure 8 and the relation between the small- and large-area measurements is logical; the small-area measurements reside at a higher breakdown field region in comparison to the large-area measurements but may still be projected vertically along the probability axis to match portions of the corresponding large-area breakdown distributions. However, the small-area breakdown distributions seem to exhibit higher Weibull β parameters in comparison to the large-area distributions and the extent of this effect varies between the materials. This effect can be associated to the area-dependence; with a small active area of 1 cm^2, the measured breakdown field is likely to reside at the high-field region and even with a relatively large number of small-area measurements (here, 60 samples) the probability to measure weaker points is still low, thus possibly resulting in an over-optimistic Weibull β. On behalf of the multi-breakdown measurement, the effect of active area and total measured film area on the breakdown distribution structure has been previously studied in [21] and resulted in similar conculsions. Similarly, a decrease of both Weibull α and β parameters with increasing electrode area has also been reported previously in the case of various BOPP films [19] and polyimide films [20].

In order to study the applicability of the Weibull area-scaling law, single 2-parameter Weibull distributions were fitted to the first breakdowns measured with the large-area multi-breakdown method for each BOPP film type. Then, Weibull-area scaling, Equation (6), was applied to the small-area breakdown results in order to analyze if the large-area (81 cm^2) dielectric strength could be predicted based on the small-area (1 cm^2) breakdown results. The results presented in Table 3 clearly show that the area-scaled results are in generally in a poor agreement with the large-area dielectric strength results; if the distribution does not contain sufficient information about the large-area performance in the first place, area-scaling, which merely shifts the small-area breakdown distribution along the breakdown field axis, cannot extrapolate to larger areas correctly.

It is acknowledged that in the case of the laboratory-stretched films, the large-area dielectric strength based on the first breakdowns does not actually represent the dielectric strength of the whole 81 cm^2 active area due to the film thickness deviation, and hence the accuracy of the above analysis may be reduced. On the other hand, such complication due to the film thickness effect is not present in the case of the capacitor-grade PP-4 films, but still the area-scaled dielectric strength is in poor agreement with the large-area dielectric strength (Table 3). Nevertheless, the point here is to emphasize the problematic nature of the Weibull area-scaling if the large-area breakdown distribution shape and structure are not fully known.

3.6 CONSIDERATIONS AND DISCUSSION

It is important to consider what a large-area multi-breakdown distribution represents. By considering the studied sample film area A_0 as a parallel network of Weibull distributed components, one can determine the breakdown characteristics of the total film area piece-by-piece by using a small-area ($<A_0$) single-breakdown approach. If the film area is covered completely, the obtained empirical distribution should represent even the weakest point of the total film area in a satisfactory way. However, inversely, if a large active area covering the whole studied film surface is utilized, the first measured breakdown corresponds to the weakest point of the total sample area A_0. In the multi-breakdown measurement, a small area A_{SH} related to the de-metallization during self-healing is removed, i.e. the active area is reduced as the measurement proceeds. In this sense, the de-metallized area A_{SH} determines the 'resolution' of the breakdown measurement. With small enough 'resolution' in multi-breakdown measurement, the breakdowns are measured in a bottom-up approach, ideally approaching a similar end-result as obtainable by the piece-by-piece small-area single-breakdown measurement of the whole film area.

Table 3. Application of the Weibull area-scaling law for predicting the large-area (81 cm^2) dielectric breakdown strength (DBS) from the small-area (1 cm^2) breakdown results. The large area dielectric strengths (first breakdowns of each sample) measured with the multi-breakdown method are presented as a reference.

	PP-1, laboratory-scale			**PP-2, laboratory-scale**			**PP-3, pilot-scale**			**PP-4, capacitor-grade**		
	Large-area DBS		Predicted	Large-area DBS		Predicted	Large-area DBS		Predicted	Large-area DBS		Predicted
	Avg. thickness	Man. thickness	from small-area results	Avg. thickness	Man. thickness	from small-area results	Avg. thickness	Man. thickness	from small-area results	Avg. thickness	*Avg. thickness**	from small-area results
Weibull α (V/μm)	563	631	***666***	560	627	***593***	591	599	***614***	512	*507**	***599***
Weibull β	10.40	9.81	***27.39***	8.05	6.16	***15.99***	12.40	8.76	***16.82***	12.01	*19.81**	***31.26***

*) Measured in atmospheric air.

In practice, the results obtainable with the multi-breakdown measurement are naturally not as ideal as described above. For example, as the de-metallized area A_{SH} is not constant and due to the self-segmentation effect (see Sub-chapter 3.1), the sample film area cannot be covered completely and the resulting empirical breakdown distribution will be truncated. In this regard, a large-area multi-breakdown distribution should be differentiated from a conventional dielectric strength distribution based on single-breakdown measurement with a constant active area. It should also be acknowledged that aside from the area-effects alone, various other aspects such as the influence of the measurement setup, non-breakdown events (as discussed earlier), increase in the leakage current along with the self-healing breakdowns, high-field conduction [36-38] as well as high-field ageing [39] and space charge processes [8] may also have an effect on the multi-breakdown measurement.

Nevertheless, the mutual comparability of the multi-breakdown distributions should not be compromised as long as as the measurement is conducted in a similar way for all the samples. The multi-breakdown measurement method has been applied to several different materials ranging from metallized commercial BOPP and bi-axially oriented polyester films [21, 31, 32] to various laboratory-scale materials such as the silica-polypropylene nanocomposites which are discussed in the Part II of this study. So far the results have been systematic and logical and the method has provided a new insight into the dependence of the large-area breakdown performance of dielectric polymer films on various parameters such as the inherent properties of the polymer, fillers and antioxidants, film processing and bi-axial orientation. The thickness deviation effect associated to the laboratory-scale films can also be mitigated by optimizing the cast processing and bi-axial orientation parameters and by cutting the sample for the multi-breakdown measurement from the center part of the oriented film.

The active area can also be increased in order to cover even larger film areas. It should be noted however that the increase in the sample capacitance with the active area also increases the discharge energy level in accordance with the Equation (3). This effect is limited by the properties of the metallization layer though, as the sheet resistance (or thickness) of the metallization layer resists the current flow into the fault spot from the active areas further away from the fault spot. It should be also noted that with very large active areas, special measures may have to be taken in order to ensure a clear trigger condition during a discharge event in the test capacitor. By improving the sample film processing and by aiming towards lower overall film thickness and deviation, most of the problems associated to high-energy self-healing can be readily mitigated and the need for insulation oil is omitted. Lastly, the multi-breakdown approach also shows a great future potential for long-term dielectric performance testing of polymer films.

4 CONCLUSION

A large-area multi-breakdown measurement method for non-metallized polymer films was presented and evaluated. Large-area self-healing breakdown measurements and comparative small-area single-breakdown measurements were performed for laboratory-scale, pilot-scale and commercial capacitor-grade BOPP films. Various aspects ranging from the sample preparation, measurement procedure and breakdown progression to discharge event characterization, breakdown data validation and statistical analysis were discussed. The influence of the film thickness deviation and insulation oil on the breakdown distribution structure were also analyzed. Lastly, implications of the electrode area effect analysis and the applicability of the Weibull area-scaling law were presented. The systematic analysis presented in this paper showed that the self-healing multi-breakdown measurement leads to sensible results and offers a unique approach for evaluating the large-area breakdown performance of polymer films. Above all, the possibility to obtain detailed breakdown fingerprints representing areas more relevant from a practical point-of-view is very attractive, especially when considering e.g. research and development of novel dielectric materials.

APPENDIX A

Figure 9a presents a detailed schematic of the measurement circuit utilized for the multi-breakdown measurement; see Sub-chapter 2.3 for further information. Figure 9b presents a photograph of the test capacitor unit (see also Figure 1). The aluminium clamp electrodes used

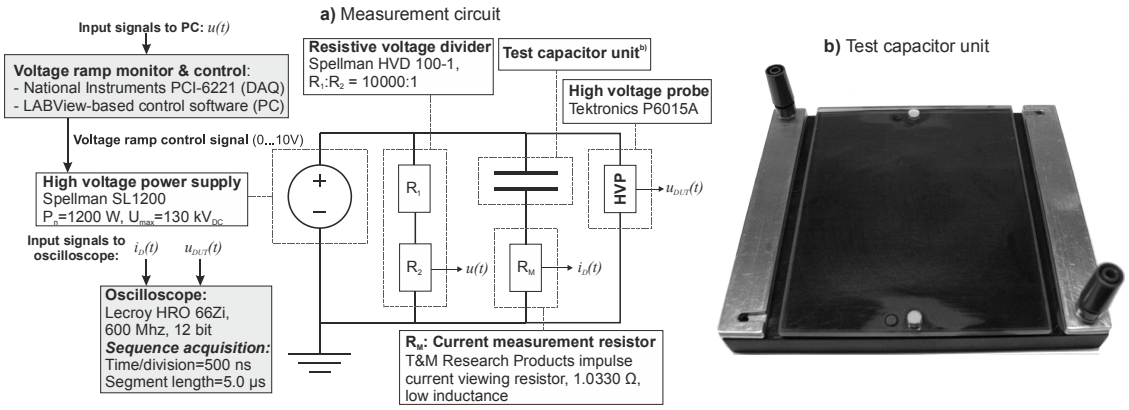

Figure 9. a) Measurement circuit used for the multi-breakdown measurement. $i_D(t)$: Discharge current, $u_{DUT}(t)$: Test capacitor voltage (during discharge), $u(t)$: General voltage signal for monitoring. **b)** A photograph of the test capacitor unit (without sample).

for making contact to the metallized electrode films can be seen at the both ends of the test capacitor unit. The aluminum clamps were lightly tightened by terminal screws and connections to the high voltage supply and ground were made accordingly. The condition of the aluminum surfaces was monitored and if necessary, they were cleaned and polished between measurements. No excessive interface discharging was observed between the metallized layers and the connector.

REFERENCES

[1] "Electric strength of insulating materials - Test methods - Part 1: Tests at power frequencies," *IEC standard 60243-1*, 2013-03.

[2] "Electric strength of insulating materials - Test methods - Part 2: Additional requirements for tests using direct voltage," IEC standard 60243-2, 2001-02.

[3] J. Ho, R. Ramprasad, and S. Boggs, "Effect of Alteration of Antioxidant by UV Treatment on the Dielectric Strength of BOPP Capacitor Film," IEEE Trans. Dielectr. Electr. Insul., Vol. 14, No. 5, pp. 1295-1301, 2007.

[4] C. A. Grabowski, S. P. Fillery, N. M. Westing, C. Chi, J. S. Meth, M. F. Durstock, and R. A. Vaia, "Dielectric Breakdown in Silica–Amorphous Polymer Nanocomposite Films: The Role of the Polymer Matrix," American Chemical Society (ACS) Applied Materials & Interfaces, Vol. 5, No. 12, pp. 5486-5492, 2013.

[5] J. Ho and T. R. Jow, "Effect of crystallinity and morphology on dielectric properties of PEEK at elevated temperature," in *Solid Dielectrics (ICSD), 2013 IEEE International Conference on*, 2013, pp. 385-388.

[6] J.-K. Tseng, S. Tang, Z. Zhou, M. Mackey, J. M. Carr, R. Mu, L.Flandin, D. E. Schuele, E. Baer and L. Zhu, "Interfacial polarization and layer thickness effect on electrical insulation in multilayered polysulfone/poly(vinylidene fluoride) films," Polymer, Vol. 55, No. 1, pp. 8-14, 2014.

[7] "IEEE Guide for the Statistical Analysis of Electrical Insulation Breakdown Data," IEEE Std 930-2004 (Revision of IEEE Std 930-1987), 2005.

[8] L. A. Dissado and J. C. Fothergill, *Electrical Degradation and Breakdown in Polymers*. Philadelphia: Peter Peregrinus Ltd., 1992.

[9] M. A. Schneider, J. R. MacDonald, M. C. Schalnat, and J. B. Ennis, "Electrical breakdown in capacitor dielectric films: Scaling laws and the role of self-healing," IEEE Int'l. Power Modulator and High Voltage Conf. (IPMHVC), pp. 284-287, 2012.

[10] S. J. Laihonen, A. Gustafsson, U. Gafvert, T. Schutte, and U. W. Gedde, "Area Dependence of Breakdown Strength of Polymer Films: Automatic Measurement Method," IEEE Trans. Dielectr. Electr. Insul., Vol. 14, No. 2, pp. 263-274, 2007.

[11] C. Xu, J. Ho, and S. Boggs, "Automatic breakdown voltage measurement of polymer films," IEEE Electr. Insul. Mag., Vol. 24, No. 6, pp. 30-34, 2008.

[12] M. Takala, M. Karttunen, P. Salovaara, S. Kortet, K. Kannus, T. Kalliohaka, "Dielectric properties of nanostructured polypropylene-polyhedral oligomeric silsesquioxane compounds," IEEE Trans. Dielectr. Electr. Insul., Vol. 15, No. 1, pp. 40-51, 2008.

[13] M. Takala, H. Ranta, P. Nevalainen, P. Pakonen, J. Pelto, M. Karttunen, S. Virtanen, V. Koivu, M. Pettersson, B. Sonerud and K. Kannus, "Dielectric properties and partial discharge endurance of polypropylene-silica nanocomposite," IEEE Trans. Dielectr. Electr. Insul., Vol. 17, No. 4, pp. 1259-1267, 2010.

[14] S. Virtanen, H. Ranta, S. Ahonen, M. Karttunen, J. Pelto, K. Kannus and M. Pettersson, "Structure and dielectric breakdown strength of nano calcium carbonate/polypropylene composites," J. Appl. Polymer Sci., Vol. 131, No. 1, pp. 39504.1-8, 2014.

[15] X. Yuan and T. C. M. Chung, "Cross-linking effect on dielectric properties of polypropylene thin films and applications in electric energy storage," Appl. Phys. Letters, Vol. 98, pp. 062901.1-3, 2011.

[16] W. Hauschild and W. Mosch, *Statistical Techniques for High-Voltage Engineering*. Philadephia: Institution of Engineering and Technology, 1992.

[17] S. Ul-Haq and G. R. G. Raju, "Weibull statistical analysis of area effect on the breakdown strength in polymer films," IEEE Conf. Electr. Insul. Dielectr. Phenomena, pp. 518-521, 2002.

[18] G. Raju, A. Katebian, and S. Z. Jafri, "Breakdown voltages of polymers in the temperature range 23°-250°C," IEEE Trans. Dielectr. Electr. Insul., Vol. 10, No. 1, pp. 117-127, 2003.

[19] S. J. Laihonen, U. Gafvert, T. Schutte, and U. W. Gedde, "DC breakdown strength of polypropylene films: Area dependence and statistical behavior," IEEE Trans. Dielectr. Electr. Insul., Vol. 14, No. 2, pp. 275-286, 2007.

[20] S. Diaham, S. Zelmat, M.-L. Locatelli, S. Dinculescu, M. Decup and T. Lebey, "Dielectric breakdown of polyimide films: Area, thickness and temperature dependence," IEEE Trans. Dielectr. Electr. Insul., Vol. 17, No. 1, pp. 18-27, 2010.

[21] I. Rytöluoto and K. Lahti, "New Approach to Evaluate Area-Dependent Breakdown Characteristics of Dielectric Polymer Films," IEEE Trans. Dielectr. Electr. Insul., Vol. 20, No. 3, pp. 937-946, 2013.

[22] K. Wu, Y. Wang, Y. Cheng, L. A. Dissado, and X. Liu, "Statistical behavior of electrical breakdown in insulating polymers," Journal of Applied Physics, Vol. 107, No. 6, pp. 064107.1-5, 2010.

[23] D. G. Shaw, S. W. Cichanowski, and A. Yializis, "A Changing Capacitor Technology - Failure Mechanisms and Design Innovations," IEEE Trans. Electr. Insul., Vol. 16, No. 5, pp. 399-413, 1981.

[24] M. Rabuffi and G. Picci, "Status quo and future prospects for metallized polypropylene energy storage capacitors," IEEE Trans. Plasma Sci., Vol. 30, No. 5, pp. 1939-1942, 2002.

[25] C. W. Reed and S. W. Cichanowski, "The fundamentals of aging in HV polymer-film capacitors," IEEE Trans. Dielectr. Electr. Insul., Vol. 1, No. 5, pp. 904-922, 1994.

[26] N. Klein and N. Levanon, "AC Electrical Breakdown in Thin Silicon Oxide Films," J. Appl. Phys., Vol. 38, pp. 3721-3728, 1967.

[27] N. Klein and E. Burstein, "Electrical Pulse Breakdown of Silicon Oxide Films," J. Appl. Phys., Vol. 40, pp. 2728-2740, 1969.

[28] N. Klein, "Electrical Breakdown in Solids," Advances in Electronics and Electron Physics, Vol. 26, pp. 309-424, 1969.

[29] R. Bartnikas, *Engineering Dielectrics Volume 2B - Electrical Properties of Solid Insulating Materials: Measurement Techniques*.: ASTM International, 1987.

[30] Z. Zhou, M. Mackey, J. Carr, L. Zhu, L. Flandind, E. Baer, "Multilayered polycarbonate/poly(vinylidene fluoride-co-hexafluoropropylene) for high energy density capacitors with enhanced lifetime," J. Polymer Sci. Part B: Polymer Phys., Vol. 50, No. 14, pp. 993-1003, 2012.

[31] I. Rytöluoto and K. Lahti, "Effect of Film Thickness and Electrode Area on the Dielectric Breakdown Characteristics of Metallized Capacitor Films," 23rd Nordic Insulation Sympos. *(NORD-IS)*, pp. 33-38, 2013.

[32] I. Rytöluoto and K. Lahti, "Effect of Inter-Layer Pressure on Dielectric Breakdown Characteristics of Metallized Polymer Films for Capacitor Applications," IEEE Int'l. Conf. Solid Dielectr. (ICSD), pp. 682-687, 2013.

[33] Y. Chen, H. Li, F. Lin, F. Lv, M. Zhang, Z. Li, D. Liu, "Study on Self-Healing and Lifetime Characteristics of Metallized-Film Capacitor Under High Electric Field," IEEE Trans. Plasma Sci., Vol. 40, No. 8, pp. 2014-2019, 2012.

[34] B. Walgenwitz, J.-H. Tortai, N. Bonifaci, and A. Denat, "Self-healing of metallized polymer films of different nature," IEEE Int'l. Conf. Solid Dielectr. (ICSD), pp. 29-32, 2004.

[35] O. A. Emel'yanov, "Electrodynamic Thermal Breakdown of a Capacitor Insulator," Technical Physics, Vol. 56, No. 11, pp. 1685-1688, 2011.

[36] J. Ho and T. R. Jow, "High field conduction in biaxially oriented polypropylene at elevated temperature," IEEE Trans. Dielectr. Electr. Insul., Vol. 19, No. 3, pp. 990-995, 2012.

[37] H. Li, Z. Li, F. Lin, D. Liu, B. Wang, Y. Chen, L. Dai, S. Fan,

"Electrical conduction of metallized BOPP films based on revised Poole–Frenkel effect," J. Electrostatics, Vol. 71, No. 6, pp. 958-962, 2013.

[38] Q. Chen, Y. Wang, X. Zhou, Q. M. Zhang, and S. Zhang, "High field tunneling as a limiting factor of maximum energy density in dielectric energy storage capacitors," Applied Physics Letters, Vol. 92, pp. 142909.1-3, 2008.

[39] D. Liufu, X. S. Wang, D. M. Tu, and K. C. Kao, "High-field induced electrical aging in polypropylene films," J. Appl. Phys., Vol. 83, No. 4, pp. 2209-2214, 1998.

Ilkka Rytöluoto (S'13) was born in Tampere, Finland on 17 April 1985. He received the M.Sc. (Tech.) degree in electrical engineering from Tampere University of Technology (TUT), Tampere, Finland in 2011. Since 2012 he has been working as a Researcher in the high voltage research group of the Department of Electrical Engineering at TUT, with the aim towards the Ph.D. degree. His current research interests include dielectric characterization of polymer and polymer nanocomposite films and analysis of the self-healing performance of metallized dielectric films.

Kari Lahti (M'01) was born in Hämeenlinna, Finland, on 8 March 1968. He received the M.Sc. and Doctoral degrees in electrical engineering from Tampere University of Technology in 1994 and 2003, respectively. Since then he has worked at the Department of Electrical Engineering at TUT, currently as a Research Manager and Adjunct Professor. Since 2002 he has been responsible for the high voltage laboratory services at TUT. His research interests are in the area of high voltage engineering, especially surge arresters, environmental testing of high voltage materials and apparatus, high voltage testing methods and dielectric characterization of insulating materials.

Mikko Karttunen was born in Tampere, Finland in 1955. He received his M.Sc. (Eng.) and Licentiate of Technology degrees in material science and plastics technology from Tampere University of Technology (TUT), in 1980 and 1986, respectively. From 1980 to 1985 he was a research scientist at TUT. From 1985 to 1988 he worked at Neste Oy as a researcher. From 1988 to 1991 he was a research scientist at VTT Technical Research Centre of Finland and since 1991 he has been senior scientist at VTT. His research interest is in electrically conductive polymer compounds and polymer nanocomposites for electromechanical films and electrical insulation materials.

Matti Koponen received the M.S. degree in mechanical engineering from the Technical University of Tampere, Finland, in 1990. He currently works as a research scientist at VTT Polymeric material processing and solutions, Tampere, Finland. His research interests include thermoplastic materials on electronic packaging and polymer processing.

Publication VI

I. Rytöluoto, K. Lahti, M. Karttunen, M. Koponen, S. Virtanen, and M. Pettersson, "Large-area dielectric breakdown performance of polymer films – Part II: Interdependence of filler content, processing and breakdown performance in polypropylene-silica nanocomposites," *IEEE Transactions on Dielectrics and Electrical Insulation*, vol. 22, no. 4, pp. 2196–2206, 2015.

The following paper is the final version accepted for publication in IEEE Transactions on Dielectrics and Electrical Insulation. The published version of this paper is available at IEEE Xplore. DOI: 10.1109/TDEI.2015.004764

Large-area Dielectric Breakdown Performance of Polymer Films – Part II: Interdependence of Filler Content, Processing and Breakdown Performance in Polypropylene-Silica Nanocomposites

I. Rytöluoto, K. Lahti
Tampere University of Technology
Department of Electrical Engineering
P.O. Box 692
FI-33101 Tampere, Finland

M. Karttunen, M. Koponen
Technical Research Centre of Finland
P.O. Box 1300
FI-33101 Tampere, Finland

S. Virtanen and **M. Pettersson**
University of Jyväskylä
Nanoscience Center, Department of Chemistry
P.O. Box 35
FI-40014 Jyväskylä, Finland

ABSTRACT

In this study, large-area dielectric breakdown performances of various bi-axially oriented polypropylene (BOPP)-silica nanocomposite films are studied by utilizing the self-healing multi-breakdown method presented in the Part I of this publication. In particular, the effects of silica filler content, pre-mixing method, co-stabilizer content and film processing on the large-area breakdown performance are analyzed. Nanostructural and film cross-sectional analyses are correlated to the breakdown responses. The optimum silica filler content is found to reside at the low fill fraction level (~1 wt-%) and automatic pre-mixing of the raw materials and the optimization of the orientation temperature are found to be preferable. The co-stabilizer Irgafos 168 is found to have a significant effect on the breakdown distribution homogeneity of the reference BOPP films. The breakdown response of the silica nanocomposites is found to be not only dependent on the active measurement area but also on the voltage ramp rate, indicating that the silica nanocomposites exhibit altered internal charge behavior under DC electric field. The area- and ramp-rate-dependence results exemplify the importance of careful breakdown strength evaluation of dielectric polymer nanocomposites. Above all, the results emphasize the fact that a thorough understanding and the optimization of the film processing parameters are crucial for achieving improved breakdown response in dielectric polymer nanocomposite films.

Index Terms — **Dielectric polymer nanocomposite, polypropylene, silica, pre-mixing, film processing, breakdown performance, area-dependence**

1 INTRODUCTION

DIELECTRIC polymer films play a vital role in short-term capacitive energy storage purposes in modern power electronics and electric power systems. The maximum theoretical energy density of a linear dielectric material is governed by the relative permittivity and the square of the breakdown field strength ($u=½\varepsilon_r\varepsilon_0|E_{BD}|^2$). In the case of polymer films, which typically exhibit small-area breakdown strengths of ~400-700 V/µm, the maximum achievable energy density is limited by the low permittivity (for typical capacitor films, ε_r=~2-4) [1, 2]. In capacitor applications, the practical energy density is further reduced as a substantial safety-margin has to be kept from the short-term small-area breakdown strength of the polymer film due to the area-dependence of the breakdown performance [3-7],

Manuscript received on 10 June 2014, accepted 11 January 2015.

film ageing processes [8, 9] and limitations in the self-healing breakdown capability [10-12]. Other constraints such as device packaging reduce the final energy density even further [13]. For instance, the state-of-the-art metallized film capacitors based on BOPP film are limited to ~2 J/cm^3 in practice. Consequently, a considerable amount of research on novel dielectric polymers has emerged over the last years in an effort to increase the capacitive energy storage ability and reliability. Materials with improved breakdown strength and permittivity while maintaining acceptable dielectric losses are highly aspired for, and while many different approaches to achieve such properties exist [2, 14-16], dielectric polymer nanocomposites [17-19] have received an increasing amount of attention recently.

The dielectric breakdown performance of polymer nanocomposites has been shown to be strongly influenced by the dielectric compatibility between the polymer matrix and the nanofillers, nanoparticle functionalization, filler content, morphology, degree of mixing and material processing [20-23]. In an attempt to achieve nanocomposites with both high permittivity and high dielectric strength, the incorporation of surface-modified high- permittivity ceramic nanoparticles such as $BaTiO_3$ in moderate to high dielectric strength polymers has been studied extensively [24-27]. However, as a high nanoparticle volume fraction of ceramic particles (10-50 v/v-%) is often needed in order to increase the effective permittivity of the composite, excess local field enhancement due to the mismatch between the matrix-filler permittivities, formation of percolative pathways, nanoparticle agglomeration and increased porosity systematically lead to a decreased breakdown strength in comparison to the neat polymer [28-31], hence negating improvement in practical energy density.

On the other hand, improvement in short-term dielectric strength and breakdown distribution homogeneity may be achieved with polymer nanocomposites of permittivity-matching constituents and preferably with low fill-fractions, as reported e.g. for nano-silica filled cross-linked polyethylene (XLPE) [21, 32], core functionalized nano-silica filled epoxy [33] and nano-silica filled BOPP films [34]. These improvements are typically attributed to charge scattering, trapping and space charge properties at the filler-matrix interface [32, 35]. Proper nanoparticle dispersion and distribution in the polymer host have been necessitated in order to achieve improved breakdown performance and the importance of dispersion assessment by quantitative techniques are emphasized [22, 36]. However, the potential advantageous effect of a smooth nanodispersion on the breakdown performance can be overwhelmed if micro-aggregates are present in the material, as demonstrated in the case of nano-$CaCO_3$-filled BOPP films in [37].

Interestingly, the dielectric properties of the polymer matrix also play a significant role in the final breakdown performance of the composite. In [38], the effect of well-dispersed nano-silica on the breakdown performance of amorphous polymethyl methacrylate (PMMA), polyimide (PI), poly-4-vinylpyridine (P4VP) and polystyrene (PS) matrices was studied up to very high fill fractions (50 v/v-%). In the higher breakdown strength polymers (PMMA and PI), the inclusion of nano-silica systematically reduced the dielectric strength which was attributed to silica particles acting as failure-inducing defect sites providing a lower energy failure mode into the composite. In contrast, with the low breakdown strength matrices (P4VP and PS) and with moderate fill fractions (<15 v/v-%), silica was found to improve the dielectric strength, presumably by hindering the propagation of failure induced from the low dielectric strength matrix by charge trapping and scattering. At the highest loadings, the breakdown performance of all the nanocomposites was found to converge to a silica-inherent region (~450 V/µm in [38]) as the failure mode of silica became dominant.

In summary, it is evident from the literature that dielectric polymer nanocomposite films show great potential for capacitor applications but a careful choice of the constituents and processing parameters is a necessity. However, the area-dependence of the breakdown performance, while an extremely important factor from the capacitor point-of-view [13], has not received much attention in nanocomposite-related studies before. Breakdown distributions based on a small amount (e.g. 10-20) of small-area (mm^2-cm^2) breakdown measurements lack in statistical significance and may not be able to reveal the characteristic breakdown distribution structure of the composite accurately, especially in the low breakdown probability region. In return to these issues, the interdependence the filler and co-stabilizer contents, pre-mixing method, film processing and large-area breakdown performance in BOPP-silica nanocomposite films is studied by utilizing the self-healing multi-breakdown measurement method presented in the Part I.

2 EXPERIMENTAL DETAILS

2.1 FILM PROCESSING

The sample details, silica filler loadings, antioxidant contents, processing parameters and average film thicknesses with the standard deviations are presented in Table 1. Unstabilized polypropylene homopolymer HC318BF in powder form (non-commercial product, from Borealis N.V.) was used as the matrix polymer. Filler loadings of 1.0, 2.0 and 4.5 wt-% of Aerosil R812S (Evonik hydrophobic fumed silica) were studied. Process stabilizer Irganox 1010 (0.47 wt-%) and co-stabilizer Irgafos 168 (0-0.35 wt-%) were added to the compounds. Silica filler content, co-stabilizer content, pre-mixing method and orientation temperature were varied in accordance with Table 1 in order to study their effects on the breakdown performance. The film processing was conducted at the VTT Technical Research Centre of Finland and at a Brückner pilot film line in Denmark.

2.1.1 PRE-MIXING

In order to ensure proper dispersion of the constituents, polypropylene and silica powders were pre-mixed together with the stabilizing agents before compounding. Four different mixing methods were investigated. Automatic premixing was made by using (i) a high-speed Papenmeier mixer, (ii) Forberg rotating mixer and (iii) a drum mixer with polyethylene bag. Alternatively (iv), the polypropylene and silica powders were pre-mixed manually in a

polyethylene bag. The Papenmeier mixer is an effective high-speed mixer e.g. for polyvinyl chloride (PVC) powder mixing. The Forberg mixer is a low-speed and a low shear-rate mixer with two counter-rotating shafts. The rotation speed of Papenmeier was adjustable while the rotation speed of Forberg was constant. The parameters for the studied mixing methods were: (i) Papenmeier; mixing time of 80 s, rotation speed 2000 rpm, (ii) Forberg; mixing time of 10 min, rotation speed 100 rpm, filling level of 40 %, (iii) drum mixing; mixing time of 3 min and (iv) manual bag-mixing in a polyethylene bag; mixing time of ~2 min.

2.1.2 COMPOUNDING

Berstorff ZE 25/48D twin screw compounder with high-shear screw geometry and two separate kneading sections was used for compounding. Melt filter (screen size 42 µm) was used in the compounding unit. Compounding was made with a continuous nitrogen gas purge (flow 2.5 l/min). The compound was cooled in a water bath under a laminar air flow hood over the cooling section. Polymers were dried at 70 °C for 1.5 h in an oven and for 0.5 h in a vacuum oven before the compounding. Compounder output was 9 kg/h for all the compounds. The realized filler amounts were determined by burning the organic polymer and additives in an oven at 600 ℃ for 30 min + 10 min (see Table 1) according to the ISO 3451-1 standard.

2.1.3 CAST FILM EXTRUSION AND BI-AXIAL ORIENTATION

Cast films were extruded by a Brabender Plasticorder single screw extruder with a three-layer screen pack. The single screw had three stages with a mixing zone and the compression was 4:1. The films were cast through a 120 mm slot die onto a chill roll at +90 °C. The cast film thickness was 500-700 µm. Screw speed was 100 rpm and cylinder temperatures were between 220 and 230 °C. Compounds were also dried before the cast film extrusion as before compounding. Finally, the laboratory-scale cast films were bi-axially oriented with a Brückner KARO IV film stretching machine (set temperature 157-165 °C, stretching ratio 5.4 x 5.4).

Pilot-scale film was produced from the PP-Ref-3 and PP-Sil-9 compounds at a Brückner pilot film line. The pilot line consisted of a single screw extruder with a flat die, a casting station, MDO and TDO units and a winder. First, the polymer compound was melted in the extruder, quenched on the casting roll and then transferred to the MDO where it was reheated and stretched in the machine direction. Thereafter, the film was reheated in the TDO unit before transverse stretching and cooled down before winding. The temperature profile of the extruder was between 214 °C to 240 °C. Chill roll temperature was 62 °C. MD stretching roll temperatures were 142 °C to 155 °C and the stretching ratio was approximately 1:4. In TD-stretching the oven section temperatures were 170 °C to 183 °C and TD-stretching ratio was approximately 1:6.

2.2 STRUCTURAL CHARACTERIZATION

For transmission electron microscopy (TEM) analysis, ultrathin sections of the cast film samples were obtained using a Diatome 35° diamond knife at room temperature with a Leica Reichert Ultracut ultramicrotome. The 90 nm thick sections were collected on a 400 mesh copper grid and imaged with a JEOL JEM-1400EX electron microscope. The dispersion of the nano-silica was studied from TEM images converted to binary format and a parameter describing the characteristic length of the unreinforced polymer domains, free-space length L_f, was used to quantify the dispersion quality [36]. L_f is defined as the width of the largest randomly placed square for which the most probable number of intersecting particles is zero. Free-space length determination was performed in MATLAB (ten repetitive calculations per material) in which a statistically large number of squares of prescribed size are placed in random locations on the binary image. The number of particles within each box is counted and L_f is chosen as the characteristic square size that corresponds to a length for which the mode of the boxes contains no particles. The code was retrieved and used according to the literature. The free-space length parameter is well-suited for comparing different filler-loadings as the measured quantity is of physical nature (the distance between the particles). However, it is not relative to random dispersion; for the same filler loading, the further the dispersion is from uniform, the longer the L_f becomes. Lastly, in addition to the TEM analysis, bi-axially oriented film samples were also broken in liquid nitrogen and the cross-sectional surface

Table 1. Sample film details, silica filler content, antioxidant content, processing parameters and average film thicknesses. SD = standard deviation.

Sample code	Silica loading (wt-%)		Antioxidants (wt-%)		Pre-mixing method	Processing	Orientation temperature (°C)	Film thickness (µm)	
	Planned	Realized	Irganox 1010	Irgafos 168				Average	SD
PP-Ref-1A	-	0	0.45	0.35	Bag mixing	a	157	21.33	2.58
PP-Ref-1B	-	0	0.45	0.35	Bag mixing	a	161	18.81	2.35
PP-Ref-1C	-	0	0.45	0.35	Bag mixing	a	165	14.96	1.93
PP-Ref-2	-	0	0.45	0	Bag mixing	a	157	21.01	2.35
PP-Ref-3	-	N/A	0.45	0.35	Drum mixer	b	b	16.24	1.68
PP-Sil-1	1.0	1.14	0.45	0.35	Bag mixing	a	157	18.73	2.39
PP-Sil-2	2.0	2.24	0.45	0.35	Bag mixing	a	157	17.64	2.29
PP-Sil-3	4.5	3.94	0.45	0.35	Bag mixing	a	157	17.34	2.06
PP-Sil-4	4.5	2.96	0.45	0.35	Forberg	a	157	22.78	2.33
PP-Sil-5A	4.5	3.78	0.45	0.35	Drum mixer	a	157	19.44	2.26
PP-Sil-5B	4.5	3.78	0.45	0.35	Drum mixer	a	161	19.96	2.40
PP-Sil-5C	4.5	3.78	0.45	0.35	Drum mixer	a	165	16.39	1.73
PP-Sil-6	4.5	4.03	0.45	0.35	Papenmeier	a	157	18.63	2.16
PP-Sil-7	4.5	3.73	0.45	0.15	Bag mixing	a	157	16.46	2.05
PP-Sil-8	4.5	3.92	0.45	0	Bag mixing	a	157	16.85	2.54
PP-Sil-9	4.5	N/A	0.45	0.35	Drum mixer	b	b	15.30	1.01

a) (1) Compounding: Berstorff ZE 25/48D twin screw compounder, (2) Cast extrusion: Brabender Plasticorder single screw extruder, (3) Bi-axial orientation: Brückner KARO IV laboratory-stretcher

b) Compounding similarly to a), extrusion and orientation at a Brückner pilot-line

morphologies were imaged with a JEOL JSM-6360LV scanning electron microscope (SEM).

2.3 LARGE-AREA MULTI-BREAKDOWN MEASUREMENT

The main aspects of the large-area multi-breakdown measurement are revised briefly in the following. For more detailed information on the method, see the Part I of this publication.

2.3.1 SAMPLE PREPARATION

All the sample films were cut to 110 mm x 110 mm dimensions. The thickness of each sample film was then measured systematically at 25 points covering a 100 mm x 100 mm area with an LE1000-1 high-precision thickness measurement gauge. The average film thicknesses with the standard deviations are presented in Table 1. As discussed in the Part I, the laboratory-stretched films exhibited more thickness deviation in comparison to the pilot-scale films, as the middle region of a laboratory-stretched film is typically thinner in comparison to the outer regions. The thickness deviation was taken into account during the breakdown field calculation. In order to realize the self-healing multi-breakdown measurement, Zn-Al-metallized BOPP film (12 μm Tervakoski PSX) was used as the electrode film (active area of 81 cm^2).

2.3.2 TEST PROCEDURE

Breakdown measurements were conducted in oil (Shell Diala DX) in accordance with IEC-60243 standard [39, 40] in order to mitigate surface flashovers and other non-breakdown events occurring at the sample and electrode film edges. The DC voltage across the test capacitor was first raised to approximately 40-60 % of the probable short-time breakdown voltage with a fast ramp speed of 400 V/s, after which a slow ramp speed of 30 V/s was used for measuring the breakdown events, roughly in accordance to the slow rate-of-rise test defined in the IEC-60243-1.

During each discharge event in the test capacitor, the discharge current $i_d(t)$, test capacitor voltage $u_{DUT}(t)$ and the time-signature of the event were recorded with a high-resolution oscilloscope operated in the sequence-acquisition mode and triggered to the positive rising edge of the discharge current signal. This allowed a detailed determination of the breakdown voltage, voltage drop, peak current, discharge energy and various pulse time parameters for each event. A video was recorded from the top of the test capacitor unit for the whole duration of the breakdown measurement, allowing a detailed chronological analysis of the breakdown progression of the sample after the measurement. Six samples were typically measured per material, resulting in 486 cm^2 of total measured area.

2.3.3 BREAKDOWN FIELD DETERMINATION

As discussed in the Part I, the basic approach to transforming the measured breakdown voltages into breakdown fields was to utilize average thickness $d_{i,avg}$ of each sample film i [39]. By utilizing the video recordings, $d_{i,avg}$ was calculated as an average of the sector thicknesses where breakdowns had occurred by the end of the breakdown measurement. Alternatively, breakdown fields were also determined manually for each event by rigorously determining the average thickness around the discharge spot (by means of the video recording) and by calculating the average breakdown field event-by-event. The manual thickness determination was performed in MATLAB. The breakdown results presented in this paper are based on the manual thickness determination.

2.3.4 BREAKDOWN DATA SELECTION PROCEDURE

As multiple self-healing breakdowns are measured from each sample, the measured data has to be validated, any non-breakdown events should be ruled out and only the breakdown events which appear independent of each other should be qualified for further analysis. A data selection procedure based on the discharge energy characteristics of the self-healing breakdown process was utilized [6]. It has been hypothesized that discharge events with the discharge energies and breakdown voltages not following the trend set by the first breakdowns may be attributed to successive breakdowns occurring close to or at previous breakdown sites or to other non-breakdown events. The data selection was based on two criteria, namely by selecting only the discharge events (i) for which the corresponding discharge energies followed the trend preset by the first measured self-healing breakdowns and (ii) for which the breakdown voltages were higher than that of the previously selected breakdown. First breakdowns were used as a basis for the data selection procedure. The procedure is discussed and evaluated in more detail in the Part I.

2.3.5 COMPARATIVE SMALL-AREA BREAKDOWN MEASUREMENT

Comparative small-area single-breakdown measurements were performed for selected materials in order to study the area-effect in the nanocomposites in more detail. The small-area breakdown measurements were performed by using a steel rod-rod electrode configuration with thin graphite plates in between rods and the sample film in order to smoothen the contact and to prevent electrode pitting. The active area was approximately 1 cm^2 and the measurements were performed in mineral oil with a 400 V/s DC voltage ramp rate in accordance to the IEC-60243 standard [39, 40]. The method was equivalent to the one previously used in [34, 37].

2.4 STATISTICAL ANALYSIS

For the statistical analysis of the breakdown data, 2-parameter Weibull distributions and additively mixed Weibull distributions were utilized:

$$F(x) = \sum_{i=1}^{S} \frac{N_i}{N} F_i(x) = \sum_{i=1}^{S} \frac{N_i}{N} \left[1 - \exp\left\{ -\left(\frac{x}{\alpha_i} \right)^{\beta_i} \right\} \right]. \quad (1)$$

In equation (1), $F_i(x)$ is the 2-parameter Weibull distribution, S is the number of subpopulations, N_i/N is the portion (%) of the subpopulation i and α_i and β_i are the Weibull parameters of subpopulation i. The scale parameter α corresponds to the value of x at the 63.2 % failure probability and the shape parameter β depicts the slope or homogeneity of the theoretical distribution. For a single 2-parameter Weibull distribution, S and the portion N_i/N in equation (1) are equal to 1 and 100 %, respectively.

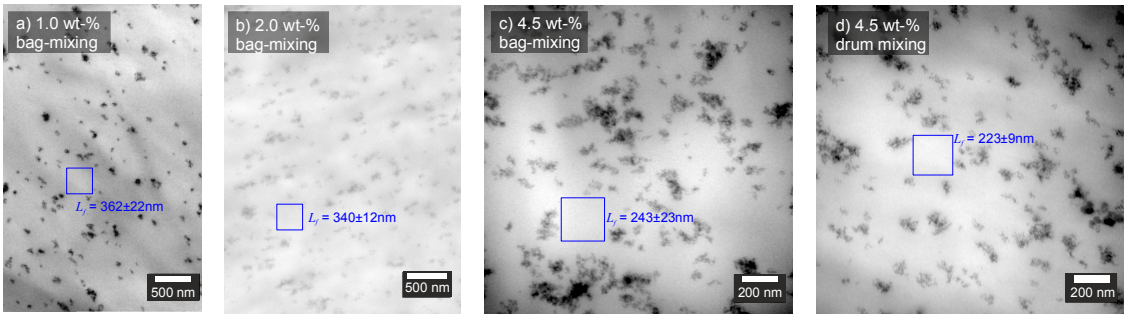

Figure 1. TEM-micrographs of ultrathin sections of silica-BOPP nanocomposites **a)** PP-Sil-1 (1.0 wt-% silica), **b)** PP-Sil-2 (2.0 wt-% silica), **c)** PP-Sil-3 (4.5 wt-% silica) pre-mixed manually in a polyethylene bag and **d)** PP-Sil-5 (4.5 wt-% silica) pre-mixed automatically with a drum mixer. The free-space lengths (L_f) chararacterizing the size of the unreinforced polymer domains are also presented for each sample.

Maximum-likelihood estimation (MLE) and non-linear regression (NLR) methods were used for the parameter estimation and the analysis was performed with Weibull++ and MATLAB software.

3 RESULTS AND DISCUSSION

3.1 QUANTITATIVE ASSESSMENT OF THE NANOCOMPOSITE STRUCTURE

TEM-micrographs of ultrathin sections of BOPP-silica nanocomposites with varying filler contents and pre-mixing methods are presented in Figure 1, depicting the typical quality of nanodispersion achieved. The dispersion state of the nanoparticles in all the composites was found to be similar. All the composites contained micron-sized silica agglomerates and even though they were relatively scarce, they contained a considerable amount of filler material, as shown in Figure 2. However, instead of focusing on the microagglomerates, the amount of silica dispersed as nanosized agglomerates was studied and the amount of unreinforced polymer was of the main interest. The free-space length values (L_f) presented in Figure 1 indicate that at the nanoscale, the dispersion can be qualified as agglomerated dispersion rather than as clustered, random, or uniform. The calculated L_f values of the 1.0 wt-% and 2.0 wt-% silica nanocomposites (Figure 1a-1b) do not differ markedly from each other and further, if they are compared with the 4.5 wt-% nanocomposites (Figure 1c-d), the difference in L_f is small when considering the increase in the silica content. These factors indicate that in addition to nanosized clusters, the filler material is also agglomerated as microparticles.

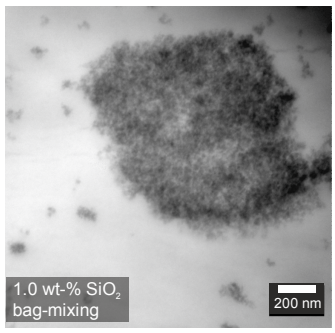

Figure 2. TEM-micrograph of a silica micro-agglomerate in a PP-Sil-1 cast film sample (1.0 wt-% silica).

Table 2. Large-area breakdown field values of the studied compounds corresponding to 5 %, 63.2 % and 95 % breakdown probabilities and the weakest spot measured from the total film area (486 cm^2). The number of breakdowns indicates the number of qualified breakdowns after the data selection procedure (see Part I).

Sample code	Large-area breakdown performance				
	N selected breakdowns	Breakdown field (V/µm) at probability			Weakest point (V/µm)
		5 %	63.2 %	95 %	
PP-Ref-1A	128	558	720	791	446
PP-Ref-1B	111	588	713	765	484
PP-Ref-1C	105	577	695	762	551
PP-Ref-2	103	614	691	735	599
PP-Ref-3	124	559	701	762	481
PP-Sil-1	155	561	658	698	503
PP-Sil-2	147	521	615	661	456
PP-Sil-3	108	506	591	654	306
PP-Sil-4	100	526	584	607	512
PP-Sil-5A	149	509	597	665	475
PP-Sil-5B	129	544	616	662	479
PP-Sil-5C	117	539	620	658	526
PP-Sil-6	149	518	603	638	480
PP-Sil-7	141	529	612	529	456
PP-Sil-8	130	524	608	669	513
PP-Sil-9	121	523	600	681	469
PP-Ref-3*	124	551	743	927	445
PP-Sil-9*	86	547	723	849	399

*) Fast rate-of-rise (400 V_{DC}/s)

3.2 LARGE-AREA BREAKDOWN PERFORMANCE

The effect of silica filler content, pre-mixing method, co-stabilizer content and orientation temperature on the large-area dielectric breakdown performance of BOPP-silica nanocomposites is presented in Figure 3a-d. If applicable, single 2-parameter Weibull distributions were fitted to the breakdown data; otherwise mixed Weibull distributions (2-3 subpopulations) were utilized on the basis of the best goodness-of-fit test result. In order to enable convenient comparison between all the distributions regardless of the distribution structure, 5, 63.2 and 95 % breakdown percentiles were calculated and are given in Table 2. In some cases, the calculated Weibull distributions do not follow the low-probability (<5 %) breakdowns in a satisfactory way (see e.g. Figure 3a). Therefore, the weakest point measured from the total film area is also presented for each material in Table 2 for comparison. Nevertheless, visual comparison of the Weibull plots is most recommended for an easy assessment of the breakdown performance and distribution homogeneity. 90 % confidence

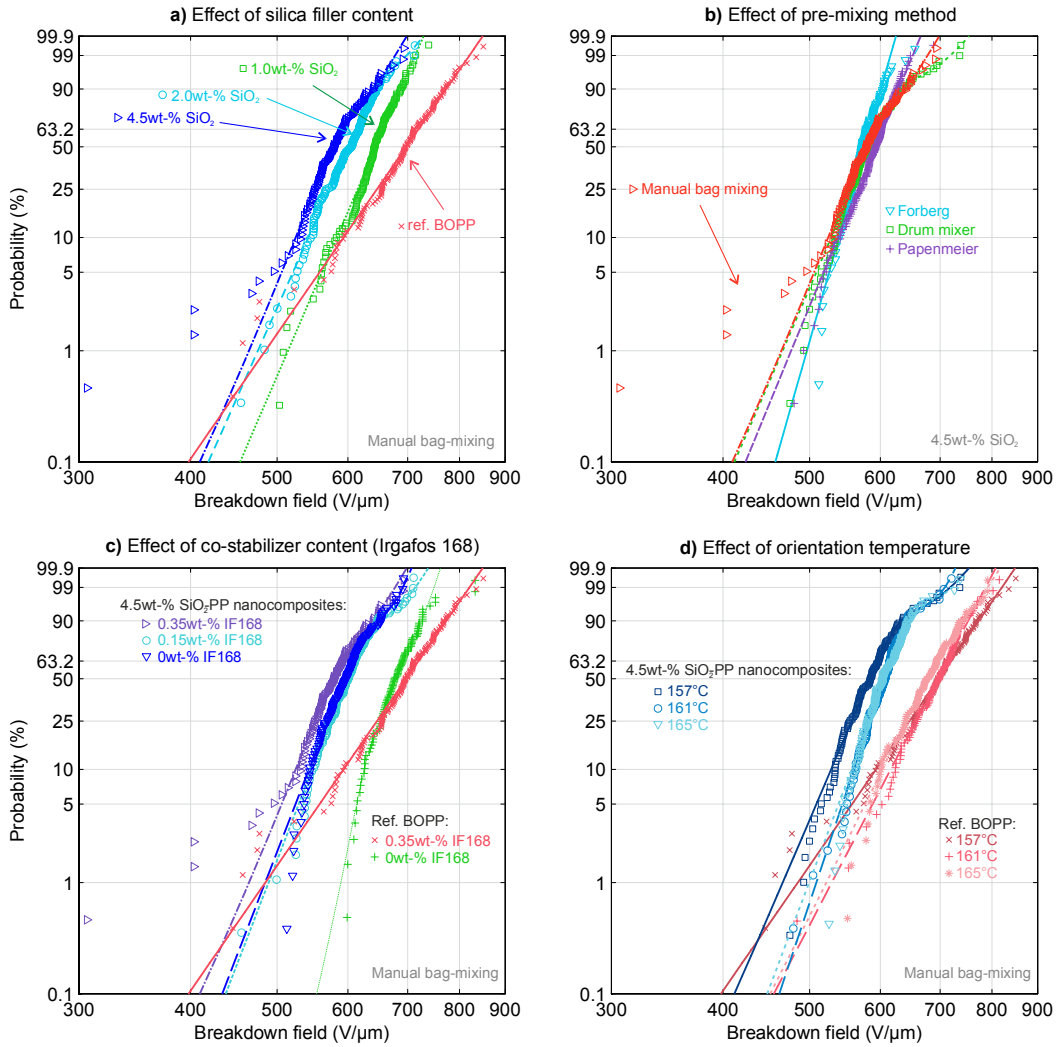

Figure 3. Large-area multi-breakdown performance of BOPP-SiO_2 and reference-BOPP films. The Weibull probability plots show the effect of **a)** nano-silica filler content, **b)** pre-mixing method, **c)** co-stabilizer (Irgafos 168) content and **d)** orientation temperature on the breakdown performance. 6 samples (486 cm^2 total film area) per material were measured. 90 % confidence bounds were calculated but are not shown for clarity. The studied materials are: a) PP-Ref-1A, PP-Sil-1, 2 and 3 (silica content); b) PP-Sil-3,4, 5A and 6 (pre-mixing method; c) PP-Ref-1A and 2, PP-Sil-3, 7 and 8 (co-stabilizer content); and d) PP-Ref-1A, B and C, PP-Sil-5A, B and C.

bounds were also calculated for each data set but they are omitted from Figure 3 for the sake of clarity. For the breakdown field calculation, the manual thickness determination approach was utilized (see Part I for further information).

Regarding the silica filler-content, it is evident from Figure 3a and Table 2 that with an increasing nano-silica fill-fraction the overall large-area breakdown performance decreases in comparison to the neat polypropylene, similarly as previously reported for various polymer-silica nanocomposites in [38] and for polystyrene-silica nanocomposites in [41]. On the other hand, the inclusion of nano-silica also increases the breakdown distribution homogeneity. In coherence with [38], this may be attributed to nano-silica introducing a lower energy failure mode into the polypropylene matrix, but due to the relatively uniform nanodispersion, the breakdown variability is concurrently reduced in comparison to the neat polymer. It is also notable that at the lowest silica fill-fraction (1 wt-%), the weak points exhibit a shift towards higher dielectric strength in comparison to the reference BOPP (503 vs. 446 V/µm). The aforementioned findings together emphasize the fact that low fill-fractions are often preferable in nanocomposite systems. A more comprehensive study of very low fill-fractions (<1 wt-%) could also be performed in the future as the optimum filler content may be below the general range studied here. It should be noted that from the practical point-of-view, increased breakdown distribution homogeneity and improvement in the low-probability breakdown behavior are substantially more relevant than the breakdown behavior at the higher (>10 %) breakdown probability region.

As can be seen in Figure 3b, the manual pre-mixing of the raw materials in a polyethylene bag prior to compounding may have a partial influence on the weak point behavior of

the nanocomposite and could be attributed to micron-sized silica agglomerates. On the other hand, the compounds pre-mixed automatically did not show any low-probability breakdowns deviating from the main distribution and together they gave a very similar response in the large-area multi-breakdown test. The small differences seen in Figure 3b may be also attributed to the realized silica contents (see Table 1). In spite of careful sealing, the Forberg mixer was found to exhibit a high leakage of silica powder and hence, it was not deemed as a suitable pre-mixing method. The drum mixer and Papenmeier mixer showed no leakage and due to its convenience, drum mixing method was seen as the most potential pre-mixing method.

The test series with the varying co-stabilizer content (Figure 3c) suggests that the breakdown performance of the silica nanocomposites is also influenced by the Irgafos 168 content; with a decreasing Irgafos 168 content, the breakdown distributions shifted slightly towards higher breakdown strength. Despite the manual bag-mixing method, the compounds with 0.15 wt-% and 0 wt-% of Irgafos 168 did not show weak spots deviating from the main breakdown distribution. However, the reference BOPP films with 0.35 wt-% and 0 wt-% of Irgafos 168 show a much more drastic difference in breakdown performance, particularly in the breakdown distribution homogeneity (Figure 3c). Although the role of the antioxidants Irganox 1010 and Irgafos 168 during the material processing phase (compounding, cast extrusion) in protecting the polypropylene from oxidative degradation is unquestionable [42], the results here indicate that Irgafos 168 has a detrimental effect on the breakdown performance of the end-product. The results can also be seen as a processing-related issue; the Irgafos 168 content and the processing parameters should be optimized so that no excess Irgafos 168 residue remains in the film after the processing is completed. It is also noteworthy that in [43] the consumption of the process stabilizer Irganox 1010 by an optimized duration of UV irradiation was found to increase the breakdown strength of BOPP films markedly.

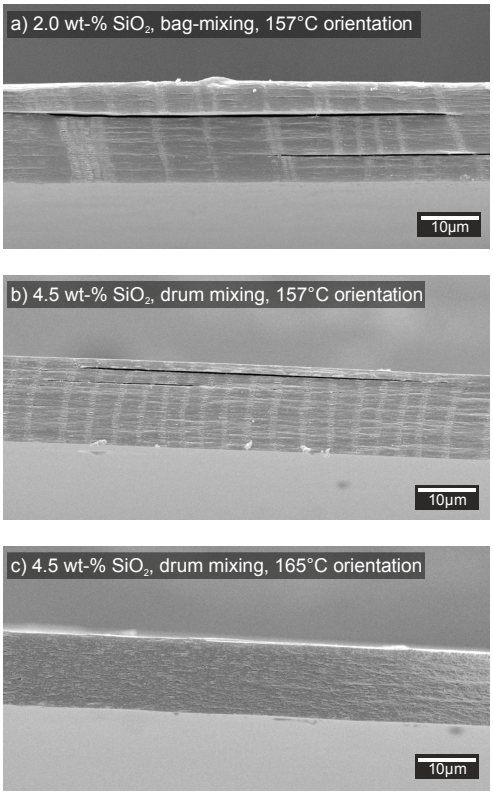

Figure 4. SEM cross-section images of **a)** PP-Sil-2 (2.0 wt-% silica, bag-mixing) and **b)** PP-Sil-5A (4.5 wt-% silica, drum mixing) films oriented in 157 °C and **c)** PP-Sil-5C (4.5 wt-% silica, drum mixing) film oriented in 165 °C. Large voids were systematically seen in films oriented at 157 °C (more profoundly in the bag-mixed compounds) whereas no voids were observed at the (set) temperature of 165 °C.

The breakdown performance of the BOPP-silica nanocomposite films was also found to improve when the orientation temperature was increased from 157 °C to 165 °C (set temperature); see Figure 3d and Table 2. Figure 4 presents the cross-section surface morphologies of various BOPP-silica nanocomposite films broken in liquid nitrogen and imaged with SEM. Generally, the fracture surface morphologies were found to vary from a fine oriented structure to a more coarse and circular structure. Films oriented at the set temperature of 157 °C were found to contain randomly distributed wide voids and fracture lines perpendicular to the film surface, especially in the case of the manually pre-mixed compounds (Figure 4a), but also in the case of the automatically pre-mixed compounds (Figure 4b). However, upon increasing the orientation temperature of the silica nanocomposites, the amount of voids and fracture lines decreased until at 165 °C (Figure 4c) a fine oriented structure was obtained and no voids were observed (the threshold temperature was approximated to be ~163 °C). It can be concluded that the silica nanoparticles may act as the origin of the voids and fracture lines during the orientation process and an optimization of the orientation temperature is required. The voids and fracture lines present in the nanocomposite films may act as weak spots and may be attributed to the differences observed in the breakdown performance in Figure 3d. It is noted however that the sample preparation method may have an influence on the fracture surface.

In summary, it is obvious that the origin of the low-probability weak spots and the overall breakdown performance is due to a complex interplay between various mechanisms and processing parameters and cannot be explained solely by the aforementioned circumstances. Nevertheless, the results presented here emphasize the fact that each material has an individual processing-dependent breakdown response (or "fingerprint", as referred to in [4]) and that a thorough understanding and the optimization of the film processing parameters are crucial for achieving improved breakdown performance in dielectric polymer nanocomposite films.

3.3 AREA- AND RAMP-RATE-DEPENDENCIES

The area dependence of the breakdown performance was studied in more detail by performing small-area (1 cm^2) single-breakdown measurements and large-area (81 cm^2) multi-breakdown measurements for the both laboratory- and pilot-scale 4.5 wt-% BOPP-Silica nanocomposites (PP-Sil-

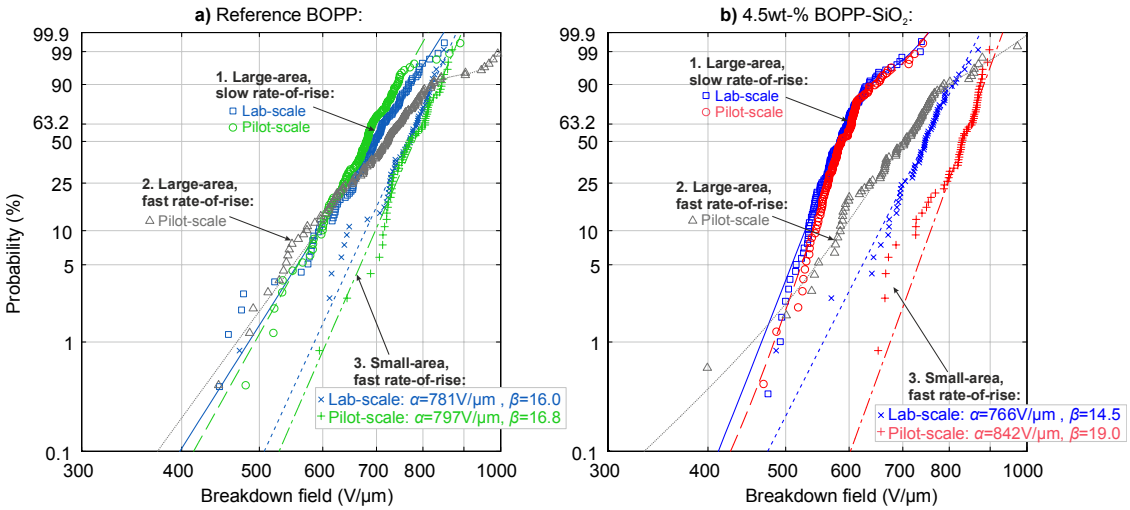

Figure 5. Area- and ramp-rate dependencies of the breakdown performance of the laboratory- and pilot-scale **a**) BOPP-silica (4.5 wt-%) and **b)** unfilled reference BOPP films. For the small-area (~1 cm^2) breakdown results (60 samples per material), the Weibull parameters (single 2-parameter Weibull) are given in the figures; see Table 2 for the numerical breakdown data of the large-area measurement. The large-area (81 cm^2) multi-breakdown measurements were performed with the slow rate-of-rise (see the text) and with a fast rate-of-rise (400 V_{DC}/s). The small-area measurements were made with a fast rate-of-rise (400 V_{DC}/s).

5A and PP-Sil-9) and for the corresponding reference films (PP-Ref-1A and PP-Ref-3). Additional large-area multi-breakdown measurements with a fast DC ramp rate of 400 V/s were performed for the pilot-scale materials (PP-Ref-3 and PP-Sil-9) in order to study the effect of voltage ramp rate on the breakdown response. The results are presented in Figure 5. Single 2-parameter Weibull distributions were fitted to the small-area single-breakdown data sets and the corresponding Weibull parameters are given in Figure 5. For the breakdown percentiles of the large-area multi-breakdown distributions, see Table 2.

In regard to the reference BOPP films (Figure 5a), the small-area single-breakdown distributions relate logically to the large-area multi-breakdown distributions, as already discussed in the Part I. The large-area multi-breakdown distributions measured with the slow and fast ramp rates show no major differences except for the slight differences in the >25 % breakdown probability region (see Figure 5a). As expected based on the area-effect, the small-area breakdown points reside at a higher breakdown field region in comparison to the large-area measurement but may still be projected vertically along the probability axis to match portions of the corresponding large-area breakdown distribution. Also, the small-area breakdown distributions show similar Weibull parameters and there is no considerable difference in the breakdown behavior between the laboratory- and pilot-scale reference BOPP films; the small- and large-area breakdown distribution structures are very similar to each other in all the cases.

As opposed to the unfilled reference BOPP films, the 4.5 wt-% BOPP-silica films (Figure 5b) show anomalous breakdown responses which cannot be explained solely by the area-effect. When measured with the slow rate of-rise, the large-area multi-breakdown distributions of both the laboratory- and pilot-scale nanocomposite films show lower overall performance but higher breakdown distribution homogeneity in comparison to the unfilled reference BOPP films, similarly as already discussed in the previous sub-chapter. However, when measured with the fast rate-of-rise, the large-area multi-breakdown response of the pilot-scale silica nanocomposite shows a drastically different breakdown behavior, see Figure 5b. It is obvious from Figure 5b that the small- and large-area breakdown distributions measured with the fast rate-of-rise relate logically to each other but on the other hand, they do not reflect the large-area response measured with the slow rate-of-rise as in the case of the reference BOPP films. Even more intriguingly, the large-area breakdown distributions of the pilot-scale reference BOPP film (Figure 5a) and the 4.5 wt-% pilot-scale silica nanocomposite film (Figure 5b) measured with the fast rate-of-rise are nearly identical with each other with 90 % confidence, i.e. the silica nanocomposite shows a breakdown response very similar to that of the reference BOPP film.

The results in Figure 5b suggest that the silica nanocomposites exhibit altered internal charge behavior under DC electric field. It is speculated that with a slow rate-of-rise, space charge accumulation at the silica-polypropylene interfaces may act as a breakdown-initiating factor, but due to the relatively uniform filler dispersion and the large interfacial volume, the breakdown distribution homogeneity is concurrently improved. Conversely, with a fast rate-of-rise, space charge does not have time to accumulate at the interfaces and the breakdown response of the nanocomposite is more representative of the BOPP-matrix alone instead of the BOPP-silica interface. Interestingly, the pilot-scale 4.5 wt-% BOPP-silica film gave the highest small-area breakdown performance in comparison to the others (Weibull α=842 V/μm, see Figure 5), suggesting that the inclusion of nano-silica may improve the short-term small-area breakdown strength of BOPP films.

The above results exemplify not only the importance of optimized film processing in achieving improved

breakdown performance, but also the importance of careful breakdown strength assessment when dielectric films of more complex internal structure are studied. Small-area breakdown strength measurement based on a fast rate-of-rise may not reveal the breakdown behavior accurately and can potentially lead to non-realistic conclusions. Especially in this sense, the results presented in this study show that the large-area multi-breakdown measurement method with a moderate ramp-rate is advantageous in approximating large-area breakdown distribution structure of polymer films in higher detail and leads to sensible results from the practical point-of-view.

4 CONCLUSION

Large-area multi-breakdown performance of laboratory- and pilot-scale BOPP-silica nanocomposite films was studied with a particular emphasis on the interdependence of filler content, pre-mixing method, co-stabilizer content, orientation temperature and the large-area breakdown behavior. The area- and ramp-rate-dependencies of the breakdown performance were also studied in detail. The results showed that the breakdown responses of the reference BOPP and BOPP-silica films are largely dependent on both the film manufacturing process and the filler content, as also supported by the structural TEM- and SEM-analyses. The optimum silica filler content was found to reside at the low fill fraction level (~1.0 wt-%) where it is more probable to achieve a good-quality silica nanodispersion without excess micro-agglomeration over large volumes. The breakdown response of the silica nanocomposites was also found to be not only dependent on the active measurement area but also on the ramp rate, indicating that the studied silica nanocomposites exhibit altered internal charge behavior under DC electric field. The results obtained exemplified not only the importance of optimized film processing in achieving improved breakdown performance, but also the importance of careful breakdown strength assessment when dielectric films of more complex internal structure are studied.

REFERENCES

[1] M. Rabuffi and G. Picci, "Status quo and future prospects for metallized polypropylene energy storage capacitors," IEEE Trans. Plasma Sci., Vol. 30, No. 5, pp. 1939-1942, 2002.

[2] Y. Wang, X. Zhou, Q. Chen, B. Chu, and Q. M. Zhang, "Recent development of high energy density polymers for dielectric capacitors," IEEE Trans. Dielectr. Electr. Insul., Vol. 17, No. 4, pp. 1036-1042, 2010.

[3] S. Ul-Haq and G. R. G. Raju, "Weibull statistical analysis of area effect on the breakdown strength in polymer films," IEEE Conf. Electr. Insul. Dielectr. Phenomena, pp. 518-521, 2002.

[4] S. J. Laihonen, U. Gafvert, T. Schutte, and U. W. Gedde, "DC breakdown strength of polypropylene films: Area dependence and statistical behavior," IEEE Trans. Dielectr. Electr. Insul., Vol. 14, No. 2, pp. 275-286, 2007.

[5] C. Xu, J. Ho, and S. Boggs, "Automatic breakdown voltage measurement of polymer films," IEEE Electr. Insul. Mag., Vol. 24, No. 6, pp. 30-34, 2008.

[6] I. Rytöluoto and K. Lahti, "New Approach to Evaluate Area-Dependent Breakdown Characteristics of Dielectric Polymer Films," IEEE Trans. Dielectr. Electr. Insul., Vol. 20, No. 3, pp. 937-946, 2013.

[7] K. Wu, Y. Wang, Y. Cheng, L. A. Dissado, and X. Liu, "Statistical behavior of electrical breakdown in insulating polymers," J. Appl. Phys., Vol. 107, No. 6, pp. 064107.1-5, 2010.

[8] L. A. Dissado and J. C. Fothergill, *Electrical Degradation and Breakdown in Polymers,* Philadelphia, Peter Peregrinus Ltd., 1992.

[9] C. W. Reed and S. W. Cichanowski, "The fundamentals of aging in HV polymer-film capacitors," IEEE Trans. Dielectr. Electr. Insul., Vol. 1, No. 5, pp. 904-922, 1994.

[10] P.-O. Sassoulas, B. Gosse, and J.-P. Gosse, "Self-healing breakdown of metallized polypropylene," IEEE 7th Int'l. Conf. Solid Dielectr., (ICSD), pp. 275-278, 2001.

[11] B. Walgenwitz, J.-H. Tortai, N. Bonifaci, and A. Denat, "Self-healing of metallized polymer films of different nature," IEEE Int'l. Conf. Solid Dielectr., (ICSD), pp. 29-32, 2004.

[12] I. Rytöluoto and K. Lahti, "Effect of Inter-Layer Pressure on Dielectric Breakdown Characteristics of Metallized Polymer Films for Capacitor Applications," IEEE 7th Int'l. Conf. Solid Dielectr., (ICSD), pp. 682-687, 2013.

[13] M. A. Schneider, J. R. MacDonald, M. C. Schalnat, and J. B. Ennis, "Electrical breakdown in capacitor dielectric films: Scaling laws and the role of self-healing," IEEE Power Modulator and High Voltage Conf. (IPMHVC), pp. 284-287, 2012.

[14] P. Barber, S. Balasubramanian, Y. Anguchamy, S. Gong, A. Wibowo, H. Gao, H. J. Ploehn and H.-C. Zur Loye, "Polymer Composite and Nanocomposite Dielectric Materials for Pulse Power Energy Storage," Materials, Vol. 2, No. 4, pp. 1697-1733, 2009.

[15] L. Zhu and Q. Wang, "Novel Ferroelectric Polymers for High Energy Density and Low Loss Dielectrics," Macromolecules, Vol. 45, No. 7, pp. 2937-2954, 2012.

[16] T. C. Mike Chung, "Functional Polyolefins for Energy Applications," Macromolecules, Vol. 46, No. 17, pp. 6671-6698, 2013.

[17] J. K. Nelson, *Dielectric Polymer Nanocomposites*.: Springer US, 2010.

[18] V. K. Thakur and M. R. Kessler, "Polymer Nanocomposites: New Advanced Dielectric Materials for Energy Storage Applications," in *Advanced Energy Materials*, John Wiley & Sons, Inc., pp. 207-257, 2014.

[19] Q. Wang and L. Zhu, "Polymer nanocomposites for electrical energy storage," J. Polymer Sci. Part B: Polymer Phys., Vol. 49, No. 20, pp. 1421-1429, 2011.

[20] J. Y. Li, L. Zhang, and S. Ducharme, "Electric energy density of dielectric nanocomposites," Appl. Phys. Letters, Vol. 90, No. 13, pp. 132901, 2007.

[21] M. Roy, J. K. Nelson, R. K. MacCrone, and L.S. Schadler, "Candidate mechanisms controlling the electrical characteristics of silica/XLPE nanodielectrics," J. Materials Sci., Vol. 42, No. 11, pp. 3789-3799, 2007.

[22] C. Calebrese, L. Hui, L. S. Schadler, and J. K. Nelson, "A review on the importance of nanocomposite processing to enhance electrical insulation," IEEE Trans. Dielectr. Electr. Insul., Vol. 18, No. 4, pp. 938-945, 2011.

[23] L. Hui, L. S. Schadler, and J. K. Nelson, "The influence of moisture on the electrical properties of crosslinked polyethylene/silica nanocomposites," IEEE Trans. Dielectr. Electr. Insul., Vol. 20, No. 2, pp. 641-653, 2013.

[24] Z.-M. Dang, Y.-Q. Lin, H.-P. Xu, C.-Y. Shi, S.-T. Li and J. Bai, "Fabrication and Dielectric Characterization of Advanced $BaTiO_3$/Polyimide Nanocomposite Films with High Thermal Stability," Advanced Functional Materials, Vol. 18, No. 10, pp. 1509-1517, 2008.

[25] P. Kim, S. C. Jones, P. J. Hotchkiss, J. N. Haddock, B. Kippelen, S. R. Marder and J. W. Perry, "Phosphonic Acid-Modified Barium Titanate Polymer Nanocomposites with High Permittivity and Dielectric Strength," Advanced Materials, Vol. 19, No. 7, pp. 1001–1005, 2007.

[26] L. A. Fredin, Z. Li, M. A. Ratner, M. T. Lanagan, and T. J. Marks, "Enhanced Energy Storage and Suppressed Dielectric Loss in Oxide Core–Shell–Polyolefin Nanocomposites by Moderating Internal Surface Area and Increasing Shell Thickness," Advanced Materials, Vol. 24, No. 44, pp. 5946-5953, 2012.

[27] K. Yu, H. Wang, Y. Zhou, Y. Bai, and Y. Niu, "Enhanced dielectric properties of $BaTiO_3$/poly(vinylidene fluoride) nanocomposites for energy storage applications," J. Appl. Phys., Vol. 113, No. 3, pp. 034105, 2013.

[28] P. Kim, N. M. Doss, J. P. Tillotson, P. J. Hotchkiss, M.-J. Pan, S. R. Marder, J. Li, J. P. Calame and J. W. Perry, "High Energy Density Nanocomposites Based on Surface-Modified $BaTiO_3$ and a Ferroelectric Polymer," ACS Nano, Vol. 3, No. 9, pp. 2581-2592, 2009.

[29] N. Guo, S. A. DiBenedetto, P. Tewari, M. T. Lanagan, M. A. Ratner and T. J. Marks "Nanoparticle, Size, Shape, and Interfacial Effects on Leakage Current Density, Permittivity, and Breakdown Strength of Metal Oxide−Polyolefin Nanocomposites: Experiment and Theory," Chemistry of Materials, Vol. 22, No. 4, pp. 1567-1578, 2010.

[30] K. Yu, Y. Niu, F. Xiang, Y. Zhou, Y. Bai and H. Wang, "Enhanced electric breakdown strength and high energy density of barium titanate filled polymer nanocomposites," J. Appl. Phys., Vol. 114, No. 17, pp. 174107, 2013.

[31] J. P. Calame, "Finite difference simulations of permittivity and electric field statistics in ceramic-polymer composites for capacitor applications," J. Appl. Phys., Vol. 99, No. 8, pp. 084101, 2006.

[32] M. Roy, J. K. Nelson, R. K. MacCrone, L. S. Schadler, C. W. Reed and R. Keefe, "Polymer nanocomposite dielectrics-the role of the interface," IEEE Trans. Dielectr. Electr. Insul., Vol. 12, No. 4, pp. 629-643, 2005.

[33] S. Virtanen, T. M. Krentz, J. K. Nelson, L. S. Schadler, M. Bell, B. Benicewicz, H. Hillborg and S. Zhao "Dielectric breakdown strength of epoxy bimodal-polymer-brush-grafted core functionalized silica nanocomposites," IEEE Trans. Dielectr. Electr. Insul., Vol. 21, No. 2, pp. 563-570, 2014.

[34] M. Takala, H. Ranta, P. Nevalainen, P. Pakonen, J. Pelto, M. Karttunen, S. Virtanen, V. Koivu, M. Pettersson, B. Sonerud, K. Kannus, "Dielectric properties and partial discharge endurance of polypropylene-silica nanocomposite," IEEE Trans. Dielectr. Electr. Insul., Vol. 17, no. 4, pp. 1259-1267, 2010.

[35] M. G. Danikas and T. Tanaka, "Nanocomposites - A Review of Electrical Treeing and Breakdown," IEEE Electr. Insul. Mag., Vol. 25, No. 4, pp. 19-25, 2009.

[36] H.S. Khare and D.L. Burris, "A quantitative method for measuring nanocomposite dispersion," Polymer, Vol. 51, No. 3, pp. 719-729, 2010.

[37] S. Virtanen, H. Ranta, S. Ahonen, M. Karttunen, J. Pelto, K. Kannus and M. Pettersson, "Structure and dielectric breakdown strength of nano calcium carbonate/polypropylene composites," J. Appl. Polymer Sci., Vol. 131, No. 1, pp. 39504.1-8, 2014.

[38] C. A. Grabowski, S. P. Fillery, N. M. Westing, C. Chi, J. S. Meth, M. F. Durstock, and R. A. Vaia, "Dielectric Breakdown in Silica–Amorphous Polymer Nanocomposite Films: The Role of the Polymer Matrix," ACS Appl. Materials Interfaces, Vol. 5, No. 12, pp. 5486-5492, 2013.

[39] "Electric strength of insulating materials - Test methods - Part 1: Tests at power frequencies," IEC standard 60243-1, 2013-03.

[40] "Electric strength of insulating materials - Test methods - Part 2: Additional requirements for tests using direct voltage," IEC standard 60243-2, 2001-02.

[41] M. Praeger, A. S. Vaughan, and S. G. Swingler, "The breakdown strength and localised structure of polystyrene as a function of nanosilica fill-fraction," IEEE Int'l. Conf. Solid Dielectrics (ICSD), pp. 863-866, 2013.

[42] R. Gensler, C. J. G. Plummer, H.-H. Kausch, E. Kramer, J.-R. Pauquet and H. Zweifel, "Thermo-oxidative degradation of isotactic polypropylene at high temperatures: phenolic antioxidants versus HAS," Polymer Degradation and Stability, Vol. 67, No. 2, pp. 195-208, 2000.

[43] J. Ho, R. Ramprasad, and S. Boggs, "Effect of Alteration of Antioxidant by UV Treatment on the Dielectric Strength of BOPP Capacitor Film," IEEE Trans. Dielectr. Electr. Insul., Vol. 14, No. 5, pp. 1295-1301, 2007.

Ilkka Rytöluoto (S'13) was born in Tampere, Finland on 17 April 1985. He received the M.Sc. (Tech.) degree in electrical engineering from Tampere University of Technology (TUT), Tampere, Finland in 2011. Since 2012 he has been working as a Researcher in the high voltage research group of the Department of Electrical Engineering at TUT, with the aim towards the Ph.D. degree. His current research interests include large-area dielectric breakdown characterization of polymer and polymer nanocomposite films and the analysis of the self-healing breakdown performance of metalized dielectric films.

Kari Lahti (M'01) was born in Hämeenlinna, Finland, on 8 March 1968. He received the M.Sc. and Doctoral degrees in electrical engineering from Tampere University of Technology in 1994 and 2003, respectively. Since then he has worked at the Department of Electrical Engineering at TUT, currently as a Research Manager and Adjunct Professor. Since 2002 he has been responsible for the high voltage laboratory services at TUT. His research interests are in the area of high voltage engineering, especially surge arresters, environmental testing of high voltage materials and apparatus, high voltage testing methods and dielectric characterization of insulating materials.

Mikko Karttunen was born in Tampere, Finland in 1955. He received his M.Sc. (Eng.) and Licentiate of Technology degrees in material science and plastics technology from Tampere University of Technology (TUT), in 1980 and 1986, respectively. From 1980 to 1985 he was a research scientist at TUT. From 1985 to 1988 he worked at Neste Oy as a researcher. From 1988 to 1991 he was a research scientist at VTT Technical Research Centre of Finland and since 1991 he has been senior scientist at VTT. His research interest is in electrically conductive polymer compounds and polymer nanocomposites for electromechanical films and electrical insulation materials.

Matti Koponen has received the M.S. degree in mechanical engineering from the Technical University of Tampere, Finland, in 1990. He currently works as a research scientist at VTT Polymeric material processing and solutions, Tampere, Finland. His research interests include thermoplastic materials on electronic packaging and polymer processing.

Suvi Virtanen was born in Helsinki, Finland in 1979. She received the M.Sc. degree in organic chemistry from the University of Jyväskylä in 2004 at the international Master's Programme of Nanoscience. Since 2004 she has been a researcher and Ph.D. student in the same university. She received the Ph.D. degree in physical chemistry in 2013. The Ph.D. thesis topic was "Structural Characterization of Dielectric Polymer Nanocomposites". Her research interests are nanomaterials and their characterization

Mika Pettersson was born in Helsinki, Finland in 1969. He received the M.Sc. and Ph.D. degrees in physical chemistry from the University of Helsinki in 1995 and 1998, respectively. He spent a post-doctoral period at the University of California, Irvine during 2000 – 2001 in Prof. V. A. Apkarian's laboratory. He was a research fellow of the Academy of Finland during 2002 - 2007. He moved to the University of Jyväskylä in 2003 upon appointment as a senior lecturer in physical chemistry. During 2008 - 2010 was an acting professor and since 2011 a full Professor in physical chemistry at the University of Jyväskylä. His research interests include optical spectroscopy, imaging, characterization and fabrication of nano-objects.

Publication VII

I. Rytöluoto, K. Lahti, M. Ritamäki, and M. Karttunen, "The role of film processing in the large-area dielectric breakdown performance of nano-silica-BOPP films," in *24th Nordic Insulation Symposium (NORD-IS 15)*, pp. 63–68, 2015.

The Role of Film Processing in the Large-Area Dielectric Breakdown Performance of Nano-Silica-BOPP Films

I. Rytöluoto[1], K. Lahti[1], M. Ritamäki[1] & M. Karttunen[2]
[1]*Tampere University of Technology, Department of Electrical Engineering, Tampere, Finland*
[2]*Technical Research Centre of Finland, Tampere, Finland*

Abstract

This paper summarizes the effects of various compositional, structural and film processing factors on the breakdown behavior of laboratory- and pilot-scale melt-compounded bi-axially oriented polypropylene (BOPP) nanocomposite films with silica fillers. A self-healing multi-breakdown measurement approach has been extensively utilized for large-area breakdown characterization of a large number of material variants from different processing trials. The results suggest that although the optimum level of silica presumably resides at the low fill-fraction range (~1 wt-%), the silica content itself is not the only determining factor, as compounds with equal silica content were found to exhibit large differences in the breakdown properties depending on the compounding and film processing steps. Dispersion quality and filler agglomeration (in both the nm- and µm-scale) appear to be of great importance. Indications of possible interaction between nano-silica and co-stabilizer Irgafos 168 are also presented. Overall, the laboratory- and pilot-scale film processing trials suggest that up-scaling of the polymer nanocomposite production is sensible with traditional melt-blending technology, although further development and optimization of nanocomposite formulations and processing is necessary.

1. Introduction

In recent years, an increasing amount of research on dielectric polymer nanocomposite (PNC) films for next-generation high-energy-density capacitor applications has emerged and improvements in properties such as dielectric breakdown strength are strongly aspired for [1]. Inclusion of low amounts (~1 wt-%) of permittivity-matching nanoparticles such as silica in a suitable polymer matrix has been shown to be a promising approach, and some improvements in the short-term dielectric strength and breakdown distribution homogeneity have been previously reported [2]–[4]. However, as the dielectric breakdown performance of polymer-based thin films is largely dependent on various processing- and material-related aspects [5], [6], a thorough understanding of the underlying factors and optimization of the film processing parameters are crucial in order to achieve improved breakdown strength in practical insulation systems. Furthermore, provided that a potential PNC formulation is developed, it is equally important to consider whether or not it is possible to up-scale the film production process towards large-scale industrial manufacturing.

Our research has previously been focused on the DC breakdown performance of melt-compounded SiO_2-BOPP PNC films. A large-area multi-breakdown measurement approach based on the self-healing breakdown capability of metallized polymer films has been extensively applied for studying the breakdown properties, as it enables a large amount of breakdown data to be acquired from a relatively large total film area hence leading to a high statistical accuracy even at low breakdown probabilities. A detailed description and evaluation of the measurement method was recently given in [7] while studies exemplifying the large-area multi-breakdown characterization of various laboratory-scale, pilot-scale and commercial BOPP and BOPP-PNC films are presented in [3], [4], [8], [9].

The purpose of this paper is to make an overview of various material- and processing-related factors and their effects on the large-area multi-breakdown performance of SiO_2-BOPP PNC films. Special emphasis is put on the compositional and processing features which considerably affect the breakdown properties. Furthermore, up-scaling aspects are discussed and breakdown properties of SiO_2-BOPP PNC films produced on a Brückner pilot film line are compared with laboratory-scale films.

2. Experimental

2.1. Materials and film processing

A number of SiO_2-BOPP PNC film production trials were carried out in order to study the effects of various processing parameters on the breakdown performance. The studied processing trials were:

1. Effect of nano-SiO_2 fill-fraction
2. Effect of antioxidants
3. Effect of pre-mixing technique
4. Effect of compounder output and screw speed
5. Effect of bi-axial orientation temperature
6. Pilot-scale film production

Figure 1 presents an overview of the film processing steps together with the processing parameters which were varied along the production chain. The film processing was conducted at the VTT Technical Research Centre of Finland and at a Brückner pilot film line in Denmark. As the total amount of studied compounds was over 25, a detailed listing of all the materials, processing parameters and film specifications is out of the scope of this paper and can be found from the related publications ([3], [4], [7]). Only the essential aspects are summarized in the following.

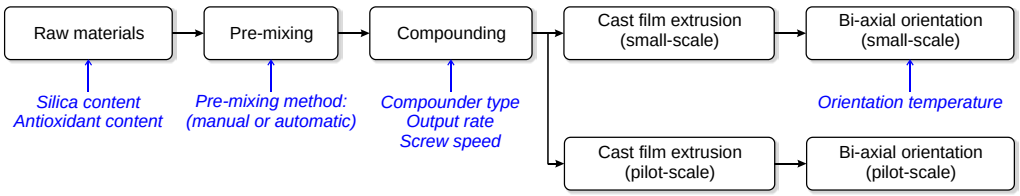

Figure 1 – SiO_2-BOPP PNC film processing steps and studied variables. (*black = processing step, blue = studied parameter*)

Unstabilized polypropylene (PP) homopolymer HC318BF in powder form (a non-commercial product from Borealis N.V.) was used as the matrix polymer. Nanofiller content of 4.5 wt-% of hexamethyldisilazane (HMDS)-treated hydrophobic fumed nano-silica (Aerosil R 812 S by Evonik) was used in most of the compounds, however, lower silica contents of 1.0 and 2.0 wt-% were also studied in one of the trials. Process stabilizer Irganox 1010 (0.47 wt-%) and co-stabilizer Irgafos 168 (0.35 wt-%) were added to the compounds in order to prevent thermo-oxidative degradation of PP during melt-processing. The co-stabilizer content was varied in one of the trials (0–0.35 wt-%).

For the laboratory-scale films, the general film processing steps were as follows. Initially, the raw materials (in powder form) were pre-mixed either manually in polyethylene bag or by using various automatic mixers and thereafter compounded mainly by a Berstorff ZE 25/48D twin screw compounder with high-shear screw geometry, two separate kneading sections and a melt filter (screen size 42 µm). The screw speed and output of the Berstorff ZE 25/48D compounder were 300 rpm and 9 kg/h, respectively, except for one trial in which the output was varied (3–15 kg/h at 300 rpm). Additionally, a high-speed twin screw Berstorff ZE 25 x 49D UTX compounder and a varying screw speed was also used in one of the trials (output 8 kg/h). The compounded strands were cooled and pelletized and thereafter extruded into ~500 µm cast films by a Brabender Plasticorder single screw extruder with a three-layer screen pack. Finally, the cast films were bi-axially oriented with a Brückner KARO IV film stretching machine (set temperature mainly 157 °C, stretching ratio 5.4 x 5.4), resulting in BOPP films ~15–23 µm in thickness. Detailed compounder and cast extrusion temperatures etc. can be found from [3].

Some of the compounds were also chosen for a pilot-scale film trial. The compounds (100–140 kg) were prepared similarly as described above. Automatic pre-mixing and the Berstorff ZE 25/48D compounder were used for the compounds presented in this paper. Pilot-scale films were then produced at a Brückner pilot film line in Denmark consisting of a single screw extruder with a flat die, a casting station, machine- and transverse direction orientation (MDO and TDO) units and a winder. The polymer compound was first melted in the extruder, quenched on the casting roll and then transferred to the MDO where it was reheated and stretched in the machine direction. Thereafter, the film was reheated in the TDO unit before transverse stretching and cooled down before winding.

2.2. Large-area multi-breakdown measurement and breakdown data analysis

Sample films for the multi-breakdown measurement were cut to 11 x 11 cm^2 dimensions from the bi-axially oriented film sheets. Thorough film thickness mapping was seen necessary in order to avoid error in the breakdown field calculation later on. Therefore, sample film thicknesses were measured systematically at 25 points covering a 10 x 10 cm^2 area with LE1000-1 high-precision thickness measurement gauge (accuracy 0.1 µm, resolution 0.05 µm). In order to realize the self-healing breakdown capability, Zn-Al-metallized BOPP film (12 µm Tervakoski PSX) was used as the electrode film. The sample film was sandwiched between two electrode films (metallized surfaces facing towards the sample film) and two additional sheets of 100 µm thick transparent polyester film in order to provide mechanical support, thus forming a test capacitor with an active area of 81 cm^2. The whole film arrangement was then fastened to a test bench consisting of a Bakelite bottom plate and a transparent acrylic plastic top plate. Electrical contacts with the metallized films were made by means of aluminum clamp electrodes at the both ends of the bottom plate. Six sample films were measured per each material resulting in 486 cm^2 total film area.

The measurements were conducted in insulating oil (Shell Diala DX) in accordance with IEC-60243 standard in order to mitigate surface flashovers. The DC voltage across the test capacitor was first raised to approximately 40–60% of the probable short-time breakdown voltage with a fast ramp speed of 400 V/s, after which a slow ramp speed of 30 V/s was used for measuring the self-healing breakdown events, roughly in accordance to the slow rate-of-rise test defined in the IEC-60243-1. The test setup and the procedure are discussed in more detail in [7].

During each discharge event in the test capacitor, the discharge current, test capacitor voltage and the time-signature of the event were recorded with a high-resolution oscilloscope operated in the sequence-acquisition mode and triggered to the positive rising edge of the discharge current signal. This allowed detailed determination of the breakdown voltage, voltage drop, peak current, discharge energy and various pulse time parameters for each event. A video was recorded from the top of the test capacitor unit for the whole duration of the breakdown measurement, allowing detailed chronological analysis of the breakdown progression of the sample after the

measurement. Breakdown fields were determined manually by rigorously determining the average thickness around the discharge spot (by means of the video recording) and by calculating the average breakdown field event-by-event in MATLAB.

Prior to the statistical analysis, a data selection procedure based on the discharge energy characteristics of the self-healing breakdown process was utilized in order to exclude non-breakdown events from the measurement data (such as partial discharges and consecutive breakdowns occurring close to or at previous breakdown sites). The breakdown data selection was performed in MATLAB. Detailed description of the procedure is omitted here and can be found elsewhere [7], [8]. Finally, for the statistical analysis of the qualified breakdown data sets, single 2-parameter Weibull distributions and, if necessary, additively mixed 2-parameter Weibull distributions were utilized:

$$F(x) = \sum_{i=1}^{S} \frac{N_i}{N} F_i(x) = \sum_{i=1}^{S} \frac{N_i}{N} \left[1 - \exp\left\{ -\left(\frac{x}{\alpha_i} \right)^{\beta_i} \right\} \right]. \quad (1)$$

In Eq. (1), $F_i(x)$ is the 2-parameter Weibull distribution, S is the number of subpopulations, N_i/N is the portion (%) of the subpopulation i and α_i and β_i are the Weibull parameters of subpopulation i. The scale parameter α corresponds to the value of x at the 63.2% failure probability and the shape parameter β depicts the slope or homogeneity of the fitted distribution. In the case of a single 2-parameter Weibull distribution, S and the portion N_i/N in Eq. (1) are equal to 1 and 100%, respectively. Maximum-likelihood estimation (MLE) and non-linear regression (NLR) methods were used for the parameter estimation and the analysis was performed with Weibull++ and MATLAB software. 90% confidence bounds were calculated for the Weibull parameters and breakdown percentiles by the Fisher Matrix (FM) method.

2.3. Nanoparticle size and dispersion quality analysis

Samples of the SiO_2-BOPP films were broken in liquid nitrogen and the cross-sectional surface morphologies were imaged with a JEOL JSM-6360LV scanning electron microscope (SEM). The SEM images were converted to binary images and the particle area distributions were determined by using ImageJ software. Moreover, a parameter describing the characteristic length of the unreinforced polymer domains, free-space length L_f, was also calculated and used to quantify the dispersion quality [3], [10]. L_f is defined as the width of the largest randomly placed square for which the most probable number of intersecting particles is zero. The MATLAB code for calculating L_f was retrieved and used according to the literature [10]. Further details about the free-space length characterization and its interpretation are available from the above publications.

3. Results and discussion

3.1. Large-area multi-breakdown results

Figure 2 presents a set of large-area multi-breakdown distributions from various processing trials on the Weibull probability scale along with the Weibull fits calculated according to Eq. (1). If applicable, single 2-parameter Weibull distributions were fitted to the breakdown data; otherwise mixed Weibull distributions were utilized on the basis of the best goodness-of-fit test result. 90 % confidence bounds were also calculated for each data set but they are omitted from Figure 2 for the sake of clarity.

As also discussed in [3], [4], Figure 2a clearly shows that an increase in silica content reduces the breakdown performance in the >5 % breakdown probability region in comparison to the unfilled reference BOPP but also leads to a concurrent improvement of the breakdown distribution homogeneity. Interestingly, the Weibull lines of the 1.0 wt-% SiO_2-BOPP PNC and the unfilled BOPP intersect in the 5–10 % breakdown probability range with the 1.0 wt-% SiO_2-BOPP PNC showing higher strength in the low probability region. This is promising, as considering film capacitors, for which the operative electric field is mandated by the electrical weak points in the polymer film, both the increase of breakdown distribution homogeneity (Weibull β) and the improvement in the low-probability breakdown behavior are substantially more relevant than the breakdown behavior in the higher (>10%) breakdown probability region.

It is remarked that transmission electron microscope (TEM) imaging revealed micron-sized agglomerates in the SiO_2-PP cast films [3] which most likely impact the breakdown performance. While the compounds presented in Figure 2a were pre-mixed manually, the possible effect of automatic mixing equipment on the dispersion quality was studied in another trial with 4.5 wt-% SiO_2-BOPP compounds (see [3]). Figure 3a–b present exemplifying SEM cross-sectional images of the films from the pre-mixing trial. Although pre-mixing technique appears to affect the silica nanodispersion, the multi-breakdown measurements suggested that the pre-mixing technique had little or no effect on the breakdown behavior. This, conversely, also confirms that automatic pre-mixing of larger batches is applicable for up-scaling purposes.

Figure 2b presents a set of previously unpublished results from another trial in which a high-speed twin screw Berstorff ZE 25 x 49D UTX compounder with a varying screw speed (300, 600 and 1200 rpm) was used for compounding 4.5 wt-% SiO_2-PP. SEM cross-sectional images and the corresponding particle analysis results of the above films are presented in Figure 3c–e. Surprisingly, the 4.5 wt-% SiO_2-BOPP compounded with the slowest (300 rpm) screw speed shows a considerable shift towards higher dielectric strength while the 600 and 1200 rpm variants reside in the same range as the 4.5 wt-% SiO_2-BOPP presented earlier in

Figure 2a. For further comparison, Figure 2b also shows the 1.0 wt-% SiO_2-BOPP from Figure 2a, which exhibits a breakdown distribution strikingly similar to that of the 4.5 wt-% SiO_2-BOPP compounded with the 300 rpm screw speed. This result suggests that the silica wt-% content alone is not the only determining factor for SiO_2-BOPP PNC breakdown performance. Speculative explanations for the exceptional behavior could be e.g. improvement in silica dispersion and distribution or reduction of silica agglomeration with slower compounding. Although Figure 3c–e suggest no major differences in the nano-scale dispersion qualities or particle sizes, it is reminded that a large number of SEM images would be required to obtain a statistically reliable estimate of the whole particle size distribution in the materials. While probably scarce in quantity, larger agglomerates may hinder the otherwise beneficial effect of good nanodispersion [11]. Indeed, a few agglomerates ~500 nm in diameter were observed in some of the SEM images of the 1200 rpm 4.5 wt-% SiO_2-BOPP compound. On the other hand, another explanation for the results could be related to differences in antioxidant depletion rate with different compounding rates. It is remarked that residual antioxidant content in BOPP films (e.g. the main process stabilizer Irganox 1010) has been shown to impair the breakdown strength [12], [13]. A more detailed analysis is however out of the scope of this paper.

The effect of varying co-stabilizer (Irgafos 168) content on the breakdown performance is presented in Figure 2c. The unfilled BOPP shows a drastic difference in breakdown distribution homogeneity depending on whether Irgafos 168 was used or not, indicating that Irgafos 168 has a detrimental effect on the breakdown performance of the end-product. Interestingly, the

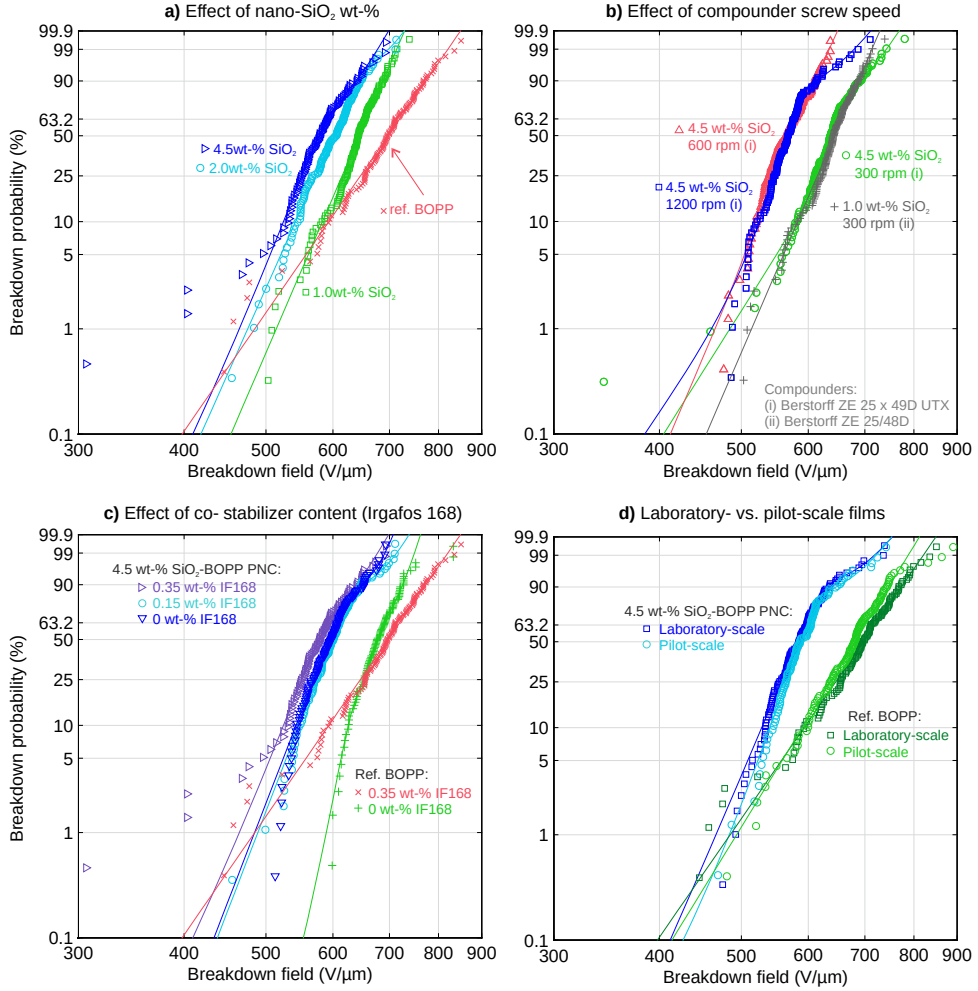

Figure 2 – Large-area multi-breakdown performance of BOPP-SiO_2 and reference-BOPP films. The Weibull probability plots show the effects of **a)** nano-silica filler content, **b)** compounder screw speed, **c)** co-stabilizer (Irgafos 168) content and **d)** a comparison of laboratory- and pilot-scale films. 6 samples (486 cm^2 total film area) per material were measured. 90 % confidence bounds were calculated but are not shown for clarity.

dependence on Irgafos 168 content is less prominent with the 4.5 wt-% SiO_2-BOPP variants which points towards possible interaction mechanism between silica and antioxidants. For example, a study by Nawaz *et al.* [14] suggests that a substantial amount of antioxidants can be adsorbed on the filler surfaces. Initial antioxidant adsorption on the nanofiller surfaces, film processing and the possible slow-release of the antioxidant residue from the adsorption sites over time may have an influence on both the short- and long-term breakdown performance of the end-product and should be investigated further in the future.

Lastly, Figure 2d presents a comparison of laboratory- and pilot-scale 4.5 wt-% SiO_2-BOPP PNC films with the corresponding unfilled reference films. It is evident that the up-scaling of the compounding and film processing stages was successful and resulted in films with similar breakdown properties as the corresponding laboratory-scale variants, in spite of the differences in the cast extrusion and bi-axial orientation steps (see [3]). Although more work is certainly needed to develop and optimize the PNC formulation, the results suggest that PNC film production for capacitor applications using traditional melt-blending technology

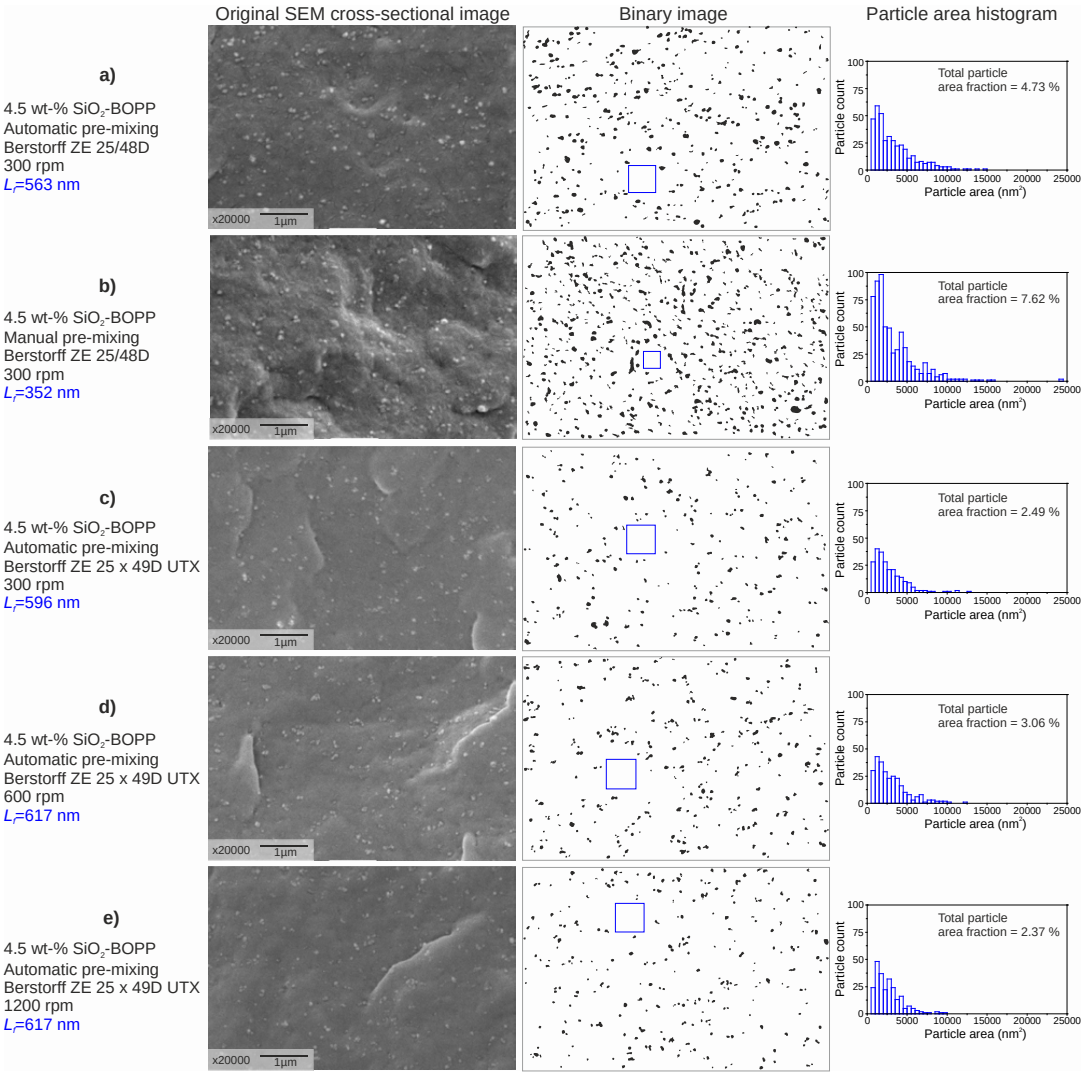

Figure 3 – SEM cross-section images (left), nanodispersion analysis (middle) and particle area histograms (right) of various 4.5 wt-% SiO_2-BOPP films. The pre-mixing method, compounder details and analysis results are given in the figure. The blue boxes (middle) denote the free-space length L_f used for the dispersion quality quantification [10]. L_f determination was performed iteratively in MATLAB (manual mode) by gradually increasing the amount of random tests up to 100000 in order to obtain high statistical accuracy. From the particle area histograms (right), the most probable particle diameter was approximated to be ~41 nm (assuming circular shape). The corresponding large-area multi-breakdown distributions for each film type are: (a) Figure 2d; (b) Figure 2a; (c), (d) and (e) Figure 2b.

is sensible. This is a positive result especially when considering the cost-effectiveness and high-volume production capability of the above technology [1].

3.2. Discussion

The results presented above cover some of the studied processing parameters and up-scaling aspects with definite effects on the final breakdown performance of SiO_2-BOPP and reference BOPP films. Other processing features with significant effects (such as the bi-axial orientation step) and less prominent effects (such as the compounder output rate) on the breakdown properties were also studied but are not presented here. Nevertheless, the previous section and the associated publications make it very clear that in addition to the compositional features (filler content, additives), the film processing stages and their optimization are in central role in achieving desirable breakdown properties with the polymer nanocomposite approach.

Aside from the material and processing related considerations alone, the breakdown measurement approach itself is also of great importance. The DC breakdown properties of the studied SiO_2-BOPP PNC films have been previously shown to exhibit strong dependence on the voltage ramp rate and sample area [3]. In a more systematic study of the 4.5 wt-% SiO_2-BOPP films as a function of DC field-ramp-rate, an increase in Weibull shape parameter of time was observed, which points towards slow deterioration of the breakdown performance over time possibly due to space charge build-up at the PP-silica and micro-agglomerate interfaces [15]. Results like this emphasize the importance of careful breakdown strength assessment when dielectric films of more complex internal structure are studied, as short-term small-area breakdown tests (as defined e.g. in IEC 60243) may lead to over-optimistic results.

4. Conclusion

In conclusion, the large-area breakdown response of laboratory- and pilot-scale SiO_2-BOPP PNC films was found to be strongly dependent on the composition and film processing. While the optimum silica content presumably resides at the low fill-fraction range (~1 wt-%), it is not the only determining factor, as compounds with equal silica content but differences in e.g. compounder screw speed were found to exhibit large differences in the breakdown response. Indications of possible silica-antioxidant interaction were also observed. The SEM-imaging analysis of the films showed that nano-structural features cannot solely explain the observed large-area breakdown behavior – this aspect points towards large-area approach being necessary for the imaging techniques as well in order to reliably establish a link between structural properties and engineering breakdown strength. Overall, the results suggest that up-scaling of PNC production is sensible with the traditional melt-blending technology, although further development and optimization of nanocomposite formulations and processing is necessary.

References

[1] J. K. Nelson, *Dielectric polymer nanocomposites*. Springer US, 2010.

[2] M. Takala, H. Ranta, P. Nevalainen, P. Pakonen, J. Pelto, M. Karttunen, S. Virtanen, V. Koivu, M. Pettersson, B. Sonerud, and K. Kannus, "Dielectric properties and partial discharge endurance of polypropylene-silica nanocomposite," *IEEE Trans. Dielectr. Electr. Insul.*, vol. 17, no. 4, pp. 1259–1267, 2010.

[3] I. Rytöluoto, K. Lahti, M. Karttunen, M. Koponen, S. Virtanen, and M. Pettersson, "Large-area Dielectric Breakdown Performance of Polymer Films – Part II: Interdependence of Filler Content, Processing and Breakdown Performance in Polypropylene-Silica Nanocomposites," *IEEE Trans. Dielectr. Electr. Insul.*, (in press), 2015.

[4] I. Rytöluoto, K. Lahti, M. Karttunen, M. Koponen, S. Virtanen, and M. Pettersson, "Influence of low amounts of nanostructured silica and calcium carbonate fillers on the large-area dielectric breakdown performance of bi-axially oriented polypropylene," in *2014 IEEE Conference on Electrical Insulation and Dielectric Phenomena (CEIDP)*, 2014, pp. 655–658.

[5] C. Calebrese, L. Hui, L. S. Schadler, and J. K. Nelson, "A review on the importance of nanocomposite processing to enhance electrical insulation," *IEEE Trans. Dielectr. Electr. Insul.*, vol. 18, no. 4. pp. 938–945, 2011.

[6] R. Bartnikas and R. Eichhorn, *Engineering Dielectrics Volume IIA Electrical Properties of Solid Insulating Materials: Molecular Structure and Electrical Behavior*. Philadelphia: ASTM International, 1983.

[7] I. Rytöluoto, K. Lahti, M. Karttunen, and M. Koponen, "Large-area Dielectric Breakdown Performance of Polymer Films – Part I: Measurement Method Evaluation and Statistical Considerations on Area-dependence," *IEEE Trans. Dielectr. Electr. Insul.*, vol. 22, no. 2, pp. 689–700, 2015.

[8] I. Rytöluoto and K. Lahti, "New approach to evaluate area-dependent breakdown characteristics of dielectric polymer films," *IEEE Trans. Dielectr. Electr. Insul.*, vol. 20, no. 3, pp. 937–946, 2013.

[9] I. Rytöluoto and K. Lahti, "Effect of Film Thickness and Electrode Area on the Dielectric Breakdown Characteristics of Metallized Capacitor Films," in *23rd Nordic Insulation Symposium (NORD-IS 13)*, 2013, pp. 33–38.

[10] H. S. Khare and D. L. Burris, "A quantitative method for measuring nanocomposite dispersion," *Polymer*, vol. 51, no. 3, pp. 719–729, 2010.

[11] S. Virtanen, H. Ranta, S. Ahonen, M. Karttunen, J. Pelto, K. Kannus, and M. Pettersson, "Structure and dielectric breakdown strength of nano calcium carbonate/polypropylene composites," *J. Appl. Polym. Sci.*, vol. 131, no. 1, p. 39504, 2014.

[12] J. Ho, R. Ramprasad, and S. Boggs, "Effect of alteration of antioxidant by UV treatment on the dielectric strength of BOPP capacitor film," *IEEE Trans. Dielectr. Electr. Insul.*, vol. 14, no. 5, pp. 1295–1301, 2007.

[13] A. Schneuwly, P. Gröning, L. Schlapbach, C. Irrgang, and J. Vogt, "Breakdown behavior of oil-impregnated polypropylene as dielectric in film capacitors," *IEEE Trans. Dielectr. Electr. Insul.*, vol. 5, no. 6, pp. 862–868, 1998.

[14] S. Nawaz, P. Nordell, H. Hillborg, and U. W. Gedde, "Antioxidant activity in aluminium oxide - Poly(ethylene-co-butyl acrylate) nanocomposites," *Polym. Degrad. Stab.*, vol. 97, no. 6, pp. 1017–1025, 2012.

[15] I. Rytöluoto, M. Ritamäki, K. Lahti, and M. Karttunen, "DC Field Ramp Rate Effect on the Large-Area Multi-Breakdown Response of SiO_2-BOPP Nanocomposites," in *2015 IEEE 11th International Conference on the Properties and Applications of Dielectric Materials (ICPADM)*, 2015.

Publication VIII

I. Rytöluoto, M. Ritamäki, K. Lahti, and M. Karttunen, "DC ramp rate effect on the breakdown response of SiO_2-BOPP nanocomposites," in *IEEE International Conference on the Properties and Applications of Dielectric Materials (ICPADM)*, pp. 496–499, 2015.

The following paper is the final version accepted for publication in IEEE Transactions on Dielectrics and Electrical Insulation. The published version of this paper is available at IEEE Xplore. DOI: 10.1109/ICPADM.2015.7295317

DC Ramp Rate Effect on the Breakdown Response of SiO_2-BOPP Nanocomposites

I. Rytöluoto[1], M. Ritamäki[1], K. Lahti[1], M. Karttunen[2]
[1]*Tampere University of Technology (TUT), Department of Electrical Engineering, Tampere, Finland*
[2]*Technical Research Centre of Finland (VTT), Tampere, Finland*

***Abstract*—The effect of voltage ramp rate on the short-term dielectric breakdown strength of polymer nanocomposites is not well-documented. In this paper, the effect of DC field ramp rate on the large-area breakdown performance of melt-extruded bi-axially oriented polypropylene (BOPP) films incorporating 4.5 wt-% of nano-silica is studied. By utilizing a self-healing multi-breakdown measurement method with a variable DC voltage ramp rate, a statistically large amount of breakdown data was obtained from a large total sample film area as a function of DC field ramp rate (0.1-50 $Vs^{-1}\mu m^{-1}$)). With a decreasing ramp rate, Weibull statistical analysis of the breakdown data suggests a systematically decreasing trend in the breakdown strength (Weibull α) and an increase in the Weibull shape parameter of time (a>1) for the nanocomposite. The observed behavior is speculated to be attributable to highly altered internal charge dynamics of the silica-BOPP nanocomposite. The results exemplify the importance of careful breakdown strength assessment when dielectric films of more complex internal structure are studied.**

Keywords—BOPP; silica; nanocomposite; breakdown; ramp rate dependence; Weibull

I. INTRODUCTION

Recently, dielectric polymer nanocomposites (PNC) incorporating <5 wt-% of inorganic nanoparticles have been envisioned as a potential approach to achieve novel dielectrics with superior energy densities for next-generation capacitive energy storage applications [1]. While improvements in short-term small-area dielectric breakdown strength have been reported for some PNC systems [1, 2], a number of conflicting reports indicating a systematic reduction of breakdown strength with increasing fill-ratio have also been presented in literature [3-7]. Possible explanations for the inconsistencies may be attributed to differences in e.g. filler-matrix compatibilization, material processing and nanofiller dispersion and distribution qualities. Breakdown measurement conditions such as sample thickness, active area, electrodes and the properties of the surrounding medium are also known to affect the measurement [8-9]. However, the effect of voltage ramp-rate on the dielectric breakdown strength of PNC dielectrics is not well documented, and given the rather large divergence of ramp-rates found in the relevant literature, it may certainly be one of the underlying factors influencing the breakdown strength results.

In this paper, the effect of DC field ramp rate on the large-area breakdown performance of melt-extruded (BOPP) films incorporating 4.5 wt-% of nano-silica is studied. The large-area breakdown measurement was based on the self-healing breakdown capability of metallized film which enables the measurement of multiple breakdowns from the sample area. A detailed description and evaluation of the measurement method was recently given in [10] while studies exemplifying the large-area multi-breakdown characterization of various laboratory-scale, pilot-scale and commercial BOPP and BOPP-nanocomposite films are presented in [6, 7, 11].

978-1-4799-8903-4/15/$31.00 ©2015 IEEE

II. EXPERIMENTAL

A. Film processing and sample details

Sample details along with the measured average film thicknesses and standard deviations are presented in Table I. Unstabilized polypropylene homopolymer HC318BF in powder form (a non-commercial product from Borealis N.V.) was used as the matrix polymer. The studied filler content was 4.5 wt-% of Aerosil R812 S (hydrophobic fumed silica by Evonik). Process stabilizer Irganox 1010 (0.47 wt-%) and co-stabilizer Irgafos 168 (0.35 wt-%) were added to the compounds in accordance with Table I. A capacitor-grade hazy BOPP film manufactured by Tervakoski Films Group was also studied as an additional commercial reference.

The raw powder materials were first pre-mixed automatically with a drum mixer (mixing time of 3 min) and thereafter compounded by a Berstorff ZE 25/48D twin screw compounder with high-shear screw geometry, two separate kneading sections and a melt filter (screen size 42 µm). The compound was cooled in a water bath under a laminar air flow hood over the cooling section. Polymers were dried at 70 °C for 1.5 hours in an oven and for 0.5 hour in a vacuum oven prior to compounding. The compounding was conducted at the VTT Technical Research Centre of Finland. Pilot-scale films were then produced from the compounds at a Brückner pilot film line in Denmark. The pilot line consisted of a single-screw extruder with a flat die, a casting station, MDO and TDO units and a winder. First, the polymer compound was melted in the extruder, quenched on the casting roll and then transferred to the MDO where it was re-heated and stretched in the machine direction. Thereafter, the film was reheated in the TDO unit before transverse stretching and cooled down before winding. The temperature profile of the extruder was between 214 °C to 240 °C. Chill roll temperature was 62 °C. MD stretching roll temperatures were 142 °C to 155 °C and the stretching ratio was approximately 1:4. In TD-stretching the oven section temperatures were 170 °C to 183 °C and TD-stretching ratio was approximately 1:6.

For the multi-breakdown measurement, sample films were cut to 11 x 11 cm^2 dimensions from the film rolls. As the pilot-scale films were found to exhibit a slightly uneven thickness profile along the TD-direction, thickness of each sample film

TABLE I. SAMPLE FILM DETAILS.

Code	Silica (wt-%)	Antioxidants (ppm)		Film thickness (µm)	
		Irganox 1010	Irgafos 168	Mean	SD
SiO_2-BOPP	4.50	4700	0	17.01	0.78
Ref-BOPP	-	4700	3500	16.10	0.74
Cap-BOPP	-	N/A	N/A	14.40	N/A

was mapped systematically at 25 points covering a 10 x 10 cm^2 area with an LE1000-1 high-precision thickness measurement gauge (accuracy 0.1 µm, resolution 0.05 µm). For the commercial film, the average thickness (14.4 µm) given by the manufacturer was used. The average sample film thicknesses and standard deviations are presented in Table I.

B. *Large-area multi-breakdown measurement with a varying DC field ramp rate*

In order to realize the self-healing multi-breakdown measurement, two 90 mm wide sheets of commercial Zn-Al-metallized BOPP film (12 µm Tervakoski PSX film, main metallization body resistivity 5-12 Ω/sq.) were used as electrode films above and under the sample film with the metallized surfaces facing towards the sample film, thus forming a test capacitor with an active area of 81 cm^2. The film arrangement was sandwiched between two sheets of 100 µm thick transparent polyester film in order to provide mechanical support for the films during the breakdown measurement. The film stack was then fastened to a test bench consisting of a Bakelite bottom plate and a transparent acrylic plastic top plate. Electrical contacts with the metalized films were made by means of aluminum clamp electrodes at the both ends of the bottom plate.

The breakdown measurements were conducted in electrically insulating oil (Shell Diala DX) in accordance with the IEC-60243 standard in order to mitigate surface flashovers and other non-breakdown events occurring at the sample and electrode film edges. The measurement circuit (Fig. 1) used for the multi-breakdown measurement consisted of a Spellman SL1200 DC high voltage source (peak power 1200 W, max. voltage 130 kV_{DC}) in parallel with the test capacitor. A 1.0330 Ω impulse current measurement resistor in series with the test capacitor and a Tektronix P6015A high voltage probe across the test capacitor were utilized for measuring the test capacitor current and voltage, respectively. The control voltage used for ramping up the high voltage source was generated with a National Instruments PCI-6221 DAQ card and LabVIEW software. A resistive voltage divider (Spellman HVD 100-1, divider ratio 1:10000) parallel to the test capacitor was used for general monitoring of the measurement voltage in LabVIEW.

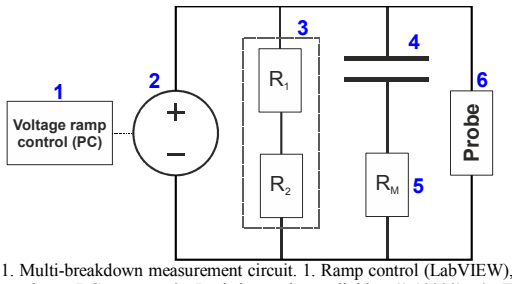

Fig. 1. Multi-breakdown measurement circuit. 1. Ramp control (LabVIEW), 2. High voltage DC source, 3. Resistive voltage divider (1:10000), 4. Test capacitor, 5. Current measurement resistor (1.0330 Ω), 6. High voltage probe.

During each discharge event in the test capacitor, the discharge current, test capacitor voltage and the time-signature of the event were recorded with a high-resolution oscilloscope (Lecroy HRO 66Zi) operated in sequence-acquisition mode and triggered to the positive rising edge of the discharge current signal. This allowed detailed determination of the breakdown voltage, voltage drop, peak current, discharge energy and various pulse time parameters for each discharge event. A video was recorded from the top of the test capacitor unit for the whole duration of the breakdown measurement, allowing detailed chronological analysis of the breakdown progression after the measurement. A linearly rising ramp profile was utilized and DC field ramp-rates of 0.25, 1, 5, 10, 25 and 50 $Vs^{-1}µm^{-1}$ were used. The corresponding DC voltage rate-of-rise was calculated for each sample film by utilizing the average sample film thickness. Four sample films were measured per each ramp-rate condition, resulting in 324 cm^2 total measured film area.

The breakdown fields of the pilot-scale films were calculated event-by-event by rigorously determining the average thickness around the each discharge spot by means of the video recording and the sample film thickness map in MATLAB. Albeit more laborious, this minimizes the error in the breakdown field calculation due to thickness deviation [10]. For the commercial film, breakdown fields were calculated by using the average thickness given by the manufacturer. Prior to the statistical analysis, a data selection procedure based on the breakdown voltage trend and discharge energy characteristics of the self-healing breakdown process was utilized in order to rule out non-breakdown events from the measurement data (such as partial discharges and consecutive breakdowns occurring close to or at previous breakdown sites). The number of discharge events considered from each sample was delimited to 50 first events. Detailed description of the procedure is omitted here and can be found elsewhere [10].

C. *Statistical analysis of the multi-breakdown data and field-ramp-rate-dependence*

Single 2-parameter Weibull distributions and, if necessary, additively mixed 2-parameter Weibull distributions were fitted to the qualified breakdown data [12]:

$$F(E)=\sum_{i=1}^{S}\frac{N_i}{N}F_i(E)=\sum_{i=1}^{S}\frac{N_i}{N}\left[1-\exp\left\{-\left(\frac{E}{\alpha_i}\right)^{\beta_i}\right\}\right]. \quad (1)$$

In Eq. (1), $F_i(E)$ is the 2-parameter Weibull distribution, S is the number of subpopulations (in this study either 1 or 2), N_i/N is the portion (%) of the subpopulation i and α_i and β_i are the Weibull parameters of subpopulation i. The scale parameter α corresponds to the electric field magnitude E at the 63.2% failure probability and the shape parameter β depicts the slope or homogeneity of the distribution. For a single 2-parameter Weibull distribution, S and the portion N_i/N in (1) are equal to 1 and 100%, respectively. Maximum-likelihood estimation (MLE) and non-linear regression (NLR) methods were used for the parameter estimation and the analysis was performed with Weibull++ software. 90% confidence bounds were calculated based on the Fisher Matrix (FM) method.

The analysis of the ramp-rate-dependence was based on the work by Hill, Dissado and co-workers [8, 13, 14]. For a ramp voltage test, assuming a linearly rising field stress, they derived a cumulative failure distribution of form:

$$F(E) = 1 - \exp\left(-C\frac{a}{a+b}E_{ramp}^{-a}E^{a+b}\right), \quad (2)$$

where E_{ramp} is the field ramp rate, E is the electric field magnitude, constants a and b correspond to the Weibull shape parameters of time and electric field, respectively, and C is the constant of proportionality. Eq. (2) can be written in a form analogous to a 2-parameter Weibull distribution $F_i(E)$ from Eq. (1), i.e., the Weibull shape parameter $\beta=a+b$. Thus, if several tests are performed at different field-ramp-rates, a log-log graph of the field ramp rate as a function of characteristic field (Weibull α) will result in a graph of slope $(a+b)/a$, thus allowing the constants a, b and C to be determined. If a mixed Weibull distribution was utilized (Eq. (1), S=2), the second subpopulation was used as a basis for the above calculation, similarly as in [15]. It is noted that Rowland *et al.* [14] have also derived a cumulative distribution for a censored compound distribution (essentially being a truncated additively mixed Weibull distribution) with a form similar to Eq. (2). However, utilization of such a distribution was not seen appropriate in the present study as the breakdown data sets showed no apparent truncation and additively mixed Weibull distributions were used only in exceptional cases.

III. Results and Discussion

Fig. 2 and Table II present the large-area multi-breakdown distributions of SiO_2-BOPP, Ref-BOPP and Cap-BOPP films with a varying DC field ramp rate on Weibull probability scale. Although single 2-parameter Weibull distributions were found to fit well to most of the breakdown data sets, in some cases distinctive weak point populations were observed in the low-probability region deviating from the "intrinsic" distribution. In such cases additively mixed Weibull distributions (Eq. (1), S=2) were utilized in order to obtain satisfactory fit to the breakdown data. The Ref-BOPP film in particular was found to show a number of random weak points and the behavior was attributed to film wrinkles and inhomogeneities originating from the film processing.

TABLE II. WEIBULL PARAMETERS.

	Ramp rate ($Vs^{-1}\mu m^{-1}$)	0.25	1	5	10	25	50
SiO_2-BOPP	Weibull α (V/µm)	498	555	606	635	677	695
	Weibull β	23.90	18.09	15.95	11.81	16.28	19.29
	a	1.51	1.15	1.01	0.75	1.03	1.22
	b	22.38	16.94	14.94	11.06	15.25	18.07
Ref-BOPP	Weibull α (V/µm)	628	660	698	712*	727	701*
	Weibull β	19.47	19.70	18.34	17.93*	15.58	12.87*
	a	0.58	0.59	0.55	0.54	0.47	0.39
	b	18.88	19.11	17.79	17.39	15.11	12.49
Cap-BOPP	Weibull α (V/µm)	584*	584*	612	621	623	617
	Weibull β	29.38*	28.03*	25.62	26.97	20.93	24.23
	a	0.49	0.47	0.43	0.45	0.35	0.40
	b	28.89	27.57	25.20	26.52	20.58	23.82

*) 2nd sub-population from Equation (1).

It is evident from Fig. 2 and Table II that the 4.5 wt-% SiO_2-BOPP nanocomposite shows a strong dependence on the DC field ramp rate, with the breakdown field at 63.2 % probability systematically decreasing from 695 to 498 V/µm as the ramp rate is decreased from 50 to 0.25 $Vs^{-1}\mu m^{-1}$. While the un-filled Ref-BOPP film also shows a slightly decreasing trend with a decreasing ramp rate, the phenomenon is less prominent and more scattered than in the case of the nanocomposite. Interestingly, SiO_2-BOPP and Ref-BOPP exhibit similar breakdown performances at the highest ramp rate. The Cap-BOPP film shows the most stable behavior as the breakdown distributions measured at 5, 10, 25 and 50 $Vs^{-1}\mu m^{-1}$ are nearly equal to each other within 90 % confidence bounds. The observed relatively weak ramp-rate-dependence of the un-filled BOPP films is consistent with previous studies on e.g. BOPP [16] and parylene F [17] films. At the slowest ramp rates (0.25 and 1 $Vs^{-1}\mu m^{-1}$) the 63.2 % the Cap-BOPP film shows a slight decrease in the high-probability breakdown region and emergence of weak point population. However, it should be

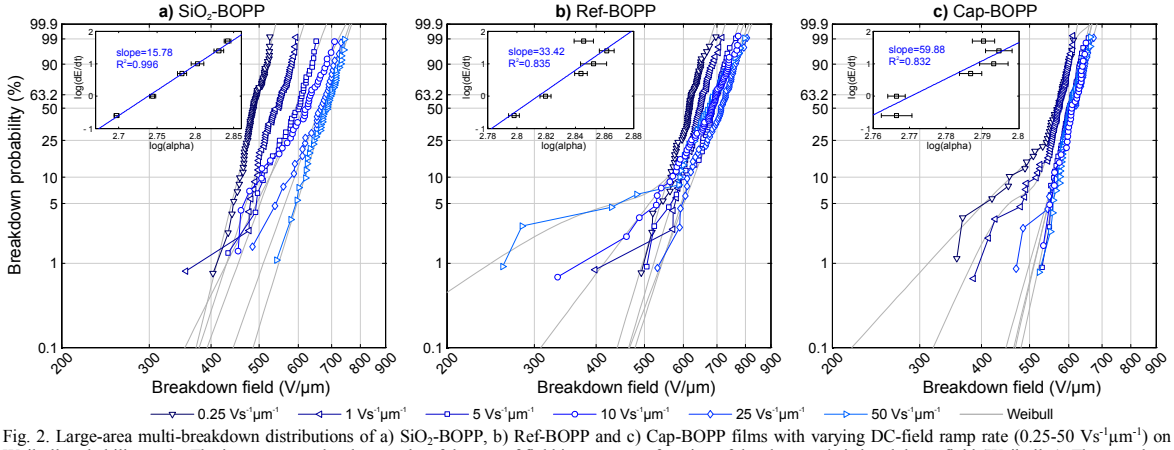

Fig. 2. Large-area multi-breakdown distributions of a) SiO_2-BOPP, b) Ref-BOPP and c) Cap-BOPP films with varying DC-field ramp rate (0.25-50 $Vs^{-1}\mu m^{-1}$) on Weibull probability scale. The insets present log-log graphs of the rate of field increase as a function of the characteristic breakdown field (Weibull α). The error bars represent 90 % confidence limits.

noted that especially at the slowest ramp rates material deterioration due to high-field ageing may also affect the breakdown properties. Lastly, considering all the studied materials, the Weibull β parameter of the 'intrinsic' breakdown distribution stays relatively constant as a function of ramp rate, as also predicted by Equation (2).

The insets in Fig. 2 show log-log graphs of the rate of field increase as a function of characteristic field (Weibull α), in which the slopes of the regression lines correspond to $(a+b)/a$. The SiO_2-BOPP nanocomposite in particular shows a nearly perfect fit with R^2 of 99.6%. Table II presents the calculated values of a and b at each ramp rate, with the mean values being a=1.11 and b=16.44 for SiO_2-BOPP, a=0.52 and b=16.80 for Ref-BOPP and a=0.43 and b=25.43 for Cap-BOPP, respectively. It is noted though that the calculation of a and b is sensitive to changes in Weibull α and β parameters [15], as is evident from Table II. In this study, film inhomogeneities, area effect and the large-area multi-breakdown measurement approach itself may at least partially explain the observed deviation. Nevertheless, when the Weibull shape parameter of time a<1, as in the case of Ref-BOPP and Cap-BOPP films, the Weibull hazard rate shows a monotonically decreasing trend, thus indicating a decreasing failure rate over time [8]. This could mean that breakdowns occurring at high fields and/or long times can be associated to inherent defects in the material instead of field-induced defects [15]. On the other hand, when 1<a<2, as for SiO_2-BOPP, the hazard rate increases over time but its rate of increase decreases, implying that breakdown probability increases and appears to stabilize to a certain level over time [8].

While the underlying reason for the stronger DC ramp-rate-dependence in the SiO_2-BOPP film is currently uncertain, the increase in a upon incorporation of nanofillers could well be attributable to altered space charge behavior due to polypropylene-silica interfaces [18], micron-sized agglomerates [6] and morphological changes in the initial cast films [19]. It is speculated that as the rate-of-rise decreases there is more time for space charge to accumulate at the interfaces which is manifested by an increase in a and a concurrent decrease in breakdown performance as discussed above. The slightly different antioxidant content (lack of Irgafos 168) in SiO_2-BOPP versus Ref-BOPP is probably not causing the observed behavior, as similar DC ramp-rate-dependence was previously observed with a 4.5 wt-% SiO_2-BOPP film with equal antioxidant content and processing as the Ref-BOPP film [6]. Either way, in conclusion, we suggest that a slow-rate-of-rise test (as e.g. in [6, 7]) or short-term testing at different ramp rates should be considered when measuring breakdown strength of PNC films in order to ascertain that the results reflect the true nature of the material.

IV. Implications and Conclusions

The study on the ramp-rate-dependence of the large-area multi-breakdown performance revealed that the 4.5 wt-% SiO_2-BOPP nanocomposite exhibits a systematic decrease in dielectric strength and increase in Weibull shape parameter of time in comparison to the un-filled BOPP films. The observed behavior was speculated to be attributable to highly altered internal charge dynamics of the silica-BOPP nanocomposite. The results exemplify the importance of careful breakdown strength assessment when dielectric films of more complex internal structure are studied. Breakdown assessment of polymer nanocomposites based solely on short-term test (as defined e.g. in IEC 60243 and ASTM D149 standards) may not reveal the breakdown properties of PNC films inclusively and, in the worst case, can lead to over-optimistic conclusions.

References

[1] J. K. Nelson, *Dielectric Polymer Nanocomposites*.: Springer US, 2010.

[2] E. David and M. Fréchette, "Polymer Nanocomposites - Major Conclusions and Achievements Reached So Far," *IEEE Electr. Insul. Mag.*, vol. 29, no. 6, pp. 29-36, 2013.

[3] S. Virtanen, H. Ranta, S. Ahonen, M. Karttunen, J. Pelto, K. Kannus and M. Pettersson, "Structure and dielectric breakdown strength of nano calcium carbonate/polypropylene composites," *J. Appl. Polymer Sci.*, Vol. 131, No. 1, pp. 39504.1-8, 2014.

[4] M. Praeger, A.S. Vaughan and S.G. Swingler, "The breakdown strength and localised structure of polystyrene as a function of nanosilica fill-fraction," *IEEE Int'l. Conf. Solid Dielectr., (ICSD)*, 2013, pp. 863-866.

[5] C. A. Grabowski, S. P. Fillery, N. M. Westing, C. Chi, J. S. Meth, M. F. Durstock and R. A. Vaia, "Dielectric Breakdown in Silica–Amorphous Polymer Nanocomposite Films: The Role of the Polymer Matrix," *ACS Appl. Materials Interfaces*, Vol. 5, No. 12, pp. 5486-5492, 2013.

[6] I. Rytöluoto, K. Lahti, M. Karttunen, M. Koponen, S. Virtanen and M. Pettersson, "Large-Area Dielectric Breakdown Performance of Polymer Films – Part II: Interdependence of Filler Content, Processing and Breakdown Performance in Polypropylene-Silica Nanocomposites," *IEEE Trans. Dielectr. Electr. Insul.*, in press, 2014.

[7] I. Rytöluoto, K. Lahti, M. Karttunen, M. Koponen, S. Virtanen and M. Pettersson, "Influence of low amounts of nanostructured silica and calcium carbonate fillers on the large-area dielectric breakdown performance of bi-axially oriented polypropylene," *IEEE Conf. Electr. Insul. Dielectr. Phenomena, (CEIDP),* 2014, pp. 655-658.

[8] L. A. Dissado and J. C. Fothergill, *Electrical Degradation and Breakdown in Polymers*. Philadelphia: Peter Peregrinus Ltd., 1992.

[9] C. Daran-Daneau, E. David, M. F. Frechette and S. Savoie, "Influence of the surrounding medium on the dielectric strength measurement of LLDPE/clay nanocomposites," *IEEE Int'l. Conf. Electrical Insulation, (ISEI)*, pp. 654-658, 2012.

[10] I. Rytöluoto, K. Lahti, M. Karttunen and M. Koponen, "Large-Area Dielectric Breakdown Performance of Polymer Films – Part I: Measurement Method Evaluation and Statistical Considerations on Area-Dependence," *IEEE Trans. Dielectr. Electr. Insul.*, in press, 2014.

[11] I. Rytöluoto and K. Lahti, "New Approach to Evaluate Area-Dependent Breakdown Characteristics of Dielectric Polymer Films," *IEEE Trans. Dielectr. Electr. Insul.*, vol. 20, no. 3, pp. 937-946, 2013.

[12] Hauschild W. and Mosch W., *Statistical Techniques for High-Voltage Engineering*. Philadephia: Institution of Engineering and Technology, 1992.

[13] R. M. Hill and L. A. Dissado, "Examination of the statistics of dielectric breakdown," *J. Phys. C: Solid State Phys.*, vol. 16, pp. 4447-4468, 1983.

[14] S. M. Rowland, R. M. Hill and L. A. Dissado, "Censored Weibull statistics in the dielectric breakdown of thin oxide films," *J. Phys. C: Solid State Physics*, vol. 19, no. 31, pp. 6263-6285, 1986.

[15] S. K. Haywood, M. M. Heyns and R. F. De Keersmaecker, "The statistics of dielectric breakdown in MOS capacitors under static and dynamic voltage stress," *Appl. Surf. Sci.*, vol. 30, no. 1-4, pp. 325-332.

[16] S. J. Laihonen, A. Gustafsson, U. Gafvert, T. Schutte and U.W. Gedde, "Area Dependence of Breakdown Strength of Polymer Films: Automatic Measurement Method," *IEEE Trans. Dielectr. Electr. Insul.*, vol. 14, no. 2, pp. 263-274, 2007.

[17] R. Khazaka, M. Bechara, S. Diaham and M.-L. Locatelli, "Parameters affecting the DC breakdown strength of parylene F thin films," *IEEE Conf. Electr. Insul. Dielectr. Phenomena, (CEIDP)*, 2011, pp. 740-743.

[18] G. Chen, Z. Junwei, S. Li and L. Zhong, "Origin of thickness dependent dc electrical breakdown in dielectrics," *Appl. Phys. Letters*, vol. 100, no. 22, 2012.

[19] A. Pustak, I. Pucić, M. Denac, I. Švab, J. Pohleven, V. Musil and I. Šmit, "Morphology of polypropylene/silica nano- and microcomposites," *Journal of Appl. Polymer Sci.*, vol. 128, no. 5, pp. 3099-3106, 2013.

Tampereen teknillinen yliopisto
PL 527
33101 Tampere

Tampere University of Technology
P.O.B. 527
FI-33101 Tampere, Finland

ISBN 978-952-15-3637-3
ISSN 1459-2045